



HAL
open science

Information-theory based measures for image analysis : development of two- and threedimensional entropy measures for image texture evaluation and their application to the biomedical field.

Mirvana Hilal

► **To cite this version:**

Mirvana Hilal. Information-theory based measures for image analysis: development of two- and threedimensional entropy measures for image texture evaluation and their application to the biomedical field.. Signal and Image Processing. Université d'Angers, 2020. English. NNT: 2020ANGE0039 . tel-03421541

HAL Id: tel-03421541

<https://theses.hal.science/tel-03421541>

Submitted on 9 Nov 2021

HAL is a multi-disciplinary open access archive for the deposit and dissemination of scientific research documents, whether they are published or not. The documents may come from teaching and research institutions in France or abroad, or from public or private research centers.

L'archive ouverte pluridisciplinaire **HAL**, est destinée au dépôt et à la diffusion de documents scientifiques de niveau recherche, publiés ou non, émanant des établissements d'enseignement et de recherche français ou étrangers, des laboratoires publics ou privés.

THÈSE DE DOCTORAT DE

L'UNIVERSITÉ D'ANGERS
COMUE UNIVERSITÉ BRETAGNE LOIRE

ÉCOLE DOCTORALE N° 601
*Mathématiques et Sciences et Technologies
de l'Information et de la Communication*
Spécialité : *Signal, Image, Vision*

Par

« **Mirvana HILAL** »

« **Information-theory based measures for image analysis :
Development of two- and three-dimensional entropy measures for
image texture evaluation and their application to the biomedical
field** »

Thèse présentée et soutenue à Angers - France, le 17 novembre 2020

Unité de recherche : Laboratoire Angevin de Recherche en Ingénierie des Systèmes - LARIS

Thèse N° : 190361

Rapporteurs avant soutenance :

Mme Christine FERNANDEZ-MALOIGNE
M Philippe RAVIER

Professeur des Universités - Université de Poitiers
Maître de Conférences HDR - Université d'Orléans

Composition du Jury :

Président : Yann GOUSSEAU
Examineurs : Christine FERNANDEZ-MALOIGNE
Jean-Marc GIRAULT
Philippe RAVIER
Dir. de thèse : Anne HUMEAU-HEURTIER

Professeur des Universités - Télécom Paris
Professeur des Universités - Université de Poitiers
Professeur HDR - ESEO Angers
Maître de Conférences HDR - Université d'Orléans
Professeur des Universités - Université d'Angers

PhD Thesis

Mirvana W. Hilal

Université d'Angers - France

Laboratoire Angevin de Recherche en Ingénierie des Systèmes - LARIS

**Information-theory based measures for image analysis:
Development of two- and three-dimensional entropy measures
for image texture evaluation and their application to the
biomedical field**

**Mesures basées sur la théorie de l'information pour
l'analyse d'images: Développement de mesures d'entropie
bidimensionnelles et tridimensionnelles pour l'évaluation de la
texture des images et applications au domaine biomédical.**

To my parents

ACKNOWLEDGEMENT

First of all, I would like express my gratitude to my supervisor, Pr Anne Humeau-Heurtier, who has been a great mentor for me. She has taught me a lot about research methodology, discipline, and determination. She has guided me through every step of the way and was always present for encouragement and support on the professional and personal levels. I am grateful for everything you have done and I want you to know that I will always look up to you and follow your steps. Without your guidance and pieces of advice, I would not have been able to accomplish this much during the past three years.

LARIS, Polytech d'Angers, and IUT d'Angers family, thank you for the work environment you provided, the friendly ambiance, and continuous help.

I gratefully acknowledge the support of LARIS and University of Angers for my PhD studies. I am thankful for this opportunity and for supporting my conference participations to represent LARIS and our research findings internationally.

I would like to thank my thesis monitoring committee members for their follow up and pieces of advice during our annual meetings.

I also take this opportunity to thank the people with whom I worked closely throughout our collaborations:

- Dr Hamed Azami for all his remarkable comments, thorough revision for part of my work, and his pieces of advice that will remain with me throughout my career.
- Pr Ludovic Martin and Dr Clemence Berthin at department of dermatology at Angers university hospital – Angers, France, for the medical information they provided, their suggestions from a medical point of view, and for being enthusiastic about all the new results and possible perspectives for our work together.
- the team at the University of Coimbra, Portugal: Pr João Cardoso, Dr Pedro G. Vaz, and Andreia Sofia F. Gaudêncio for the hard work, continuous follow up, and all that we have accomplished together.

— Andreia in particular, for all the fruitful discussions, hard work, and enthusiasm. I was so happy to work with you during your internship in Angers. Keep up the amazing energy and motivation that you have within, wishing you a bright continuation in every step of the way.

Furthermore, I am grateful for everyone I worked with during those past three years and for all the contributions by either providing the medical images, providing information, or simply discussions that helped in achieving the work presented in this manuscript.

My parents, Wafic and Sawsan, I dedicate this thesis and every accomplishment in my life to you. You have been patient, loving, and supportive all along this journey. I know that the whole idea of me settling abroad and pursuing my studies in France, was not easy for you as well, but you believed in me and helped me achieve my dream since the very first day. Your guidance, support, and inspiration are the reason I am here today. I trust that I can always aim for the stars with you by my side. Thanks a million!

My sister and brothers, Hanaa, Ribal, and Rabih, thank you for being always there for me, making me laugh even on my worst days, being great listeners, and following up with every detail.

A special dedication goes to my special one and best friend for life, for being supportive all the time, being patient during this journey, and helping me in the most difficult moments, to which the global pandemic was added! To many more success stories together my love, through thick and thin.

Last but not least, I would like to thank my close friends in France and Lebanon for following up with me during this amazing PhD journey. Cheers to many more successful journeys for each and everyone of you.

Sincerely,
Mirvana Hilal

“Nothing in life is to be feared, it is only to be understood”

“Sans la curiosité de l’esprit, que serions-nous?”

*Telle est bien la beauté et la noblesse de la science :
désir sans fin de repousser les frontières du savoir, de traquer
les secrets de la matière et de la vie sans idée préconçue des
conséquences éventuelles”*

Marie Curie



TABLE OF CONTENTS

| | |
|---|-----------|
| Résumé | 23 |
| Introduction | 27 |
| 1 Work Background | 31 |
| 1.1 Texture Analysis | 31 |
| 1.1.1 Texture analysis methods | 33 |
| 1.1.2 Colored texture analysis methods | 36 |
| 1.2 Entropy | 38 |
| 1.3 Entropy in Information Theory | 40 |
| 1.4 Entropy Measures | 41 |
| 1.4.1 Unidimensional entropy measures | 42 |
| 1.4.2 Bidimensional entropy measures | 49 |
| 1.5 Multiscale Bidimensional Entropy Measures | 57 |
| 1.6 Medical Applications | 59 |
| 1.6.1 Imaging modality: dermoscopy | 59 |
| 1.6.2 Skin: microcirculation | 60 |
| 1.6.3 Pseudoxanthoma elasticum (PXE) | 62 |
| 1.6.4 Melanoma | 66 |
| 1.6.5 Chronic obstructive pulmonary diseases (COPD) | 67 |
| 1.6.6 Idiopathic pulmonary fibrosis (IPF) | 68 |
| 1.6.7 Uterine fibroids | 70 |
| 1.6.8 COVID-19 | 71 |
| 1.7 Conclusion | 72 |
| 2 Methodology: Developed Bidimensional Entropy Measures | 73 |
| 2.1 Introduction | 73 |
| 2.2 Bidimensional Fuzzy Entropy | 74 |
| 2.2.1 Definition of $FuzEn_{2D}$ | 74 |
| 2.2.2 Definitions of $FuzEnL_{2D}$ and $FuzEnGL_{2D}$ | 77 |

TABLE OF CONTENTS

| | | |
|----------|---|-----------|
| 2.3 | Multiscale Bidimensional Fuzzy Entropy | 78 |
| 2.3.1 | Multiscale bidimensional fuzzy entropy MSF_{2D} | 79 |
| 2.3.2 | Modified multiscale bidimensional fuzzy entropy $MMSF_{2D}$ | 81 |
| 2.4 | Colored Fuzzy Entropy Measures | 81 |
| 2.4.1 | Single-channel approach $FuzEnC_{2D}$ | 82 |
| 2.4.2 | Multi-channel approach $FuzEnV_{2D}$ | 85 |
| 2.4.3 | Modified multi-channel approach $FuzEnM_{2D}$ | 86 |
| 2.5 | Conclusion | 89 |
| 3 | Methodology: Developed Tridimensional Entropy Measures | 91 |
| 3.1 | Tridimensional Entropy Measures | 91 |
| 3.2 | Pseudo-tridimensional Multiscale Fuzzy Entropy Measure $pMFuzEn_{3D}$ | 92 |
| 3.3 | Tridimensional Fuzzy Entropy $FuzEn_{3D}$ | 93 |
| 3.4 | Multiscale Tridimensional Fuzzy Entropy MSF_{3D} | 95 |
| 3.5 | Conclusion | 96 |
| 4 | Validation Tests and Analysis | 99 |
| 4.1 | Introduction | 99 |
| 4.2 | Evaluation Data | 99 |
| 4.2.1 | MIX(p) processes | 100 |
| 4.2.2 | Noise images with different power spectra | 102 |
| 4.2.3 | Artificial periodic and synthesized texture images | 103 |
| 4.2.4 | Other texture datasets | 103 |
| 4.3 | $FuzEn_{2D}$ and MSF_{2D} Validation Tests | 106 |
| 4.3.1 | Comparing $FuzEn_{2D}$ to $FuzEn_{1D}$ | 106 |
| 4.3.2 | Sensitivity to variation in parameters r , \mathbf{m} , and n | 107 |
| 4.3.3 | Rotation and translation | 109 |
| 4.3.4 | Shuffling | 109 |
| 4.3.5 | $FuzEn_{2D}$ for MIX $_{2D}(p)$ images | 111 |
| 4.3.6 | WGN_{2D} and $1/f^\beta$ noise images | 112 |
| 4.3.7 | Gray scale image with additive noise | 113 |
| 4.3.8 | $FuzEn_{2D}$ for artificial periodic and synthesized texture images | 115 |
| 4.3.9 | Multiscale $FuzEn_{2D}$ for $1/f^\beta$ noise images | 116 |
| 4.3.10 | Multiscale $FuzEn_{2D}$ for synthetic images | 117 |
| 4.4 | $FuzEn_{2D}$, $FuzEnL_{2D}$, and $FuzEnGL_{2D}$ Comparison | 118 |

| | | |
|----------|---|------------|
| 4.5 | MSF_{2D} and $MMSF_{2D}$ Comparison | 123 |
| 4.6 | First Colored Fuzzy Entropy Approach $FuzEnC_{2D}$ | 124 |
| 4.6.1 | Sensitivity to change in tolerance level r | 125 |
| 4.6.2 | $MIX_{2D}(p)$ | 125 |
| 4.6.3 | Colored Brodatz images | 125 |
| 4.7 | $FuzEnC_{2D}$, $FuzEnV_{2D}$, and $FuzEnM_{2D}$ Validation Tests | 128 |
| 4.7.1 | Sensitivity to initial parameters | 129 |
| 4.7.2 | Detecting colored image irregularity | 129 |
| 4.7.3 | Studying texture images | 133 |
| 4.7.4 | Computation cost of $FuzEnC_{2D}$, $FuzEnV_{2D}$, and $FuzEnM_{2D}$ | 135 |
| 4.8 | $FuzEn_{3D}$ and MSF_{3D} Validation Tests | 136 |
| 4.8.1 | Sensitivity to variation in parameters r and \mathbf{m} | 136 |
| 4.8.2 | $FuzEn_{3D}$ for $MIX_{3D}(p)$ volumes | 137 |
| 4.8.3 | Shuffling | 138 |
| 4.8.4 | Pattern-based volumes | 140 |
| 4.8.5 | MSF_{3D} for noise volumes | 141 |
| 4.9 | Conclusion | 142 |
| 5 | Medical Applications and Discussion | 143 |
| 5.1 | Introduction | 143 |
| 5.2 | Bidimensional Entropy for PXE Dermoscopic Images | 143 |
| 5.2.1 | Gray scale dermoscopic images | 144 |
| 5.2.2 | Colored dermoscopic images | 147 |
| 5.2.3 | Conclusion | 148 |
| 5.3 | Melanoma and Melanocytic Nevi | 150 |
| 5.3.1 | Gray scale dermoscopic images | 151 |
| 5.3.2 | Colored dermoscopic images | 152 |
| 5.4 | Cutaneous Microcirculation Assessment | 158 |
| 5.5 | Chronic Obstructive Pulmonary Diseases (COPD) | 161 |
| 5.6 | Idiopathic Pulmonary Fibrosis (IPF) | 162 |
| 5.7 | COVID-19 | 167 |
| 5.8 | Uterine Artery Embolization (UAE) | 170 |
| 5.9 | Conclusion | 172 |
| | Conclusion and Perspectives | 173 |

TABLE OF CONTENTS

| | |
|--|------------|
| Extra Activities and Publications | 177 |
| 6 Annex | 181 |
| 6.1 Annex Chapter 1 | 181 |
| 6.2 Annex Chapter 5 | 181 |
| Bibliography | 185 |

LIST OF FIGURES

| | | |
|------|--|----|
| 1.1 | Example of texture images from Kylberg dataset. | 32 |
| 1.2 | Example of texture images ordered from regular to stochastic. | 33 |
| 1.3 | An example for calculating GLCM of a 4×4 gray level image. | 35 |
| 1.4 | Example of water states. | 40 |
| 1.5 | Schematic demonstration for $ApEn_{1D}$ and $SampEn_{1D}$ | 43 |
| 1.6 | Heaviside function. | 45 |
| 1.7 | MSE_{1D} for time series. | 48 |
| 1.8 | $SampEn_{2D}$ illustration | 52 |
| 1.9 | Schematic diagram for the two dimensional extension of permutation entropy. | 56 |
| 1.10 | Schematic diagram for a dermoscope. | 59 |
| 1.11 | Schematic demonstration of the dermal and subdermal plexus. | 60 |
| 1.12 | Microcirculation anatomy. | 61 |
| 1.13 | Autosomal recessive diseases | 63 |
| 1.14 | Neck papules | 64 |
| 1.15 | Eye angiod streaks | 64 |
| 1.16 | PXE manifestation | 65 |
| 1.17 | Image of melanoma (right) and melanocytic nevi (left) | 66 |
| 1.18 | Emphysema and chronic bronchitis | 67 |
| 1.19 | Idiopathic Pulmonary Fibrosis (IPF) | 69 |
| 1.20 | Uterine fibroids embolization. | 70 |
| 1.21 | COVID-19 patients examples. | 71 |
| 2.1 | Illustration for $FuzEn_{2D}$ of a gray scale image. | 75 |
| 2.2 | Illustrative schema for $FuzEn_{2D}$ algorithm. | 76 |
| 2.3 | Illustration for MSF_{2D} of an image. | 80 |
| 2.4 | Illustration for $FuzEnC_{2D}$ of an RGB color space image having $\mathbf{m} = [2, 2]$ | 83 |
| 2.5 | Illustrative schema for $FuzEnC_{2D}$ algorithm. | 84 |
| 2.6 | Illustration for $FuzEnV_{2D}$ of an RGB color space image with $\mathbf{m} = [2, 2, 2]$ | 87 |
| 2.7 | Illustration for $FuzEnM_{2D}$ of RGB color space image with $\mathbf{m} = [2, 2, 3]$ | 89 |

| | | |
|------|--|-----|
| 3.1 | Illustration diagram for $pMFuzEn_{3D}$. | 92 |
| 3.2 | Illustration for $FuzEn_{3D}$ of a volume. | 93 |
| 3.3 | Illustration for MSF_{3D} of a volume. | 97 |
| 4.1 | A representation for the exponential function $\exp(-(d_{ij}^m)^n/r)$. | 100 |
| 4.2 | $MIX_{1D}(p)$ family of signals. | 101 |
| 4.3 | $MIX_{2D}(p)$ family of images. | 102 |
| 4.4 | $MIX_{3D}(p)$ family of volumes. | 102 |
| 4.5 | Power spectral density (PSD) of four noise-based volumes. | 103 |
| 4.6 | Artificial periodic and synthesized textures. | 104 |
| 4.7 | Example of Brodatz texture images. | 105 |
| 4.8 | Pattern based volumes created for $FuzEn_{3D}$ evaluation. | 105 |
| 4.9 | Multiscale $FuzEn_{1D}$ and $FuzEn_{2D}$ comparison. | 107 |
| 4.10 | $FuzEn_{2D}$ and $SampEn_{2D}$ for pink noise image. | 108 |
| 4.11 | $FuzEn_{2D}$ for WGN_{2D} images. | 108 |
| 4.12 | Four randomly chosen Mondial Marmi granite images. | 109 |
| 4.13 | The results for hardware, bicubic, and bilinear rotated images. | 110 |
| 4.14 | $FuzEn_{2D}$ and $SampEn_{2D}$ for $MIX_{2D}(p)$ images. | 111 |
| 4.15 | $FuzEn_{2D}$ and $SampEn_{2D}$ for $MIX_{2D}(p)$ images of varying size. | 112 |
| 4.16 | $FuzEn_{2D}$ and $SampEn_{2D}$ for WGN_{2D} , blue, pink, and brownian noise images. | 113 |
| 4.17 | The widely used 512×512 pixels Lena gray scale image. | 114 |
| 4.18 | MSF_{2D} and MSE_{2D} for ten pink, brownian, blue and white 2D noise images. | 117 |
| 4.19 | MSF_{2D} and MSE_{2D} for WGN_{2D} , pink noise, and $MIX_{2D}(0.2)$ images. | 118 |
| 4.20 | Bidimensional fuzzy entropy measures comparison | 119 |
| 4.21 | Multiscale bidimensional fuzzy entropy measures for a 300×300 WGN_{2D} and pink noise images, \mathbf{m} from 1 to 3. | 120 |
| 4.22 | Multiscale bidimensional Fuzzy entropies for a 300×300 WGN_{2D} and pink noise images, \mathbf{m} from 4 to 6. | 121 |
| 4.23 | MSF_{2D} for WGN_{2D} , pink noise, and $MIX_{2D}(0.2)$. | 123 |
| 4.24 | $MMSF_{2D}$ for WGN_{2D} , pink noise, and $MIX_{2D}(0.2)$ images. | 123 |
| 4.25 | Images used for evaluating $FuzEnC_{2D}$. | 125 |
| 4.26 | Sensitivity of $FuzEnC_{2D}$ to variation in the values of r and \mathbf{m} . | 126 |
| 4.27 | $FuzEnC_{2D}$ for checker board pattern added with $MIX_{2D}(p)$. | 126 |
| 4.28 | 640×640 pixels colored Brodatz textures. | 127 |

| | | |
|------|--|-----|
| 4.29 | $FuzEnC_{2D}$ results for the red, green, and blue channels of the colored Brodatz image. | 130 |
| 4.30 | $FuzEnV_{2D}$ results with varying r and \mathbf{m} of the colored Brodatz image. . . | 131 |
| 4.31 | $FuzEnM_{2D}$ results with varying r and \mathbf{m} of the colored Brodatz image. . . | 131 |
| 4.32 | $FuzEnC_{2D}$ mean and standard deviation for $MIX_{2D}(p)$ images. | 132 |
| 4.33 | $FuzEnV_{2D}$ mean and standard deviation for $MIX_{3D}(p)$ images. | 133 |
| 4.34 | $FuzEnM_{2D}$ mean and standard deviation for $MIX_{3D}(p)$ images. | 133 |
| 4.35 | Colored Brodatz texture images, CBT. | 134 |
| 4.36 | $FuzEnC_{2D}$ results for the 144 sub-images and 300×300 pixels of the CBT in the three color spaces: RGB, HSV, and YUV. | 135 |
| 4.37 | $FuzEnV_{2D}$ results for the 144 sub-images and 300×300 pixels of the CBT in the three color spaces: RGB, HSV, and YUV. | 135 |
| 4.38 | $FuzEnM_{2D}$ results for the 144 sub-images and 300×300 pixels of the CBT in the three color spaces: RGB, HSV, and YUV. | 136 |
| 4.39 | $FuzEn_{3D}$ for white noise cubes with a varying tolerance level. | 137 |
| 4.40 | Mean and standard deviation of $FuzEn_{3D}$ for ten repetitions applied to $MIX_{3D}(p)$ using $\mathbf{m} = 1, 2, \text{ and } 3$ | 138 |
| 4.41 | $FuzEn_{3D}$ for shuffled images. | 139 |
| 4.42 | MSF_{3D} for noise cubes with different power spectra $(1/f^\beta)$ | 141 |
| 5.1 | FotoFinder bodystudio ATBM for total body mapping and dermoscopy. . . | 145 |
| 5.2 | Dermoscopic images for zones with papules and normal zones | 145 |
| 5.3 | MSF_{2D} and MSE_{2D} for normal zones and zones with PXE papules. | 147 |
| 5.4 | $FuzEnC_{2D}$ for 30 colored dermoscopic images of a region showing PXE papules and healthy skin region. | 148 |
| 5.5 | $FuzEnV_{2D}$ for 30 dermoscopic images of a region showing PXE papules and a healthy skin region. | 149 |
| 5.6 | $FuzEnM_{2D}$ for 30 dermoscopic images of a region showing PXE papules and a healthy skin region. | 149 |
| 5.7 | Image of melanoma (right) and melanocytic nevi (left) in gray scale. | 151 |
| 5.8 | MSF_{2D} for 15 melanoma and 15 melanocytic nevi dermoscopic images. . . | 152 |
| 5.9 | Dermoscopic images segmentation for choosing the ROI. | 153 |
| 5.10 | $FuzEnV_{2D}$ and Haralick features p -values of 40 melanoma and 40 melanocytic nevi dermoscopic images. | 155 |

LIST OF FIGURES

5.11 $FuzEnM_{2D}$ and Haralick features p -values of 40 melanoma and 40 melanocytic nevi dermoscopic images. 156

5.12 ROC curves for $FuzEnC_{2D}$ results of the 40 melanoma and 40 melanocytic nevi images. 157

5.13 ROC curve for $FuzEnV_{2D}$ results of the 40 melanoma and 40 melanocytic nevi images. 157

5.14 ROC curve for $FuzEnM_{2D}$ results of the 40 melanoma and 40 melanocytic nevi images. 158

5.15 $FuzEnC_{2D}$ for the dermoscopic images at rest and with vasodilation. 160

5.16 $pMFuzEn_{3D}$ for an HRCT scans. 163

5.17 Illustration for the selection process of the volume to be evaluated by MSF_{3D} from the HRCT scans [27]. 165

5.18 MSF_{3D} for the healthy subjects and IPF patients' CT scans. 166

5.19 Mean and standard deviation for the MSF_{3D} values for healthy subjects, idiopathic pulmonary fibrosis (IPF), and COVID-19 patients for scale factors $\tau = 1$ to 10. 169

5.20 Complexity index for COVID-19, IPF, and healthy subjects' results. 170

5.21 Mean and standard deviation for the complexity index for MSF_{3D} from $\tau=8$ till $\tau=10$ for UAE patients at the three time intervals D0, D10, and M6. 172

6.1 Skin diagram 181

6.2 Boxplots of $SampEn_{2D}$ from dermoscopy images. 182

LIST OF TABLES

| | | |
|------|---|-----|
| 1.1 | Definition of the computed Haralick features [48]. | 36 |
| 4.1 | $FuzEn_{2D}$ results upon translation of 3 Brodatz images. | 110 |
| 4.2 | $DistrEn_{2D}$, $SampEn_{2D}$, and $FuzEn_{2D}$ values for shuffled images | 110 |
| 4.3 | CVs for $FuzEn_{2D}$ and $SampEn_{2D}$ of 100×100 pixels WGN_{2D} and $1/f^\beta$ noise image. | 114 |
| 4.4 | $FuzEn_{2D}$ for a gray scale image (Lena image) added with different levels of WGN_{2D} | 115 |
| 4.5 | $FuzEn_{2D}$ for a gray scale image (Lena image) added with different densities of SPN noise. | 115 |
| 4.6 | $FuzEn_{2D}$ for artificial periodic textures and their synthesized textures (please see Figure 4.6). | 116 |
| 4.7 | Average calculation time for $FuzEn_{2D}$, $FuzEnL_{2D}$, and $FuzEnGL_{2D}$ (see text for details on the computer performance). | 122 |
| 4.8 | MSF_{2D} and $MMSF_{2D}$ computation cost comparison in seconds (see text for details on the computer performance). | 124 |
| 4.9 | $FuzEnC_{2D}$ for colored Brodatz textures (640×640 pixels). | 127 |
| 4.10 | Mean and standard deviation of $FuzEnC_{2D}$ for colored Brodatz textures sub-images (320×320 pixels). | 128 |
| 4.11 | Mean and standard deviation of the computation time for $FuzEnC_{2D}$, $FuzEnV_{2D}$, and $FuzEnM_{2D}$ for a 100×100 pixels colored Brodatz image. | 136 |
| 4.12 | $FuzEn_{3D}$ results for pattern-based volumes. | 140 |
| 5.1 | Interpretation of the Cohen's d values [164, 167]. | 146 |
| 5.2 | Cohen's d values for MSF_{2D} and MSE_{2D} at $\tau = 1, 2, 3$, and 4 for the normal skin regions vs. the regions with papules in pseudoxanthoma elasticum images. | 146 |

LIST OF TABLES

5.3 Cohen’s d -values for $FuzEnC_{2D}$, $FuzEnV_{2D}$, and $FuzEnM_{2D}$ of 40 melanoma and 40 melanocytic nevi dermoscopic images in the 3 color spaces: RGB, HSV, and YUV. 154

5.4 Mann-Whitney u test p -values for $FuzEnC_{2D}$, $FuzEnV_{2D}$, and $FuzEnM_{2D}$ of 40 melanoma and 40 melanocytic nevi dermoscopic images in the 3 color spaces: RGB, HSV, and YUV. 154

5.5 ROC analysis for $FuzEnC_{2D}$, $FuzEnV_{2D}$, and $FuzEnM_{2D}$ results of 40 melanoma and 40 melanocytic nevi images in RGB. 155

5.6 ROC analysis for $FuzEnC_{2D}$, $FuzEnV_{2D}$, and $FuzEnM_{2D}$ results of 40 melanoma and 40 melanocytic nevi images in HSV. 156

5.7 ROC analysis for $FuzEnC_{2D}$, $FuzEnV_{2D}$, and $FuzEnM_{2D}$ results of 40 melanoma and 40 melanocytic nevi images in YUV. 157

5.8 Mean and standard deviation of Haralick features for \mathbf{U}_R , \mathbf{U}_G , and \mathbf{U}_B for dermoscopic images of 9 individuals. 160

5.9 Characteristics of the studied population. 168

5.10 Mann–Whitney U test p -values and Cohen’s d values for MSF_{3D} results of healthy, IPF, and COVID-19 confirmed subjects. The * sign indicates the presence of a statistically significant difference between the compared groups at a given scale factor. 169

5.11 The p -values for the complexity index for $\tau_1=8$ and $\tau_2=10$ between pairs of D0, D10, and M6. 171

RÉSUMÉ

La texture est souvent définie comme étant la disposition spatiale des motifs, des couleurs et des intensités apparaissant dans un contenu visuel. La description d'un contenu visuel se fait souvent par ses deux composantes de base : la couleur et la texture.

L'analyse et la description de la texture sont parmi les problèmes les plus difficiles en vision par ordinateur. De nombreux algorithmes ont été proposés pour l'extraction de caractéristiques de texture au cours des dernières années et ce domaine de recherche fait toujours l'objet de nombreuses investigations [1, 2, 3, 4, 5, 6, 7, 8, 9].

Plusieurs méthodes ont été mises au point pour l'analyse de la texture et ont trouvé des applications dans divers domaines, tels que : domaine biomédical [10, 11, 12], automatisation industrielle [13, 14], télédétection [15, 16], reconnaissance faciale [17], récupération d'images basée sur le contenu [18].

L'une des méthodes les plus récentes introduites dans le domaine de l'analyse de texture est l'entropie [19, 20, 21, 22, 23, 24, 25]. Comme l'entropie, issue de la théorie de l'information, permet d'étudier l'irrégularité des signaux et des images, nous proposons de l'utiliser pour l'analyse de texture de données en niveaux de gris et couleurs.

Nous développons d'abord l'entropie bidimensionnelle floue, $FuzEn_{2D}$, et sa version multiéchelle pour étudier l'irrégularité et la complexité des images texturées. Après cela, nous proposons des approches colorées basées sur $FuzEn_{2D}$ pour étudier des images texturées colorées. Nous avons employé l'approche colorée pour révéler l'information cachée dans les composants de couleur. Nous présentons tout d'abord l'approche mono-canal $FuzEnC_{2D}$. Puis l'approche multicanal $FuzEnV_{2D}$ qui s'inspire du concept volumétrique. Enfin, l'approche multicanal modifiée $FuzEnM_{2D}$ est présentée comme une amélioration de $FuzEnV_{2D}$. Les algorithmes que nous proposons ont trouvé des applications prometteuses dans l'analyse de texture pour différents cas médicaux tels que le mélanome, le pseudoxanthome élastique et l'analyse de la microcirculation cutanée.

Suite aux résultats encourageants obtenus avec les mesures bidimensionnelles (2D) développées, une mesure d'entropie tridimensionnelle pour l'étude de volumes, ainsi que son extension multiéchelle, sont proposés. Ils ont été utilisés pour étudier des tomographies (CT), des tomographies haute résolution (HRCT), et des images obtenues par résonance

magnétique (IRM). Ceci nous a permis de traiter des examens volumétriques pour les patients atteints de COVID-19, de fibrose pulmonaire idiopathique et de fibrome utérin.

Dans ce manuscrit, plusieurs tests de validation communs sont présentés pour les méthodes développées, en plus des tests spécialement conçus pour chacune d'elles. Les mesures sont validées sur la base: des modifications des paramètres initiaux, leur capacité à quantifier les degrés d'irrégularité croissants aux niveaux bidimensionnel et tridimensionnel, et leur capacité d'évaluation de la complexité dans les images et les volumes à travers l'approche multiéchelle. Nos résultats montrent que les méthodes développer permettent d'analyser l'irrégularité des images en niveaux de gris, des images colorées, et enfin des volumes [26, 27, 28, 29, 30, 31].

Plan du manuscrit

Le manuscrit est organisé comme suit :

- Le chapitre 1 présente l'analyse bibliographique en lien avec nos travaux. Nous définissons ainsi le concept d'entropie, les mesures précédemment développées dans ce domaine, et les cas médicaux sur lesquels nos mesures proposées seront appliquées.
- Le chapitre 2 présente les mesures d'entropie bidimensionnelle que nous avons élaborées. Nous expliquons d'abord l'algorithme sous-jacent à l'entropie bidimensionnelle floue $FuzEn_{2D}$ et son extension multiscalaire MSF_{2D} . Ensuite, les algorithmes des mesures d'entropies floues bidimensionnelles colorées sont définis, $FuzEnC_{2D}$, $FuzEnV_{2D}$, et $FuzEnM_{2D}$.
- Le chapitre 3 présente les mesures d'entropies tridimensionnelles que nous avons proposées pour étendre notre application aux données volumétriques. Tout d'abord, une approche directement basée sur MSF_{2D} pour traiter les données volumétriques est présentée: une mesure multiéchelle pseudo-tridimensionnelle d'entropie floue, $pMFuzEn_{3D}$. Ensuite, l'entropie floue tridimensionnelle $FuzEn_{3D}$ et son extension multiéchelle MSF_{3D} sont décrites en détail avec leurs équations correspondantes.
- Le chapitre 4 présente les tests de validation utilisés pour chaque mesure développée.
- Le chapitre 5 présente les résultats obtenus avec nos mesures pour les images médicales 2D et 3D. Nos mesures 2D sont appliquées à des images dermoscopiques de mélanome, de psuedoxanthome élastique et pour l'analyse de la microcirculation

cutanée. Pour les examens volumétriques 3D, nos mesures ont permis l'étude de données enregistrées dans le cas de COVID-19, de fibrose pulmonaire idiopathique et de fibrome utérin.

INTRODUCTION

Introduction

Texture is often referred to as the spatial arrangement of the visual patterns, colors, and intensities appearing in a visual content. The description of a visual content is often done by its two basic components: color and texture.

Texture analysis and description are among the most challenging problems in computer vision. Many algorithms have been proposed for texture features extraction in the past years and this research area is still the subject of many investigations [1, 2, 3, 4, 5, 6, 7, 8, 9].

Several methods have been developed for texture analysis and found application in various domains, such as: biomedical field [10, 11, 12], industrial automation [13, 14], remote sensing [15, 16], face recognition [17], content-based image retrieval [18].

Texture analysis through entropy measures (issued from the information theory field) is at its very beginning but revealed promising results [19, 20, 21, 22, 23, 24, 25]. In this PhD manuscript work, we propose to extend these preliminary studies and we propose new entropy measures for texture analysis in the gray scale and colored spaces.

We first develop the bidimensional fuzzy entropy, $FuzEn_{2D}$, and its multiscale version to study the texture images' irregularity and complexity. The choice for using the fuzzy entropy concept is based on several previous publications, comparison tests that we performed on unidiemnsional and bidimensional levels, and the advantages of using fuzzy entropy over other entropy measures.

After that, we propose colored approaches based on $FuzEn_{2D}$ to study colored texture images. We employ the colored approach to reveal information hidden within the color components of our studied images. We thus first present the single-channel approach $FuzEnC_{2D}$ and then the multi-channel approach for colored images $FuzEnV_{2D}$ which is inspired by the volumetric concept. Finally, the modified multi-channel colored approach $FuzEnM_{2D}$ is proposed as an enhancement for $FuzEnV_{2D}$. Our proposed algorithms find promising applications in texture analysis for different medical cases such as melanoma, pseudoxanthoma elasticum, and cutaneous microcirculation analysis.

After the encouraging results with the developed bidimensional (2D) measures, a tridimensional entropy measure and its multiscale extension to study volumes are proposed. These measures extend our possible applications to volumetric scans. They are employed to study computed tomography (CT) scans, HRCT scans, and magnetic resonance imaging (MRI) scans. The medical investigation using our algorithms handle volumetric scans for COVID-19, idiopathic pulmonary fibrosis, and uterine fibroma patients.

In this manuscript, several common validation tests are presented for the developed methods, in addition to the specially designed tests for each. The measures are validated upon: changes in the initial parameters, their ability to quantify the increasing irregularity degrees in the bidimensional and tridimensional levels, and their complexity evaluation ability in images and volumes through the multiscale approach. These methods are illustrated to possess an ability to analyze irregularity of gray scale images, colored images, and finally volumes [26, 27, 28, 29, 30, 31].

In this thesis manuscript, we present entropy measures based on the information theory concept that illustrated a significant ability in this field.

In order to avoid having certain major errors that might occur due to the subjective judgment of a medical doctor sometimes, computer based measures come to be of great importance. They provide an objective assessment based on certain components that cannot be always identified or linked visually.

Moreover, as the medical field in several cases proves the need for computer based platforms for validating the diagnosis, for assisting in prognosis and for giving objective decisions, the research for computerized methods becomes essential. Computer based analysis methods could aid medical doctors and unify the worldwide decision making platforms – with a specific importance – for rare medical cases by being accessible all over the planet, by providing fast outcome based on the concrete background in comparison, and unifying the diagnosis criteria. The medical doctors' monitoring remains indispensable, however can be accompanied by a more objective computer based tool that could unify the medical decision making worldwide.

Outline of the thesis

This manuscript is organized as follows:

- Chapter 1 presents the background literature review of our work. In this chapter we define the entropy concept, the previously developed measures in this field, and the medical cases on which our proposed measures will be applied.
- Chapter 2 presents the bidimensional entropy measures that we developed. We first explain the algorithm behind bidimensional fuzzy entropy $FuzEn_{2D}$ and its multiscale extension MSF_{2D} . Then, the algorithms behind the colored bidimensional fuzzy entropy measures are defined, $FuzEnC_{2D}$, $FuzEnV_{2D}$, and $FuzEnM_{2D}$.
- Chapter 3 presents the tridimensional entropy measures that we propose to extend our application to volumetric data. First, an approach directly based on MSF_{2D} to deal with volumetric data is presented, pseudo-tridimensional multiscale fuzzy entropy measure, $pMFuzEn_{3D}$. Then, tridimensional fuzzy entropy $FuzEn_{3D}$ and its multiscale extension MSF_{3D} are described in details with their corresponding equations.
- Chapter 4 presents the validation tests employed for each developed measure.
- Chapter 5 presents the results obtained with our measures for the 2D and 3D medical images. Our 2D measures find application for dermoscopic images of melanoma, pseudoxanthoma elasticum, and cutaneous microcirculation analysis. For the 3D volumetric scans, our measures find application for COVID-19, idiopathic pulmonary fibrosis, and uterine fibroma patients.

WORK BACKGROUND

In this chapter we will first present a number of the existing texture analysis methods and detail some of them (section 1.1). One of the most recent methods introduced into the domain of texture analysis is entropy [19, 20, 21, 22, 23, 24, 25]. As information theory entropy studies the irregularity of signals and images, we propose its application for texture analysis in the gray scale and colored spaces. For this purpose, we will define, in section 1.2, entropy in various fields: thermodynamics and information theory. In the information theory field, we will detail the entropy algorithms that are used to assess irregularity of time series, unidimensional (1D) data (section 1.4.1). We will also present the very recent developments that have been proposed to assess irregularity of bidimensional (2D) data images (section 1.4.2). In this chapter, we will finally present the medical cases on which our developed entropy measures were applied. This involves:

- pseudoxanthoma elasticum, PXE
- cutaneous microcirculation
- melanoma and melanocytic nevi
- chronic obstructive pulmonary diseases, COPD, mainly emphysema and chronic bronchitis
- idiopathic pulmonary fibrosis, IPF
- uterine fibroids, UF
- COVID-19

1.1 Texture Analysis

Texture is often referred to as the spatial arrangement of the visual patterns, colors, and intensities appearing in an image. The description of a visual content is often done by its two basic components: color and texture. Developing tools for image analysis are first tested on texture images and their ability to analyze image textures of different irregularity degrees, patterns, and colors is assessed, before they are employed as texture analysis

tools. So textures form the evaluation platform allowing fast escalation in this field. Texture analysis finds application in various domains, such as: biomedical field [10, 11, 12], industrial automation [13, 14], remote sensing [15, 16], face recognition [17], content-based image retrieval [18].

Several 2D datasets were created for serving image analysis purposes and training computer aided tools [32, 33, 34, 35, 36, 37]. They are often used for evaluating and comparing texture measures, their sensitivity to noise, and geometric transforms. An example is Kylberg texture dataset shown in Figure 1.1. It is composed of 28 classes with 160 unique samples in each class. The samples are 576×576 pixels large and stored as gray scale 8-bit png-images [38]. Some other datasets that we used in our work will be detailed in section 4.2.4.

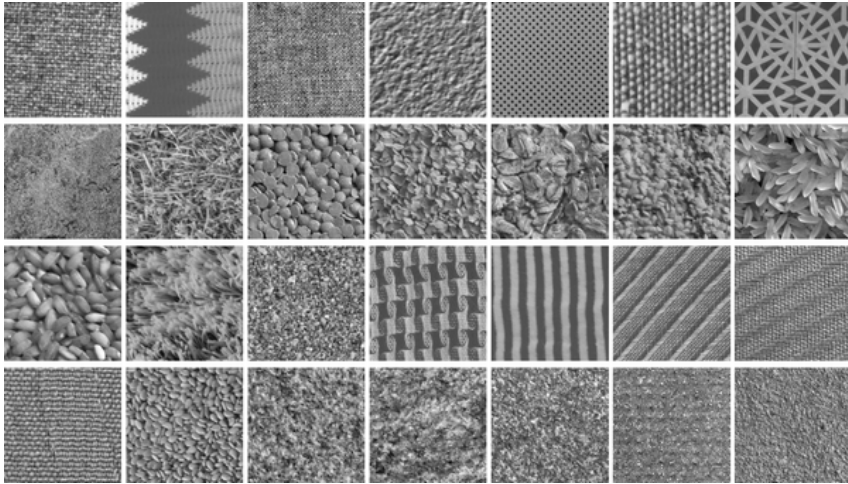


Figure 1.1 – Example of texture images from Kylberg dataset.

Texture analysis and description are among the most challenging problems in computer vision. Many algorithms have been proposed for texture features extraction in the past years and this research area is still the subject of many investigations [1, 2, 3, 4, 5, 6, 7, 8, 9]. Texture features are of the utmost importance in segmentation, classification, synthesis of images and many other image processing steps. However, no precise definition of texture has been adopted yet.

Although texture has no exact definition, it has long been an essential subject in human perception [39]. Precisely, regularity has been illustrated to play a major role in texture perception [40]. For example, a study by [39] propose quantitative measurements to characterize near-regular textures based two main components, see Figure 1.2. Other studies

propose six major textural features: coarseness, contrast, directionality, line-likeness, regularity, and roughness, to be considered in computation [41]. Some other studies rely on the visual identification of irregularity or other visual perception features.

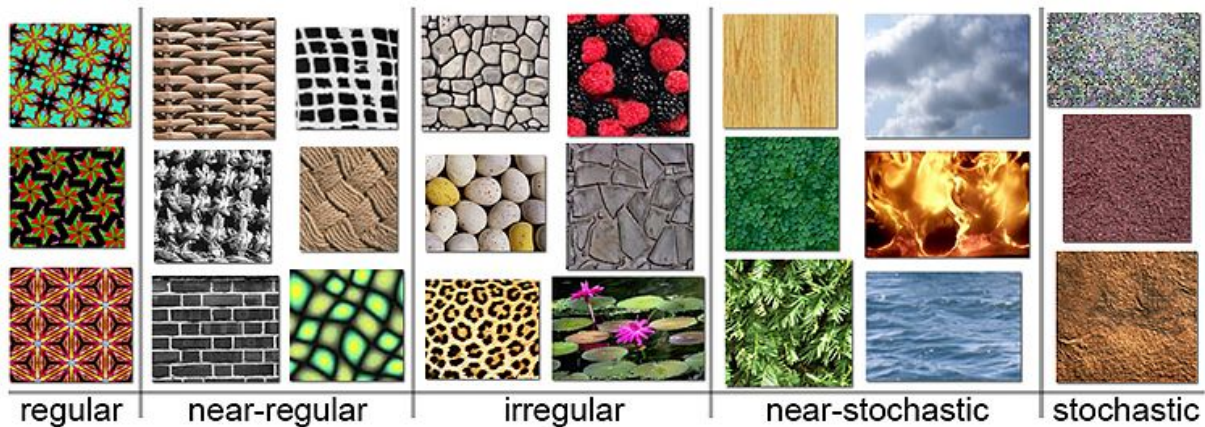


Figure 1.2 – Example of texture images ordered from regular to stochastic (left to right) based on two quantitative measures. Adapted from [39].

Recently, a review paper proposed to classify the texture feature extraction methods into seven classes [1]: statistical approaches (among which we can find the well-known co-occurrence matrices), structural approaches, transform-based approaches (Fourier transform-based approaches, among others), model-based approaches (such as the random field models), graph-based approaches (as the local graph structures), learning-based approaches, and entropy-based approaches. The two latter classes (learning-based approaches and entropy-based approaches) are the most recent ones. Several studies showed that the entropy-based measures are promising for texture analysis [23, 19, 25, 20, 42, 43]. Despite the fact that they have the great advantage of relying on well-known unidimensional, 1D, entropy-based measures (issued from the information theory field), these studies are only at their beginning.

1.1.1 Texture analysis methods

As mentioned above, texture analysis methods can be divided into seven categories [1]. We list them herein and detail the ones with the widest utilization in the field of image processing. The selected texture analysis methods usually depend on the target application. For instance, some applications require more focus on the texture patterns, others

are more concerned about the pixel intensities or image regions identification. In what follows we will briefly present class of the statistical approaches (as some of these approaches will be used in our work) and list the other classes. Several texture databases were created or adapted to become compatible for texture analysis purposes and classification [1, 44, 45].

Statistical approaches

Statistical approaches for texture analysis rely on the non-deterministic properties of the gray level distribution in the texture images. They consider the local features reflecting the spatial distribution of gray values. They are divided into 3 main categories: first order statistics, second order statistics, and higher order statistics. These methods include: gray level co-occurrence matrices (GLCM), gray level run-length matrix, autocorrelation-based approaches, histogram of gradient magnitudes, local mapped patterns-based approaches, local energy pattern, variogram, Tamura features, local binary patterns and variants, shape index histograms, weber local descriptor, and deterministic walk [1].

GLCM are probably the most common texture analysis technique, not only as a statistical approach, but also as a straight forward, easily implemented, and popular image analysis method used in several fields [46]. This technique is detailed below as it was used in our work.

Gray level co-occurrence matrices

Gray level co-occurrence matrices (GLCM) are a very well known image analysis technique that allows features extraction from gray scale images. Later, they were also upgraded for colored images using the approaches that will be detailed in the following section.

GLCM are first calculated by defining directions and an interpixel distances, d . Then, pixels separated by d are counted for each given direction separately; *i.e.* a count of the occurrence of pixel pairs that have a given distribution of gray level values is grouped into a GLCM for a given orientation and d . This is repeated for all d values in each orientation. For GLCM, four main orientations are usually chosen and a number of interpixel values. For a better illustration, please consider the following example in Figure 1.3, for a small 4×4 pixels gray scale image, for simplicity reasons.

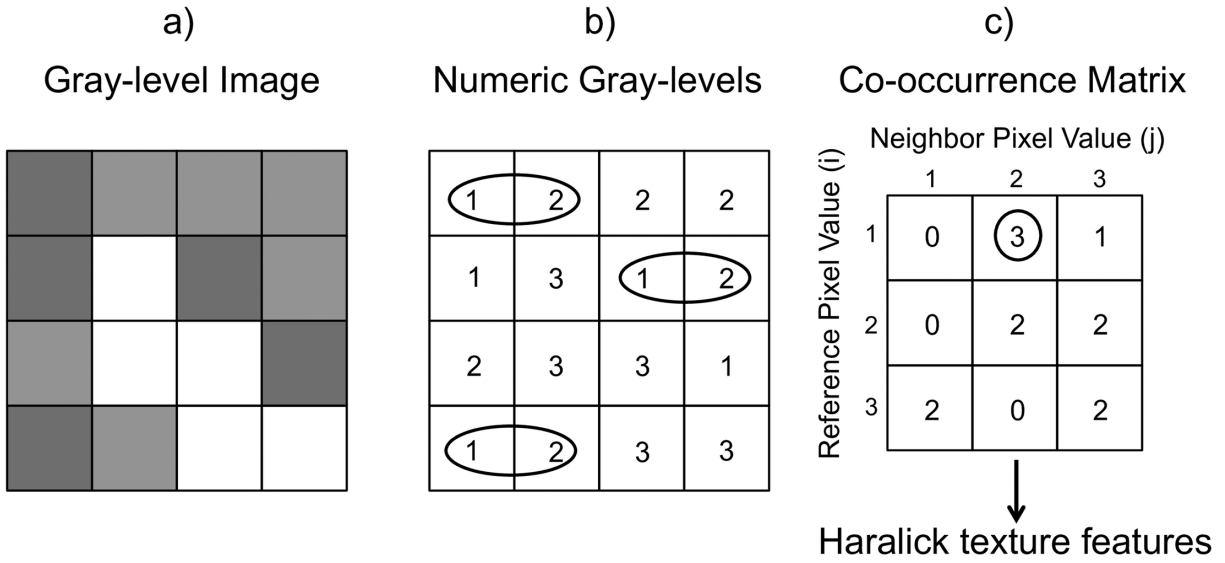


Figure 1.3 – (a) An example of a 4×4 gray scale matrix showing 3 levels; (b) Numerical values for the matrix’s gray levels. Circled in black: choosing interpixel distance $d=1$ and horizontal direction (0°), we consider the occurrence of two neighboring (1, 2) pixels; (c) The occurrence of paired pixels is counted and indicated in the GLCM. As shown above it is three times for (1, 2) horizontal pixel pairs (circled). The same procedure is calculated for all pixel pairs in the chosen direction and d . Adapted from [47].

After that, Haralick features are calculated from the GLCM matrices and used in classification, identification, and analysis of image textures. In fact, among the 14 features originally proposed by Haralick *et al.* [48], only six are commonly employed by researchers due to their correlation with the other eight, see Table 1.1.

This GLCM concept is upgraded also to 3D to study volumetric data [49]. Usually co-occurrence matrices are calculated for four main directions or orientations (0° , 45° , 90° , and 135°) in the 2D case and for 13 orientations in the 3D case, taking different interpixel or intervoxel distances d (we chose 4 interpixel distances $d=1, 2, 4$, and 8). Moreover, 8 gray levels ($N_g=8$) are usually considered. Therefore, the aforementioned parameters will be employed during our 2D and 3D co-occurrence matrices calculations.

Other methods

Other texture analysis techniques are classified into [1, 50, 51, 11, 10]:

- Structural approaches in which textures are divided into texels or basic small elements. The difference among the structural approaches is in the way the elements are chosen.

Table 1.1 – Definition of the computed Haralick features [48].

| Haralick feature | Annotation |
|---------------------|---|
| Uniformity (Energy) | $\sum_i \sum_j P^2(i, j)$ |
| Contrast | $\sum_{n=0}^{N_g-1} n^2 (\sum_{i=1}^{N_g} \sum_{j=1}^{N_g} P(i, j)), i - j = n$ |
| Correlation | $\sum_i \sum_j (ij) P(i, j) - \mu_x \mu_y / \sigma_x \sigma_y$ |
| Variance | $\sum_i \sum_j (i - \mu)^2 P(i, j)$ |
| Homogeneity | $\sum_i \sum_j P(i, j) / (1 + ((i - j)^2))$ |
| Entropy | $-\sum_i \sum_j P(i, j) \log P(i, j)$ |

where P represents the elements of the co-occurrence matrices and $\mu_x, \mu_y, \sigma_x,$ and σ_y are the means and standard deviations of row and column sums, respectively.

- Transform-based approaches, in which textures are considered in a space that can be interpreted in a similar way to texture characteristics. They include mainly the Fourier transform-based, Gabor decomposition-based, wavelet-based methods as well as filter banks (Law’s texture features).
- Model-based approaches in which a texture image is taken as a probability model; *i.e.* a set of basic functions form the texture through a linear combination. Those approaches include fractal model and Markov model.
- Graph-based approaches such as local graph structures and shortest paths in graphs.
- Learning-based approaches; *i.e.* machine and deep learning methods that are attaining more and more attention recently in several fields of application. They basically include training of texture images and then classification based on several features. They require very large dataset for optimal results and effective training.
- Entropy-based approaches use the information theory concept applied to signals at first and then recently developed for textures. They study the patterns within images and could be optimized through the initial defined parameters. Those will be detailed in section 1.4.2.

1.1.2 Colored texture analysis methods

Beside texture, color is essential not only in human perception for images but also in digital image processing [52, 53, 54, 55, 56, 57]. It is becoming of a greater impact. Unlike the intensity that is translated as scalar gray values for a gray scale image, color

is a vectorial feature that is appointed to each pixel for a colored image [52]. In contrast to gray scale images that could be handled in a straight forward manner, colored images could be analyzed in several possible ways. This depends on many factors, such as the need to analyze texture or color, separately or combined, directly from the image or through a transformation, among other factors [52, 57, 58].

Only few studies were performed on colored texture analysis and most of them were by adapting the application of gray scale textures analysis methods (listed in Section 1.1.1) to be applied on colored images. Therefore, in the following, we will state the possible approaches to handle colored images.

A study on colored texture analysis methods proposed dividing the colored texture analysis methods into three categories [52]:

- Parallel approaches: separate the color and texture concepts. Color is measured from the color histogram neglecting the local neighboring pixels characteristics. Texture is measured from the relationship of the intensities (gray scale version of images) neglecting the color properties. Color and texture results are combined to form a final feature vector.
- Sequential approaches: consider the color analysis from the color histogram. They employ a segmentation procedure in which the images' color histograms are labeled and then the features are extracted.
- Integrative approaches: combine the analysis of color and textural concepts, through which the information dependency between the two is taken into consideration. Those could be divided into single- or multi-channel strategies.

Parallel approaches are the most commonly employed as they can utilize the known gray-scale analysis methods directly. Sequential approaches were shown to be reliable in certain fields. However, they rely on the segmentation procedure that considers several parameters and, therefore, do not provide reproducible results. Finally, integrative approaches have the advantages of accounting for the color and textural features in a colored image simultaneously [52]. Moreover, the single-channel strategies possess an easily implemented adaptation from gray scale image analysis techniques and show significantly improved results compared to the parallel approaches [54]. Multi-channel strategies analyze two or more color channels at the same time. They have been also adapted for some well known feature extraction methods.

Several gray scale image analysis techniques have been extended for colored image analysis mostly as parallel approaches, such as: local linear transforms, Gabor filters [54],

co-occurrence matrices [54, 52], wavelet based Markov model [55], and fractal descriptors [53].

1.2 Entropy

Life is Chaos! The universe tends to be in disorder.

If you look at it thoroughly, you can see that, the aging of a human body, the natural evolution of all living beings, the structure of things tend to become in disorder unless we perform an action to force them to become ordered. Such as the simple example of our room: our spontaneous behavior leads to an unorganized room and this is normal, so the possibility of our room being totally ordered upon our spontaneous natural behavior is unlikely with a very low probability. However, now when we want to clean our room and put it back into order we are exerting an effort to force things to get back to the organized state. Putting a system in order requires other systems to be unorganized, to continue with the example: to organize our room it requires putting into disorder our spontaneous behavior and following a certain pattern of moves to achieve our target.

“Any spontaneous process increases the disorder or randomness of the universe”. Well if we take a second to think about it logically, it is True! Among the few possibilities of things to be in a perfect order there are infinite possibilities for them to be in all the other states: from daily life events and the physical placement of objects in our apartment, street, and office to the particles and energy in this universe. This is a simple explanation of the actual established second law of thermodynamics by Boltzmann that was later refined to state that: *The total entropy of a closed system cannot decrease. However, within a system, entropy of one system can decrease by raising entropy of another system.*

“A given system can never of its own accord go over into another equally probable state but only into a more probable one [59]”

The more probable state is always the degraded state and never back to the initial state. In thermodynamics world, Entropy is this measure of this disorder. First established by Boltzmann as:

$$S = k_B \ln \Omega, \tag{1.1}$$

where S is the entropy value, k_B Boltzmann constant and Ω is the number of microstates. The microstates are the properties of the system at a certain instant. This equation relates

the microscopic properties of the system (microstates) to the macroscopic thermodynamic behavior. In the case of a process where the system is moving from a less probable to a more probable state, there is a change in entropy that reflects the actual change of the system's properties. With Ω_1 as the initial number of microstates and Ω_2 as the final number of microstates, change in entropy could be calculated as:

$$\Delta S = k_B \ln \frac{\Omega_2}{\Omega_1}. \quad (1.2)$$

After several decades, in 1948 [60], Shannon introduced the revolutionary notion of “Information Entropy” which will be detailed in section 1.3. In information theory and thermodynamics **Entropy** is a fundamental quantity. It is a common concept for various scientific fields. In simple words it is the measure of disorder in a system. However this might not be always a very precise definition. In thermodynamics world, entropy is the measure of energy distribution in a system; the more spread it is, the higher the entropy is and vice versa. However, in information theory world, the entropy is the measure of uncertainty. The more obvious and certain an outcome is, the lower the entropy value and vice versa.

As an illustration, consider the three different states of water: solid (ice), liquid (water), and gas (vapor), Figure 1.4. If we want to relate entropy characterization for each of them, we would say that the ice has the lowest entropy values because it has fixed particles; *i.e.* we can always know how the particles are arranged, they are steady. Liquid state water has a medium entropy as it reflects a bigger spread of the particles and more possible arrangements. However, the water vapor has the highest entropy value among them because the arrangement of particles is so random, there is a bigger spread of the particles and they are more free to move. Now translating that into the information theory concept, in the ice cube we have the highest knowledge (certainty) about the particles' location and possible distribution which is rendered into low entropy value as it carries low information. However, for the vapor (gas) we have the lowest knowledge about the particles distribution and they are free to spread, thus it has a high entropy value as the system contains the highest information.

When moving our system from one state to another, we can visualize the change in entropy values. As an ice cube melts, we can obviously visualize the increase in entropy value (increase in disorder) as its particles become more randomly distributed and spread. We then have less knowledge about their arrangement (more possibilities). In other words,

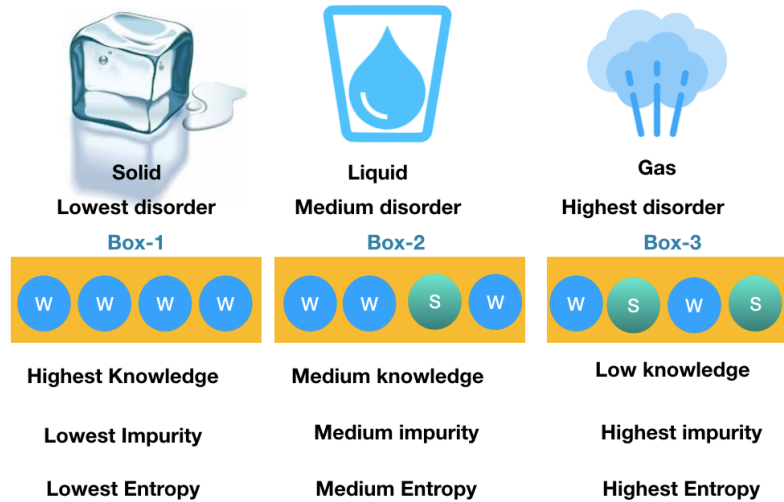


Figure 1.4 – Example of water states illustrating entropy as a function of the distribution and spread of particles. Blue balls ‘W’ represent water molecules and green balls ‘S’ represent any other molecule. In simple words, if we need to pick a ball from each state, we have 100% certainty of picking ‘W’ in the solid state. This percentage decreases gradually for liquid and gas states as we become less certain about the outcome of our random pick. Adapted from [61].

we become more **uncertain** about their arrangement, thus its state carries more **information**. The key explanation of information theory is that:

- Entropy is inversely proportional to certainty of a system.
- Entropy of a variable reflects its amount of information.

1.3 Entropy in Information Theory

Entropy measures are being used in several scientific disciplines, such as: information theory, statistical mechanics, chaos theory, neural networks, mathematical linguistics, and taxonomy [62]. In dynamics system world, entropy is the rate of information production. It was first established by Shannon as an average measure of disorder or uncertainty in a system [60].

The entropy of a variable is the amount of information contained in it. The variable could be a phone call, a signal, a sequence of letters, the news, or any other form. For one

message state or event E , the information content I is calculated as:

$$I(E) = \log\left(\frac{1}{P(E)}\right) = -\log(P(E)), \quad (1.3)$$

with E being the message and $P(E)$ the message's probability of occurrence. Intuitively, high probability messages carry low information content because they are already predictable, whereas the low probability messages that are the least expected carry high information content [63, 64]. Let us use a numerical example to better explain the idea:

If we have two equally possible events, $E1$ and $E2$, with $P(E1) = P(E2) = \frac{1}{2}$ then $I(E1) = I(E2) = -\log_2\left(\frac{1}{2}\right) = 1$ bit of information. On the other side, if one event is more likely to occur than the other such as having $P(E1) = \frac{3}{4}$ and $P(E2) = \frac{1}{4}$, for example, then the information outcome would be $I(E1) = -\log_2\left(\frac{3}{4}\right) = 0.415$ and $I(E2) = -\log_2\left(\frac{1}{4}\right) = 2$. The event with a higher probability carries lower information content and vice versa [63]. We present the Shannon entropy herein. Consider a discrete random variable X with elements $\{x_i\} = \{x_1, x_2, \dots, x_n\}$ and probability distribution $p(x)$. The entropy H_x is defined as:

$$H_x = \sum_{x \in X} p(x) I(X). \quad (1.4)$$

where by observing X and knowing its probability distribution $p(x)$, $I(X)$ is the measure of information perceived by us. This quantity is defined by Shannon as $I(X) = -\log_2(p(x))$ [60]. So, finally, the entropy definition is Eq. 1.5. The maximum entropy is obtained when the events have equal probabilities [60, 64].

$$H_x = - \sum_{x \in X} p(x) \log_2(p(x)). \quad (1.5)$$

1.4 Entropy Measures

Biomedical signal processing methods have attained major importance by being able to extract information that is not identified visually from signals. Information is of great interest. It enables scientists to detect behavior, redundancy, or noise information from the biomedical signals [62]. A number of entropy measures—based on some concepts in information theory—have been developed to serve this purpose: one dimensional

approximate entropy ($ApEn_{1D}$) [65, 66], sample entropy ($SampEn_{1D}$) [67], fuzzy entropy ($FuzEn_{1D}$) [68], distribution entropy ($DistrEn_{1D}$) [69], permutation entropy ($PermEn_{1D}$) [70], and dispersion entropy ($DispEn_{1D}$) [71, 72]. Besides, these entropy measures have been implemented in various fields within the biomedical domain through their application to physiological time series, such as, electroencephalographic (EEG) [73, 74, 71], electrocardiographic (ECG) [75, 69], electromyographic (EMG) [68, 76, 77], and electrohysterographic (EHG) signals [78]. Due to the successful findings on the unidimensional level, bidimensional definitions were later proposed [19, 20, 21, 22, 23, 24, 25]. In the following, we will describe the unidimensional entropy methods that are the most often used to analyze time series, the definitions of some of them and their various applications.

1.4.1 Unidimensional entropy measures

Unidimensional approximate and sample entropy measures

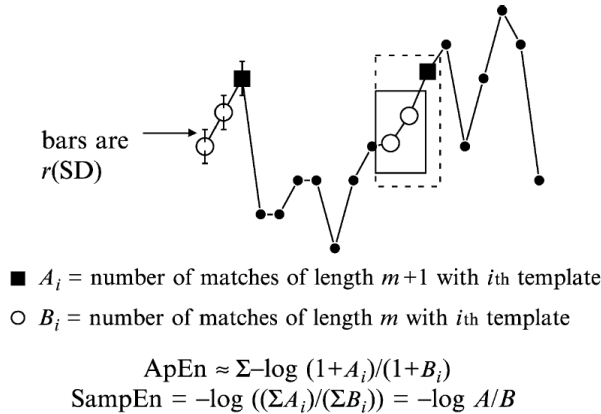
Entropy measures were first established in the discipline of understanding complex phenomena. The first developed entropy measure as a regularity quantifier is $ApEn_{1D}$ [65]. Thus, in 1991, Pincus [65] established $ApEn_{1D}$ as a measure of information in a finite data series based on vectors' similarity within the signal. $ApEn_{1D}$, by definition, is a measure of the likelihood that a consecutive number of points (defined by a window m) of a time series that are similar (within a range lower than or equal to a parameter r) remain similar on the next incremental comparisons (when adding one extra point).

$ApEn_{1D}$ was applied to clinical cardiovascular studies: in heart rate data in specific, it can significantly discriminate healthy controls from diseased subjects [65, 79]. It also found application in EEG classification for psychiatric diseases, like schizophrenia [80], epilepsy [81], and addiction. However, $ApEn_{1D}$ considers self matches, has certain bias, and is heavily dependent on the signal's length [67].

Therefore, to handle the sensitivity of $ApEn_{1D}$ to the length of signals and avoid self similarity considerations, $SampEn_{1D}$ was later proposed by Richman and Moorman [67, 82]. As illustrated in Figure 1.5, $ApEn_{1D}$ shows a high risk of obtaining undefined ($\log(0)$) values if no matches were found for each and every template of lengths m and $(m + 1)$. This suggested adding a value of 1 to the numerator and denominator of the equation (in each comparison). However, $SampEn_{1D}$ solved this issue by introducing the idea of

summing all the number of matches before introducing the natural logarithmic function. The latter led to excluding self matches, obtaining more accurate assessment, and saving computation time.

In $SampEn_{1D}$, by definition, “each” time series template of length m is compared to its neighboring m -length templates by scanning the whole time series for similar matches; if the difference between the corresponding scalar components is less than or equal to a value $r \times standard\ deviation(time\ series)$, - r is the tolerance level – then the patterns are considered similar. Thus, a unit value is added to the number of matches of length m (A_i in Figure 1.5). However, if the difference between the corresponding scalar components is greater than $r \times standard\ deviation(time\ series)$ then nothing is added. Similarly, B_i for matches of $(m + 1)$ -length templates is calculated. After that, A_i and B_i for m - and $(m + 1)$ -length templates, respectively, are summed and the natural negative logarithm is calculated. It is important to mention that, the similarity degree in $ApEn_{1D}$ and $SampEn_{1D}$ is based on a two-state binary classifier determined by r . Therefore the outcome is highly dependent on the choice of the parameter r and the results are also sensitive to any slight change in this value. $SampEn_{1D}$ found applications for various physiological time series such as: clinical cardiovascular datasets [67], ECG [83], EMG [84], among others.



For regular, repeating data, A/B nears 1 and entropy nears 0.

Figure 1.5 – Schematic demonstration for $ApEn_{1D}$ and $SampEn_{1D}$. Adapted from [82].

$ApEn_{1D}$ and $SampEn_{1D}$ algorithms definition:

For $ApEn_{1D}$ and $SampEn_{1D}$ calculations, the time series length N , length of the compare sequence m (moving template), and the tolerance for accepting matches r are defined. Tolerance is usually multiplied by the standard deviation, std , of the series, \mathbf{u} . However, for a normalized series $std(\mathbf{u}) = 1$ so $r \times std(\mathbf{u}) = r$. At first a vector sequence $\mathbf{x}_i^m = \{u_i, u_{i+1}, \dots, u_{i+m-1}\}$ ($i = 1, \dots, N - m$) is formed.

$$\mathbf{x}_i^m = \{u_i, u_{i+1}, \dots, u_{i+m-1}\}. \quad (1.6)$$

Similarly, \mathbf{x}_i^{m+1} for $m + 1$ points is formed. The distance d_{x_i, x_j}^m between vectors \mathbf{x}_i^m and \mathbf{x}_j^m is defined as the maximum difference between their corresponding scalar components:

$$d_{i,j}^m = d[\mathbf{x}_i^m, \mathbf{x}_j^m] = \max_{k \in (0, m-1)} |(u(i+k) - u(j+k))|. \quad (1.7)$$

Define B_i as the number of vectors \mathbf{x}_j^m within r of vectors \mathbf{x}_i^m and A_i as the number of vectors \mathbf{x}_j^{m+1} within r of \mathbf{x}_i^{m+1} . Thus for each \mathbf{x}_i , B_i and A_i are incremented by:

$$\begin{cases} 1 & \text{if } d \text{ is } \leq r & (\text{similar patterns}) \\ 0 & \text{if } d \text{ is } > r & (\text{non - similar patterns}) \end{cases} \quad (1.8)$$

Then each of $ApEn_{1D}$ and $SampEn_{1D}$ is defined as follows [82]:

$$ApEn_{1D} = -\frac{1}{N-m} \sum_{i=1}^{N-m} \ln\left(\frac{A_i}{B_i}\right) \quad (1.9)$$

$$SampEn_{1D} = -\ln\left(\frac{\sum_{i=1}^{N-m} A_i}{\sum_{i=1}^{N-m} B_i}\right) \quad (1.10)$$

As stated previously, both $ApEn_{1D}$ and $SampEn_{1D}$ showed promising results but are too sensitive to their parameters and may even result in misleading findings. That is because the vectors' similarity is defined based on the Heaviside function that has a rigid boundary [85]. The Heaviside function is a two-state binary classifier that gives a unity value if the difference in distance between the compared vectors is within threshold r ; otherwise it gives a zero value, please see Figure 1.6. There is no intermediate value. Thus, any slight change in r will probably change the entropy value [85]. As an enhancement, Chen *et al.* [68] utilized the concept of fuzzy membership function and developed the $FuzEn_{1D}$ method that will be extensively detailed below.

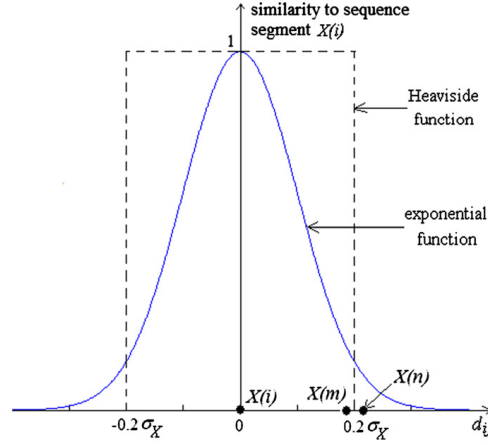


Figure 1.6 – Heaviside function compared to an exponential function. Adapted from [86]).

Unidimensional fuzzy entropy

In 2007, $FuzEn_{1D}$ was first proposed as a measure for surface EMG time series regularity to overcome the poor statistical stability of $ApEn_{1D}$ and $SampEn_{1D}$ [68]. In the research of information theory and complex systems analysis, several studies suggested that $FuzEn_{1D}$ outperforms $ApEn_{1D}$ and $SampEn_{1D}$ [68, 86, 85, 76, 87]. Since then, it has been used for characterizing different types of biomedical signals such as electromyogram (EMG) [68], heart rate variability [86, 73], and electroencephalogram (EEG) [73].

Unlike $ApEn_{1D}$ and $SampEn_{1D}$, $FuzEn_{1D}$ gives a membership value to each element of a time series based on fuzzy sets and membership degree functions. For evaluating the similarity degree in $FuzEn_{1D}$, Chen *et al.* [68] proposed replacing the Heaviside function used in $ApEn_{1D}$ and $SampEn_{1D}$ – that assigns a value of 0 or 1 to the elements compared – by a continuous exponential function as their membership degree. Therefore, all the time series elements have contributions in the final entropy output by a continuous function as their membership degree.

$FuzEn_{1D}$ is computed as follows [68]:

For an N sample time series \mathbf{u} , $\{u(i) : 1 \leq i \leq N\}$, given an embedding dimension m , a vector sequence $\mathbf{x}_i^m = \{u_i, u_{i+1}, \dots, u_{i+m-1}\}$ ($i = 1, \dots, N - m$) is formed. Every element of the vector sequence is generalized by removing the sequence's baseline $\{u_0(i) = \frac{1}{m} \sum_{j=0}^{m-1} u_{i+j}\}$:

$$\mathbf{x}_i^m = \{u_i, u_{i+1}, \dots, u_{i+m-1}\} - u_0(i). \quad (1.11)$$

Similarly, \mathbf{x}_i^{m+1} for $m + 1$ points is formed. The distance $d_{i,j}^m$ between vectors \mathbf{x}_i^m and \mathbf{x}_j^m

is defined as the maximum difference between their corresponding scalar components:

$$d_{i,j}^m = d[\mathbf{x}_i^m, \mathbf{x}_j^m] = \max_{k \in (0, m-1)} |(u(i+k) - u_0(i)) - (u(j+k) - u_0(j))|. \quad (1.12)$$

Given tolerance level r and fuzzy power n , the similarity degree $D_{i,j}^m(n, r)$ between \mathbf{x}_i^m and \mathbf{x}_j^m is calculated through a fuzzy function $\{ \mu(d_{i,j}^m, n, r) \}$ as:

$$D_{i,j}^m(n, r) = \mu(d_{i,j}^m, n, r) = \exp\left(-\frac{(d_{i,j}^m)^n}{r}\right). \quad (1.13)$$

Then, the functions Φ^m and Φ^{m+1} are defined as:

$$\Phi^m(n, r) = \frac{1}{N-m} \sum_{i=1}^{N-m} \Phi_i^m(r), \quad (1.14)$$

$$\Phi^{m+1}(n, r) = \frac{1}{N-m} \sum_{i=1}^{N-m} \Phi_i^{m+1}(r), \quad (1.15)$$

where Φ_i^m and Φ_i^{m+1} are the average of all the similarity degrees of vectors \mathbf{x}_i^m and \mathbf{x}_i^{m+1} , respectively, with their neighboring vectors \mathbf{x}_j^m and \mathbf{x}_j^{m+1} :

$$\Phi_i^m(n, r) = \frac{1}{N-m-1} \sum_{j=1, j \neq i}^{N-m} D_{i,j}^m, \quad (1.16)$$

$$\Phi_i^{m+1}(n, r) = \frac{1}{N-m-1} \sum_{j=1, j \neq i}^{N-m} D_{i,j}^{m+1}. \quad (1.17)$$

Then $FuzEn_{1D}$ measure is defined as:

$$FuzEn_{1D}(m, n, r) = \lim_{N \rightarrow \infty} [\ln \Phi^m(n, r) - \ln \Phi^{m+1}(n, r)]. \quad (1.18)$$

It is estimated by the statistics for finite datasets, *i.e.* time series in our case:

$$FuzEn_{1D}(\mathbf{u}, m, n, r) = \ln \Phi^m(n, r) - \ln \Phi^{m+1}(n, r). \quad (1.19)$$

Finally, $FuzEn_{1D}$ is formulated as:

$$FuzEn_{1D}(\mathbf{u}, m, n, r) = \ln \frac{\Phi^m(n, r)}{\Phi^{m+1}(n, r)}. \quad (1.20)$$

In addition to the above detailed entropy measures, some other unidimensional entropy measures were later developed: distribution entropy 1D ($DistrEn_{1D}$) [69], dispersion entropy 1D ($DispEn_{1D}$) [71, 72], permutation entropy ($PermEn_{1D}$) [70]. We will detail the bidimensional versions of the aforementioned measures in section 1.4.2.

Unidimensional multiscale approach

In the unidimensional domain, the previously detailed entropy measures $ApEn_{1D}$ [65], $SampEn_{1D}$ [67], and $FuzEn_{1D}$ [68] are able to quantify the irregularity of physiological time series. However no analysis was performed on multiple scale factors until Costa *et al.* [88] proposed the concept of coarse-graining process with entropy measures. They introduced the multiscale entropy (MSE_{1D}) and studied the biological series behavior over several scale factors to explain the fact that some pathologic processes have a lower complexity than healthy processes [88]. In fact, MSE can be considered as a filter bank of overlapping band-pass filters [89].

Unidimensional multiscale approach MSE_{1D}

MSE is a two-step procedure: first coarse-graining the original time series, then applying $SampEn_{1D}$ to each coarse-grained time series. Elements of the coarse-grained time series are obtained from the original one $\mathbf{x} = \{x_1, x_2, x_3, \dots, x_N\}$ with length N by the equation: $y_j^{(\tau)} = \frac{1}{\tau} \sum_{i=(j-1)\tau+1}^{j\tau} x_i$, $1 \leq j \leq \frac{N}{\tau}$, given a scale factor τ [88, 90], see Figure 1.7. It involves dividing the original time series into consecutive non-overlapping windows and averaging the data points within each window to obtain multiple average values that form the new coarse-grained time series $\mathbf{y}^{(\tau)}$ [88, 90, 91]. The length of the coarse-grained time series is the length of the original time series divided by the scale factor: N/τ . At scale one, the coarse-grained time series is the original time series itself. After that, $SampEn_{1D}$ is calculated for each coarse-grained time series and plotted as a function of the scale factor τ .

For the MSE analysis, two major patterns should be considered [91]:

- For two time series \mathbf{a} and \mathbf{b} , if the entropy values at most of the scale factors for \mathbf{a} are higher than those for \mathbf{b} , then \mathbf{a} is more complex than \mathbf{b} .
- If entropy values decrease monotonically with scale then the significant information is only found at the smallest scales of the original time series.

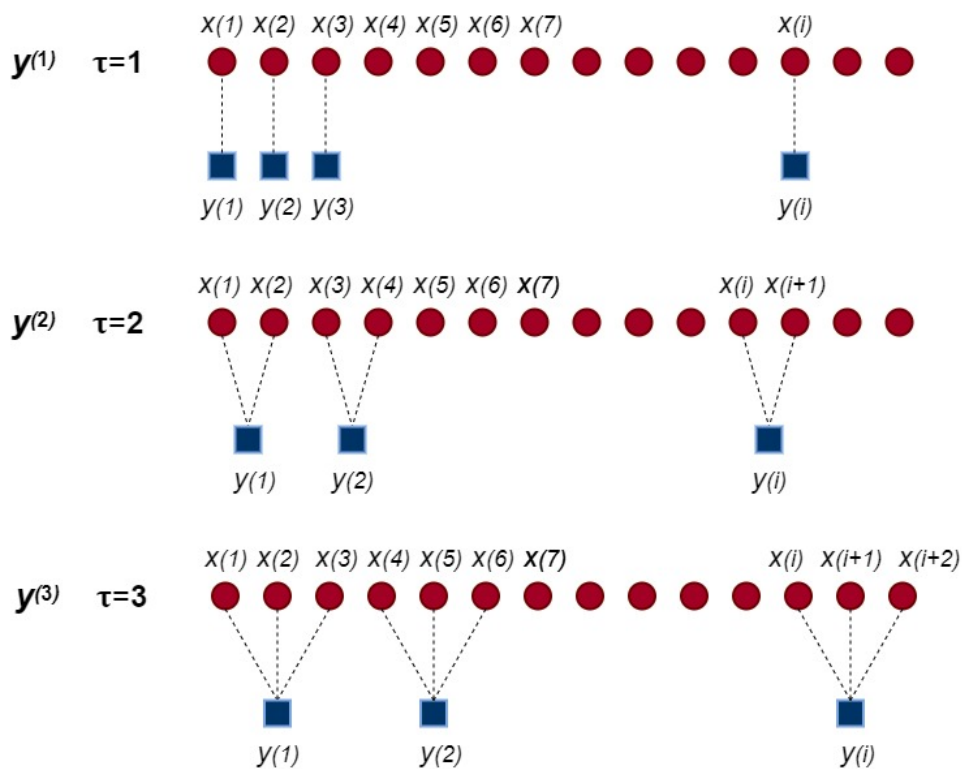


Figure 1.7 – Illustration of MSE_{1D} for time series. τ is the number of points taken in each window to form the new coarse grained time series $y^{(\tau)}$.

It has been shown that it is better to study the complexity of biological systems on the multiscale level because they naturally operate across multiple temporal scales [91].

Modified multiscale entropy $MMSE_{1D}$

Modified multiscale entropy $MMSE_{1D}$ [92] is composed of two main steps like MSE_{1D} : first coarse-graining the original time series $\mathbf{x} = \{x_k\} = \{x_1, x_2, x_3, \dots, x_N\}$, of length N , then applying $SampEn_{1D}$ to each coarse-grained time series. However, the coarse graining procedure is performed using overlapping moving templates. The length of the τ coarse-grained time series is $N-\tau+1$. The algorithm is defined as follows:

- An overlapping moving template scans the whole original time series to form the coarse-grained versions $\mathbf{y}^{(\tau)} = \{y_j^{(\tau)}\}$ as:

$$y_j^{(\tau)} = \frac{1}{\tau} \sum_{k=(j-1)\tau+1}^{k=j\tau} x_k, \quad (1.21)$$

where j goes from 1 to $(\frac{N}{\tau} + 1)$ (rounded down).

- For each coarse-grained time series $\mathbf{y}^{(\tau)}$, $SampEn_{1D}$ is computed.

Unidimensional multiscale fuzzy entropy MSF_{1D}

Similar to the previously defined multiscale analysis, MSF_{1D} [72] is a two-step procedure: first coarse-graining the original time series following [88], then applying $FuzEn_{1D}$ to each coarse-grained time series. It involves dividing the original time series into consecutive non-overlapping windows and averaging the data points within each window to obtain multiple average values that form the new coarse-grained time series $\mathbf{y}^{(\tau)}$.

- Elements of the coarse-grained time series are obtained from the original one $\mathbf{x} = \{x_1, x_2, x_3, \dots, x_N\}$ with length N by the equation: $y_j^{(\tau)} = \frac{1}{\tau} \sum_{i=(j-1)\tau+1}^{j\tau} x_i$, $1 \leq j \leq \frac{N}{\tau}$, given a scale factor τ
- The obtained coarse-grained time series are evaluated using $FuzEn_{1D}$.

1.4.2 Bidimensional entropy measures

In the field of biomedical signal processing, several unidimensional (1D) entropy measures have been developed to characterize the irregularity of physiological signals, as mentioned above. Successful findings based on entropy measures on 1D data [65, 67, 68],

signals, encourage the development of bidimensional (2D) entropy metrics for 2D data, images. Starting in 2011, the bidimensional entropy measures for studying images irregularity emerged and showed promising findings [19, 20, 21, 22, 23, 24, 25]. The 2D entropy measures can extract some 2D information from an image and study the irregularity within its patterns in a similar manner to that implemented for signals [1]. In the following we will mention all the existing bidimensional entropy measures, including the most recent ones. Furthermore, we will thoroughly explain the first developed bidimensional measure: bidimensional sample entropy, $SampEn_{2D}$.

Bidimensional sample entropy

In 2011, Yeh *et al.* [23] followed by the work of Silva *et al.* [19] proposed the first 2D entropy measure, 2D sample entropy ($SampEn_{2D}$) for quantifying the irregularity of images as an extension of 1D sample entropy ($SampEn_{1D}$) [67].

For an image $\mathbf{U}=\{u(i, j)\}_{i=1,2,\dots,H}^{j=1,2,\dots,W}$ with height H and width W :

1. Let $\mathbf{V}_m(i, j)$ be the m -length square window of \mathbf{U} with origin at $u(i, j)$:

$$\mathbf{V}_m(i, j) = \begin{bmatrix} u(i, j) & \dots & u(i, j + m - 1) \\ u(i + 1, j) & \dots & u(i + 1, j + m - 1) \\ \dots & \dots & \dots \\ u(i + m - 1, j) & \dots & u(i + m - 1, j + m - 1) \end{bmatrix}. \quad (1.22)$$

Let N_m be the total number of square windows within \mathbf{U} that are generated for m and $m + 1$ size: $N_m = (W - m) \times (H - m)$. For a similarity threshold r , compute $G^m(r)$ as:

$$G^m(r) = \frac{1}{N_m} \sum_{i=1, j=1}^{i=H-m, j=W-m} G_{ij}^m(r), \quad (1.23)$$

where, $G_{ij}^m(r) = \frac{1}{N_m - 1} \times$ number of $\mathbf{V}_m(a, b)$ such that $d[\mathbf{V}_m(i, j), \mathbf{V}_m(a, b)] \leq r$, where a and b range from 1 to $H - m$ and from 1 to $W - m$, respectively. The distance d is calculated as follows:

$$d[\mathbf{V}_m(i, j), \mathbf{V}_m(a, b)] = \max_{0 \leq k \leq m-1, 0 \leq l \leq m-1} |u(i + k, j + l) - u(a + k, b + l)|. \quad (1.24)$$

2. Then, compute $G1^m(r)$ as:

$$G1^m(r) = \frac{1}{N_m} \sum_{i=1, j=1}^{i=H-m, j=W-m} G1_{ij}^m(r), \quad (1.25)$$

where, $G1_{ij}^m(r) = \frac{1}{N_m - 1} \times$ number of $\mathbf{V}_{m+1}(a, b)$ such that $d[\mathbf{V}_{m+1}(i, j), \mathbf{V}_{m+1}(a, b)] \leq r$, where a and b range from 1 to $H - m$ and from 1 to $W - m$, respectively. This means the similarity is considered as:

$$\left\{ \begin{array}{ll} 1 & \text{if } d \text{ is } \leq r \quad (\text{similar patterns}) \\ 0 & \text{if } d \text{ is } > r \quad (\text{non - similar patterns}) \end{array} \right\} \quad (1.26)$$

3. Finally, calculate the bidimensional Sample entropy, $SampEn_{2D}$:

$$SampEn_{2D}(m, r, \mathbf{U}) = -\ln\left(\frac{G1^m(r)}{G^m(r)}\right). \quad (1.27)$$

4. In $SampEn_{2D}$, two patterns are considered to match if the absolute difference between all their corresponding components is lower than the threshold r .

$SampEn_{2D}$ was tested on synthetic images, texture images, and real biological images. $SampEn_{2D}$ is similar to its unidimensional definition $SampEn_{1D}$ [67]. As an illustration for pattern comparisons using $SampEn_{2D}$ please see Figure 1.8. The results obtained by $SampEn_{2D}$ were very promising and illustrated its ability to extract some meaningful 2D features of an image. It was applied to nerves histological images [19]. However, $SampEn_{2D}$ still has the drawback of resulting in undefined values especially for small sized images [22]. Moreover, it is very sensitive to its parameters' values, like its 1D version. The latter will be shown in our manuscript as well (Chapter 4).

Bidimensional distribution entropy

Later, in 2017, Azami *et al.* developed the 2D distribution entropy ($DistrEn_{2D}$) [20]. $DistrEn_{2D}$ was developed based on its unidimensional $DistrEn_{1D}$ [69] concept that showed advantages in the results over other unidimensional entropy measures for short signals [69]. Thus, $DistrEn_{2D}$ – its 2D version – deals especially with small-sized texture images.

$DistrEn_{2D}$ is based on a histogram approach with M bins to estimate the empirical probability density function (ePDF) of the distance matrix (\mathbf{D}), where \mathbf{D} is the greatest

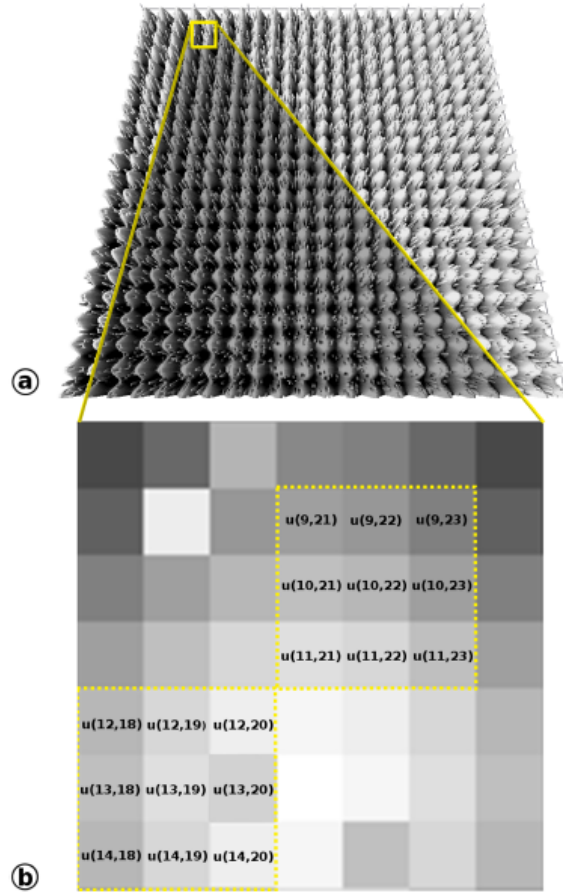


Figure 1.8 – An illustration for pattern comparisons using $SampEn_{2D}$ depicted from [19]. (a) is an example of a gray image with a certain irregularity degree. (b) is an amplified view of a window to explain the similarity calculations. Two patterns (dotted yellow squares) are considered to be similar if the difference between all their corresponding scalar components is lower than or equal a tolerance value r ; *i.e.* $|u(12, 18) - u(9, 21)| \leq r$, $|u(12, 19) - u(9, 22)| \leq r$, ..., $|u(14, 20) - u(11, 23)| \leq r$.

absolute difference between the compared patterns. $DistrEn_{2D}$ algorithm is explained below. Consider an image $\mathbf{U}=\{u_{i,j}\}_{i=1,2,\dots,h}^{j=1,2,\dots,w}$ of size $H \times W$:

1. \mathbf{U} is normalized to 0 to 1 range. Then template matrices of $m_H \times m_W$ size are created $\mathbf{X}_{k,l}^m$ (Eq. 1.28) where $k = 1, 2, \dots, H - (m_H - 1)$ and $l = 1, 2, \dots, W - (m_W - 1)$. The embedding dimension vector \mathbf{m} is taken as $[m_H, m_W]$.

$$\mathbf{X}_{i,j}^m = \begin{bmatrix} u_{i,j} & \dots & u_{i,j+m_W-1} \\ u_{i+1,j} & \dots & u_{i+1,j+m_W-1} \\ \dots & \dots & \dots \\ u_{i+m_H-1,j} & \dots & u_{i+m_H-1,j+m_W-1} \end{bmatrix}. \quad (1.28)$$

2. Then, the distance matrix \mathbf{D} is calculated as the absolute difference between the corresponding scalar components of $\mathbf{X}_{k,l}^m$ and $\mathbf{X}_{a,b}^m$, in which, variables a and b range from 1 to $H - (m_H - 1)$ and from 1 to $W - (m_W - 1)$, respectively, excluding $(k, l) = (a, b)$ to reduce bias.
3. After that, the histogram approach is implemented with M bins to estimate the empirical probability density function (ePDF) of the distance matrix (\mathbf{D}). The probability of each bin is represented by p_t (frequency).
4. Finally the 2D distribution entropy, $DistrEn_{2D}$, is calculated as:

$$DistrEn_{2D}(\mathbf{U}, \mathbf{m}, M) = - \sum_{t=1}^M p_t \times \log_2(p_t). \quad (1.29)$$

For testing $DistrEn_{2D}$, a set of synthetic images based on several concepts in image processing, including power of noise and degree of randomness, and real texture datasets were employed [20]. $DistrEn_{2D}$ results in defined entropy values for images where $SampEn_{2D}$ is not defined.

Bidimensional dispersion entropy

In 2019, as an extension of $DispEn_{1D}$ [71, 72], $DispEn_{2D}$ [22] was introduced for 2D data. In $DispEn_{2D}$, the pixels of an image are mapped into classes and then correspondingly into dispersion patterns. The relative frequency for each dispersion pattern is calculated. Afterwards, those relative frequencies of the dispersion patterns are summed up by a definition based on Shannon entropy to obtain the final entropy value.

Consider an image $\mathbf{U}=\{u(i, j)\}_{i=1,2,\dots,H}^{j=1,2,\dots,W}$ of $H \times W$ size:

1. Map $u(i, j)$ elements into c classes, using linear and non-linear methods [93], to form $z_{i,j}^c = \text{round}(c \times y_{i,j} + 0.5)$. The number of classes c could be an integer from 3 till 9. In order to avoid having most of the $u(i, j)$ elements in few classes out of the 1 to c , a sigmoid function is often used where:

$$y_{i,j} = \frac{1}{\sigma\sqrt{2\pi}} \int_{-\infty}^{u_{i,j}} e^{-\frac{(t-\mu)^2}{2\sigma^2}} dt, \quad (1.30)$$

with μ and σ being the mean and standard deviation of the original image \mathbf{U} .

2. Let \mathbf{m} be the embedding dimension vector $[m_H, m_W]$ to define $\mathbf{z}_{k,l}^{\mathbf{m},c}$ such as:

$$\mathbf{z}_{k,l}^{\mathbf{m},c} = \begin{bmatrix} z_{k,l}^c & z_{k,l+1}^c & \cdots & z_{k,l+(m_W-1)}^c \\ z_{k+1,l}^c & z_{k+1,l+1}^c & \cdots & z_{k+1,l+(m_W-1)}^c \\ \cdots & \cdots & \cdots & \cdots \\ z_{k+(m_H-1),l}^c & z_{k+(m_H-1),l+1}^c & \cdots & z_{k+(m_H-1),l+(m_W-1)}^c \end{bmatrix}, \quad (1.31)$$

where k range from 1 to $w - (m_W - 1)$ and l ranges from 1 to $h - (m_H - 1)$.

3. After that, map $\mathbf{z}_{k,l}^{\mathbf{m},c}$ to a dispersion pattern $\pi_{v_0, v_1 \dots v_{m_H \times m_W - 1}}$. For each $\mathbf{z}_{k,l}^{\mathbf{m},c}$, $c^{m_H \times m_W}$ dispersion patterns can be formed.
4. Calculate the relative frequency for each of the $c^{m_H \times m_W}$ dispersion patterns $\pi_{v_0, v_1 \dots v_{m_H \times m_W - 1}}$:

$$p(\pi_{v_0, v_1 \dots v_{m_H \times m_W - 1}}) = \frac{\#\{k, l, \mathbf{z}_{k,l}^{\mathbf{m},c} \text{ has type } \pi_{v_0, v_1 \dots v_{m_H \times m_W - 1}}\}}{(h - (m_H - 1))(w - (m_W - 1))}, \quad (1.32)$$

where $l \leq w - (m_W - 1)$ and $k \leq h - (m_H - 1)$.

5. Finally, $DispEn_{2D}$ is calculated as:

$$DispEn_{2D}(\mathbf{U}, \mathbf{m}, c) = - \sum_{\pi=1}^{c^{m_H \times m_W}} p(\pi_{v_0, v_1 \dots v_{m_H \times m_W - 1}}) \times \ln(p(\pi_{v_0, v_1 \dots v_{m_H \times m_W - 1}})). \quad (1.33)$$

$DispEn_{2D}$ was also tested on several synthetic images and real datasets [22]. It illustrated successful performance, especially regarding the speed of calculations. In comparison to $SampEn_{2D}$, $DispEn_{2D}$ is faster, more stable, and leads to less undefined values.

Bidimensional approximate entropy

In addition, 2D approximate entropy ($ApEn_{2D}$) [21] was developed as a structure metric to detect some image structural details that are unrecognized by the gray scale metrics. It was applied to raw computed tomography (CT) and cone beam computed tomography (CBCT) images and compared to the 2D Laplace transformation of their corresponding raw images. $ApEn_{2D}$ operates in a different way compared to $SampEn_{2D}$, and $DistrEn_{2D}$, it re-displays the image showing its structural details by defining the entropy measure around each pixel of the image. Thus, it is not actually a measure of image's irregularity.

Complexity-entropy causality plane

Complexity-entropy causality plane is a method introduced recently as a combination of the permutation entropy concept with a relative entropy concept [94, 24].

Permutation entropy [70], $PermEn_{1D}$, is another popular metric in this field. Although this method is fast, it is too sensitive to noise and does not address the problem of equal values in embedding vectors [24]. This method relies on linking symbolic sequences to portions of the time series. This relies on the presence of local order in these portions. After that, the probability distribution of these symbolic sequences is calculated.

The nature of $PermEn_{1D}$ allowed to extend it to higher dimension data. Consider a two-dimensional array, *i.e.* an image, $\{y_i^j\}_{j=1, \dots, n_x}^{i=1, \dots, n_y}$ with size $n_x \times n_y$. The bidimensional extension of $PermEn_{1D}$, $PermEn_{2D}$ [94] is defined as follows:

1. $d_x \times d_y$ dimensional matrices, (s_x, s_y) , with $d_x, d_y > 1$ are defined as:

$$(s_x, s_y) \rightarrow \begin{bmatrix} y_{s_x-(d_x-1)}^{s_y-(d_y-1)} & y_{s_x-(d_x-2)}^{s_y-(d_y-1)} & \dots & y_{s_x-1}^{s_y-(d_y-1)} & y_{s_x}^{s_y-(d_y-1)} \\ y_{s_x-(d_x-1)}^{s_y-(d_y-2)} & y_{s_x-(d_x-2)}^{s_y-(d_y-2)} & \dots & y_{s_x-1}^{s_y-(d_y-2)} & y_{s_x}^{s_y-(d_y-2)} \\ \vdots & \vdots & \ddots & \vdots & \vdots \\ \vdots & \vdots & \ddots & \vdots & \vdots \\ y_{s_x-(d_x-1)}^{s_y-1} & y_{s_x-(d_x-2)}^{s_y-1} & \dots & y_{s_x-1}^{s_y-1} & y_{s_x}^{s_y-1} \\ y_{s_x-(d_x-1)}^{s_y} & y_{s_x-(d_x-2)}^{s_y} & \dots & y_{s_x-1}^{s_y} & y_{s_x}^{s_y} \end{bmatrix},$$

with $s_x = d_x, d_x + 1, \dots, n_x$ and $s_y = d_y, d_y + 1, \dots, n_y$.

2. Then the possible permutation is evaluated for the $(n_x - d_x + 1)(n_y - d_y + 1)$ matrices:

$$\pi = (r_0, u_0), (r_1, u_0), \dots, (r_{d_x-1}, u_0), \dots, (r_0, u_{d_y-1}), (r_1, u_{d_y-1}), \dots, (r_{d_x-1}, u_{d_y-1}),$$

of $(0, 1, \dots, d_x d_y - 1)$ defined by $y_{s_x-r_{d_x-1}}^{s_y-u_{d_y-1}} \leq y_{s_x-r_{d_x-2}}^{s_y-u_{d_y-1}} \leq \dots \leq y_{s_x-r_1}^{s_y-u_{d_y-1}} \leq y_{s_x-r_0}^{s_y-u_{d_y-1}} \leq \dots \leq y_{s_x-r_{d_x-1}}^{s_y-u_0} \leq y_{s_x-r_{d_x-2}}^{s_y-u_0} \leq \dots \leq y_{s_x-r_1}^{s_y-u_0} \leq y_{s_x-r_0}^{s_y-u_0}$

3. After that the system can access the $(d_x d_y)!$ states. Then the probability distribution is calculated $\mathbf{P}=\{p(\pi)\}$ as relative frequencies:

$$p(\pi) = \frac{\#s_x, s_y | s_x \leq n_x - d_x \text{ and } s_y \leq n_y - d_y + 1; (s_x, s_y)}{(n_x - d_x + 1)(n_y - d_y + 1)} \quad (1.34)$$

4. See Figure 1.9 for an illustrative example. The patterns for π are ordered column by column.

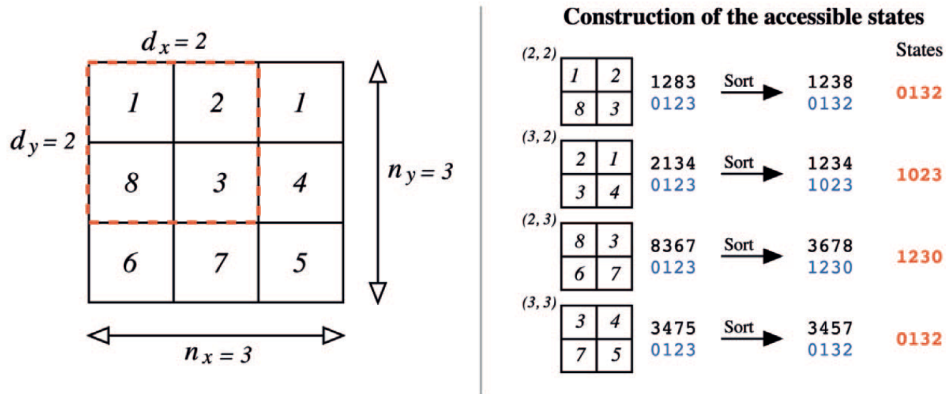


Figure 1.9 – Schematic diagram for the two dimensional extension of permutation entropy. Adapted from [24].

Permutation entropy has two major drawbacks: some amplitude information are ignored and it is highly sensitive to noise [70, 22]. Note that $FuzEn_{1D}$ has generally a better performance in this scope.

1.5 Multiscale Bidimensional Entropy Measures

One- and two-dimensional entropy methods, such as sample entropy, are used to quantify the irregularity of signals or images at one scale. They assess repetitive patterns and return maximum values for completely random processes (*e.g.*, white noise). However, such approaches are very sensitive to high frequency components and may fail to account for the multiple scales inherent in data [89]. To deal with the problem, multiscale entropy-based techniques were proposed to quantify the irregularity of a signal or image over multiple scale factors to illustrate their corresponding complexity. This is achieved by evaluating the entropy measure for the original and coarse-grained versions of the data under study.

Moreover, in analyzing biological systems in specific (biomedical signals and images) it is of importance to study the overall complexity, *i.e.*, at several scale factors, as previously addressed in [88, 91]. Single scale measurements could be misleading in determining the actual complexity of a system. Taking the classical example of pink and white noise, it has already been shown in several papers that the entropy value of white noise shows higher irregularity than pink noise ($\frac{1}{f}$) but as the evaluation is performed over several scale factors, white noise shows a decrease in irregularity with scale factor whereas pink noise shows higher entropy values with scale factors and eventually a higher complexity. This agrees with the fact that pink noise is of long term correlations whereas white noise is of short term correlations and is thus less complex. This is also reflected in the biological system's behavior where some pathologic processes have a lower complexity than healthy processes unlike what is indicated by the traditional entropy measurement on the single scale factor [88].

Only one bidimensional entropy measure (beside our work) has been extended to its multiscale version. Multiscale bidimensional sample entropy based on two different coarse-graining methods will be explained below.

Multiscale bidimensional sample entropy MSE_{2D}

We start by introducing the multiscale bidimensional sample entropy, MSE_{2D} [42]. It is a two-step procedure based on the Bidimensional Sample Entropy, $SampEn_{2D}$, detailed in section 1.4.2. For an image \mathbf{U} of W width and H height, a coarse-graining procedure is performed. Then $SampEn_{2D}$ is applied to each coarse-grained version $\mathbf{G}^{(\tau)} = \{g_{i,j}^{(\tau)}\}$.

The whole procedure is therefore the following:

1. a non-overlapping window scans the whole original image to form the coarse-grained versions $\{\mathbf{G}^{(\tau)}\}$ as:

$$g_{i,j}^{(\tau)} = \frac{1}{\tau^2} \sum_{k=(i-1)\tau+1, l=(j-1)\tau+1}^{k=i\tau, l=j\tau} u_{k,l}, \quad (1.35)$$

where i goes from 1 to $\lceil \frac{H}{\tau} \rceil$ and j goes from 1 to $\lceil \frac{W}{\tau} \rceil$.

2. for each coarse-grained image $\mathbf{G}^{(\tau)}$, $SampEn_{2D}$ (see section 1.4.2) is computed.

Modified multiscale bidimensional sample entropy $ModMSE_{2D}$

The modified multiscale bidimensional sample entropy was proposed to overcome the image size limitations when dealing with small images in specific. In fact, the coarse-graining procedure used for MSE_{2D} reduces the images sizes considerably. Thus, $ModMSE_{2D}$ is proposed to tackle this issue.

Similar to the MSE_{2D} concept, $ModMSE_{2D}$ is also a two step procedure in which $SampEn_{2D}$ is calculated for the coarse-grained versions of an original image [42]. However the coarse-grained versions are composed differently. It is defined as follows:

1. an overlapping window scans the whole original image to form the coarse-grained versions $\mathbf{Q}^{(\tau)} = \{q_{i,j}^{(\tau)}\}$ as:

$$q_{i,j}^{(\tau)} = \frac{1}{\tau^2} \sum_{k=i, l=j}^{k=i+\tau-1, l=j+\tau-1} u_{k,l}. \quad (1.36)$$

where i goes from 1 to $(H - \tau + 1)$ and j goes from 1 to $(W - \tau + 1)$

2. for each coarse-grained image $\mathbf{Q}^{(\tau)}$, $SampEn_{2D}$ (see section 1.4.2) is computed.

1.6 Medical Applications

1.6.1 Imaging modality: dermoscopy

Dermoscopy or Epiluminescence Microscopy (ELM), is one of the well-known non-invasive techniques used for cutaneous diseases inspection and diagnosis on which most research studies are conducted. Dermoscopy is a noninvasive imaging modality that allows obtaining an *in vivo* evaluation of colors and microstructures of the epidermis, the dermoepidermal junction, and the papillary dermis that cannot be seen by the naked eye [95, 96, 97, 98]. Figure 1.10 shows a simple illustration for the structure of a dermoscope coupled with a digital camera. Usually, gel is applied to the skin surface. The transparent spacer is placed in a firm position in contact with the skin. Moderate pressure is applied in a way to avoid having air bubbles between the transparent spacer and the skin, while at the same time, avoiding to exert a lot of pressure on the skin surface. Then, the macro converging lens and high resolution digital camera are positioned.

The use of dermoscopy in a clinical exam is an essential part, as it provides diagnostic information that are invisible to the naked eye. A dermoscope could be thought of as the *dermatologist's stethoscope*, as it is easy to use and carry around [99, 97]. Dermoscopy was first used for the identification of melanocytic skin lesions (nevi and melanoma), then it became used for the inspection of several other cutaneous tumors: nonmelanocytic pigmented and nonpigmented lesions.

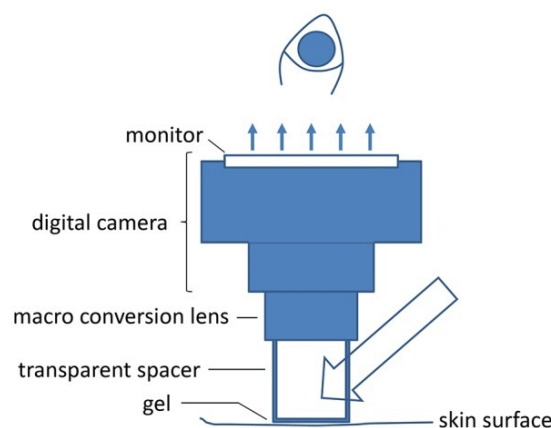


Figure 1.10 – Schematic diagram for a dermoscope. Adapted from [100].

However, dermoscopy alone is not always sufficient. In fact, it has been shown that dermoscopy may lower the accuracy of diagnosis for several medical cases if handled by inexperienced dermatologists [101, 96]. Also for melanoma identification, several studies emphasized that only for “experienced dermatologists” dermoscopy provides more accurate diagnosis than naked eye clinical examination. Knowing that, un-aided eye diagnosis is about 60% accurate [98]. In addition, even experienced clinicians have diagnostic accuracy below 85% [102]. Thus, it could be stated that the dermoscopy accuracy is directly related to the examiners’ experience degree. Furthermore, a dermatologist’s decision based on dermoscopy alone remains subjective; so computer-based analysis techniques would be of great importance to give objective judgment and diagnosis for the dermoscopic images and aid the medical doctors in clinical decision making. Consequently, for the dermoscopy field images we employed our developed measures.

1.6.2 Skin: microcirculation

Skin is the largest body organ that is the primary barrier against external agents, a thermoregulator, a platform for perceiving sensation, and an excreter for some forms of body wastes (ex. minerals and water) among other functions. To achieve some of its roles, skin has a high-vessel density structure, known as cutaneous microcirculation. This microcirculation consists of two important horizontal plexuses in the dermis [103, 104]:

- the upper horizontal plexus located at 1 – 1.5 *mm* from the skin surface (at the level of the dermal papillae), and
- the lower horizontal plexus at the dermal subcutaneous junction.

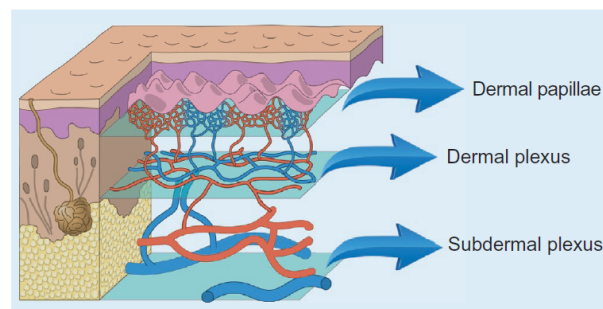


Figure 1.11 – Schematic demonstration of the dermal and subdermal plexus. We can notice two important dermal horizontal plexuses: the upper horizontal plexus located at 1 – 1.5 *mm* from the skin surface (at the level of dermal papillae), and the lower horizontal plexus at the dermal subcutaneous junction. Adapted from [104].

Referring to Figure 1.11, we can notice that the upper dermal plexus contains the capillary network and that the two aforementioned plexuses are linked by the ascending arterioles and descending venules.

Microcirculation is the key central element of the cardiovascular system. It has the role of delivering nutrients and oxygen, providing the essential fluids exchange, and getting rid of waste products between the blood circulation and body tissues. The microcirculation represents the arteries with diameter less than $150\ \mu\text{m}$, arterioles, capillaries, and venules [105], please see Figure 1.12.

The arterioles are vessels with an external diameter between 17 and $26\ \mu\text{m}$. They have a smooth muscle layer that allows them to control the pressure gradient according to the tissues' metabolic demand, by their ability to adjust their diameters. Capillaries have an external diameter smaller than $12\ \mu\text{m}$. They are the structures in which the exchange of gasses, nutrients, and cellular excreta happens. They are very thin such that their walls are of 2 to $3\ \mu\text{m}$ thickness to allow the flow of fluids. Venules are vessels with an external diameter between 18 and $23\ \mu\text{m}$. They are extensions of capillaries (with thicker walls) and form parallel structures to the arterioles. Moreover, venules do not have the smooth muscle layer [106, 105, 104].

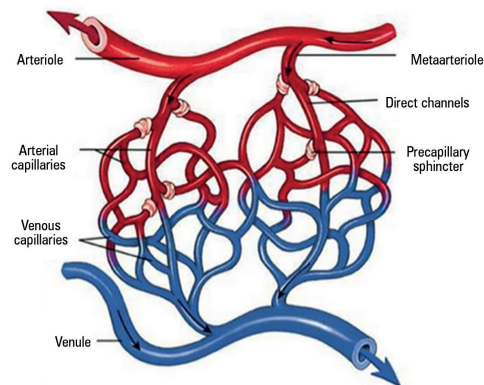


Figure 1.12 – Schematic demonstration for microcirculation anatomy. It shows the arteriole and venule connected by the capillaries where the main exchange of nutrients happens. Adapted from [106].

For patients with critical illness, shock, and other bedridden cases, establishing “hemodynamic coherence” [107] is one of the important targets for resuscitation. Besides monitoring the macrocirculatory segments (heart rate, blood pressure, *etc.*), assessing the microcirculatory segments should be considered to supervise the highly probable dissociation

between micro- and macrocirculatory aspects, *i.e.* loss of hemodynamic coherence [108, 106]. This fact supports the need to develop a fast and accessible method for analyzing the microcirculatory blood flow and monitoring its accordance with the global blood flow control. Simultaneously, skin is the largest organ, the most accessible in critical cases, and could provide direct access for possible microcirculatory alterations [108]. Thus, it would be compelling to develop a computerized cutaneous microcirculation evaluation technique [108].

The study of cutaneous microcirculation has gained increasing interest in the past few years because it was associated with a number of pathological processes [109, 110]. Furthermore, endothelial dysfunction is progressively perceived as an early key element in pathogenesis of cardiovascular pathologic conditions such as hypertension, coronary artery condition, hypercholesterolemia *etc.* [111, 106]. Therefore, the assessment of tissue microcirculation and comparing it to the macro-hemodynamic parameters is important. Although such practices are not fully created and integrated in the clinical applications yet [106], they may become achievable in the near future as several research studies cover this topic including our recent study [29]. The study dealing with cutaneous microcirculation is performed in collaboration with the department of dermatology at Angers university hospital – Angers, France represented by Pr Ludovic Martin and Dr Clemence Berthin.

1.6.3 Pseudoxanthoma elasticum (PXE)

Despite the crucial medical research advancements, some diseases are still incurable. Pseudoxanthoma elasticum (PXE) is one of these diseases, also known as Grönblad-Strandberg syndrom. It is also known as Gronblad-Strandberg syndrome. PXE is rare, with an approximate worldwide prevalence in 1 per 25,000 – 70,000 people [112]. It is a hereditary disorder caused by mutations in the ABCC6 gene encoding a transporter protein. In fact, PXE is an autosomal recessive disease, which means if the parents are carriers with no apparent symptoms there is 25 % possibility that the children would have PXE; *i.e.* if they obtained the mutated gene from both parents, see Figure 1.13.

PXE is accompanied by calcification of soft tissues and degeneration of elastic fibers [114, 115]. It targets the skin, retina, and cardiovascular system. The elastic fibers in these sites degenerate and slowly become calcified (mineralized), eventually losing their elastic function [114, 115, 116, 117, 118]. PXE is known for its systemic manifestations, usually first in skin as yellow cutaneous papules of 1 – 5 mm diameter on the lateral

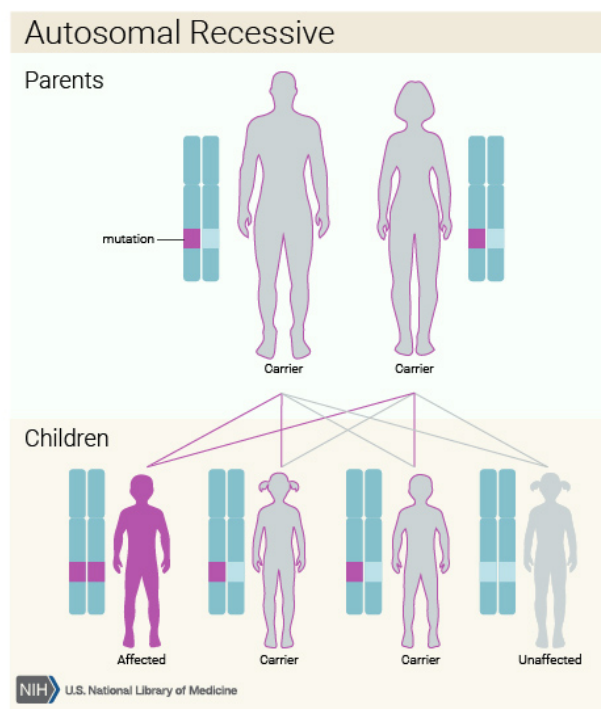


Figure 1.13 – PXE is a hereditary autosomal recessive disease for which the probability of occurrence in the children if the parents are carriers is illustrated above. Adapted from [113].

neck (see Figure 1.14) and supraclavicular regions that are generally the primary physical signs of developing PXE. These physical signs gradually extend to more distal flexural sites over several years followed by a loss of elasticity [119, 114, 115, 117, 118].



Figure 1.14 – PXE skin manifestations: cutaneous papules appearing on the neck of a PXE patient in an advanced stage. CHU Angers - department of Dermatology.

The degenerative calcification of the body's elastic structures is manifested mainly in [119, 114, 115, 117, 118]:

- skin's mid and deep dermis elastic fibers (see Figure 6.1 in the Annexes) especially on the neck, underarms, back of the knee, and any skin area that touches when joint bends.
- the eye by lesions of the posterior segment of the eye including peau d'orange, it causes the calcification of the Bruch's membrane and subsequently cracks causing angioid streaks (see Figure 1.15).
- the cardiovascular system's endocardium and arteries causing several complications leading to several cardiovascular diseases and eventually death.
- No evidence for its effect on the lung's elastic tissue has been yet observed.



Figure 1.15 – PXE ophthalmic manifestations: florescent angiogram for the the Bruch's membrane cracks "Angioid streaks" caused by the calcification due to PXE proliferation. Adapted from [114].

The diagnosis of PXE relies mainly on the physical skin manifestations that usually

appear during childhood or adolescence [112]. These manifestations progress in an unpredictable manner during adulthood and are followed by serious ophthalmic and cardiovascular manifestations due to the degenerative transformations in the elastic tissues [112, 114]. Figure 1.16 presents an illustration of the mineralisation in the connective tissues, in specific the elastic structures of several body organs.

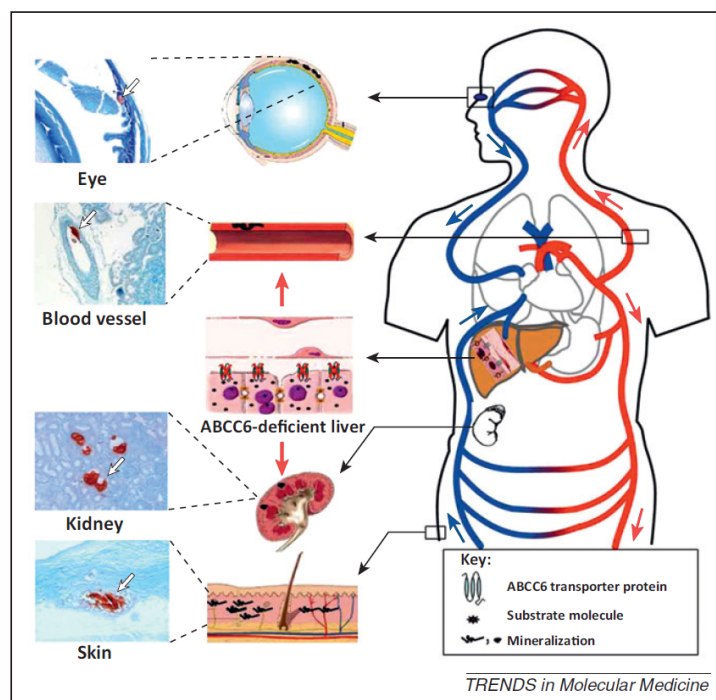


Figure 1.16 – PXE manifestations in the body targeting the elastic fibers and connective tissues mainly in the eyes, arteries, and skin. Adapted from [120].

Despite the fact that there is no definite treatment for PXE yet the diagnosis in the very early stage (skin manifestations) is essential. It aids the implementation of prophylactic lifestyle, preventive diet plans, psychological guidance, and better surveillance of the possible clinical complications that would arise [116, 121, 119]. Several therapeutic measures might be implemented at the early stages. These measures could at least enhance the quality of the patient's life and result in less complications during the natural clinical course of PXE.

One of the imaging modalities used for detecting PXE's primary skin symptoms is dermoscopy because papules alter the skin texture. However, dermoscopy alone is not always sufficient. In fact, it has been shown that dermoscopy may lower the accuracy of diagnosis if handled by inexperienced dermatologists [101]. Therefore, in order to reduce

diagnostic errors that result from the difficulty and subjectivity of visual interpretation, and the possible variability of human perception, the development of computerized image analysis techniques is of great importance [96]. The study on PXE is performed in collaboration with the department of dermatology at Angers university hospital – Angers, France represented by Pr Ludovic Martin and Dr Clemence Berthin.

1.6.4 Melanoma

According to the World Health Organization, one in every three diagnosed cancer cases is a skin cancer and the incidence rate has been increasing over the past years. In cancer diagnosis, the number of melanoma (skin cancer) cases is augmenting more than any other cancer type. The real challenge is in the early detection for melanoma because it is often mistaken for the benign melanocytic nevi and cannot be always identified in dermoscopic images; even experienced clinicians have diagnostic accuracy below 85% [102], see Figure 1.17.

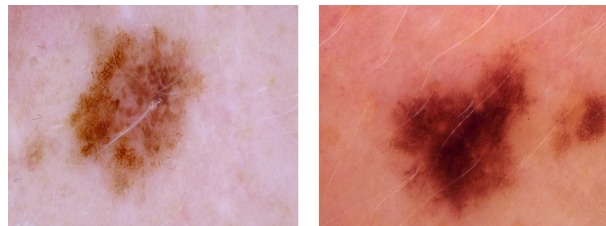


Figure 1.17 – Image of melanoma (right) and melanocytic nevi (left).

Dermoscopy is one of the well-known non-invasive techniques used for skin cancer diagnosis on which most research studies are conducted, please refer to section 1.6.1. However, visual diagnosis alone might be misleading and subjective even when performed by experts. Thus, dermoscopy image analysis (DIA) using computer-aided diagnosis (CAD) systems is essential to help medical doctors. Several studies proposed computer-extracted texture features for cutaneous lesions diagnosis, in specific for the most aggressive type, melanoma [122, 123, 124]. Melanoma is metastatic, thus, its early diagnosis and excision would definitely increase the survival rate. Some DIA methods focus only on the dermoscopic images structure/patterns [125, 126], others rely on colors [127, 128, 129], and certain consider both [130], for more details please refer to [122, 123, 124]. Nevertheless, most studies propose learning-based approaches and only few, until now, suggest

entropy-based measures. Consequently, in this manuscript we will be presenting entropy measures and evaluating melanoma and melanocytic nevi images in gray scale and colored dermoscopic images.

1.6.5 Chronic obstructive pulmonary diseases (COPD)

Chronic Obstructive Pulmonary Diseases (COPD) are a group of progressive lung diseases. The most common are emphysema and chronic bronchitis. Emphysema is manifested by the destruction of alveoli's elastic fibers which are the basic structures for gas exchange between the external environment and the blood circulation. They become severely damaged and lose their elastic properties. In chronic bronchitis, inflammation and excess mucus causes narrowing of the bronchitis (bronchoconstriction) and eventually causing airflow limitation. For illustration, please see Figure 1.18. COPD is characterized by a progressive and irreversible decline in lung function [131, 132]. It causes shortness in breathing (dyspnea) and chronic cough with irreversible effects.

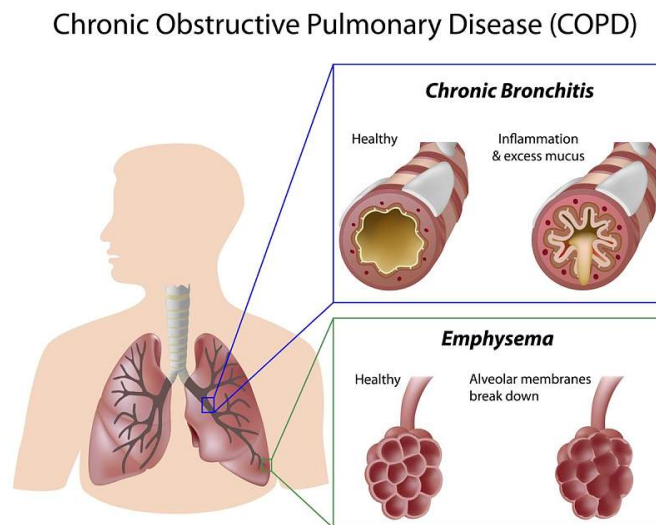


Figure 1.18 – Illustration of the manifestation of COPD in the respiratory system: chronic bronchitis (top pannel) where bronchoconstriction occurs and emphysema (bottom pannel) where the alveolus become damaged. Both cause shortness in breath (dyspnea) and chronic cough. Adapted from [133].

In 2015, COPD affected about 174.5 million (2.4%) of the global population and resulted in 3.2 million deaths. According to the World Health Organization (WHO) it is expected that by year 2030 it will become the 4th leading cause of death worldwide.

In addition, according to a study made on the numbers between 1990-2015, COPD is among the leading causes of death in the world already (rank 14th) [134]. There is no treatment for COPD yet, however early diagnosis and potential treatment measures can help ease the symptoms, lower the chance of complications, and generally improve quality of life [131].

Lung diseases are one of the main causes of death worldwide. Identifying their phenotypes and staging their severity can be obtained through computed tomography (CT) images of the pathological site. However, CT can lead to a huge amount of data (many 2D-scans for one region are studied to represent its volume) that can be difficult to analyze and interpret.

In our work we propose a new entropy-based measure, termed pseudo-tri dimensional multiscale fuzzy entropy, to quantify the irregularity of high resolution CT scans (HRCT). This work is performed in collaboration with Dr Lars Pilegaard Thomsen at the Aalborg university–Denmark for a presentation in an invited session entitled “Identification of Cardiopulmonary Function” at IEEE EMBC 2019. Data are obtained from University Hospital of Aalborg–Department of Respiratory Diseases (Aalborg, Denmark). Data from three groups of subjects are processed: one normal group and two other groups with chronic obstructive pulmonary diseases characterized by a progressive and permanent decline in lung function. The results are interesting for HRCT scan slices, allowing us to further extend this study to a larger number of patients in the future. Also, a very recent study on lung CT images of COPD patients shows texture analysis as a promising quantitative measure [135]. Thus, the scope of our study comes to be innovative and encouraging.

1.6.6 Idiopathic pulmonary fibrosis (IPF)

Idiopathic Pulmonary Fibrosis (IPF) is a chronic and destructive lung disease with irreversible effect. It has no known cure yet, but a lung transplant might be an option in some cases. IPF causes shortness in breath and chronic dry cough and symptoms that worsen with time.

IPF is a similar disease to COPD. The main difference between IPF and COPD is the kind of physical lung damage that each of them causes. IPF results in scarring of lungs that causes the alveolar sacs to thicken and the lungs become stiff. Consequently, this reduces the gas exchange and oxygen intake specifically; see Figure 1.19.

As we can notice that for the normal lung, Figure 1.19 (A), a capillary network sur-

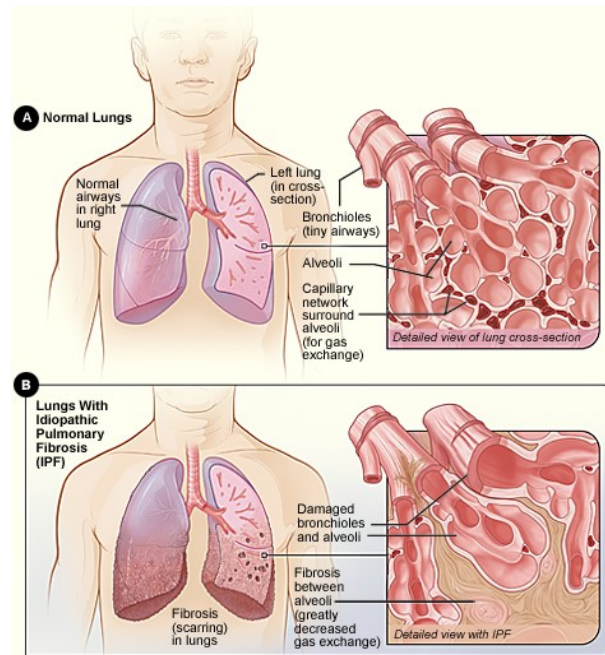


Figure 1.19 – Idiopathic Pulmonary Fibrosis (IPF) main lung symptoms. Adapted from [136].

rounds the alveoli to ensure the gas passage into the blood stream. However, for lungs with IPF, Figure 1.19 (B), scars known as fibrosis are formed between the alveoli, eventually decreasing drastically the ability for gas exchange. This causes shortage in oxygen intake, progressive dyspnea, and chronic cough.

The diagnosis of IPF usually relies on HRCT scans or lung biopsy. In HRCT, medical doctors try to identify the fibrosis or lung inflammation and often localize a pattern known as “honey comb”. In a lung biopsy, they scan the tissue for signs of changes or scars, in specific patterns of usual interstitial pneumonitis (UIP) [136, 137, 138, 139, 135].

In this manuscript, we propose an entropy measure and apply it to volumetric HRCT scans for healthy individuals and IPF patients to characterize the entropy behavior and irregularity of both cases. This work is performed in collaboration with University of Coimbra–Portugal represented by Pr João Cardoso, Dr Pedro G. Vaz, and Andreia Sofia F. Gaudêncio, and the competence center for rare pulmonary diseases in the department of Respiratory Medicine at Rennes University Hospital–France represented by Dr Guillaume Mahé and Dr Mathieu Lederlin. The main goal is to differentiate the two groups successfully using our proposed entropy measure. This could be a useful tool in the evaluation of HRCT of patients with IPF for early detection and quantification of the UIP

patterns, through an irregularity assessment.

1.6.7 Uterine fibroids

Uterine fibroids are benign growth in the uterus muscle. One of the possible treatments for uterine fibroids is the non-surgical uterine artery embolization (UAE). This procedure involves injecting embolic agents into the blood vessels that supply the uterus. Thus, the blood flow is cut off the fibroids so that they become smaller and then destroyed, see Figure 1.20. This leads to shrinking fibroids and easing their symptoms in a minimally invasive manner.

In our study we also performed the texture analysis of uterine fibroids on MRI scans before and after arterial embolization. There is no software for performing this task yet. However, recent promising studies are still investigating the possibility of depending on texture analysis.

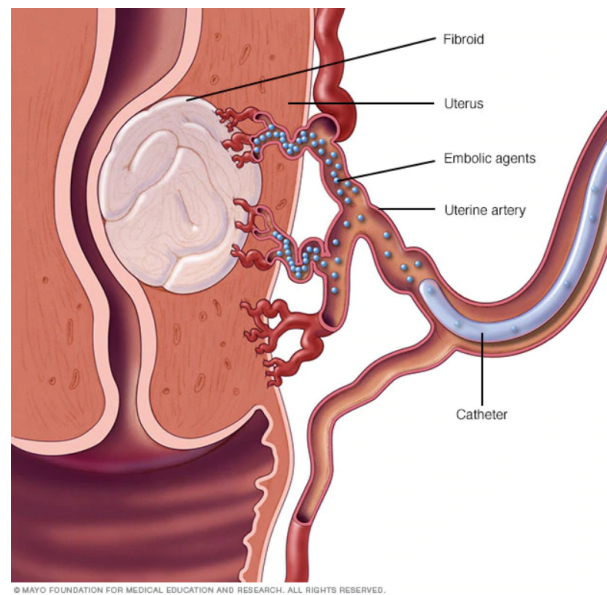


Figure 1.20 – The embolic agents which are very small particles are injected into the arteries that supply the uterus using a small catheter. These agents stay in the arteries supplying the fibroids and cut off the blood flow reaching them. Eventually, the fibroids shrink and die. Adapted from [140].

Several recent studies are encouraging radiomic analysis and feature extraction methods for MRI images of prostate cancer, uterine sarcoma, and rectal cancer among others [141, 142, 143, 144, 145] and they showed promising possible future outcomes. That is why in this manuscript, we present a preliminary work for analyzing MRI uterine

images of uterine fibroids before and after embolization in two time intervals (after 10 days and after 6 months from embolization). This study is performed in collaboration with Brest University Hospital—France represented by Pr Michel Nonent and Sonia Saib, and the Lebanese University—Lebanon represented by Pr Jamal Charara and Rakelle Haidar.

1.6.8 COVID-19

The first officially reported human case of COVID-19 case was dated back December 2019 referring to WHO reports on the situation. Soon after that, the severe acute respiratory syndrome coronavirus-2, SARS-CoV-2, virus causing COVID-19 showed a huge spread worldwide [146, 147, 148]. SARS-CoV-2 is the seventh known type coronavirus to infect human beings [148] and the one with the widest spread.

The SARS-CoV-2 infection leads to pulmonary interstitial damages, which may cause severe pneumonia, acute respiratory distress syndrome, multiple organ failure, and death [147, 148, 149, 150, 151].

According to [152], with a study done on 99 patients, most of them showed fever (83%) cough (82%), and considerable percentage showed shortness of breath (31%). Those remain the most common symptoms in most COVID-19 case. Upon showing symptoms, COVID-19 patients are confirmed to have the disease through a reverse transcription polymerase chain reaction (RT-PCR) test. Two examples for COVID-19 manifestation in the lungs are shown in Figure 1.21.

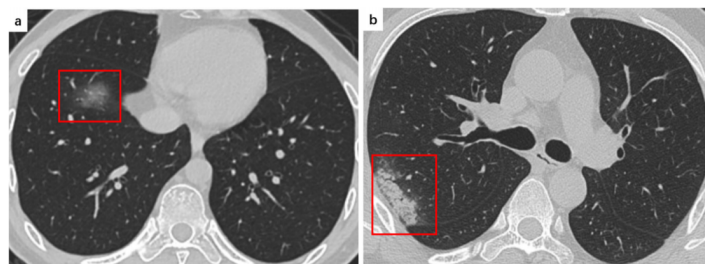


Figure 1.21 – (a) COVID-19 patient of 35 years old presenting fever and headache for one day. A pure ground glass opacity is shown in the right lower lobe. (b) COVID-19 patient of 47 years old presenting fever for 7 days. Consolidation is shown in the right lobe subpleural area. the right lower lobe (red frame). Adapted from [147].

COVID-19 is perhaps the most famous disease nowadays. Everyone is talking

about it, its causes, its effects, and its long term consequences. This pandemic spread made the people of almost the whole planet change their lifestyles and adapt to the new circumstances. In our turn, we performed a study on CT scans for clinically confirmed COVID-19 patients and presented the results analysis. This study is performed in collaboration with University of Coimbra–Portugal represented by Pr João Cardoso, Dr Pedro G. Vaz, and Andreia Sofia F. Gaudêncio, and the competence center for rare pulmonary diseases in the department of Respiratory Medicine at Rennes University Hospital–France represented by Dr Guillaume Mahé and Dr Mathieu Lederlin.

1.7 Conclusion

In this chapter we presented the most common texture analysis methods and the important role of texture analysis in several fields. Then, we explained one of the recently introduced methods that is developing entropy measures based on information theory concept. The latter is our proposed basic concept for texture analysis throughout this manuscript. After that, we introduced the medical cases and types of images that we will handle in Chapter 5. This includes: PXE, melanoma, cutaneous microcirculation structure, COPD, IPF, UAE, and COVID-19.

METHODOLOGY: DEVELOPED BIDIMENSIONAL ENTROPY MEASURES

2.1 Introduction

$FuzEn_{2D}$ is based on the unidimensional Fuzzy Entropy ($FuzEn_{1D}$) that is a result of integrating fuzzy logic with the research of complex systems and nonlinear dynamics. It exploits the concept of fuzzy membership function to study the irregularity of dynamic systems. $FuzEn_{1D}$ was also used to provide a noise floor for denoising signals [68, 85, 76, 153]. Another $FuzEn_{1D}$ application is epileptic seizures detection and classification [154].

Consequently, due to the importance of studying images irregularity, the advantages of $FuzEn_{1D}$ over other 1D irregularity measures [86, 85, 76], and several tests that we performed, we decided to introduce the 2D version of the fuzzy entropy technique, $FuzEn_{2D}$, as a measure of images irregularity (based on fuzzy logic), section 2.2. We also propose its multiscale extension, MSF_{2D} , in section 2.3. After that, we implement MSF_{2D} to come up with the pseudo-multiscale fuzzy entropy 3D, $pMFuzEn_{3D}$ (see section 3.2).

Moreover, due to the encouraging results for gray scale images in the bidimensional application, we propose several fuzzy-entropy-based measures to analyze colored textures: the single-channel approach, $FuzEnC_{2D}$ (see section 2.4.1), the multi-channel approach, $FuzEnV_{2D}$ (see section 2.4.2), and the modified multi-channel approach, $FuzEnM_{2D}$ (see section 2.4.3).

Finally, we establish the tridimensional entropy versions of $FuzEn_{2D}$, tridimensional fuzzy entropy measure $FuzEn_{3D}$ and its multiscale version MSF_{3D} , in the following chapter, sections 3.3 and 3.4.

2.2 Bidimensional Fuzzy Entropy

Due to the advantages of $FuzEn_{1D}$ over other unidimensional entropy measures [86, 85, 76], and the importance of having image irregularity and complexity measures, we introduce $FuzEn_{2D}$. Our $FuzEn_{2D}$ measure maintains the original $FuzEn_{1D}$ properties and extends its application to images. $FuzEn_{2D}$ is defined as the negative natural logarithm of the conditional probability that two patterns similar for their corresponding $m \times m$ points will remain similar when the $(m + 1) \times (m + 1)$ points are considered. Thus, images with repeating-periodic structures (regular patterns) would hold a low entropy value. On the contrary, images with non-repeating structures (irregular unpredictable patterns) would hold a high entropy value. The membership degree μ of an element x in a set is expressed by a continuous graduated similarity classifier which is an exponential function. This exponential function associates each element with a value of membership between 0 and 1. The closer the exponential function's value to unity is, the higher the membership degree of the element in the set will be. In fuzzy entropy, this concept is imported using a family of exponential functions $\exp(-(d_{ij}^m)^n/r)$ to describe the degree of similarity between vectors based on their shapes [68].

2.2.1 Definition of $FuzEn_{2D}$

Let us consider a standardized image \mathbf{U} with width W and height H , see Figure 2.1. Define $\mathbf{X}_{i,j}^m$ as the m -length square window or pattern of origin $u(i, j)$. $\mathbf{X}_{i,j}^m$ represents the group of pixels in the image \mathbf{U} of indices ranging from line i to $i + m - 1$ and from column j to $j + m - 1$ as follows:

$$\mathbf{X}_{i,j}^m = \begin{bmatrix} u_{i,j} & \dots & u_{i,j+m-1} \\ u_{i+1,j} & \dots & u_{i+1,j+m-1} \\ \dots & \dots & \dots \\ u_{i+m-1,j} & \dots & u_{i+m-1,j+m-1} \end{bmatrix}. \quad (2.1)$$

Similarly, $\mathbf{X}_{i,j}^{m+1}$ is defined as the $(m + 1)$ square window. Let $N_m = (W - m)(H - m)$ be the total number of square windows in \mathbf{U} that can be generated for both the $\mathbf{m}=[m,m]$ and $(\mathbf{m}+1)=[m + 1, m + 1]$ sizes. The last m -length line and m -length column of the image are excluded to ensure that $\mathbf{X}_{i,j}^m$ and $\mathbf{X}_{i,j}^{m+1}$ are defined for all indices $1 \leq i \leq H - m$ and $1 \leq j \leq W - m$. For $\mathbf{X}_{i,j}^m$ and its neighboring windows $\mathbf{X}_{a,b}^m$, the distance function

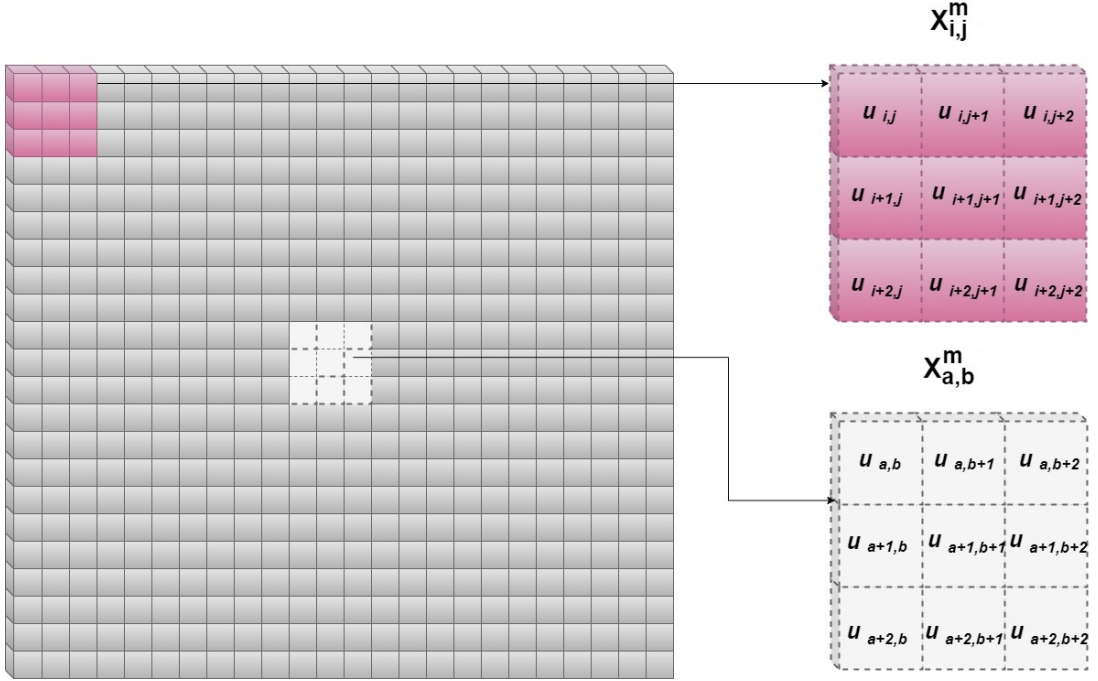


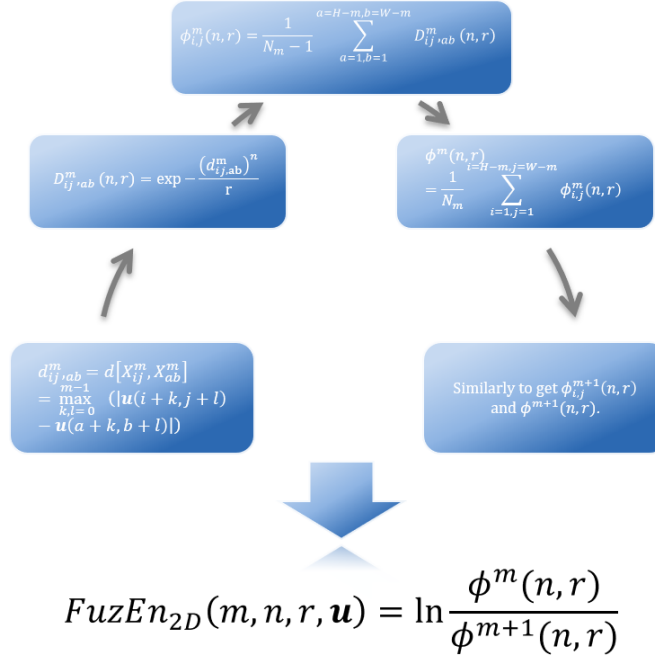
Figure 2.1 – Illustration for $FuzEn_{2D}$ of a gray scale image with $m = 3$.

$d_{ij,ab}^m$ between them is defined as the maximum absolute difference of their corresponding scalar components. Knowing that a goes from 1 to $H - m$ and b goes from 1 to $W - m$ with $(a, b) \neq (i, j)$, the distance function is expressed as follows:

$$d_{ij,ab}^m = d[\mathbf{X}_{i,j}^m, \mathbf{X}_{a,b}^m] = \max_{k,l \in (0, m-1)} (|u(i+k, j+l) - u(a+k, b+l)|). \quad (2.2)$$

Herein, we did not remove the local mean of the compared windows $\mathbf{X}_{i,j}^m$ before obtaining the distance function as Chen *et al.* did for sequences [68]. Removing the local mean accounts only for local characteristics of the studied sequence, unlike sample and approximate entropy measures that consider the sequence's global characteristics [155]. Thus, we suggest studying the global characteristics for images as well and using that in our following applications. However, we introduce the local $FuzEn_{2D}$ algorithm, $FuzEnL_{2D}$, in the next section (see section 2.2.2). In addition, $FuzEn_{2D}$ avoids some unnecessary similarity considerations that could be caused by the local mean removal. Some studies (e.g., Liu *et al.* [86]) proposed the calculation of $FuzEn_{1D}$ using the local and global characteristics of a signal. Please see Figure 2.2 as an illustration for the $FuzEn_{2D}$ algorithm.

The similarity degree $D_{ij,ab}^m$ of $\mathbf{X}_{i,j}^m$ with its neighboring patterns $\mathbf{X}_{a,b}^m$ is defined by a


 Figure 2.2 – Illustrative schema for $FuzEn_{2D}$ algorithm.

fuzzy function $\mu(d_{ij,ab}^m, n, r)$:

$$D_{ij,ab}^m(n, r) = \mu(d_{ij,ab}^m, n, r) = \exp(-(d_{ij,ab}^m)^2/r). \quad (2.3)$$

Then, the similarity degree of each pattern is averaged to obtain:

$$\Phi_{i,j}^m(n, r) = \frac{1}{N_m - 1} \sum_{a=1, b=1}^{a=H-m, b=W-m} D_{ij,ab}^m, \quad (2.4)$$

with $(a, b) \neq (i, j)$, to construct:

$$\Phi^m(n, r) = \frac{1}{N_m} \sum_{i=1, j=1}^{i=H-m, j=W-m} \Phi_{i,j}^m(n, r). \quad (2.5)$$

Similarly for $m + 1$, to obtain $\Phi^{m+1}(n, r)$. Finally, bidimensional fuzzy entropy of the image \mathbf{U} is:

$$FuzEn_{2D}(\mathbf{U}, m, n, r) = \ln \frac{\Phi^m(n, r)}{\Phi^{m+1}(n, r)}. \quad (2.6)$$

For most $FuzEn_{2D}$ tests we choose $r = 0.25$ which is within the range recommended

by some previous studies on 1D [74, 76, 156, 85], $n = 2$, and we study the sensitivity of $FuzEn_{2D}$ to different embedding dimension $m \times m$ values.

2.2.2 Definitions of $FuzEnL_{2D}$ and $FuzEnGL_{2D}$

We also developed the local version of $FuzEn_{2D}$, $FuzEnL_{2D}$, that considers the local characteristics of the image's patterns. Even if this measure finds less application for our medical images we present in what follows the equations behind its algorithm and few tests in Chapter 4. Finally, we will present $FuzEnGL_{2D}$, that considers both the local and global characteristics of the studied images.

In a similar concept to the preceding algorithm, consider a standardized image \mathbf{U} having W width and H height. Define $\mathbf{X}_{i,j}^m$ as the $m \times m$ square window of origin $u(i, j)$ that is generalized by removing the the window's baseline; *i.e.* removing $\{u_0(i, j) = \frac{1}{m \times m} \sum_{I=0}^{m-1} \sum_{J=0}^{m-1} u_{i+I, j+J}\}$. Thus, $\mathbf{X}_{i,j}^m$ for $FuzEnL_{2D}$ is the group of pixels in the image \mathbf{U} defined as follows:

$$\mathbf{X}_{i,j}^m = \begin{bmatrix} u_{i,j} & \cdots & u_{i,j+m-1} \\ u_{i+1,j} & \cdots & u_{i+1,j+m-1} \\ \cdots & \cdots & \cdots \\ u_{i+m-1,j} & \cdots & u_{i+m-1,j+m-1} \end{bmatrix} - u_0(i, j). \quad (2.7)$$

Similarly, $\mathbf{X}_{i,j}^{m+1}$ is defined for $m+1 \times m+1$ points. Let $N_m = (W-m) \times (H-m)$ be the total number of square windows in \mathbf{U} that could be generated for both $m \times m$ and $(m+1) \times (m+1)$ sizes. We define the distance function $d_{ij,ab}^m$ between $\mathbf{X}_{i,j}^m$ and its neighboring windows $\mathbf{X}_{a,b}^m$ as the maximum absolute difference between their corresponding scalar components (with a from 1 to $H-m$ and b from 1 to $W-m$ having $(a, b) \neq (i, j)$):

$$\begin{aligned} d_{ij,ab}^m &= d[\mathbf{X}_{i,j}^m, \mathbf{X}_{a,b}^m] \\ &= \max_{k,l \in (0, m-1)} (|(u(i+k, j+l) - u_0(i, j)) - (u(a+k, b+l) - u_0(a, b))|). \end{aligned} \quad (2.8)$$

The similarity degree $D_{ij,ab}^m$ of $\mathbf{X}_{i,j}^m$ with its neighboring patterns $\mathbf{X}_{a,b}^m$ is defined by a fuzzy function $\mu(d_{ij,ab}^m, n, r)$ as:

$$D_{ij,ab}^m(n, r) = \mu(d_{ij,ab}^m, n, r) = \exp(-(d_{ij,ab}^m)^n / r). \quad (2.9)$$

Afterwards, the average of the similarity degree of each pattern is obtained by:

$$\Phi_{i,j}^m(n, r) = \frac{1}{N_m - 1} \sum_{a=1, b=1}^{a=H-m, b=W-m} D_{ij,ab}^m, \quad (2.10)$$

with $(a, b) \neq (i, j)$, to construct:

$$\Phi^m(n, r) = \frac{1}{N_m} \sum_{i=1, j=1}^{i=H-m, j=W-m} \Phi_{i,j}^m(n, r). \quad (2.11)$$

Similarly for $m + 1$ to obtain $\Phi_{i,j}^{m+1}(n, r)$ and $\Phi^{m+1}(n, r)$. Finally, the bidimensional local fuzzy entropy of image \mathbf{U} is defined as:

$$FuzEnL_{2D}(m, n, r, \mathbf{U}) = \ln \frac{\Phi^m(n, r)}{\Phi^{m+1}(n, r)}. \quad (2.12)$$

Moreover, we also established the bidimensional version of Liu *et al.* [86] fuzzy measure entropy, $FuzEnGL_{2D}$, that considers both the global and local characteristics of the studied images. $FuzEnGL_{2D}$ consists of summing the local fuzzy entropy value and the global value obtained by $FuzEnL_{2D}$ and $FuzEn_{2D}$, respectively.

$$FuzEnGL_{2D} = FuzEn_{2D} + FuzEnL_{2D}. \quad (2.13)$$

For our following developed measures, $FuzEn_{2D}$ concept will be employed due to its significance, less computation cost, and the fact that it considers the global characteristics of an image.

2.3 Multiscale Bidimensional Fuzzy Entropy

The complexity-based approaches include two main steps: (1) a coarse-graining process: removing high-frequency signal or image components with a digital low-pass filter and downsampling the filtered data by scale factor τ ; and (2) the calculation of an entropy value for each coarse-grained data at each scale τ [89]. Nevertheless, most entropy measures were used to deal with unidimensional signals until recently. For the bidimensional multiscale approach (MSE_{2D}), a 2D extension of the 1D coarse-graining process is used to study the complexity of images, *i.e.*, over several scale factors τ [43]. The interpretation of its results is as follows: if there is no noticeable change in entropy values

over the first several scale factors, this means that the image contains complex structures across multiple scale factors (complex image). However, if there is a considerable decrease in entropy values over scale factors, the image can be irregular but not structurally complex. In fact, in the complexity-based methods, high to low frequency-components (from low to high scale factors) are considered, whereas a single-scale entropy technique tends to deal with higher frequency components [89]. Only *SampEn*_{2D} was extended to its multiscale version until now, so herein we introduce our proposed multiscale bidimensional fuzzy entropy using two different coarse-graining versions.

After illustrating the advantages of fuzzy entropy measures on the 1D and 2D levels, we propose herein two methods based on the fuzzy bidimensional approach, the multiscale bidimensional fuzzy entropy, *MSF*_{2D}, and the modified multiscale bidimensional fuzzy entropy *MMSF*_{2D}. *MSF*_{2D} and *MMSF*_{2D} are based on Costa's [88] and Wu's [92] methods, respectively, for the coarse-graining procedure. Let us consider an image $\mathbf{U}=\{u_{i,j}\}$ with width W and height H . *MSF*_{2D} and *MMSF*_{2D} algorithms are explained in the following sections.

2.3.1 Multiscale bidimensional fuzzy entropy *MSF*_{2D}

*MSF*_{2D} is defined as a two-step procedure explained below. Figure 2.3 illustrates an example for $\tau = 1, 2,$ and 3 .

1. A non-overlapping 2D window scans the whole image and the pixels of each window are averaged. The obtained mean values form the coarse-grained images $\mathbf{Y}^{(\tau)}$, which are not subsets of the original image. Alternatively, they carry information about the whole original image. $\mathbf{Y}^{(\tau)} = \{y_{i,j}^{(\tau)}\}$, with $1 \leq i \leq (H - \tau + 1)$ and $1 \leq j \leq (W - \tau + 1)$, given a scale factor τ are defined as:

$$y_{i,j}^{(\tau)} = \frac{1}{\tau^2} \sum_{a=i, b=j}^{a=i+\tau-1, b=j+\tau-1} u_{a,b}. \quad (2.14)$$

2. *FuzEn*_{2D} is applied to each coarse-grained image.

$$MSF_{2D} = \{FuzEn_{2D}(m, n, r, \mathbf{Y}^{(\tau)})\} \quad (2.15)$$

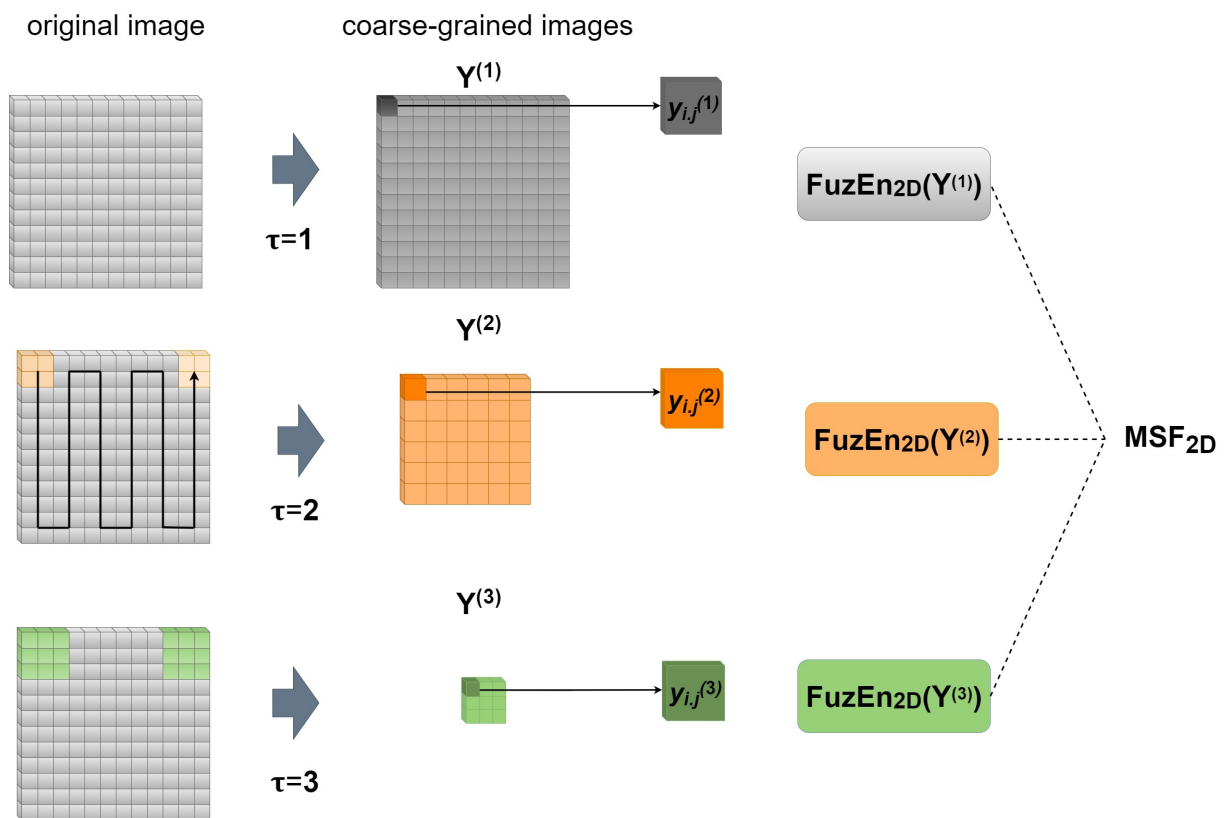


Figure 2.3 – Illustration for MSF_{2D} of an image $U = \{u_{i,j}\}$ for $\tau = 1, 2,$ and 3 .

2.3.2 Modified multiscale bidimensional fuzzy entropy $MMSF_{2D}$

$MMSF_{2D}$ is defined as a two-step procedure similar to MSF_{2D} . However, the coarse-graining procedure is different from the latter and is based on the work performed by Wu *et al.* [92] for the 1D multiscaling. $MMSF_{2D}$ is calculated as follows:

1. An overlapping 2D window scans the whole image and the pixels of each window are averaged. The obtained averaged values form the coarse-grained images $\mathbf{Z}^{(\tau)}$, which are not subsets of the original image. Alternatively, they carry information about the whole original image. $\mathbf{Z}^{(\tau)} = \{z_{i,j}^{(\tau)}\}$, with $1 \leq i \leq \frac{H}{\tau}$ and $1 \leq j \leq \frac{W}{\tau}$, given a scale factor τ are defined as:

$$z_{i,j}^{(\tau)} = \frac{1}{\tau^2} \sum_{a=(i-1)\tau+1, b=(j-1)\tau+1}^{a=i\tau, b=j\tau} u_{a,b}. \quad (2.16)$$

2. $FuzEn_{2D}$ is applied to each coarse-grained image.

$$MMSF_{2D} = \{FuzEn_{2D}(m, n, r, \mathbf{Z}^{(\tau)})\} \quad (2.17)$$

2.4 Colored Fuzzy Entropy Measures

Only few studies proposed bi-dimensional entropy-based measures for color image textures [25] including two recent publications by our team [29, 31]. Nevertheless, color and texture are probably the most important components of visual features. Many biomedical images are color-textured: dermoscopy images, histological images, endoscopy data, fundus and retinal images, among others. Most published studies investigate the texture features for gray images only.

At first, we developed bidimensional fuzzy entropy, $FuzEn_{2D}$ and its multiscale extension MSF_{2D} [26, 28]. These entropy measures revealed interesting results for some dermoscopic images but were limited to gray scale images. Therefore, based on $FuzEn_{2D}$, we propose two approaches to deal with colored images: the single-channel bidimensional fuzzy entropy, $FuzEnC_{2D}$ [29, 31], which considers the characteristics of each channel independently, and the multi-channel bidimensional fuzzy entropy, $FuzEnV_{2D}$, which takes into consideration the inter-channel characteristics (presented in the section 2.4.2). After that we present the modified colored bidimensional fuzzy entropy, $FuzEnM_{2D}$, see section 2.4.3. Our measures are developed for images composed of three color spaces. They

could be easily adapted in our future work for multi-spectral applications as well.

For a colored image \mathbf{U} of W width, H height, and K channels ($W \times H \times K$ pixels) the initial parameters: tolerance level r , fuzzy power n , and embedding dimension \mathbf{m} are first set (see below). The algorithms to compute $FuzEnC_{2D}$, $FuzEnV_{2D}$, and $FuzEnM_{2D}$ are presented in the following sections.

2.4.1 Single-channel approach $FuzEnC_{2D}$

\mathbf{U} is separated into its corresponding color channels $K1$, $K2$, and $K3$, as \mathbf{U}_{K1} , \mathbf{U}_{K2} , and \mathbf{U}_{K3} , respectively (see Figure 2.4 (a)). For each channel composed of $u_K(i, j)$ elements, $\mathbf{X}_{i,j,K}^m$ is designated as the $m \times m$ square window:

$$\begin{bmatrix} u_K(i, j) & \dots & u_K(i, j + m - 1) \\ u_K(i + 1, j) & \dots & u_K(i + 1, j + m - 1) \\ \dots & \dots & \dots \\ u_K(i + m - 1, j) & \dots & u_K(i + m - 1, j + m - 1) \end{bmatrix}, \quad (2.18)$$

with $K = K1, K2$, or $K3$. The $(m + 1) \times (m + 1)$ square window, $\mathbf{X}_{i,j,K}^{m+1}$ is defined in the same way. In each of \mathbf{U}_{K1} , \mathbf{U}_{K2} , and \mathbf{U}_{K3} , the total number of defined square windows for both \mathbf{m} and $\mathbf{m}+1$ sizes is $N_m = (W - m)(H - m)$. Sizes \mathbf{m} and $\mathbf{m}+1$ stand for $[m, m]$ and $[m + 1, m + 1]$ that are made up of $m \times m$ and $(m + 1) \times (m + 1)$ pixels, respectively.

Based on the original fuzzy entropy, $FuzEn_{1D}$, definition [68], a distance function $d_{ij,ab,K}^m$ between $\mathbf{X}_{i,j,K}^m$ and its neighboring windows $\mathbf{X}_{a,b,K}^m$ is defined as the maximum absolute difference of their corresponding scalar components. Please also see Figure 2.5 as an illustration for the $FuzEnC_{2D}$ algorithm.

We compose $d_{ij,ab,K}^m$ as follows:

$$d_{ij,ab,K}^m = d[\mathbf{X}_{i,j,K}^m, \mathbf{X}_{a,b,K}^m] = \max_{s,t \in (0, m-1)} (|u_K(i + s, j + t) - u_K(a + s, b + t)|), \quad (2.19)$$

with a ranging from 1 to $H - m$ and b ranging from 1 to $W - m$. The similarity degree $D_{ij,ab,K}^m$ of $\mathbf{X}_{i,j,K}^m$ with its neighboring patterns $\mathbf{X}_{a,b,K}^m$ is defined by a continuous fuzzy function $\mu(d_{ij,ab,K}^m, n, r)$:

$$D_{ij,ab,K}^m(n, r) = \mu(d_{ij,ab,K}^m, n, r) = \exp(-(d_{ij,ab,K}^m)^n / r). \quad (2.20)$$

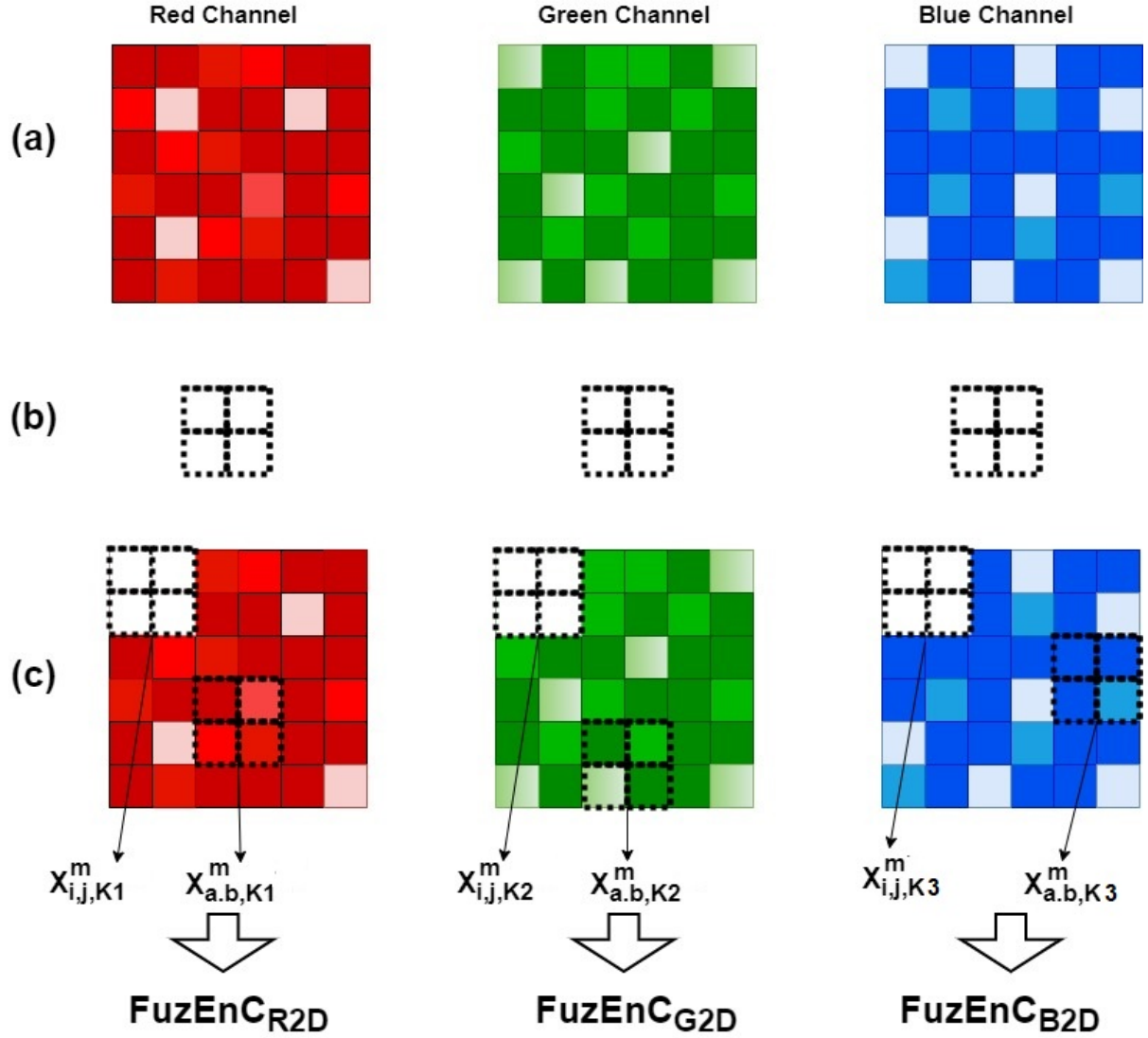
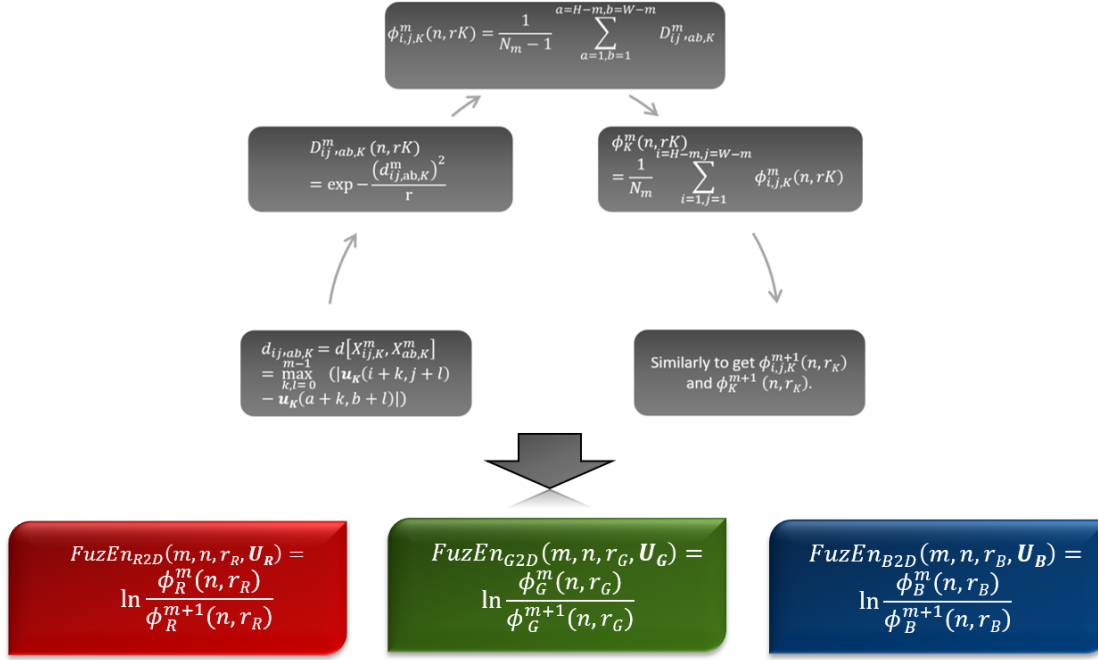


Figure 2.4 – Illustration for $FuzEnC_{2D}$ of an RGB color space image. (a) the image U is split into its corresponding channels U_R , U_G , and U_B , respectively from left to right; (b) the embedding dimension pattern of size $m \times m$ having $\mathbf{m} = [2, 2]$; (c) $X_{i,j,K}^m$ and $X_{a,b,K}^m$ for $K = K1, K2$, and $K3$ being the R, G, and B color channels, respectively.


 Figure 2.5 – Illustrative schema for $FuzEnC_{2D}$ algorithm.

Then, the similarity degree of each $\mathbf{X}_{i,j,K}^m$ is averaged to obtain:

$$\Phi_{i,j,K}^m(n, r) = \frac{1}{N_m - 1} \sum_{a=1, b=1}^{a=H-m, b=W-m} D_{ij,ab,K}^m, \quad (2.21)$$

with $(a, b) \neq (i, j)$, to construct:

$$\Phi_K^m(n, r) = \frac{1}{N_m} \sum_{i=1, j=1}^{i=H-m, j=W-m} \Phi_{i,j,K}^m(n, r). \quad (2.22)$$

Similarly, for $(m + 1) \times (m + 1)$ patterns to obtain $\Phi_K^{m+1}(n, r)$. Consequently, $FuzEn_{2D}$ of each channel is calculated as:

$$FuzEnC_{K2D}(m, n, r, \mathbf{U}_K) = \ln \frac{\Phi_K^m(n, r)}{\Phi_K^{m+1}(n, r)}. \quad (2.23)$$

Finally, $FuzEnC_{2D}$ is defined in each channel as the natural logarithm of the conditional probability that similar patterns with $m \times m$ pixels would remain similar for the next

$(m + 1) \times (m + 1)$ pixels:

$$FuzEnC_{2D}(m, n, r, \mathbf{U}) = [FuzEnC_{K1,2D}, FuzEnC_{K2,2D}, FuzEnC_{K3,2D}]. \quad (2.24)$$

For better illustration, we show in Figure 2.4 an example for $FuzEnC_{2D}$ of an RGB color space image for an embedding dimension of $\mathbf{m} = [2, 2]$; *i.e.* $m \times m$ pixels for each channel. This single-channel approach treats each channel independently. It has the advantage of allowing us to selectively study certain channels which is of special importance when it comes to images in different color spaces and natures (intensity, color, and texture). In our study we used $n = 2$. Thus, the similarity degree is expressed by a Gaussian function $\exp(-(d_{ij,ab,K}^m)^2/r)$.

2.4.2 Multi-channel approach $FuzEnV_{2D}$

For image \mathbf{U} composed of $u_{i,j,k}$ voxels, $\mathbf{X}_{i,j,k}^m$ is defined as the $m \times m \times m$ cube. $\mathbf{X}_{i,j,k}^m$ represents the group of voxels in the image \mathbf{U} of indices from line i to $i + m - 1$, column j to $j + m - 1$ and the depth k to $k + m - 1$ as follows:

$$(2.25)$$

Similarly, $\mathbf{X}_{i,j,k}^{m+1}$ is defined as the $(m + 1) \times (m + 1) \times (m + 1)$ cube. Let $N_m = (W - m)(H - m)(K - m)$ be the total number of cubes that can be generated from \mathbf{U} for both \mathbf{m} and $\mathbf{m}+1$ sizes. Sizes \mathbf{m} and $\mathbf{m}+1$ stand for $[m, m, m]$ and $[m + 1, m + 1, m + 1]$ that are made up of $m \times m \times m$ and $(m + 1) \times (m + 1) \times (m + 1)$ voxels, respectively.

For $\mathbf{X}_{i,j,k}^m$ and its neighboring cubes $\mathbf{X}_{a,b,c}^m$, the distance function $d_{ijk,abc}^m$ between them is defined as the maximum absolute difference of their corresponding scalar components, knowing that a, b , and c range from 1 to $H - m$, $W - m$, and $K - m$, respectively. Having $(a, b, c) \neq (i, j, k)$, the distance function is depicted as follows:

$$d_{ijk,abc}^m = d[\mathbf{X}_{i,j,k}^m, \mathbf{X}_{a,b,c}^m] = \max_{e,f,g \in (0, m-1)} (|u(i+e, j+f, k+g) - u(a+e, b+f, c+g)|). \quad (2.26)$$

The similarity degree $D_{ijk,abc}^m$ of $\mathbf{X}_{i,j,k}^m$ with its neighboring cubes $\mathbf{X}_{a,b,c}^m$ is defined by a fuzzy function $\mu(d_{ijk,abc}^m, n, r)$:

$$D_{ijk,abc}^m(n, r) = \mu(d_{ijk,abc}^m, n, r) = \exp(-(d_{ijk,abc}^m)^n / r). \quad (2.27)$$

Then, the similarity degree of each cube is averaged to obtain:

$$\Phi_{i,j,k}^m(n, r) = \frac{1}{N_m - 1} \sum_{a=1, b=1, c=1}^{a=H-m, b=W-m, c=K-m} D_{ijk,abc}^m, \quad (2.28)$$

with $(a, b, c) \neq (i, j, k)$, to construct:

$$\Phi^m(n, r) = \frac{1}{N_m} \sum_{i=1, j=1, k=1}^{i=H-m, j=W-m, k=K-m} \Phi_{i,j,k}^m(n, r). \quad (2.29)$$

Similarly, for $(m + 1) \times (m + 1) \times (m + 1)$ size cubes, to obtain $\Phi^{m+1}(n, r)$. Finally, the multi-channel bidimensional fuzzy entropy of the colored image \mathbf{U} is defined as the natural logarithm of the conditional probability that cubes similar for their $m \times m \times m$ points would remain similar for their $(m + 1) \times (m + 1) \times (m + 1)$ points:

$$FuzEnV_{2D}(m, n, r, \mathbf{U}) = \ln \frac{\Phi^m(n, r)}{\Phi^{m+1}(n, r)}. \quad (2.30)$$

For better illustration, we show in Figure 2.6 an example for $FuzEnV_{2D}$ of an RGB color space image for an embedding dimension of $\mathbf{m} = [2, 2, 2]$. The multi-channel approach has the advantage of extracting inter-channel features. However, we limit our study herein to 3-channel colored images. Thus, the embedding dimension \mathbf{m} values could be equal to $[1, 1, 1]$ or $[2, 2, 2]$; *i.e.* moving cubic template of $1 \times 1 \times 1$ or $2 \times 2 \times 2$ voxels for \mathbf{m} , to avoid exceeding the maximum possible $3 \times 3 \times 3$ voxels cubes for the $\mathbf{m}+1$ calculations. Herein, n is taken to be 2 (Gaussian function, $\exp(-(d_{ijk,abc}^m)^2 / r)$).

2.4.3 Modified multi-channel approach $FuzEnM_{2D}$

$FuzEnV_{2D}$ gave very promising results and proved proper assessment for colored texture images. Based on its encouraging results and the fact that its embedding dimension window size was limited to $\mathbf{m} = [1, 1, 1]$ and $\mathbf{m} = [2, 2, 2]$, we introduce herein a modified

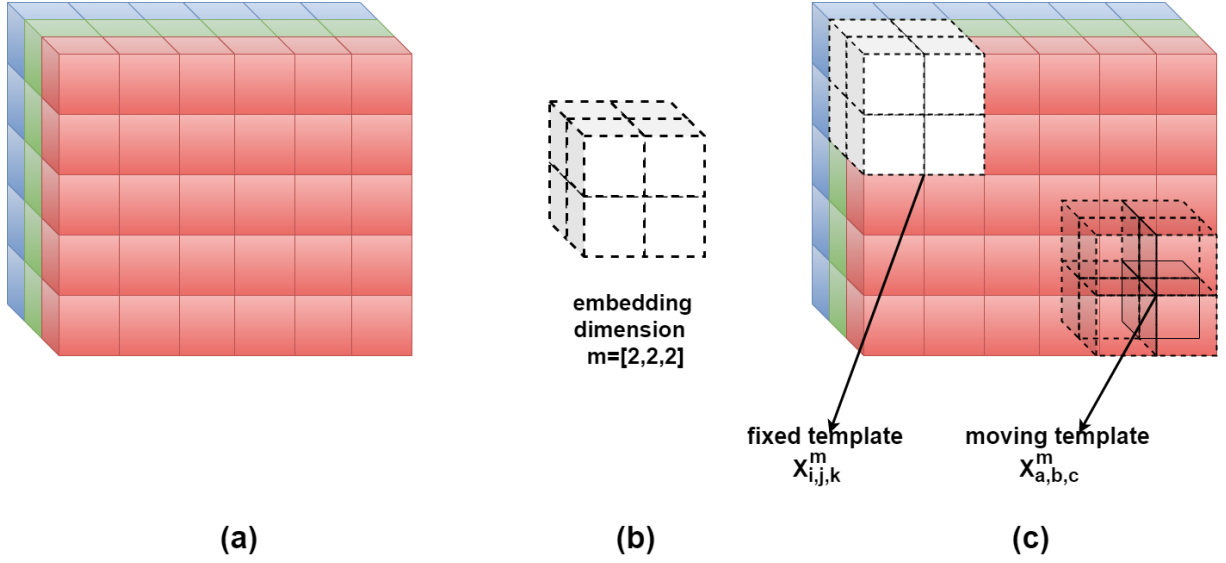


Figure 2.6 – Illustration for $FuzEnV_{2D}$ of an RGB color space image having $\mathbf{m} = [2, 2, 2]$. (a) represents a portion of the colored image \mathbf{U} with its R, G, and B channels; (b) the scanning pattern or embedding dimension with $\mathbf{m} = [2, 2, 2]$ that is a $2 \times 2 \times 2$ cube; (c) $\mathbf{X}_{i,j,k}^m$ and $\mathbf{X}_{a,b,c}^m$.

colored multi channel approach that can take up to any \mathbf{m} value. This method is similar to $FuzEnV_{2D}$ except for the fact that the embedding dimension is a cuboid of $m \times m \times 3$ voxels for $FuzEnM_{2D}$.

For image \mathbf{U} composed of $u_{i,j,k}$ voxels, $\mathbf{X}_{i,j,k}^m$ is defined as the $m \times m \times 3$ cuboid. $\mathbf{X}_{i,j,k}^m$ represents the group of voxels in the image \mathbf{U} of indices from line i to $i + m - 1$, column j to $j + m - 1$ and the depth of K-channels as follows:

$$\begin{array}{|c|} \hline u_{i,j,3} \quad \dots \quad u_{i,j+m-1,3} \\ \hline \dots \quad \dots \quad \dots \\ \hline u_{i,j,1} \quad \dots \quad u_{i,j+m-1,1} \\ \hline \vdots \quad \ddots \quad \vdots \\ \hline u_{i+m-1,j,1} \quad \dots \quad u_{i+m-1,j+m-1,1} \\ \hline \end{array} \quad \begin{array}{l} \\ \\ -m-1,3 \\ \\ \\ \end{array} \quad (2.31)$$

Similarly, $\mathbf{X}_{i,j,k}^{m+1}$ is defined as the $(m+1) \times (m+1) \times 3$ cuboid. Let $N_m = (W-m)(H-m)$ be the total number of cuboids that can be generated from \mathbf{U} for both \mathbf{m} and $\mathbf{m}+1$ sizes. Sizes \mathbf{m} and $\mathbf{m}+1$ stand for $[m, m, 3]$ and $[m+1, m+1, 3]$ that are made up of $m \times m \times 3$ and $(m+1) \times (m+1) \times 3$ voxels, respectively.

For $\mathbf{X}_{i,j,k}^m$ and its neighboring cuboids $\mathbf{X}_{a,b,c}^m$, the distance function $d_{ijk,abc}^m$ between them

is defined as the maximum absolute difference of their corresponding scalar components, knowing that a and b range from 1 to $H - m$ and $W - m$, respectively, whereas c is 1. Having $(a, b, c) \neq (i, j, k)$, the distance function is depicted as follows:

$$d_{ijk,abc}^m = d[\mathbf{X}_{i,j,k}^m, \mathbf{X}_{a,b,c}^m] = \max_{e,f \in (0,m-1), g \in (0,2)} (|u(i+e, j+f, k+g) - u(a+e, b+f, c+g)|). \quad (2.32)$$

The similarity degree $D_{ijk,abc}^m$ of $\mathbf{X}_{i,j,k}^m$ with its neighboring cuboids $\mathbf{X}_{a,b,c}^m$ is defined by a fuzzy function $\mu(d_{ijk,abc}^m, n, r)$:

$$D_{ijk,abc}^m(n, r) = \mu(d_{ijk,abc}^m, n, r) = \exp(-(d_{ijk,abc}^m)^n / r). \quad (2.33)$$

Then, the similarity degree of each cuboid is averaged to obtain:

$$\Phi_{i,j,k}^m(n, r) = \frac{1}{N_m - 1} \sum_{a=1, b=1, c=1}^{a=H-m, b=W-m, c=K-m} D_{ijk,abc}^m, \quad (2.34)$$

with $(a, b, c) \neq (i, j, k)$, to construct:

$$\Phi^m(n, r) = \frac{1}{N_m} \sum_{i=1, j=1, k=1}^{i=H-m, j=W-m, k=K-m} \Phi_{i,j,k}^m(n, r). \quad (2.35)$$

Similarly, for $(m+1) \times (m+1) \times 3$ cuboids, to obtain $\Phi^{m+1}(n, r)$. Finally, multi-channel bidimensional fuzzy entropy of the colored image \mathbf{U} is defined as the natural logarithm of the conditional probability that cuboids similar for their $m \times m \times 3$ voxels would remain similar for their $(m+1) \times (m+1) \times 3$ voxels:

$$FuzEnM_{2D}(m, n, r, \mathbf{U}) = \ln \frac{\Phi^m(n, r)}{\Phi^{m+1}(n, r)}. \quad (2.36)$$

For better illustration, we show in Figure 2.7 an example for $FuzEnM_{2D}$ of an RGB color space image for an embedding dimension of $\mathbf{m} = [2, 2, 3]$; *i.e.* moving \mathbf{m} sized cuboid is $2 \times 2 \times 3$. $FuzEnM_{2D}$ has the advantage of extracting inter-channel features and always considering all the color channels of texture images. However, as mentioned previously, we limit our study herein to 3-channel colored images which could be adapted to higher number as well. Herein, n is taken to be 2 (Gaussian function, $\exp(-(d_{ijk,abc}^m)^2 / r)$).

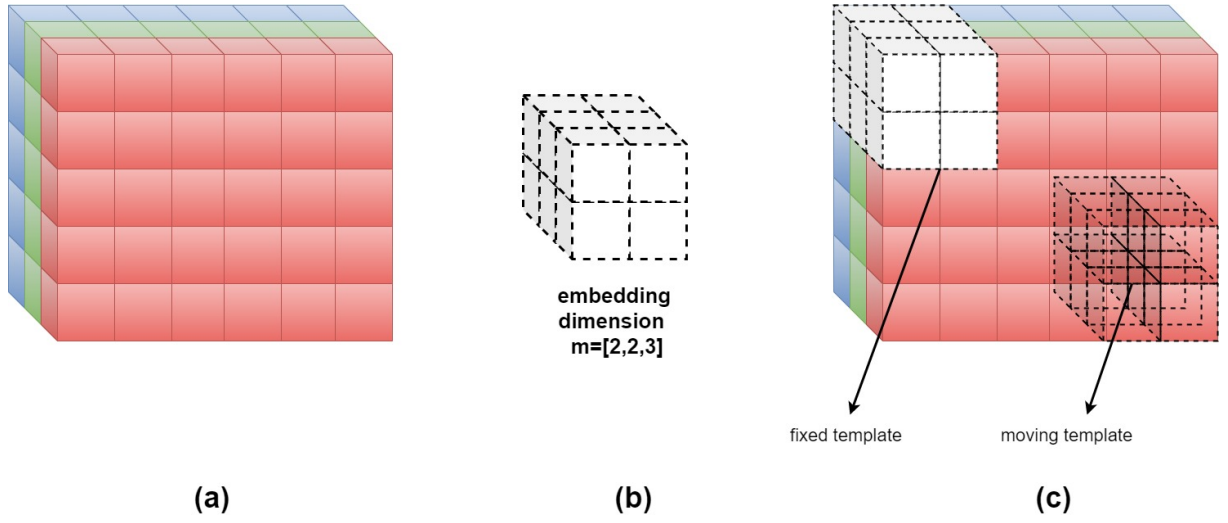


Figure 2.7 – Illustration for $FuzEnM_{2D}$ of RGB color space image having $\mathbf{m} = [2, 2, 3]$.

2.5 Conclusion

In this chapter we introduced our $FuzEn_{2D}$ and its multiscale version to study the texture images' irregularity and complexity. After that we define the proposed colored approaches based on $FuzEn_{2D}$. We present the single-channel approach $FuzEnC_{2D}$, that is a direct extension of $FuzEn_{2D}$. Then, the multi-channel approach for colored images $FuzEnV_{2D}$ which is inspired by the volumetric concept, yet limited to embedding dimension $\mathbf{m} = [2, 2, 2]$. Finally, the modified multi-channel colored approach $FuzEnM_{2D}$ as an enhancement for $FuzEnV_{2D}$.

METHODOLOGY: DEVELOPED TRIDIMENSIONAL ENTROPY MEASURES

3.1 Tridimensional Entropy Measures

The bidimensional entropy measures that we developed led to promising results for several kinds of medical applications. This is why we proposed to developed the tridimensional forms for some of them. These tridimensional versions study volumes in a similar way to images. However, they deal with cubes of data instead of 2D patterns. We applied these tridimensional entropy measures to CT and HRCT scans, as well as to MRI scans. They could be also employed for any other type of tridimensional data. Studying 3D volumes provides additional information-content to be analyzed and extends the possible application of entropy measures to almost all types of medical images so far. As mentioned previously, computer aided diagnosis methods are necessary for faster, more objective, and more precise medical decision making.

Excluding our work, there is no developed entropy measure to evaluate volumes, following the original entropy measures definitions as irregularity and complexity quantifiers yet. Nevertheless, $ApEn_{3D}$ was established by [157, 158, 159] based on its original definition proposed by Pincus *et al.* [79] for signals. Nonetheless, unlike $ApEn_{1D}$, $ApEn_{3D}$ does not study the irregularity of the whole volume. It calculates the local entropy values for small cubes inside the studied volume and re-displays the obtained values as the new volume to be analyzed. Thus, it is an entropy measure-inspired study but not actually an entropy method for volumes that reflects the irregularity: it provides new images to be analyzed and not actual features.

3.2 Pseudo-tridimensional Multiscale Fuzzy Entropy Measure $pMFuzEn_{3D}$

We propose first, a pseudo-tridimensional multiscale fuzzy entropy measure ($pMFuzEn_{3D}$) to process computed tomography (CT) scan volumes based on our developed MSF_{2D} . $pMFuzEn_{3D}$ consists in computing $FuzEn_{2D}$ for each scan at several scale factors and to gather all the entropy measures on the same plot. Consider a volume composed of several scans $\mathbf{S} = \{\mathbf{S1}, \mathbf{S2}, \dots, \mathbf{Sn}\}$. $pMFuzEn_{3D}$ is computed as:

$$pMFuzEn_{3D}(m, n, r, \mathbf{S}, \tau) = \begin{bmatrix} MSF_{2D}(\mathbf{S1}) \\ MSF_{2D}(\mathbf{S2}) \\ \dots \\ MSF_{2D}(\mathbf{Sn}) \end{bmatrix} = \begin{bmatrix} \{FuzEn_{2D}(m, n, r, \mathbf{S1}^{(1)})\} \\ \{FuzEn_{2D}(m, n, r, \mathbf{S2}^{(2)})\} \\ \dots \\ \{FuzEn_{2D}(m, n, r, \mathbf{Sn}^{(n)})\} \end{bmatrix} \quad (3.1)$$

We studied high resolution CT scans of patients with chronic obstructive pulmonary diseases (COPD) using $pMFuzEn_{3D}$. The results and procedure will be detailed and discussed in Chapter 5 section 5.5. This study inspired our following work on actual volumetric quantification for data. Figure 3.1 presents a simplified visual illustration for $pMFuzEn_{3D}$.

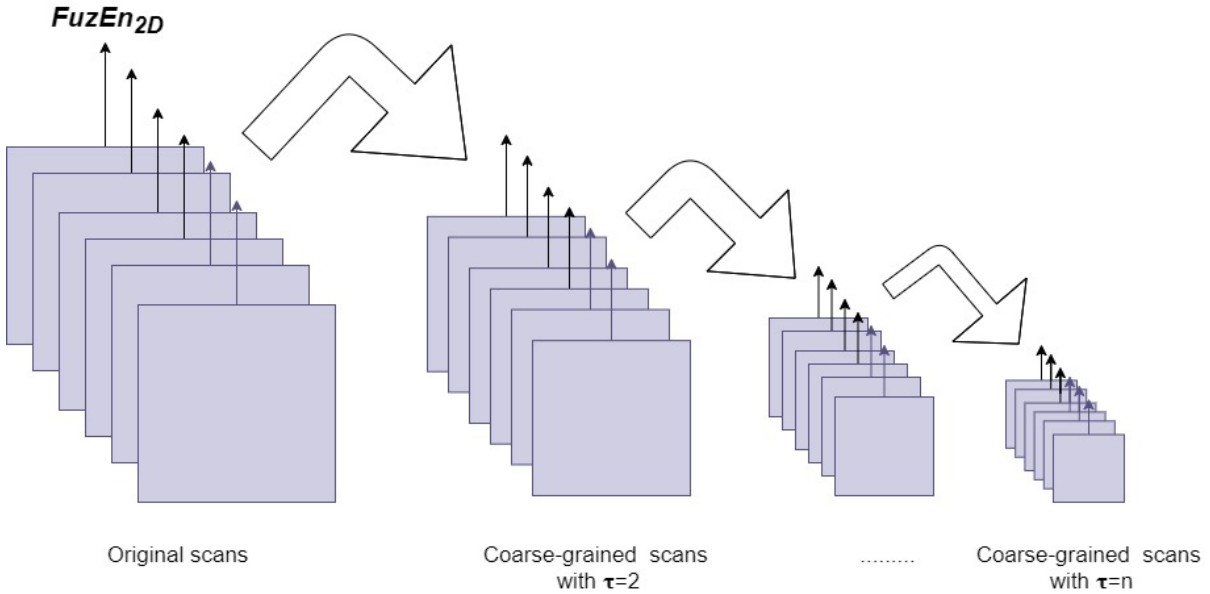


Figure 3.1 – Illustration for $pMFuzEn_{3D}$ of a volume of several 2D scans. $pMFuzEn_{3D}$ is the $FuzEn_{2D}$ measure values from the original volume and its coarse-grained 2D scans.

3.3 Tridimensional Fuzzy Entropy $FuzEn_{3D}$

After developing the $FuzEn_{2D}$ for studying image textures, we propose the tridimensional fuzzy entropy measure, $FuzEn_{3D}$, to study volumes using the information theory concept and fuzzy function. Following its bidimensional definition, $FuzEn_{3D}$ studies the irregularity in volumes.

$FuzEn_{3D}$ is the natural negative logarithm of the conditional probability that two cubes within a volume that are similar for their corresponding $m \times m \times m$ voxels ($\mathbf{m} = [m, m, m]$), will remain similar for $(m + 1) \times (m + 1) \times (m + 1)$ voxels. $FuzEn_{3D}$ also uses the concept of membership degree represented by a continuous function. It associates each element with a value of membership between 0 and 1 to express the cubes' membership degree. The more the value approaches unity, the higher the degree of membership is.

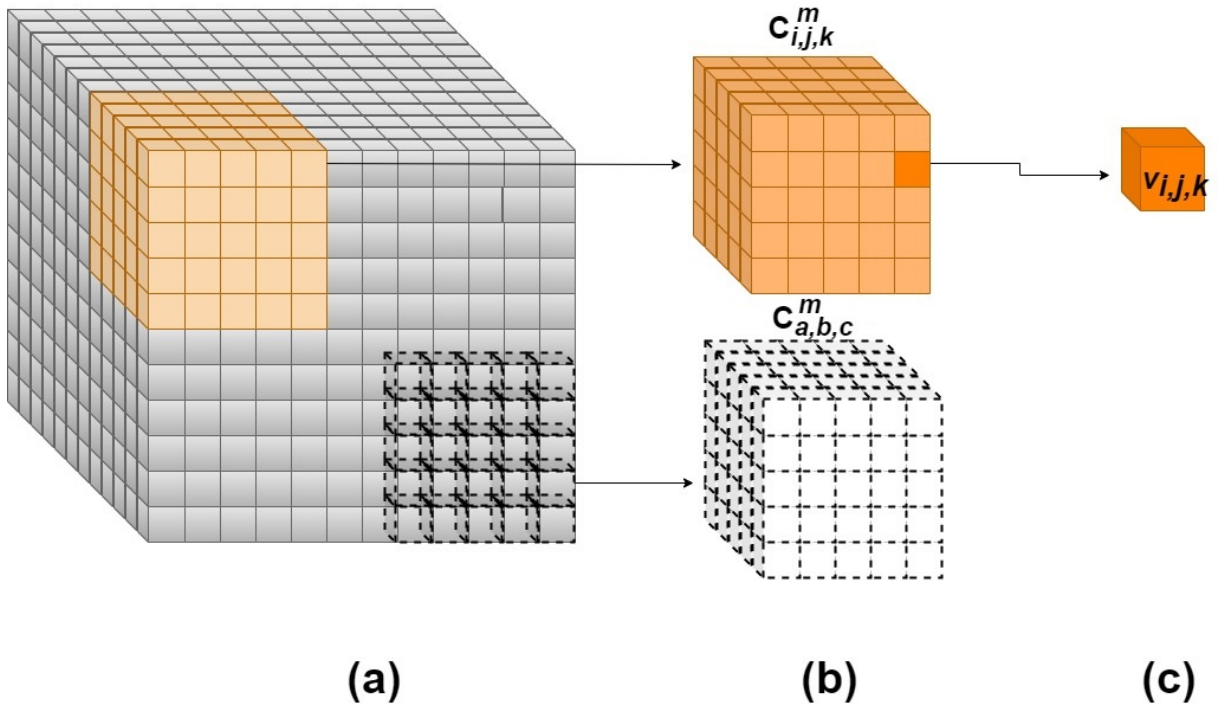
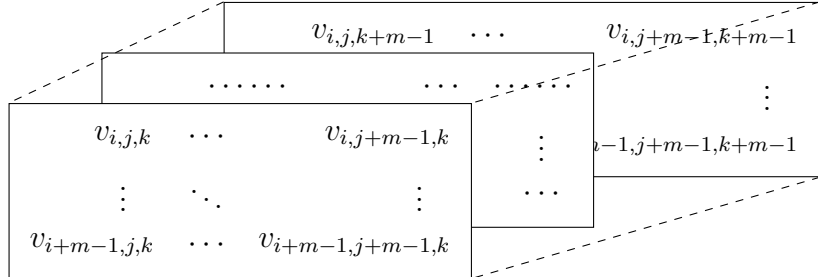


Figure 3.2 – Illustration for $FuzEn_{3D}$ of a volume having $\mathbf{m} = [5,5,5]$. (a) represents a portion of the volume \mathbf{V} to be studied; (b) the fixed $C_{i,j,k}^m$ and scanning $C_{a,b,c}^m$ cubic patterns for $\mathbf{m} = [5,5,5]$ size; (c) a voxel $v_{i,j,k}$ from \mathbf{V} .

FuzEn_{3D} definition

Let us consider a volume $\mathbf{V} = \{v_{i,j,k}\}$ of dimensions $W \times L \times H$ with W width, L length, and H height. The indices i , j , and k could go from 1 to W , 1 to L , and 1 to H , respectively. The embedding dimension of template \mathbf{m} is defined. We then define the cubic templates of \mathbf{V} , $\mathbf{C}_{i,j,k}^m$ of origin $v_{i,j,k}$ with size of $m \times m \times m$:



$$(3.2)$$

Similarly, we define the cubic templates $\mathbf{C}_{i,j,k}^{m+1}$ as the $(m+1) \times (m+1) \times (m+1)$ volume cubes, see Figure 3.2 for an illustration of $\mathbf{m} = [5,5,5]$ embedding dimension case.

Let $N_m = (W-m)(L-m)(H-m)$ be the total number of cubic patterns that could be created from \mathbf{V} for both \mathbf{m} and $\mathbf{m}+1$ sizes. For $\mathbf{C}_{i,j,k}^m$ and its neighboring cubes $\mathbf{C}_{a,b,c}^m$, the distance function $d_{ijk,abc}^m$ between them is defined as the maximum absolute difference of their corresponding scalar components, knowing that a , b , and c range from 1 to $W-m$, $L-m$, and $H-m$, respectively. The distance function is defined as follows, knowing that $(a, b, c) \neq (i, j, k)$ to avoid self similarities:

$$d_{ijk,abc}^m = d[\mathbf{C}_{i,j,k}^m, \mathbf{C}_{a,b,c}^m] = \max_{e,f,g \in (0, m-1)} (|u(i+e, j+f, k+g) - u(a+e, b+f, c+g)|). \quad (3.3)$$

We define the similarity degree $D_{ijk,abc}^m$ of $\mathbf{C}_{i,j,k}^m$ with its neighboring cubes $\mathbf{C}_{a,b,c}^m$ by a continuous fuzzy function $\mu(d_{ijk,abc}^m, n, r)$:

$$D_{ijk,abc}^m(n, r) = \mu(d_{ijk,abc}^m, n, r) = \exp(-(d_{ijk,abc}^m)^n / r). \quad (3.4)$$

Then, the similarity degree of each cubic template is averaged to obtain:

$$\Phi_{i,j,k}^m(n, r) = \frac{1}{N_m - 1} \sum_{a=1, b=1, c=1}^{a=W-m, b=L-m, c=H-m} D_{ijk,abc}^m, \quad (3.5)$$

with $(a, b, c) \neq (i, j, k)$, to construct:

$$\Phi^m(n, r) = \frac{1}{N_m} \sum_{i=1, j=1, k=1}^{i=W-m, j=L-m, k=H-m} \Phi_{i,j,k}^m(n, r). \quad (3.6)$$

Similarly, for $(m+1) \times (m+1) \times (m+1)$ cubic templates, to obtain:

$$\Phi_{i,j,k}^{m+1}(n, r) = \frac{1}{N_m - 1} \sum_{a=1, b=1, c=1}^{a=W-m, b=L-m, c=H-m} D_{ijk,abc}^{m+1}, \quad (3.7)$$

with $(a, b, c) \neq (i, j, k)$, to construct:

$$\Phi^{m+1}(n, r) = \frac{1}{N_m} \sum_{i=1, j=1, k=1}^{i=W-m, j=L-m, k=H-m} \Phi_{i,j,k}^{m+1}(n, r). \quad (3.8)$$

Finally, tridimensional fuzzy entropy measure, $FuzEn_{3D}$, for a volume \mathbf{V} is defined as the natural logarithm of the conditional probability that two cubic templates similar for their $m \times m \times m$ voxels would remain similar for the next $(m+1) \times (m+1) \times (m+1)$ voxels:

$$FuzEn_{3D}(m, n, r, \mathbf{V}) = \ln \frac{\Phi^m(n, r)}{\Phi^{m+1}(n, r)}. \quad (3.9)$$

3.4 Multiscale Tridimensional Fuzzy Entropy MSF_{3D}

Thus, encouraged by the interesting results with MSF_{1D} and MSF_{2D} we introduce the multiscale tridimensional fuzzy entropy measure, MSF_{3D} . In order to study, not only the irregularity in volumes, but also the actual complexity, MSF_{3D} is used. First, scale factor τ is defined and the volume is coarse-grained into $\mathbf{Y}^{(\tau)}$ volumes. For a volume \mathbf{V} of dimensions $W \times L \times H$ we obtain τ coarse-grained volumes each of size $\frac{W}{\tau} \times \frac{L}{\tau} \times \frac{H}{\tau}$ voxels. MSF_{3D} consists of two main steps:

1. A non-overlapping cube scans the whole image and the pixels of each cubic pattern are averaged. The obtained averaged values form the coarse-grained volumes. The coarse-grained volumes are modeled as:

$$\mathbf{Y}^{(\tau)} = \{y_{i,j,k}^{(\tau)}\}, \quad (3.10)$$

where,

$$y_{i,j,k}^{(\tau)} = \frac{1}{\tau^3} \sum_{\substack{a=i\tau \\ b=j\tau \\ c=k\tau \\ a=(i-1)\tau+1 \\ b=(j-1)\tau+1 \\ c=(k-1)\tau+1}} v_{a,b,c}, \quad (3.11)$$

with $1 \leq i \leq \frac{W}{\tau}$, $1 \leq j \leq \frac{L}{\tau}$, and $1 \leq k \leq \frac{H}{\tau}$.

2. Applying $FuzEn_{3D}$ for each coarse-grained volume (with each scale factor τ).

$$MSF_{3D} = \{FuzEn_{3D}(m, n, r, \mathbf{Y}^{(\tau)})\} \quad (3.12)$$

The result would be τ values of $FuzEn_{3D}$ that reflect the actual complexity of the studied volume. The coarse-grained volumes carry information about the whole original image over several scale factors. Figure 3.3 shows an example of coarse-grained versions of an original volume for $\tau = 1, 2$, and 3.

3.5 Conclusion

In this chapter, we first presented our 3D adapted $pMFuzEn_{3D}$. Then, in section 3.3 we introduced our $FuzEn_{3D}$ for studying volumes and its multiscale version MSF_{3D} (section 3.4). These measures extend the application of entropy based methods to the tridimensional domain and enable possible applications on all kinds of 3D medical images analysis. The testing for the aforementioned measures will be shown in Chapter 4 and the results for their applications on medical images will be illustrated in Chapter 5.

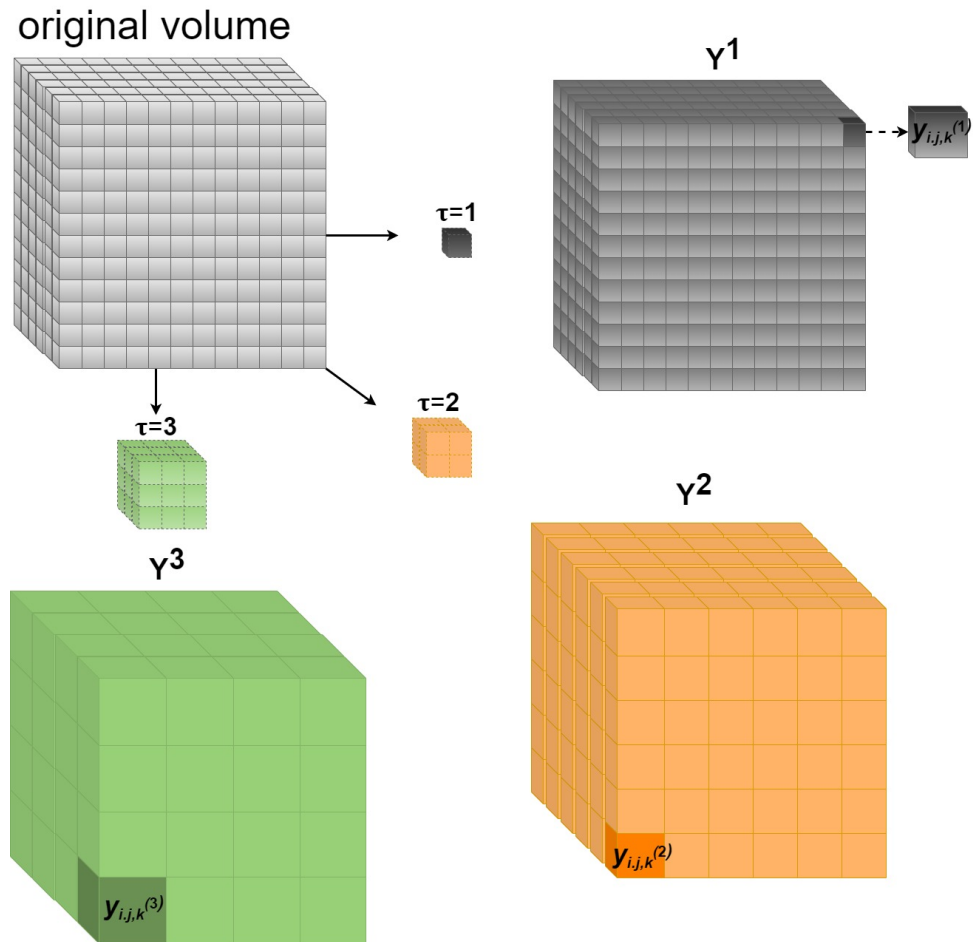


Figure 3.3 – Illustration for MSF_{3D} coarse-grained volumes $\mathbf{Y}^{(1)}$, $\mathbf{Y}^{(2)}$, and $\mathbf{Y}^{(3)}$ of an original volume, having $\tau = 1, 2$, and 3 .

VALIDATION TESTS AND ANALYSIS

4.1 Introduction

In this chapter we present the validation tests for our proposed entropy measures. We investigate their sensitivity to the choice of initial parameters, their behavior with different degrees of irregularity, and also perform adapted tests for each measure separately.

In Figure 4.1 we show the continuous function, fuzzy functions, employed as similarity degrees for some n and r values for all our developed fuzzy entropy measures. Nevertheless, we use $\exp(-(d_{ij}^m)^2/r)$ in the case of our fuzzy entropy measures. Parameter r is usually chosen within the range recommended by some previous studies on 1D [74, 76, 156, 85]. Moreover, we study the variability of the results with the different choices of \mathbf{m} and r for each proposed measure. In what follows, and for simplicity reasons, we will use the notation \mathbf{m} for the embedding dimension value as explained in Chapters 2 and 3 for each entropy measure. Take an example $\mathbf{m} = 2$ instead of: $m = 2$, $\mathbf{m} = [2,2]$, or $\mathbf{m} = [2,2,2]$, for the uni-, bi-, or tridimensional approaches, respectively.

4.2 Evaluation Data

To evaluate our proposed measures, we use several synthetic and real images: various noise data with different power spectra ($1/f^\beta$), *WGN*, *MIX(p)* processes, artificial periodic textures and their synthesized textures, and different synthetic images of varying sizes with repetitions. In what follows, we briefly present some of the testing data. We should note that the test images were all normalized by removed the mean and dividing by the standard deviation. This serves in comparing all images with the same interval and consequently the background intensity would not affect in the texture discrimination process.

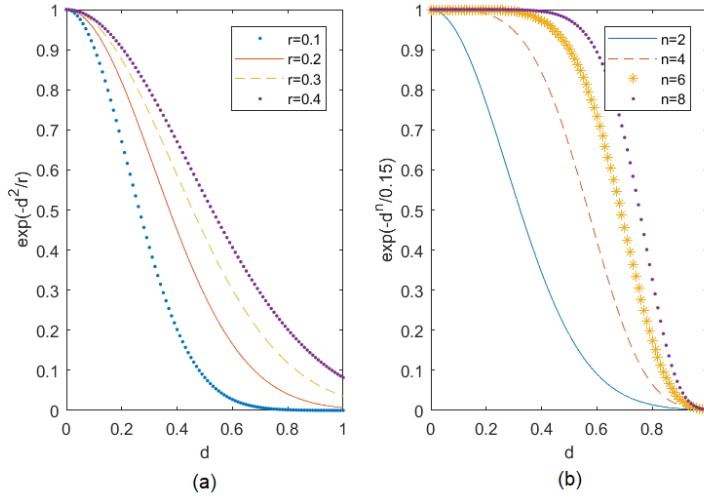


Figure 4.1 – A representation for the exponential function $\exp(-(d_{ij}^m)^n/r)$ with different parameters choice. (a) Exponential function for fixed fuzzy power $n = 2$ and varied r (0.1, 0.2, 0.3, and 0.4). (b) Exponential function for fixed $r = 0.15$ and varied n (2, 4, 6, and 8).

4.2.1 MIX(p) processes

MIX_{1D}(p) processes

MIX_{1D}(p) was first introduced by Pincus *et al.* [65] to test the properties of unidimensional entropy measures. MIX_{1D}(p) is a family of stochastic random processes that replaces a sine function points with completely random dynamics according to the value of p (p ranges from 0 to 1) [65]. MIX_{1D}(p) is an N -point sine wave time series, where $N \times p$ randomly chosen points are replaced with random noise. For $p = 0$, the signal is a periodic sine wave. The higher the value of p is, the more random the signal will be, see Figure 4.2.

MIX_{2D}(p) processes

Based on the MIX_{1D}(p) definition, the MIX_{2D}(p) processes were established [19, 26]. In fact, they are images of varying white noise levels as p increases from 0 (totally periodic sinusoidal images) to 1 (highly irregular images). The higher the value of p , the lower the spatial regularity of the image is, see Figure 4.3. That is the image has always the same background periodic image (sinusoid) and a p -percentage of pixels (out of the total number of pixels) are replaced by uniformly distributed random values (white noise). MIX_{2D}(p) allows us to evaluate the ability of our proposed methods in quantifying images with

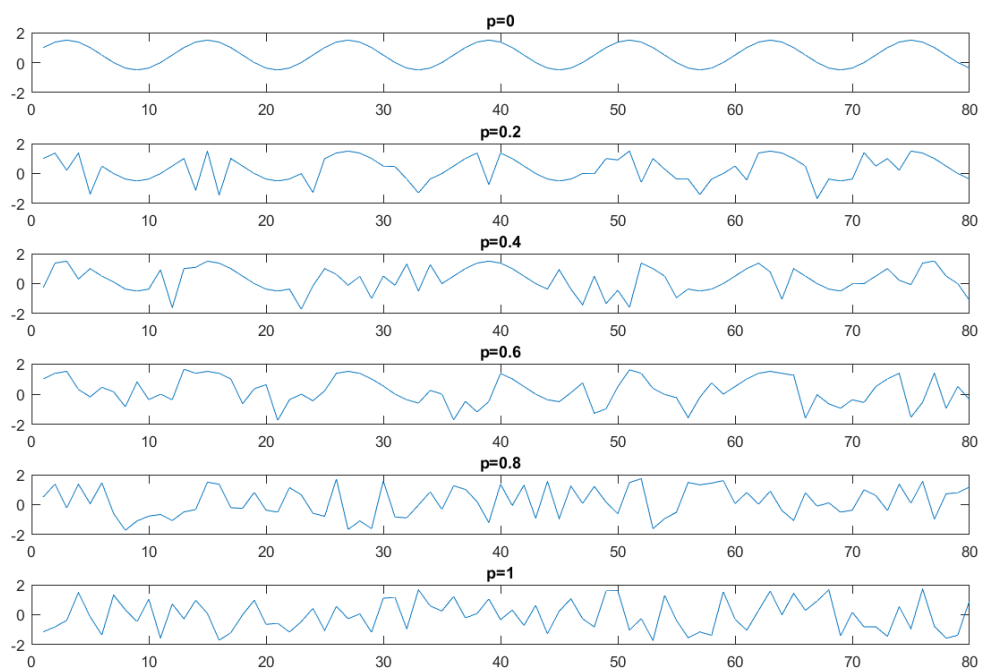


Figure 4.2 – $MIX_{1D}(p)$ family of signals. The higher the p value is, the higher the degree of the irregularity will be (p ranging from 0 to 1).

different irregularity/randomness degrees.



Figure 4.3 – $MIX_{2D}(p)$ family of images. The higher the p value is, the higher the degree of the irregularity will be (p ranging from 0 to 1).

$MIX_{3D}(p)$ processes

Based on the bidimensional $MIX_{2D}(p)$ we also introduce the three-dimensional $MIX_{3D}(p)$ processes [27]. They are volumes of varying irregularity degrees as p increases from 0 (totally periodic volume) up to 1 (highly irregular volume), see Figure 4.4.

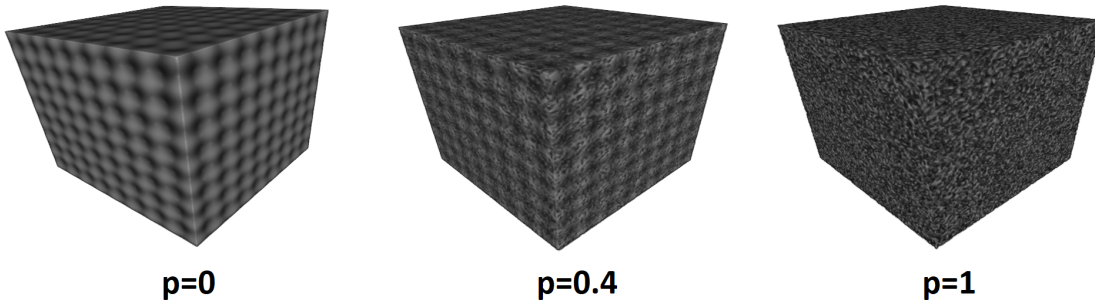


Figure 4.4 – $MIX_{3D}(p)$ family of volumes. The higher the p value is, the higher the degree of the irregularity will be (p ranging from 0 to 1).

4.2.2 Noise images with different power spectra

Tests using $1/f^\beta$ noise data allow us to illustrate the ability of our proposed measures to quantify the dynamical variability of different kinds of noises, *i.e.* for several coarse-grained versions of the original data. These types of noise data were of particular importance to evaluate the performance of our multiscale algorithms. $1/f^\beta$ noise data are studied with β being the power-law scaling exponent: pink ($\beta = 1$), brownian ($\beta = 2$),

blue ($\beta = -1$), and white noise ($\beta = 0$). Figure 4.5 shows the power spectral density (PSD) of four noise-based data, adapted from [27].

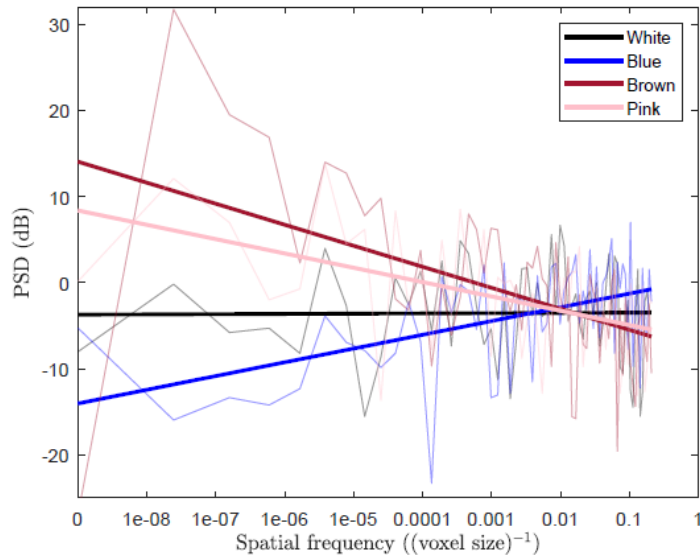


Figure 4.5 – Power spectral density (PSD) of four noise-based volumes of $1/f^\beta$: brown (dark red), pink (light pink), white (black), and blue (dark blue) noise. The trend-lines are presented as thicker lines. Adapted from [27].

4.2.3 Artificial periodic and synthesized texture images

In order to evaluate $FuzEn_{2D}$'s behavior when an artificial periodic texture is transformed into its corresponding synthesized texture, we employed 3 pairs of periodic textures and their synthesized ones from [35]. These 256×256 pixels textures are presented in Figure 4.6. We also rescaled those images to different sizes (50×50 pixels, 100×100 pixels, 150×150 pixels, and 200×200 pixels) to evaluate the consistency of $FuzEn_{2D}$ upon different texture sizes.

4.2.4 Other texture datasets

Brodatz and colored Brodatz datasets

Brodatz gray scale texture album [32, 34] is a very well known texture database that has been widely used as a validation dataset for image processing techniques. It is made

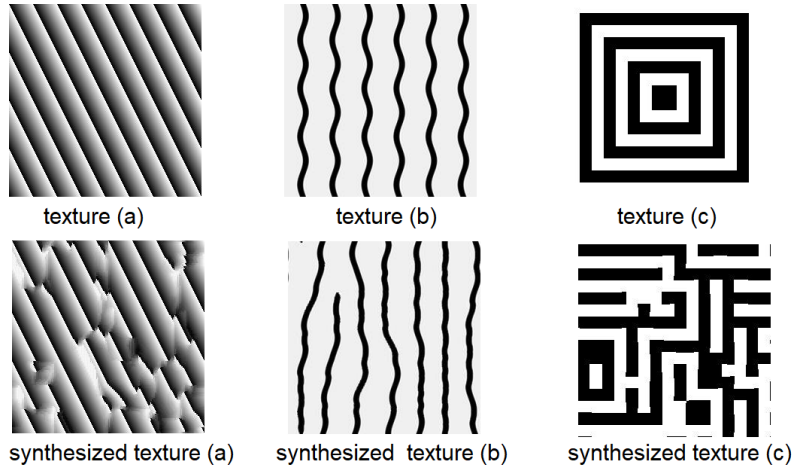


Figure 4.6 – Artificial periodic textures a, b, c (top panels) and their corresponding synthesized textures (bottom panels) from [35].

up of 112 gray scale images that represent a large variety of natural gray scale textures. Some of them are shown in Figure 4.7.

Colored Brodatz database is an extension for the original gray scale Brodatz dataset into its colored version [33, 34]. Examples of those images will be displayed later in the manuscript.

Mondial Marmi dataset

Mondial Marmi dataset is a collection of granite classes images for image processing purposes [36, 37]. The images have been acquired under controlled lighting conditions. Hardware-rotated images are taken in nine rotation angles. In addition, the dataset provides software-rotated images obtained through bilinear and bicubic interpolation, for more information about the dataset please refer to [36, 37]. Examples of Mondial Marmi dataset images will be shown later in the manuscript.

Pattern-based volumes

We generated six pattern-based cubes of $50 \times 50 \times 50$ voxels size to test the differentiation ability of $FuzEn_{3D}$ of different textural/pattern behavior [27]. The cubes are displayed in Figure 4.8.

Please find below the cubes' description according to which their irregularity outcome could be pre-assumed:

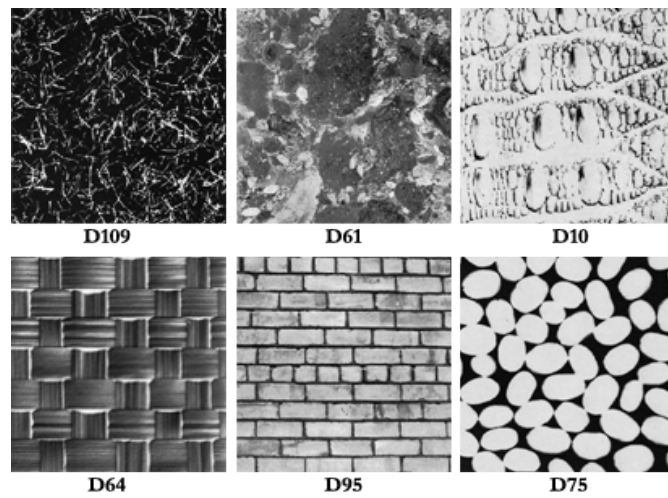


Figure 4.7 – Example of Brodatz texture images. The labels beneath each image are those used in the original Brodatz album.

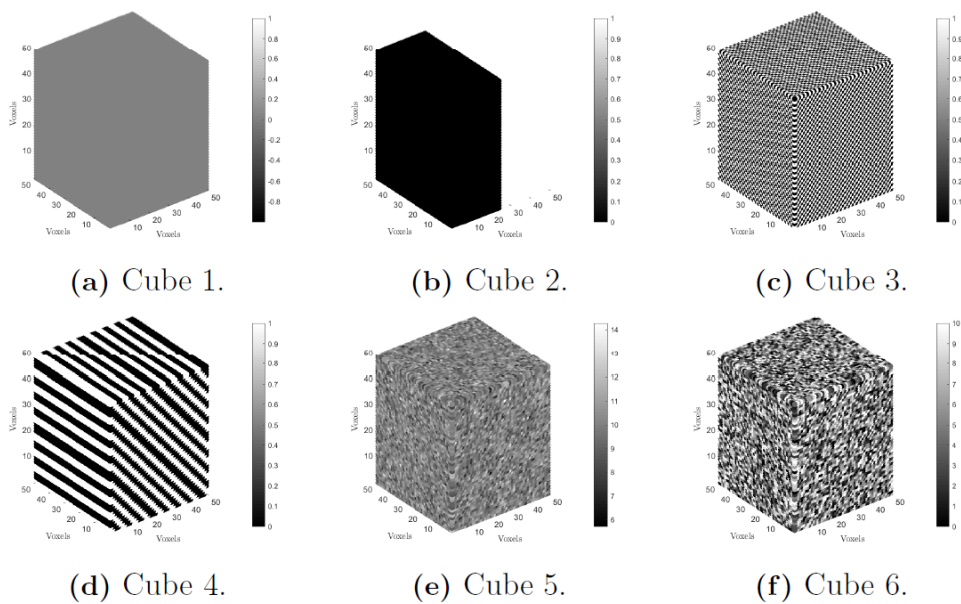


Figure 4.8 – Pattern based volumes created for $FuzEn_{3D}$ evaluation.

- cube 1: all black volume with voxels values as low as 1×10^{-9} , see Figure 4.8(a).
- cube 2: half white and half black volume, see Figure 4.8(b).
- cube 3: volumetric checkerboard pattern, see Figure 4.8(c).
- cube 4: volumetric diagonal stripes, see Figure 4.8(d).
- cube 5: Gaussian distribution of voxels with mean $\mu=0$ and standard deviation $\sigma=1$, see Figure 4.8(e).
- cube 6: integer values between 1 and 10 following a uniform random distribution, see Figure 4.8(f).

It is observed that cubes 1 till 4 possess a more regular pattern behavior than cubes 5 and 6. An assumption could be also made regarding the regularity order of those patterns in theory and visually according to their nature.

4.3 $FuzEn_{2D}$ and MSF_{2D} Validation Tests

As $FuzEn_{2D}$ represents the basic measure for most our developed methods, we present in this section a thorough analysis for its behavior and its multiscale extension MSF_{2D} . First, we compare $FuzEn_{2D}$ to its unidimensional version over multiple scale factors. Then, we study its sensitivity to initial parameters compared to the already existing $SampEn_{2D}$. After that, we introduce some validation tests for its behavior with texture images with different irregularity degrees.

4.3.1 Comparing $FuzEn_{2D}$ to $FuzEn_{1D}$

To compare the behavior of $FuzEn_{2D}$ and $FuzEn_{1D}$ [68], we applied multiscale $FuzEn_{2D}$ and multiscale $FuzEn_{1D}$ on white Gaussian noise (WGN) and pink noise. We set the initial parameters as: $n = 2$, $\mathbf{m} = 2$, $r = 0.25$, and scale factor τ from 1 to 20. The comparison was performed using $FuzEn_{2D}$ and $FuzEn_{1D}$ for 300×300 pixels image size and 3000 points signal length, respectively.

As we can observe in Figure 4.9, at scale factor $\tau = 1$ and for both the 1D and 2D cases, WGN has a higher entropy value than pink noise. However, as the scale factor increases, the entropy value for WGN monotonically decreases and the pink noise maintains higher entropy values than WGN. This is in agreement with the literature and the fact that WGN contains information only in the smallest scale factors whereas pink noise contains complex structures across multiple scale factors. The difference between $FuzEn_{1D}$ and $FuzEn_{2D}$

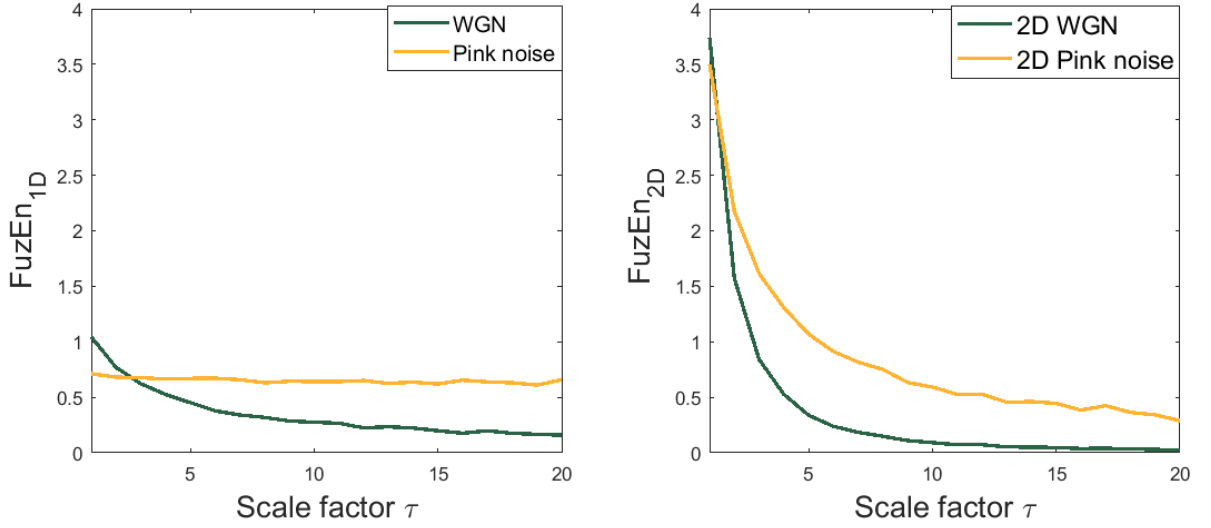


Figure 4.9 – Multiscale $FuzEn_{1D}$ and $FuzEn_{2D}$ for WGN and pink noises with $n = 2$, $\mathbf{m} = 2$, and $r = 0.25$.

lies in the fact that for unidimensional pink noise, the entropy value for the higher scale factors is almost constant, showing equivalent complex structure over the different scale factors (equivalent irregularity per scale). Nevertheless, for the bidimensional pink noise, fuzzy entropy values decrease with the scale factor but still show the presence of more complex structures in pink noise than WGN. The same is observed for WGN_{2D} and bidimensional pink noise when evaluated by $SampEn_{2D}$ (defined in section 1.4.2).

4.3.2 Sensitivity to variation in parameters r , \mathbf{m} , and n

For testing the sensitivity of $FuzEn_{2D}$ to r and \mathbf{m} , we performed $FuzEn_{2D}$ calculations for 256×256 pink noise images while changing tolerance level r from 0.06 up to 0.48 (step 0.06) for $\mathbf{m} = 1, 2$, and 3 and compared them to those obtained using $SampEn_{2D}$ [19]. In addition, for testing the sensitivity of $FuzEn_{2D}$ to the fuzzy function's power n , we evaluated twenty 200×200 pixels WGN_{2D} images using $FuzEn_{2D}$. The parameters were set to: $\mathbf{m} = 2$, $r = 0.25$, and fuzzy power increased from $n = 2$ to $n = 352$.

When changing \mathbf{m} and r , $FuzEn_{2D}$ showed much lower sensitivity than $SampEn_{2D}$, see Figure 4.10. This refers mainly to the fact that patterns' similarity in sample entropy is defined based on the two-state classifier (Heaviside function) with a rigid boundary depending on the value of r . However, in fuzzy entropy, the patterns are always associated with a continuous membership degree and all the pixels contribute in the final entropy

value. Moreover, upon varying n , for the twenty generated WGN_{2D} images, $FuzEn_{2D}$ showed low sensitivity as indicated by Figure 4.11. Thus $FuzEn_{2D}$ is proven to be a measure that has low sensitivity to the changes in parameters.

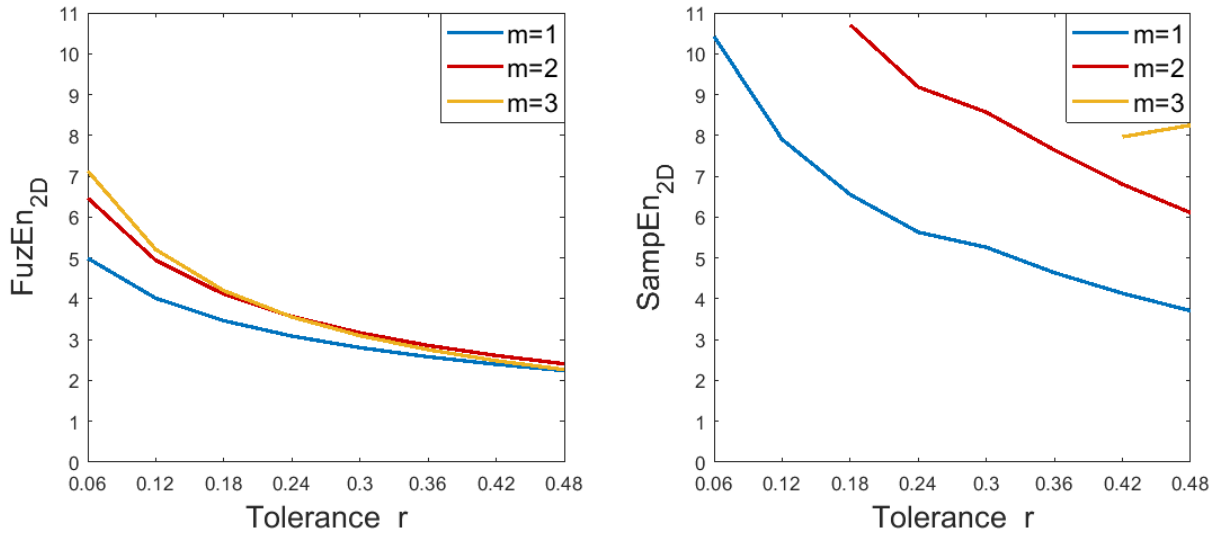


Figure 4.10 – $FuzEn_{2D}$ and $SampEn_{2D}$ for a 256×256 pink noise image with varying tolerance level r .

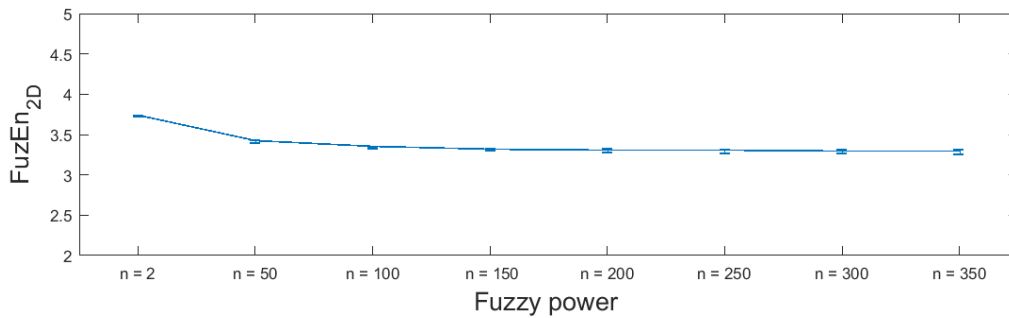


Figure 4.11 – $FuzEn_{2D}$ for twenty WGN_{2D} images upon increasing n .

For $SampEn_{2D}$ the similarity degree represented by the Heaviside function has a rigid boundary. The Heaviside function is a two-state binary classifier that gives a unity value if the difference in distance between the compared vectors is within threshold r ; otherwise it gives a zero value. Thus, any slight change in r will probably change the entropy value. It judges the vectors as either "similar" or "dissimilar" with no intermediate states. However, in the fuzzy entropy the vectors are always associated with a continuous membership

degree. This ensures continuity and smoothness for different values of r and leads to the contribution of all the time series elements in the final entropy output.

4.3.3 Rotation and translation

To study the effect of rotation we used the Mondial Marmi dataset [36, 37]. We chose an image from each of the four different granite classes shown in Figure 4.12, each image is of size 544×544 pixels.

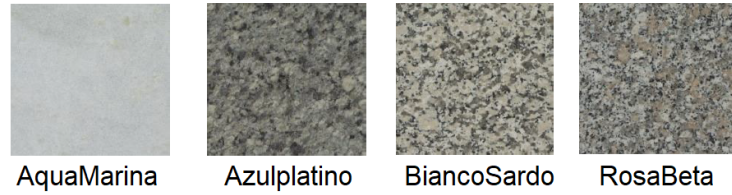


Figure 4.12 – Four randomly chosen Mondial Marmi granite images.

To study the effect of translation, we employed three Brodatz images [32, 34] and translated them with 10×10 , 100×100 , and 500×500 pixels. Translation, by definition, is a 2D geometric transformation which maps the position of each pixel in an input image into a new position in an output image, where the dimensionality of the two images often is the same.

Results for Mondial Marmi dataset upon software and hardware rotations are displayed in Figure 4.13. As we can observe, $FuzEn_{2D}$ shows invariance upon hardware, bicubic, and bilinear rotated images. Based on those results and due to the fact that rotations in images would also rotate reference patterns in $FuzEn_{2D}$, the membership degree values would be the same. Therefore, $FuzEn_{2D}$ is invariant to rotation. The same reasoning can be applied to image translation and proven by the results of Table 4.1. This leads to the conclusion that $FuzEn_{2D}$ is translation invariant as well. Being translation and rotation invariant, $FuzEn_{2D}$ can be considered a useful tool for studying medical images especially because those images are not always taken from the same angle of view.

4.3.4 Shuffling

Theoretically, shuffling increases the irregularity of data. Thus entropy values are expected to increase upon shuffling. We tested the change in bidimensional entropy values

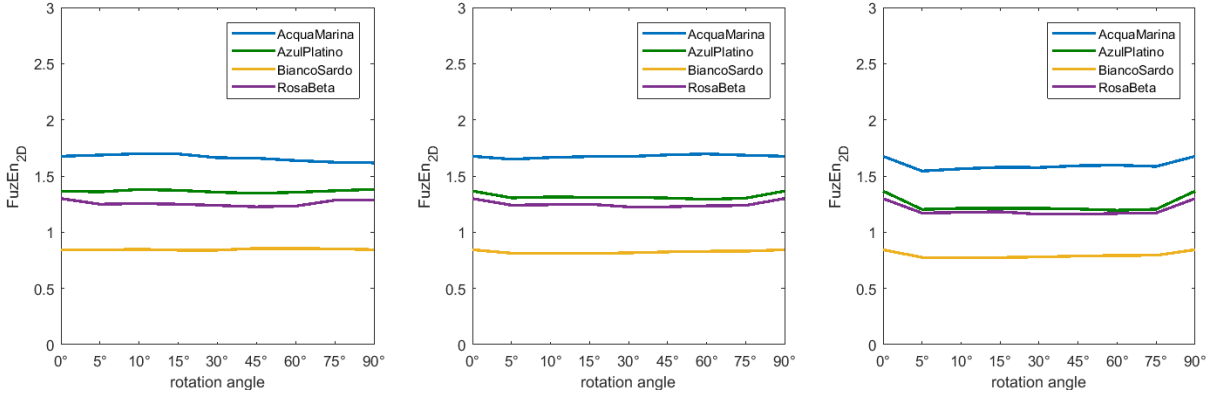


Figure 4.13 – The results for hardware, bicubic, and bilinear rotated images from left to right.

Table 4.1 – $FuzEn_{2D}$ results upon translation of 3 Brodatz images.

| Translation Pixels | 10×10 | 100×100 | 500×500 |
|--------------------|--------|---------|---------|
| Brodatz 1 | 1.0258 | 1.0258 | 1.0258 |
| Brodatz 2 | 1.2378 | 1.2378 | 1.2378 |
| Brodatz 3 | 1.8836 | 1.8836 | 1.8836 |

for $DistrEn_{2D}$ [20], $FuzEn_{2D}$, and $SampEn_{2D}$ [19]. The objective was to compare the outcomes of the three bidimensional entropy measures. We generated a $MIX_{2D}(0.1)$ image and 10 shuffled images from it. Then, we calculated the bidimensional entropy values for the original $MIX_{2D}(0.1)$ and its corresponding shuffled images.

Shuffling data decreased the $DistrEn_{2D}$ values whereas it increased the $FuzEn_{2D}$ and $SampEn_{2D}$ values, see Table 4.2. As shuffling increases the irregularity of data, $FuzEn_{2D}$ and $SampEn_{2D}$ are more reliable than $DistrEn_{2D}$ from this perspective. The results illustrate the advantage of $FuzEn_{2D}$ and $SampEn_{2D}$ over $DistrEn_{2D}$ in this issue.

Table 4.2 – $DistrEn_{2D}$, $SampEn_{2D}$, and $FuzEn_{2D}$ values for shuffled images

| | $DistrEn_{2D}$ | $SampEn_{2D}$ | $FuzEn_{2D}$ |
|----------|---------------------|---------------------|---------------------|
| Original | 0.7188 | 1.7411 | 1.4193 |
| Shuffled | 0.6914 ± 0.0015 | 2.5645 ± 0.0527 | 1.9056 ± 0.0321 |

4.3.5 $FuzEn_{2D}$ for $MIX_{2D}(p)$ images

We generated 256×256 pixels $MIX_{2D}(p)$ images and analyzed them by $FuzEn_{2D}$ and $SampEn_{2D}$. We set $\mathbf{m} = 1, 2, 3$, $p = 0$ to 1 with a step of 0.1, and repeated the calculation for 10 images each. The results, presented in Figure 4.14, concur with the fact that a higher entropy corresponds to a $MIX_{2D}(p)$ image with a higher p value, see Figure 4.3. In fact, a higher p value in a $MIX_{2D}(p)$ image describes a higher spatial irregularity. $FuzEn_{2D}$, unlike $SampEn_{2D}$, does not have the problem of undefined entropy values for $\mathbf{m} = 1, 2$, and 3. Moreover, for $MIX_{2D}(0.9)$ and $MIX_{2D}(1)$ with $\mathbf{m} = 2$, $SampEn_{2D}$ quantifies a lower irregularity than that of $MIX_{2D}(0.8)$ which is misleading due to the fact that $MIX_{2D}(p)$ describes a higher spatial irregularity when p increases.

Thus, $FuzEn_{2D}$ can be considered as an appropriate metric for quantifying the images' irregularity as it is able to correctly quantify the irregularity of $MIX_{2D}(p)$ images. It is also observed to outperform $SampEn_{2D}$, especially for $\mathbf{m} = 2$ and 3.

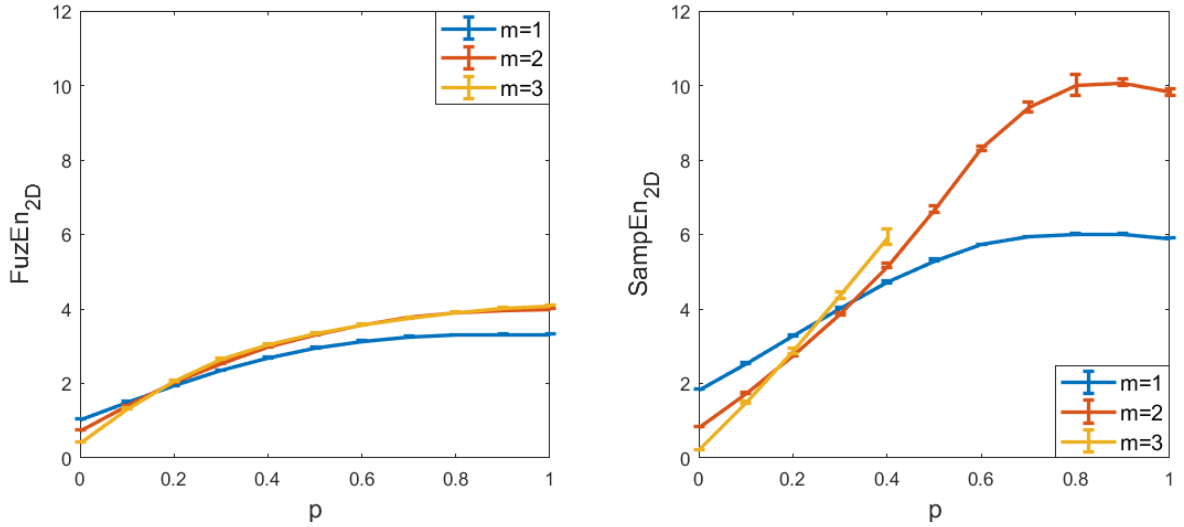


Figure 4.14 – Ten $FuzEn_{2D}$ and $SampEn_{2D}$ repetitions for 256×256 pixels of $MIX_{2D}(p)$ images ($\mathbf{m} = 1, 2, 3$).

Another test was to study $MIX_{2D}(p)$ with different sizes to understand the reliability of our proposed $FuzEn_{2D}$ method, compared with $SampEn_{2D}$, by measuring the irregularity of images with different sizes. We calculated $FuzEn_{2D}$ and $SampEn_{2D}$ for $MIX_{2D}(p)$ with an increase in the size of images from 50×50 to 200×200 pixels, $\mathbf{m} = 2$, $p = 0$ to 1

with a step of 0.1, and 10 repetitions each. The results for $FuzEn_{2D}$ show a consistent profile with the change in image size, see Figure 4.15 (a). In contrast, $SampEn_{2D}$ leads to some undefined values for small-sized images and has a higher standard deviation upon repetition, see Figure 4.15 (b). This illustrates that $FuzEn_{2D}$ has a low sensitivity to change in image size, whereas $SampEn_{2D}$ shows a high sensitivity to change in image size and inconsistent behavior upon repetition.

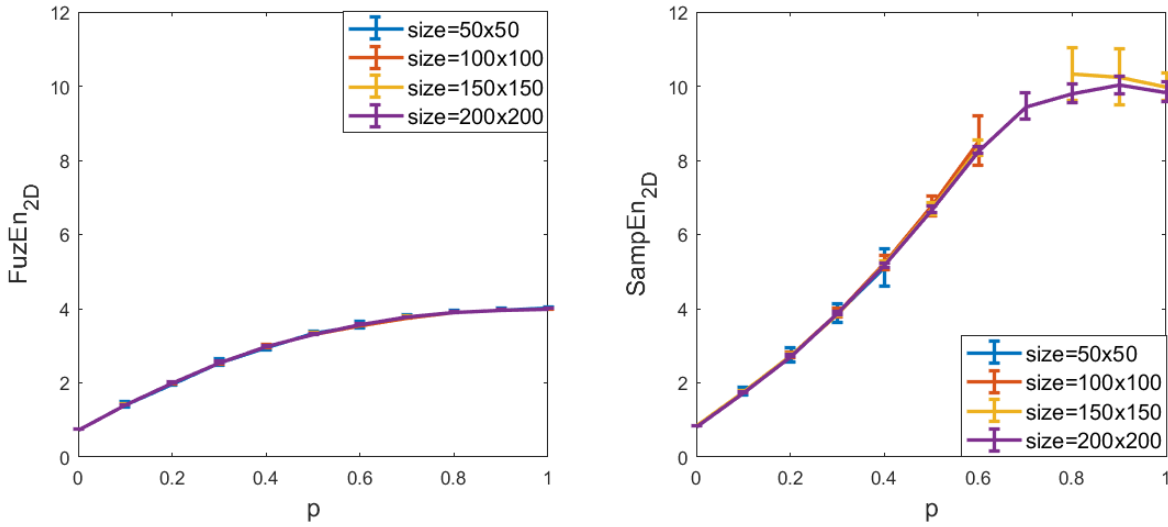


Figure 4.15 – Ten $FuzEn_{2D}$ and $SampEn_{2D}$ repetitions for $MIX_{2D}(p)$ images of varying size in pixels ($\mathbf{m}=2$).

4.3.6 WGN_{2D} and $1/f^\beta$ noise images

To assess the ability of $FuzEn_{2D}$ to evaluate small images irregularity, validate repeatability, and better understand the effect of image size on the results, we created WGN_{2D} and $1/f^\beta$ ($\beta = -1, 1, \text{ and } 2$) noise images with sizes ranging from 20×20 to 200×200 pixels (with a step of 20×20 pixels). Forty images were generated for each size and $FuzEn_{2D}$ was calculated for $\mathbf{m} = 1, 2, \text{ and } 3$. Same calculations were performed using $SampEn_{2D}$ for comparison purposes. The results are displayed as box plots in Figure 4.16. The upper plots demonstrate the stability and consistency of $FuzEn_{2D}$ upon forty repetitions and its low sensitivity for varying image sizes as well as the low sensitivity to the change in \mathbf{m} . In addition, $FuzEn_{2D}$ shows clear differentiation ability between the four noise types, especially for images larger than 20×20 pixels. However, upon repetition,

$SampEn_{2D}$ shows overlapping values for pink, blue, and WGN_{2D} with $\mathbf{m}=1$, inconsistency for small images with $\mathbf{m}=2$, and undefined outcome with $\mathbf{m}=3$ for the four noise types, see Figure 4.16.

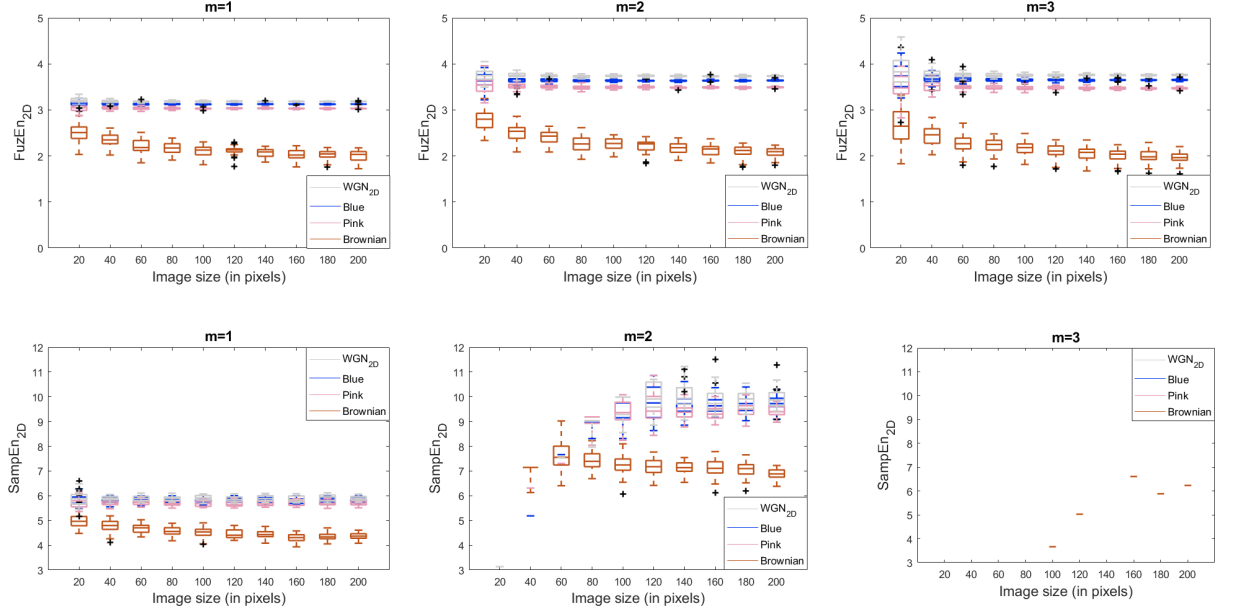


Figure 4.16 – $FuzEn_{2D}$ and $SampEn_{2D}$ for 40 WGN_{2D} , blue, pink, and brownian noise images of sizes 20×20 up to 200×200 pixels (with $\mathbf{m}=1$, $\mathbf{m}=2$, and $\mathbf{m}=3$).

Furthermore, we calculated the coefficients of variation (CV) of $FuzEn_{2D}$ for the 100×100 pixels WGN_{2D} and $1/f^\beta$ noise images with $\mathbf{m}=1, 2$, and 3 . The CVs are presented in Table 4.3 (– shows undefined CV). The results illustrate that $FuzEn_{2D}$ leads to more stable results (lower CVs) than $SampEn_{2D}$ for different kinds of noises. Note that as MSF_{2D} uses $FuzEn_{2D}$ for multiple scale factors, it could be inferred that MSF_{2D} , compared with MSE_{2D} , will result in more stable entropy values.

4.3.7 Gray scale image with additive noise

We used Lena 512×512 pixels gray scale image, see Figure 4.17, added with different noise amounts to evaluate the ability of $FuzEn_{2D}$ to detect different levels of WGN_{2D} and salt and pepper noise (SPN). The images were standardized by subtracting their mean and dividing them by the standard deviation. Different levels of WGN_{2D} (increasing its mean and variance: 0.01, 0.05, and 0.09) and different densities of SPN (0.01, 0.05, and 0.09) were added.

Table 4.3 – CVs for $FuzEn_{2D}$ and $SampEn_{2D}$ of 100×100 pixels WGN_{2D} and $1/f^\beta$ noise image.

| | m | Blue | Brownian | WGN_{2D} | Pink |
|---------------|----------|-------|----------|------------|-------|
| $FuzEn_{2D}$ | 1 | 0.003 | 0.053 | 0.003 | 0.005 |
| | 2 | 0.005 | 0.056 | 0.005 | 0.007 |
| | 3 | 0.008 | 0.071 | 0.008 | 0.011 |
| $SampEn_{2D}$ | 1 | 0.017 | 0.048 | 0.018 | 0.020 |
| | 2 | – | 0.056 | – | – |
| | 3 | – | – | – | – |

Figure 4.17 – The widely used 512×512 pixels Lena gray scale image.

$FuzEn_{2D}$ parameters were set as: embedding dimension $\mathbf{m}= 2$, threshold $r = 0.24$, and fuzzy power $n = 2$. The results are shown in Tables 4.4 and 4.5. A higher entropy value is observed when WGN_{2D} of higher mean and variance is added. Moreover, adding a higher density of SPN to the gray scale image leads to a higher entropy value as well. These results illustrate the ability of $FuzEn_{2D}$ to detect different amounts of WGN_{2D} and SPN.

Table 4.4 – $FuzEn_{2D}$ for a gray scale image (Lena image) added with different levels of WGN_{2D} .

| Noise type | Level added | Entropy value |
|----------------|------------------------|---------------|
| original image | – | 0.2887 |
| WGN_{2D} | mean and variance 0.01 | 1.2465 |
| WGN_{2D} | mean and variance 0.05 | 2.5782 |
| WGN_{2D} | mean and variance 0.09 | 3.0927 |

Table 4.5 – $FuzEn_{2D}$ for a gray scale image (Lena image) added with different densities of SPN noise.

| Noise type | Level added | Entropy value |
|----------------|--------------|---------------|
| original image | – | 0.2887 |
| SPN | density 0.01 | 0.4513 |
| SPN | density 0.05 | 1.0509 |
| SPN | density 0.09 | 1.5723 |

By adding noise to gray scale images, we wanted to prove the ability of $FuzEn_{2D}$ to detect different degrees of added noise to the original image, and thus the ability to quantify accordingly even slight changes in the studied images. $FuzEn_{2D}$ should be able to spot any changed textural behavior and behave upon its degree. In other words, we have a higher entropy value for a higher added noise degree which is logically the expected performance. The results are in agreement with those obtained by Azami *et al.* for $DistrEn_{2D}$ [20].

4.3.8 $FuzEn_{2D}$ for artificial periodic and synthesized texture images

$FuzEn_{2D}$ was calculated for three artificial periodic texture images and their corresponding synthesized textures depicted in Figure 4.6, setting $\mathbf{m}= 2$. The results, illustrated in Table 4.6, show that $FuzEn_{2D}$ values are higher for synthesized textures than

those of their corresponding periodic textures. This demonstrates that $FuzEn_{2D}$ is able to discriminate periodic from synthesized textures and to quantify the images' periodicity. The results are in agreement with those presented by Azami *et al.* for $DistrEn_{2D}$ [20].

Table 4.6 – $FuzEn_{2D}$ for artificial periodic textures and their synthesized textures (please see Figure 4.6).

| | | |
|-------------------------|-------------------------|-------------------------|
| texture (a) | texture (b) | texture (c) |
| 0.0965 | 0.0904 | 0.1191 |
| synthesized texture (a) | synthesized texture (b) | synthesized texture (c) |
| 0.1852 | 0.1036 | 0.1343 |

The images were also resized to evaluate the differentiation ability of $FuzEn_{2D}$ upon variation in image sizes. We studied the original 256×256 pixels artificial periodic texture images and their synthesized textures as well as their corresponding versions of 50×50 pixels up to 200×200 pixels (step of 50×50 pixels) with $\mathbf{m} = 1, 2, \text{ and } 3$. The results show that all the values for the periodic textures are lower than those of their corresponding synthesized ones (data not shown here). This demonstrates that $FuzEn_{2D}$ is able to properly discriminate periodic from synthesized textures by assigning lower entropy values for periodic textures (highly ordered textures), for different \mathbf{m} and image sizes.

4.3.9 Multiscale $FuzEn_{2D}$ for $1/f^\beta$ noise images

For assessing MSF_{2D} behavior and comparing it to MSE_{2D} , we employed noise images of known nature in terms of complexity, i.e. outcome over several scales factors. We utilized pink, brownian, blue, and white, namely the $1/f^\beta$ noise images. Ten images from each kind of noise were generated and evaluated using MSF_{2D} and MSE_{2D} . We set the initial parameters as $\mathbf{m} = 2$ and scale factor τ from 1 to 15. The results are displayed in Figure 4.18.

MSF_{2D} results for brownian and pink noise images show that they possess complex structures over scale factors, which agrees with the fact that they are described as persistent processes with long term correlations. However, white and blue noise images show a decrease in entropy value with scale factor, as by definition they are of short term memory anti-correlated processes [160]. This illustrates the ability of MSF_{2D} to quantify the degree of complexity in the studied images and its consistency. Compared to MSE_{2D} , MSF_{2D} shows a lower standard deviation and better consistency upon repetition. Moreover, MSE_{2D} for Brownian noise images from $\tau=6$ shows undefined values. To compare

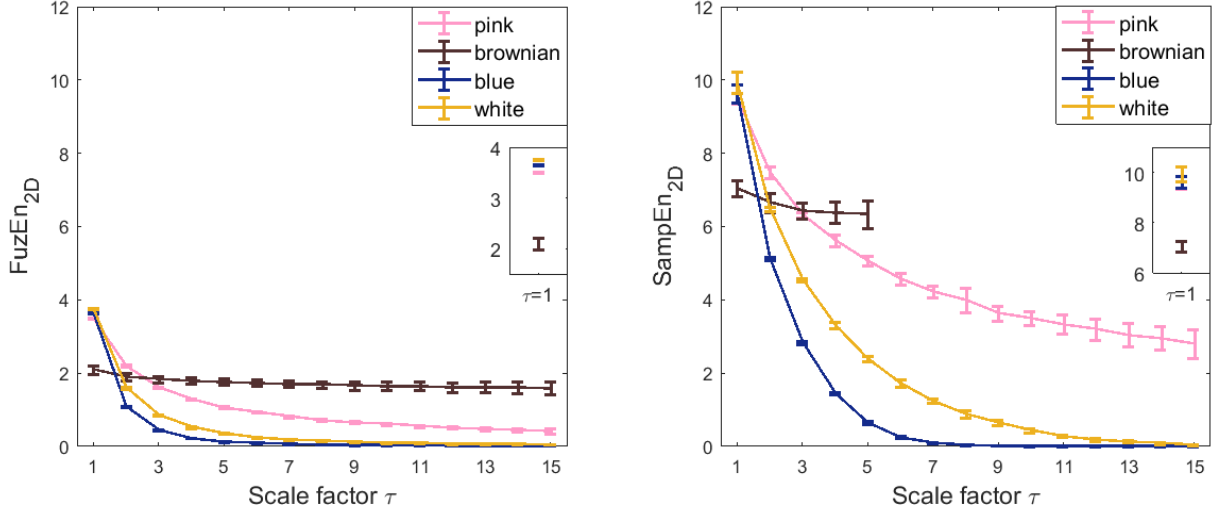


Figure 4.18 – MSF_{2D} and MSE_{2D} for ten pink, brownian, blue and white 2D noise images.

the actual behavior of $FuzEn_{2D}$ and $SampEn_{2D}$ (i.e., at scale factor $\tau=1$) we zoomed in on the first scale factor values, see Figure 4.18 (small box). We can notice that $FuzEn_{2D}$ is able to identify the different noise images in the proper order of irregularity as: white \rightarrow blue \rightarrow pink \rightarrow brownian, from highest to lowest, whereas $SampEn_{2D}$ shows overlapping values with no clear differentiation ability.

4.3.10 Multiscale $FuzEn_{2D}$ for synthetic images

We evaluated MSF_{2D} for WGN_{2D} , $MIX_{2D}(0.2)$, and pink noise images for parameters $\mathbf{m}=2$ and scale factor τ from 1 to 20. We compared the results with those of MSE_{2D} . We increased image size from 50×50 pixels to 600×600 pixels with an increment of 50×50 pixels, see Figure 4.19. The results for MSF_{2D} show that the entropy values are stable for all scale factors starting from 50×50 pixels images for the three image types. However, for MSE_{2D} the entropy values look stable from 100×100 pixels for WGN_{2D} and from 150×150 pixels for $MIX_{2D}(0.2)$ and pink noise images. For both entropy measures, the results for $MIX_{2D}(0.2)$ show a lower complexity than those for WGN_{2D} and pink noise images, as expected theoretically.

The results for WGN_{2D} and pink noise images agree with the literature for the irregularity quantification at each scale factor [88, 91]. Entropy values for WGN_{2D} show higher irregularity than pink noise for small scale factors ($\tau=1$). However, as the scale factor increases, WGN_{2D} shows a decrease in irregularity with scale factor, whereas pink noise

shows higher entropy values and also a higher overall complexity. This is in accordance with the fact that pink noise has long term correlations whereas white noise has short-term correlations and thus is not structurally complex [160, 91, 88]. This is also reflected in the biological systems' behavior where some pathologic processes have a lower complexity than healthy processes unlike what is indicated by the traditional entropy measurement at a single scale [91, 88]. Therefore, the results suggest that MSF_{2D} is a proper complexity measure for images. It is able to quantify images complexity properly, i.e., at different scale factors (as illustrated by the multiscale tests) and shows a consistent outcome for increasing image sizes from 50×50 to 600×600 pixels. These results, compared with those for MSE_{2D} , suggest that MSF_{2D} overcomes the drawback of undefined MSE_{2D} values especially for small-sized images.

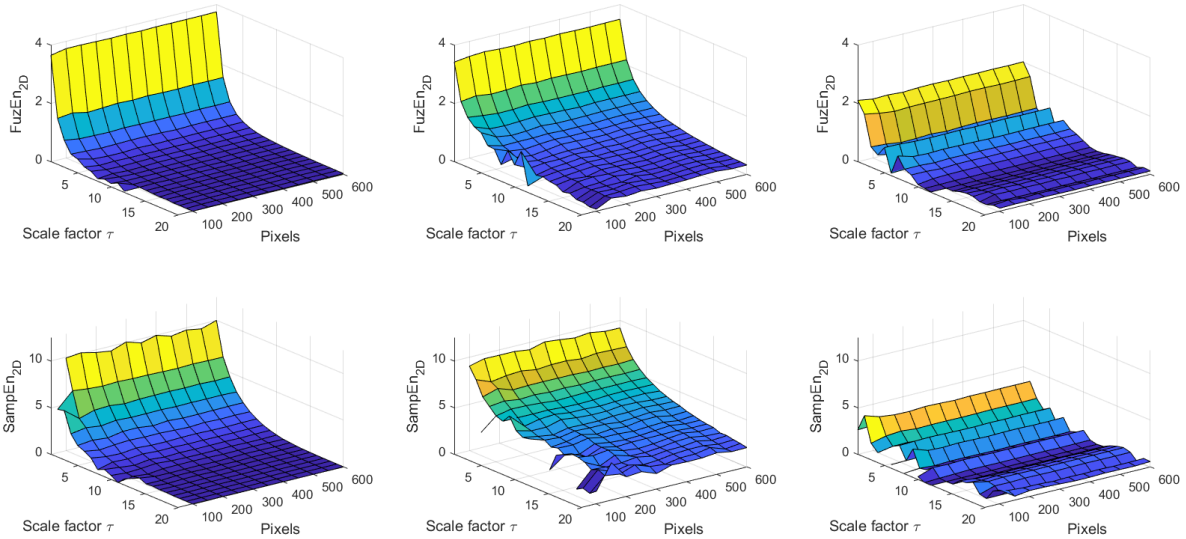


Figure 4.19 – MSF_{2D} and MSE_{2D} for WGN_{2D} , pink noise, and $MIX_{2D}(0.2)$ images (from left to right) with $\mathbf{m}=2$, and $r=0.25$.

4.4 $FuzEn_{2D}$, $FuzEnL_{2D}$, and $FuzEnGL_{2D}$ Comparison

We performed some other tests to compare global bidimensional fuzzy entropy approach, $FuzEn_{2D}$, the local bidimensional fuzzy entropy approach $FuzEnL_{2D}$, and $FuzEnGL_{2D}$ that considers both the global and local characteristics. The tests use pink

and WGN_{2D} images.

Test for fuzzy entropy measures

To test the discrimination ability and the sensitivity to tolerance level r of $FuzEn_{2D}$ (global fuzzy entropy), $FuzEnL_{2D}$, and $FuzEnGL_{2D}$, we generated $MIX_{2D}(0.1)$, $MIX_{2D}(0.5)$, and $MIX_{2D}(0.9)$ images and processed them by those fuzzy entropy measures while varying tolerance r from 0.06 to 0.48 with a step of 0.06 . $FuzEn_{2D}$, $FuzEnL_{2D}$, and $FuzEnGL_{2D}$ were able to differentiate between the different $MIX_{2D}(p)$ images, see Figure 4.20. $FuzEnGL_{2D}$ showed a better discrimination ability for the different r values but also illustrated a high sensitivity to the choice of r (see the lowest and highest value for the fuzzy entropy for one of the $MIX_{2D}(p)$ images).

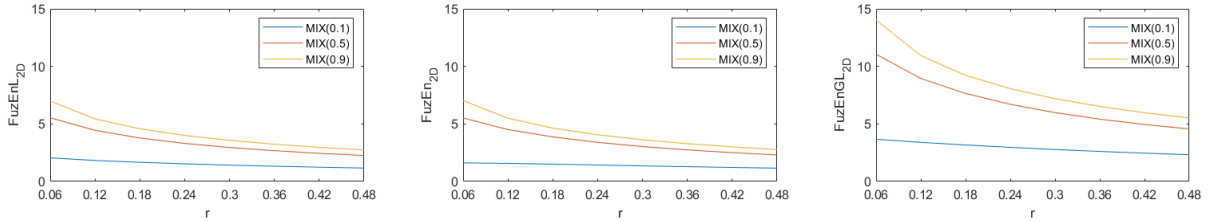


Figure 4.20 – Bidimensional fuzzy entropy measures for a 200×200 $MIX_{2D}(0.1)$, $MIX_{2D}(0.5)$, and $MIX_{2D}(0.9)$.

The three fuzzy entropy measures, $FuzEn_{2D}$, $FuzEnL_{2D}$, and $FuzEnGL_{2D}$, illustrate a capability to differentiate $MIX_{2D}(0.1)$, $MIX_{2D}(0.5)$, and $MIX_{2D}(0.9)$, but the $FuzEn_{2D}$ and $FuzEnL_{2D}$ are shown to be the more stable than $FuzEnGL_{2D}$ even when r varies. Although $FuzEnGL_{2D}$ shows the highest discrimination, it has a much higher sensitivity to the choice of r .

Multiscale test for fuzzy entropy measures

To compare the fuzzy entropy measures on the multiscale level, we generated 300×300 pixels of WGN_{2D} and pink noise images. These images were analyzed by the multiscale extensions of $FuzEn_{2D}$, $FuzEnL_{2D}$ and $FuzEnGL_{2D}$. The parameters were defined as: $n = 2$, $r = 0.25$, scale factor τ from 1 to 20, and \mathbf{m} varied from 1 to 6. The results are previewed in the following figures 4.21 and 4.22.

There was no drastic difference between the multiscale $FuzEn_{2D}$ and $FuzEnL_{2D}$ in the above described tests: they show a very similar behavior on pink and WGN_{2D} . On

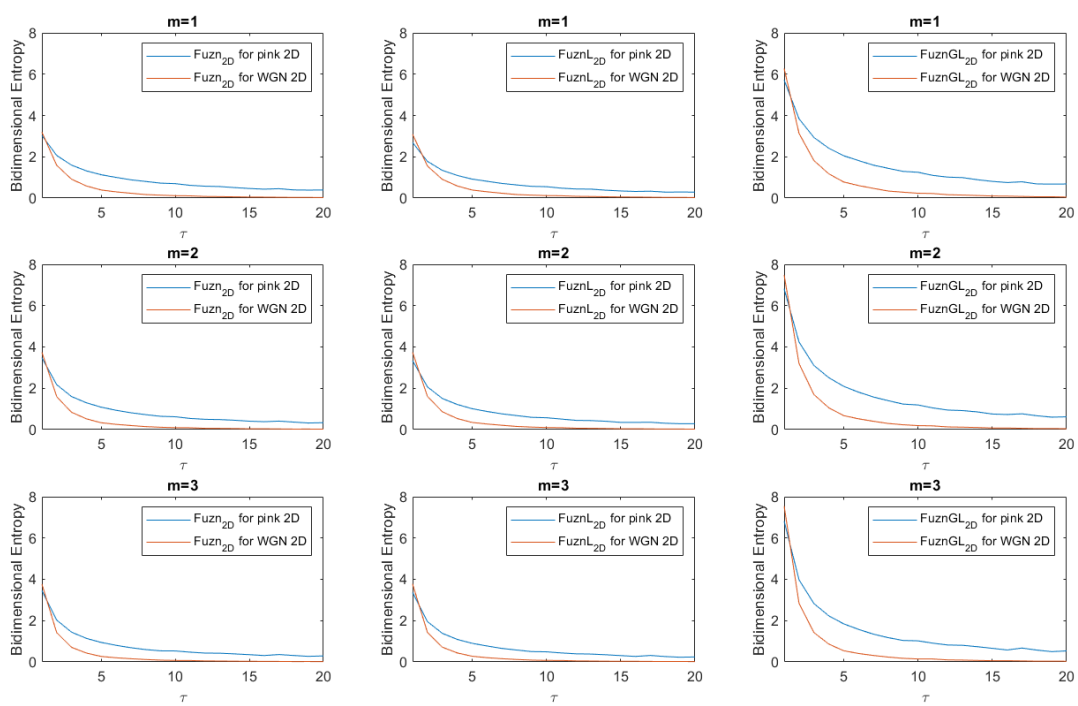


Figure 4.21 – Multiscale bidimensional fuzzy entropy measures for a 300×300 WGN_{2D} and pink noise images, m from 1 to 3.

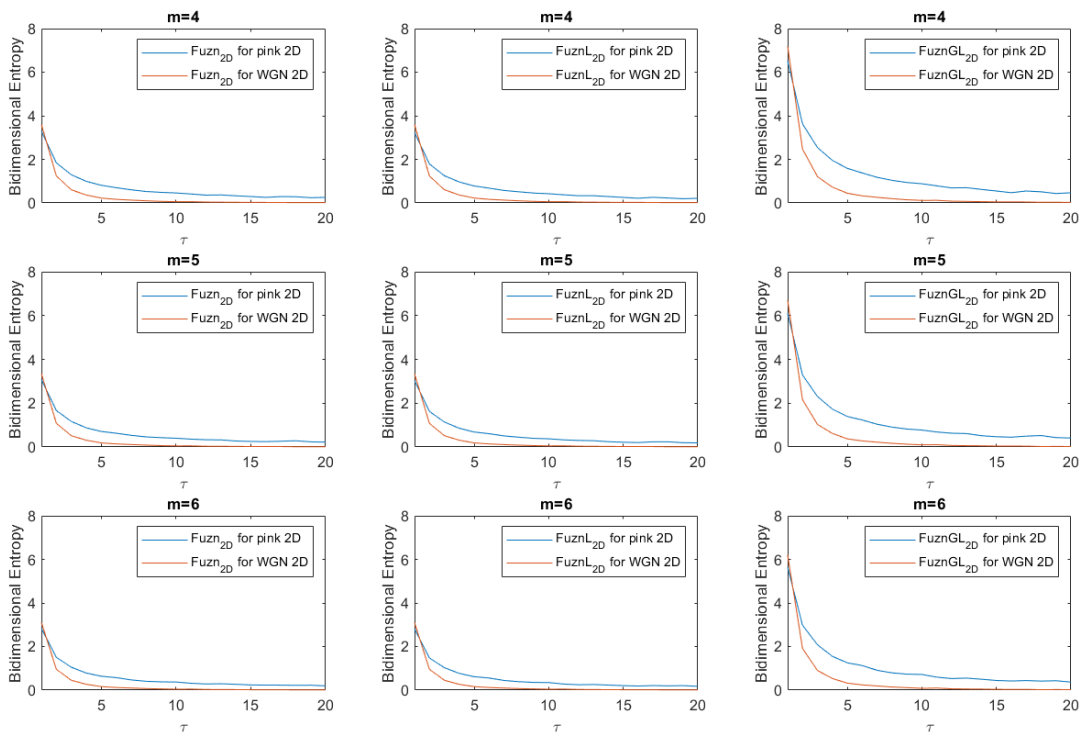


Figure 4.22 – Multiscale bidimensional Fuzzy entropies for a 300×300 WGN_{2D} and pink noise images, m from 4 to 6.

the other side $FuzEnGL_{2D}$ could be described as an amplifier for the preceding results for a better view and better discrimination between pink and WGN_{2D} . The results are in agreement with the literature and the fact that WGN_{2D} has a higher irregularity for small scale factors but pink noise express a higher irregularity for higher scale factor thus it is more complex.

Computation cost

For comparing the computational cost of $FuzEn_{2D}$ and $FuzEnL_{2D}$ with that of $FuzEnGL_{2D}$, we performed the entropy calculations for thirty 256×256 pixels of pink noise images and calculated the average time in seconds taken by each entropy measure. We set the initial parameters as $n = 2$, $\mathbf{m} = 2$, and $r = 0.24$ for all bidimensional entropy measures. The simulations were carried out by Windows 10 laptop equipped with 8-GB RAM and Intel(R) Core(TM) i7-6500U CPU processor using MATLAB R2017a. $FuzEnGL_{2D}$'s computational cost is found to be almost double that of $FuzEn_{2D}$, see Table 4.7. Even though $FuzEnGL_{2D}$ shows higher discrimination ability for some cases, the computation time taken by $FuzEn_{2D}$ is considerably the lowest.

Table 4.7 – Average calculation time for $FuzEn_{2D}$, $FuzEnL_{2D}$, and $FuzEnGL_{2D}$ (see text for details on the computer performance).

| Entropy | Average time taken per image |
|----------------|------------------------------|
| $FuzEn_{2D}$ | $324.15 \pm 3.04s$ |
| $FuzEnL_{2D}$ | $345.94 \pm 16.8s$ |
| $FuzEnGL_{2D}$ | $646.99 \pm 49.8s$ |

Medical images in general are large images that would favor a high speed performance in the processing algorithm. Thus, based on the higher computational cost for both $FuzEnL_{2D}$ and $FuzEnGL_{2D}$, and the higher sensitivity to the change in tolerance level of $FuzEnGL_{2D}$, we decided to use $FuzEn_{2D}$. Moreover, it is better to consider the global characteristics of an image rather than the local ones to better assess the actual overall irregularity on the single scale calculations and the overall complexity for the multiscale calculations.

4.5 MSF_{2D} and $MMSF_{2D}$ Comparison

In order to study the effect of downsampling we performed some tests to compare MSF_{2D} to $MMSF_{2D}$. We proposed $MMSF_{2D}$ that consists of an overlapping window to coarse grain the images based on [92] and compared the results to those downsampled with a non-overlapping window using MSF_{2D} . We calculated MSF_{2D} for WGN_{2D} , pink, and $MIX_{2D}(0.2)$ noise images for parameters: $n = 2$, $\mathbf{m} = 2$, $r = 0.25$, and scale τ from 1 to 20, see Figure 4.23. Similarly we repeat this test without downsampling the coarse grained images using $MMSF_{2D}$, Figure 4.24.

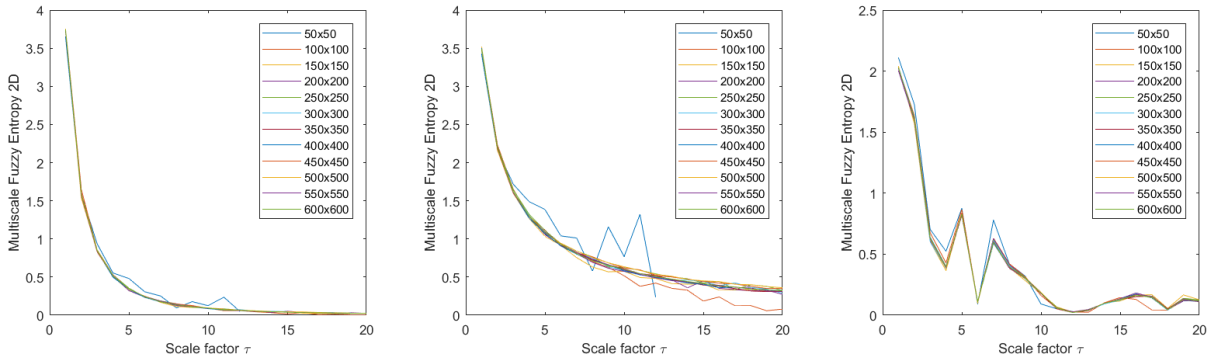


Figure 4.23 – MSF_{2D} for WGN_{2D} , pink noise, and $MIX_{2D}(0.2)$ images (from left to right) with $n = 2$, $\mathbf{m} = 2$, and $r = 0.25$.

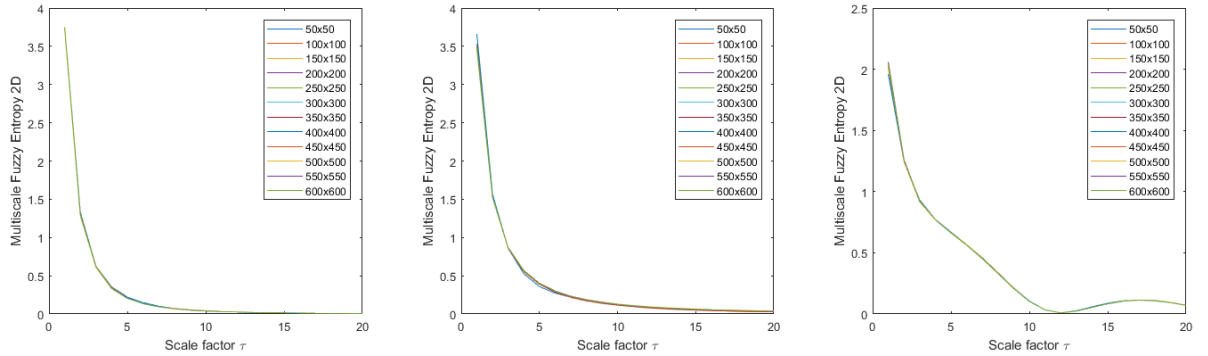


Figure 4.24 – $MMSF_{2D}$ for WGN_{2D} , pink noise, and $MIX_{2D}(0.2)$ images (from left to right) with $n = 2$, $\mathbf{m} = 2$, and $r = 0.25$ without downsampling.

The results for both methods were consistent and showed proper behavior with noise images. However, with $MMSF_{2D}$ the results took a longer time to be obtained. Thus, a computation cost comparison will be presented in the following section.

A wider study will be performed later on handling this issue in specific and the different possible methods for coarse-graining by referring to the papers “Coarse-Graining Approaches in Univariate Multiscale Sample and Dispersion Entropy”, [89], “Two-dimensional Multiscale Entropy Analysis: Applications to Image Texture Evaluation”, [42], and “Refined multiscale fuzzy entropy based on standard deviation for biomedical signal analysis” [72].

Computation cost

For the computation cost comparison we performed a test using pink and white noise 256×256 pixels images for 30 repetitions. The parameters were set to $\mathbf{m}=2$, $r=0.24$, $n=2$, and $\tau_{max}=15$. The mean and standard deviation for the time taken by both algorithms for 30 repetitions are displayed in Table 4.8. The simulations were carried out by Windows 10 computer equipped with 8-GB RAM and Intel(R) Xeon(R) E5-1603 CPU processor using MATLAB R2017a.

Table 4.8 – MSF_{2D} and $MMSF_{2D}$ computation cost comparison in seconds (see text for details on the computer performance).

| | MSF_{2D} time in seconds | $MMSF_{2D}$ time in seconds |
|-------------|----------------------------|------------------------------|
| Pink noise | 350.39 ± 1.26 | $4.365 \times 10^3 \pm 9.96$ |
| White noise | 349.96 ± 0.84 | $4.359 \times 10^3 \pm 8.99$ |

The results show the huge difference in the computation time taken by both algorithms. The average time taken by $MMSF_{2D}$ algorithm in seconds is almost 12 times larger than that taken by MSF_{2D} . This comes back to the fact that with MSF_{2D} the images are down-sampled and become of a smaller size with increasing τ value. Consequently, MSF_{2D} is the measure that we use for all our coming work based on the original coarse-graining method proposed by [88].

4.6 First Colored Fuzzy Entropy Approach

$FuzEnC_{2D}$

We started with tests using the first developed colored fuzzy entropy approach $FuzEnC_{2D}$ [29, 31] without normalizing the testing images. The results are presented

below.

4.6.1 Sensitivity to change in tolerance level r

We studied the effect of changes in r by evaluating a 256×256 pixels colored Brodatz image [33] using $FuzEnC_{2D}$, see Figure 4.25 (b). r was defined from 0.06 to 0.48 (step of 0.06) and windows' length $\mathbf{m} = 1, 2, \text{ and } 3$. The results in Figure 4.26 prove that $FuzEnC_{2D}$ is defined upon variation of r and \mathbf{m} and we note its low sensitivity for the three channels (\mathbf{U}_R , \mathbf{U}_G , and \mathbf{U}_B). This proves the reliability of $FuzEnC_{2D}$ for different choices of initial parameters.



Figure 4.25 – Images used for evaluating $FuzEnC_{2D}$: 256×256 pixels checker board image (a), 256×256 pixels colored Brodatz texture (b).

4.6.2 $MIX_{2D}(p)$

We generated checker board image as alternating white and black squares with periodic behavior and expected zero entropy value, see Figure 4.25 (a). Then $MIX_{2D}(p)$ [19] were added to the checker board image. p being from 0 (periodic sinusoidal image) to 1 (totally random image). Ten $MIX_{2D}(p)$ images were generated for each p value to validate the consistency of our results. The parameters were set as $r = 0.2$ and $\mathbf{m} = 1, 2, \text{ and } 3$. As we can observe in Figure 4.27, $FuzEnC_{2D}$ values for each channel increase as p increases. Thus, the results for background checker board images added with $MIX_{2D}(p)$ processes illustrate that $FuzEnC_{2D}$ has the ability to distinguish different degrees of added randomness and has a relatively low sensitivity to the choice of \mathbf{m} .

4.6.3 Colored Brodatz images

Colored Brodatz images of 640×640 pixels (see Figure 4.28) were divided into 4 equal sub-images of 320×320 pixels and all of them were evaluated by $FuzEnC_{2D}$. The pa-

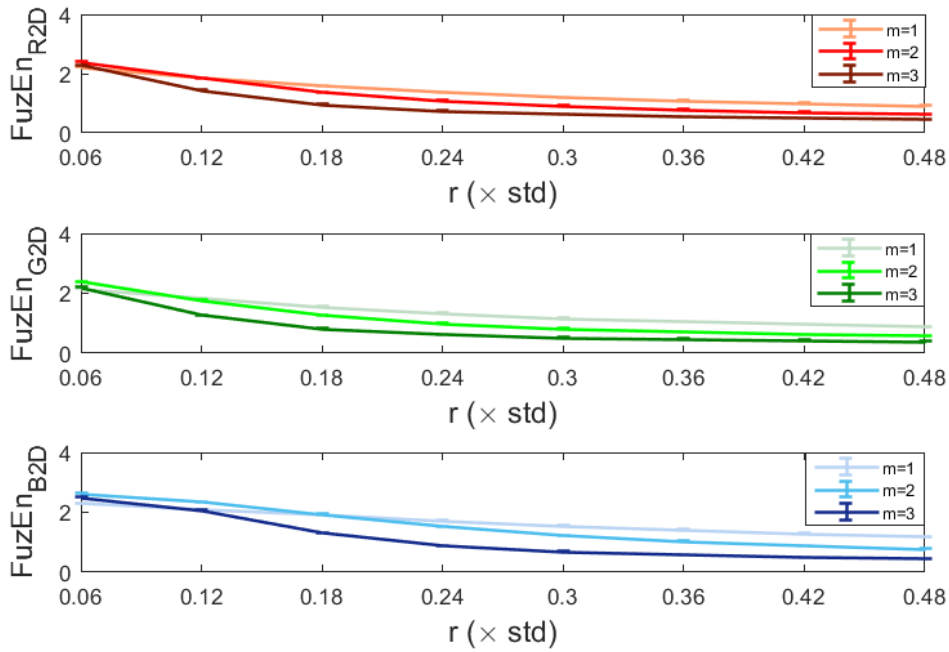


Figure 4.26 – Sensitivity of $FuzEnC_{2D}$ to variation in the values of r and \mathbf{m} .

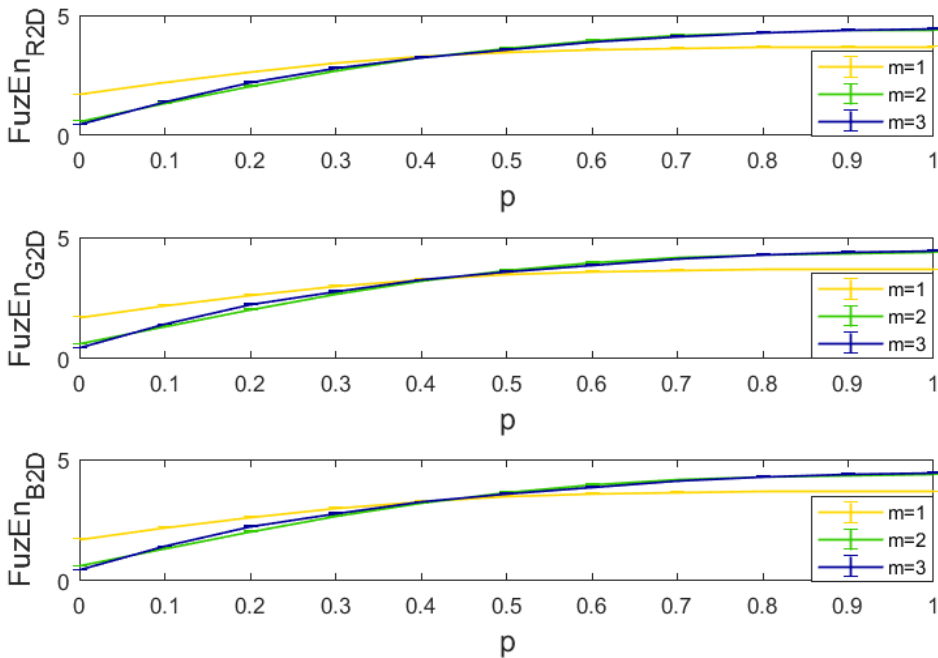


Figure 4.27 – $FuzEnC_{2D}$ for checker board pattern added with $MIX_{2D}(p)$.

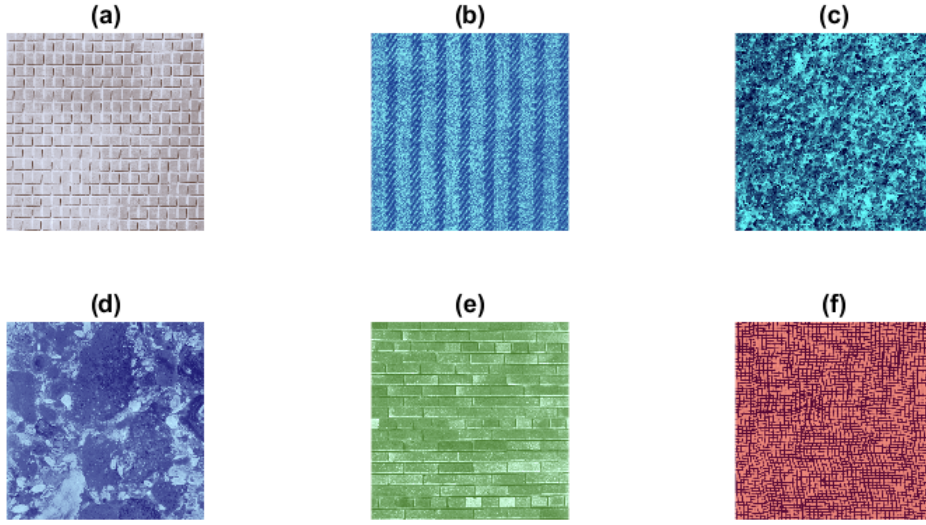


Figure 4.28 – 640x640 pixels colored Brodatz textures.

rameters are chosen to be $r = 0.2$, $\mathbf{m} = 2$, and $n = 2$. $FuzEnC_{2D}$ values for the original 640×640 pixels textures and the mean and standard deviation of the 4 sub-images are displayed in Tables 4.9 and 4.10, respectively. For the sub-images, $FuzEnC_{2D}$ shows results similar to those of Table 4.9 with a small standard deviation (≤ 0.04). This shows the ability of $FuzEnC_{2D}$ to recognize sub-images belonging to the same textural behavior.

Table 4.9 – $FuzEnC_{2D}$ for colored Brodatz textures (640x640 pixels).

| | $FuzEn_{R2D}$ | $FuzEn_{G2D}$ | $FuzEn_{B2D}$ |
|-------------|---------------|---------------|---------------|
| texture (a) | 0.19 | 0.22 | 0.24 |
| texture (b) | 0.55 | 0.78 | 0.52 |
| texture (c) | 0.34 | 0.61 | 0.52 |
| texture (d) | 0.26 | 0.30 | 0.24 |
| texture (e) | 0.35 | 0.34 | 0.41 |
| texture (f) | 0.82 | 0.78 | 0.56 |

Table 4.10 – Mean and standard deviation of $FuzEnC_{2D}$ for colored Brodatz textures sub-images (320×320 pixels).

| | FuzEn $_{R2D}$ | FuzEn $_{G2D}$ | FuzEn $_{B2D}$ |
|-------------|----------------|----------------|----------------|
| texture (a) | 0.19±0.02 | 0.22±0.02 | 0.23±0.03 |
| texture (b) | 0.55±0.01 | 0.78±0.02 | 0.52±0.01 |
| texture (c) | 0.33±0.00 | 0.61±0.01 | 0.52±0.01 |
| texture (d) | 0.26±0.02 | 0.30±0.02 | 0.24±0.02 |
| texture (e) | 0.35±0.03 | 0.35±0.03 | 0.41±0.04 |
| texture (f) | 0.82±0.02 | 0.78±0.02 | 0.56±0.01 |

4.7 $FuzEnC_{2D}$, $FuzEnV_{2D}$, and $FuzEnM_{2D}$ Validation Tests

After our first successful application on colored images using $FuzEnC_{2D}$ we developed other entropy measures based on different concepts for analyzing a colored image. We limited our study for trichromatic color space images. In what follows we study $FuzEnC_{2D}$, $FuzEnV_{2D}$, and $FuzEnM_{2D}$ applied to images of several color spaces.

$FuzEnC_{2D}$'s algorithm is the same as that one tested in the previous section. However we enhanced its computation speed (using the MATLAB parallel computing toolbox) and added images' normalization for all the studied texture images.

To validate the proposed colored bidimensional entropy measures, we studied their sensitivity to different parameters values. We also applied the algorithms to images with different degrees of randomness and colored Brodatz dataset [33]. The images were normalized by subtracting their mean and dividing by their standard deviation before processing and all the tests were performed using MATLAB.

In addition to the most common trichromatic color space RGB (Red, Green, Blue) we transform the studied texture images into two other color spaces [161]: HSV (Hue and Saturation: chrominance, Value: intensity) and YUV (Y: luminance, U and V: chrominance) to investigate the effect of color space transformations on $FuzEnC_{2D}$ and $FuzEnV_{2D}$ outcomes. By the latter, we choose one of each of the most widely used color spaces families: the primary color spaces (RGB), the perceptual color spaces (HSV), and the luminance–chrominance color spaces (YUV). In RGB color space, the intensity and color are combined to give us the final display, whereas for HSV and YUV color spaces intensity and color are separated.

4.7.1 Sensitivity to initial parameters

To study the sensitivity of our proposed measures, $FuzEnC_{2D}$, $FuzEnV_{2D}$, and $FuzEnM_{2D}$ to different embedding dimensions \mathbf{m} and tolerance levels r , we evaluated 100×100 pixels of a colored Brodatz image (Figure 4.35 (f)) using different parameters choices.

- For $FuzEnC_{2D}$, the embedding dimension \mathbf{m} was taken as 1, 2, 3, 4, and 5, and the tolerance level r from 0.06 up to 0.48 (step 0.06). The results are displayed in Figure 4.29.
- For $FuzEnV_{2D}$, the embedding dimension \mathbf{m} was taken as 1 and 2, since the maximum possible cube volume for $(m + 1)$ -length cubes is $3 \times 3 \times 3$ pixels (the 3 color channels). The results are displayed in Figure 4.30.
- For $FuzEnM_{2D}$, the embedding dimension \mathbf{m} was taken as 1, 2, 3, 4, and 5, and the tolerance level r from 0.06 up to 0.48 (step 0.06). The results are displayed in Figure 4.31.

We observe that $FuzEnC_{2D}$, $FuzEnV_{2D}$, and $FuzEnM_{2D}$ remain defined for different chosen initial parameters. Also the algorithms show low variability upon changes in r and \mathbf{m} . This proves their low sensitivity to r and \mathbf{m} , allowing a certain degree of freedom in our choice of initial parameters without restrictions.

4.7.2 Detecting colored image irregularity

$MIX_{2D}(p)$ [19] is a family of images of stochastic processes that are moderated by the probability of irregularity, p , see section 4.2.1. We used $MIX_{2D}(p)$ for the single-channel approach, and $MIX_{3D}(p)$, our proposed volumetric extension for $MIX_{2D}(p)$ [27], for the multi-channel approach.

We generated 256×256 pixels $MIX_{2D}(p)$ in three channels and $256 \times 256 \times 3$ pixels $MIX_{3D}(p)$ images and analyzed them by single channel ($FuzEnC_{2D}$) and multi-channel approaches ($FuzEnV_{2D}$ and $FuzEnM_{2D}$), respectively.

- $FuzEnC_{2D}$: we set $r = 0.15$, $\mathbf{m} = 1, 2, 3, 4, 5$, and $p = 0$ to 1 with a step of 0.1, and repeated the calculation for 10 images each. The results are depicted in Figure 4.32.
- $FuzEnV_{2D}$: we set $r = 0.15$, $\mathbf{m} = 1$ and 2 (as the maximum possible cube volume for $m + 1$ could only be $3 \times 3 \times 3$ pixels), $p = 0$ to 1 with a step of 0.1, and repeated

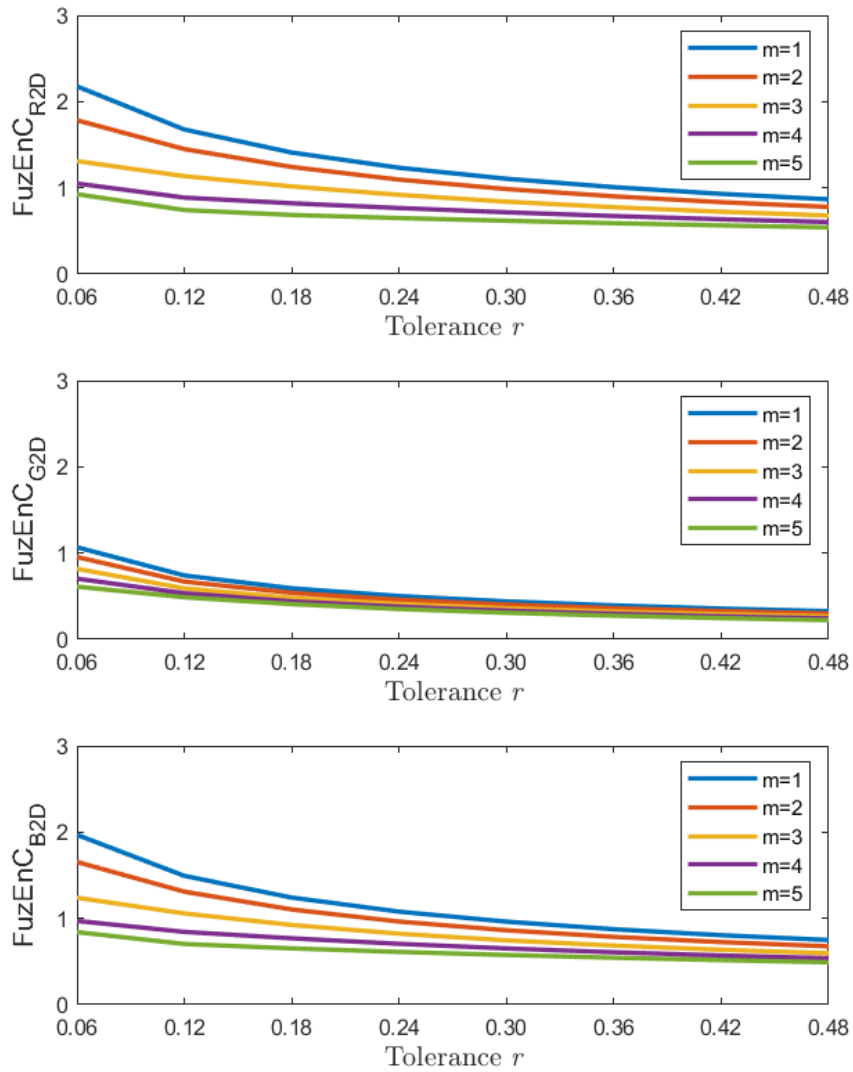


Figure 4.29 – $FuzEnC_{2D}$ results for the red, green, and blue channels (left to right) of the colored Brodatz image, Figure 4.35 (f), with varying r and \mathbf{m} .

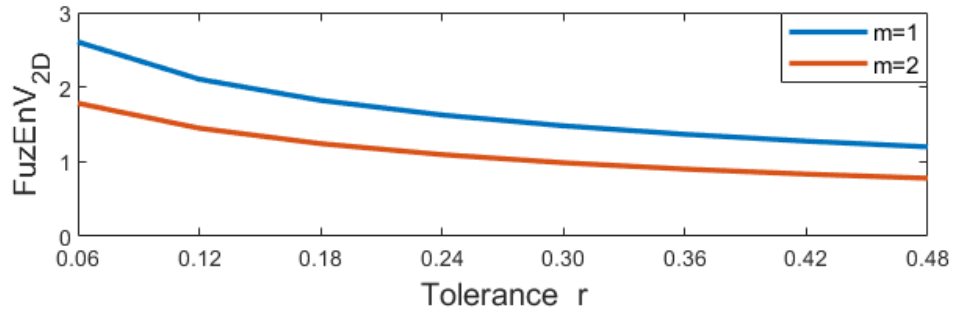


Figure 4.30 – $FuzEnV_{2D}$ results with varying r and m of the colored Brodatz image, Figure 4.35 (f).

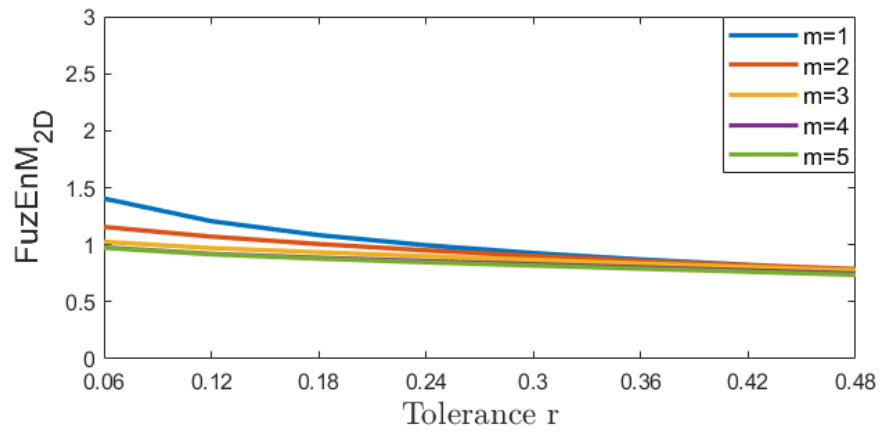


Figure 4.31 – $FuzEnM_{2D}$ results with varying r and m of the colored Brodatz image, Figure 4.35 (f).

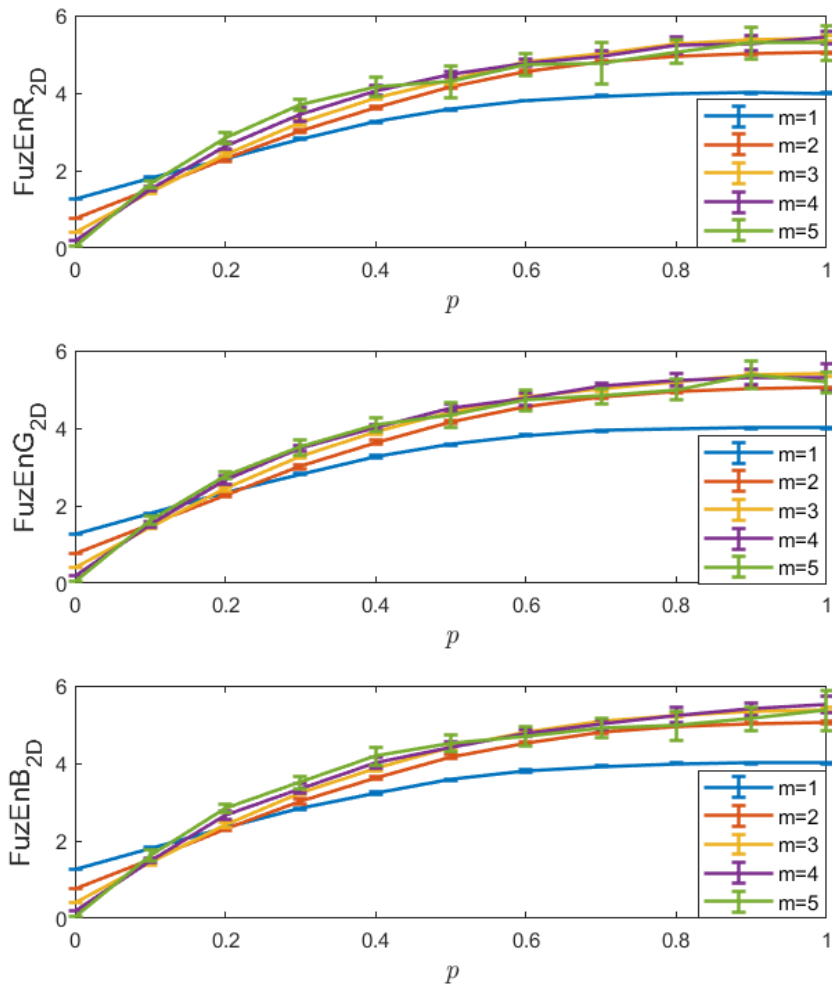


Figure 4.32 – $FuzEnC_{2D}$ mean and standard deviation for $MIX_{2D}(p)$ images with 10 repetitions.

the calculation for 10 images each. The results are depicted in Figure 4.33.

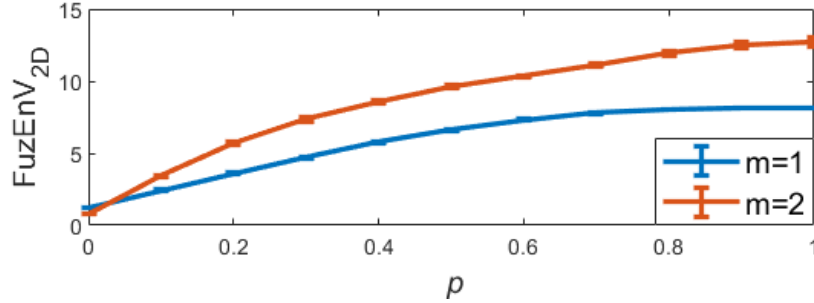


Figure 4.33 – $FuzEnV_{2D}$ mean and standard deviation for $MIX_{3D}(p)$ images with 10 repetitions.

- $FuzEnM_{2D}$: we set $r = 0.15$, $\mathbf{m} = 1, 2, 3,$ and 4 , and $p = 0$ to 1 with a step of 0.1 , and repeated the calculation for 10 images each. The results are depicted in Figure 4.34.

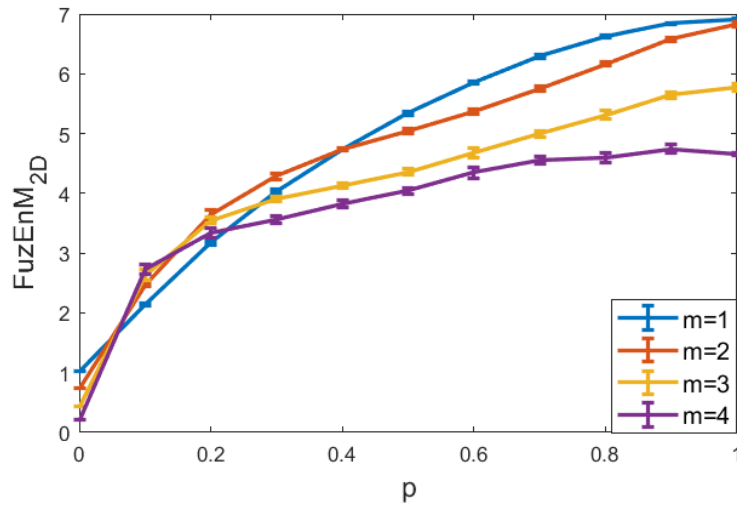


Figure 4.34 – $FuzEnM_{2D}$ mean and standard deviation for $MIX_{3D}(p)$ images with 10 repetitions.

The results show that, the single, multi-channel, and the modified approaches, lead to increasing entropy values with increasing irregularity degree, p . This illustrates their ability to properly quantify increasing irregularity degrees and their consistency upon repetition.

4.7.3 Studying texture images

For texture validation tests we used the very well known Colored Brodatz Texture (CBT) [162] images, see Figure 4.35. CBT presents colored textures with different degrees

of visible irregularity. We can notice that, for example, the CBT images (a), (b), and (e) show more regularity and periodic repetitive patterns than (c), (f), and (i).

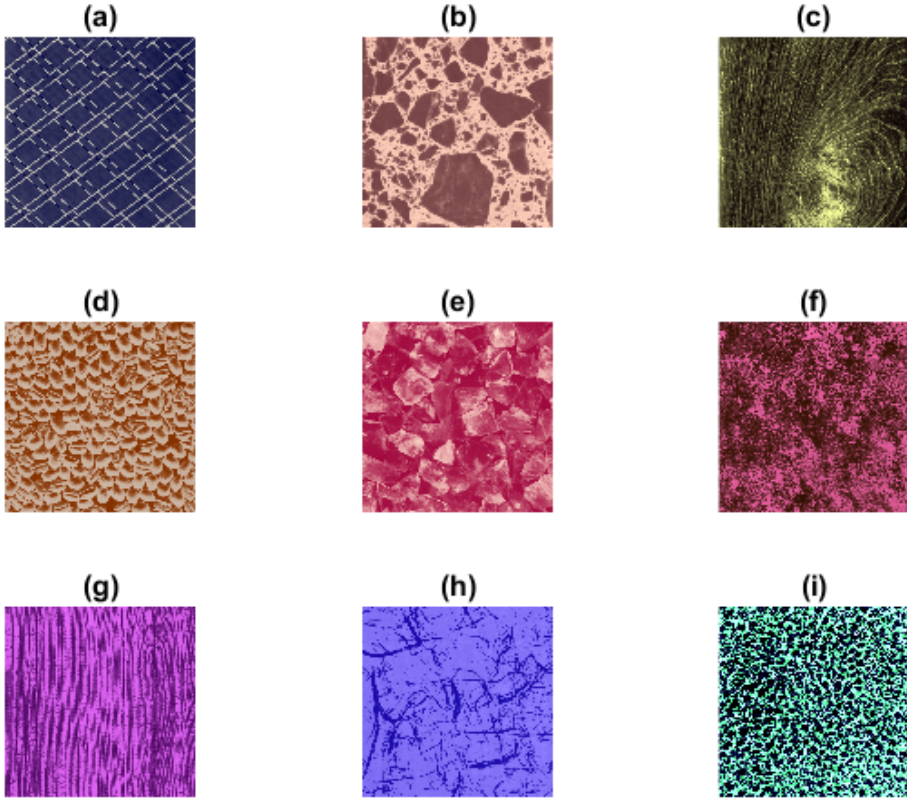


Figure 4.35 – Colored Brodatz texture images, CBT.

The nine CBT [33, 162] images of 640×640 pixels, see Figure 4.35, were split into 144 sub-images of sizes 50×50 pixels. $FuzEnC_{2D}$, $FuzEnV_{2D}$, and $FuzEnM_{2D}$ were calculated for these sub-images and for a 300×300 pixels region from each corresponding original CBT image. The parameters r and \mathbf{m} were set to 0.15 and 2, respectively. The results are depicted in Figures 4.36, 4.37, and 4.38. We observe that, especially for the RGB color space, most of the $FuzEnC_{2D}$, $FuzEnV_{2D}$, and $FuzEnM_{2D}$ averages of the sub-images overlap with or are very similar to the value of their corresponding image's 300×300 pixels region. Moreover, we notice their differentiation ability between different CBT images. In the HSV and YUV color spaces, the multi-channel approaches (Figures 4.37 and 4.38) overperforms $FuzEnC_{2D}$ (Figure 4.36) in differentiating the CBT images. We can also observe that for the RGB color space the CBT images that are per-

ceived visually to be of higher irregularity, Figure 4.35 (c), (f), and (g), obtained higher entropy values than the others, whereas those that appear to be of periodic well defined repetitive patterns, Figure 4.35 (a), (b), and (e), resulted in lower entropy values for the three measures $FuzEnC_{2D}$, $FuzEnV_{2D}$, and $FuzEnM_{2D}$. This is in accordance with the literature of entropy measures and information theory concept applied to gray level texture images [19, 20, 42, 43, 26, 28].

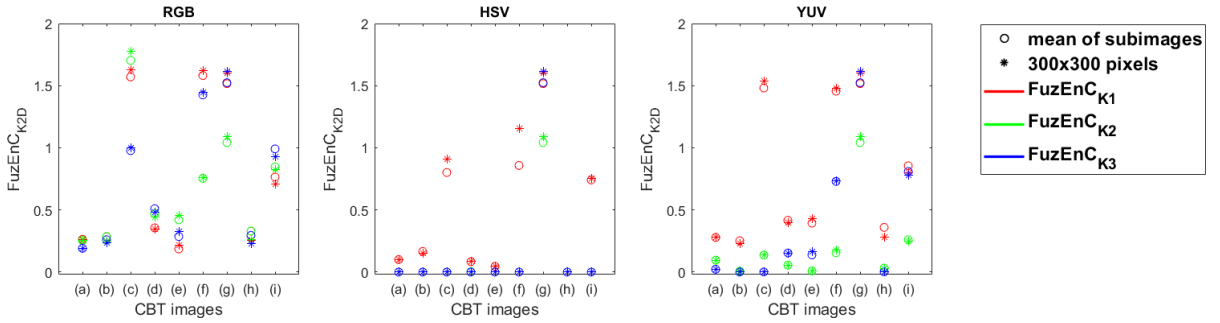


Figure 4.36 – $FuzEnC_{2D}$ results for the 144 sub-images and 300×300 pixels of the CBT in the three color spaces: RGB, HSV, and YUV, with $K1$, $K2$, and $K3$ being the first, second, and third channel, respectively. The mean of the 144 subimages is displayed as a "o" sign and the value for the 300×300 pixels is displayed as "*".

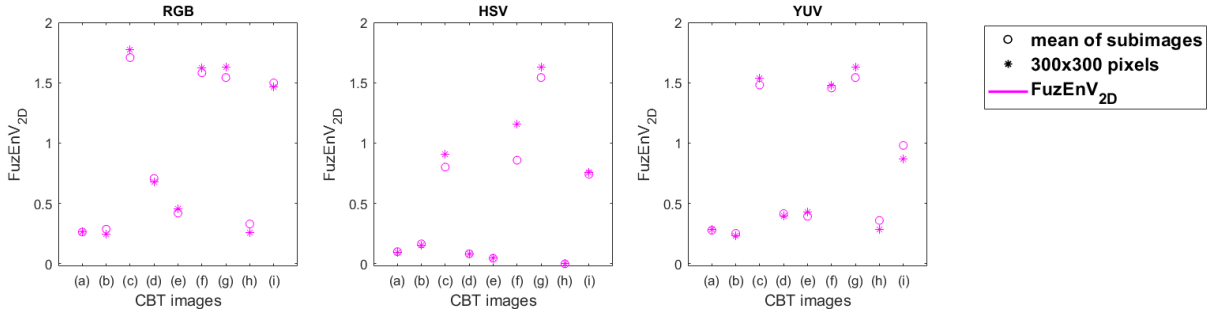


Figure 4.37 – $FuzEnV_{2D}$ results for the 144 sub-images and 300×300 pixels of the CBT in the three color spaces: RGB, HSV, and YUV. The mean of the 144 subimages is displayed as a "o" sign and the value for the 300×300 pixels is displayed as "*".

4.7.4 Computation cost of $FuzEnC_{2D}$, $FuzEnV_{2D}$, and $FuzEnM_{2D}$

For comparing the computation cost for the three developed measures for colored textures we employed 100×100 pixels colored Brodatz image (D12) and repeated the

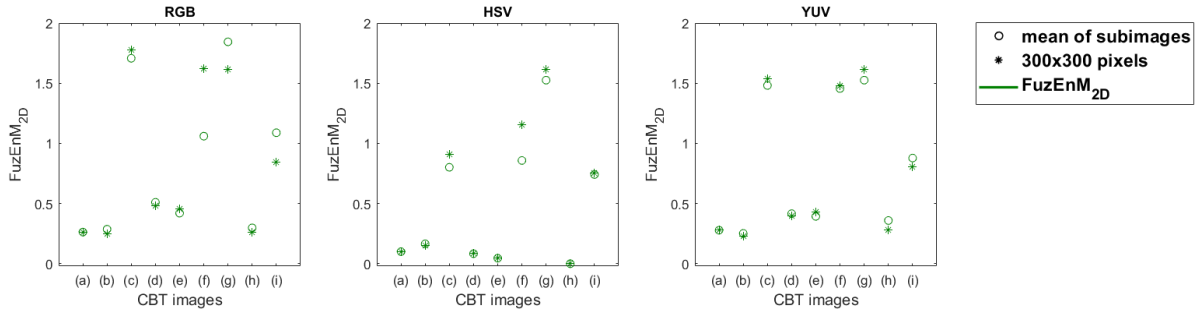


Figure 4.38 – $FuzEnM_{2D}$ results for the 144 sub-images and 300×300 pixels of the CBT in the three color spaces: RGB, HSV, and YUV. The mean of the 144 subimages is displayed as a "o" sign and the value for the 300×300 pixels is displayed as "*".

calculations for ten times. The parameters were set as $r = 0.15$ and $\mathbf{m} = 2$. The results are displayed in Table 4.11. The simulations were carried out by Windows 10 laptop equipped with 8-GB RAM and Intel(R) Core(TM) i7-6500U CPU processor using MATLAB R2020a.

Table 4.11 – Mean and standard deviation of the computation time for $FuzEnC_{2D}$, $FuzEnV_{2D}$, and $FuzEnM_{2D}$ for a 100×100 pixels colored Brodatz image.

| | $FuzEnC_{2D}$ | $FuzEnV_{2D}$ | $FuzEnM_{2D}$ |
|----------------------|-------------------|------------------|------------------|
| Computation time (s) | 48.59 ± 89.66 | 28.65 ± 0.52 | 21.76 ± 0.68 |

$FuzEnM_{2D}$ showed the lowest computational cost. This indicates that it will be more suitable for large images, more particularly with the fact that medical images are often of a large size.

4.8 $FuzEn_{3D}$ and MSF_{3D} Validation Tests

The behavior of our proposed 3D entropy measures is validated using several tests such as: sensitivity to parameters test, ability to identify several degrees of irregularity, and pattern-based volumes quantification among others.

4.8.1 Sensitivity to variation in parameters r and \mathbf{m}

For testing the sensitivity of $FuzEn_{3D}$ to r and \mathbf{m} , we performed $FuzEn_{3D}$ calculations for white noise cubes with a varying tolerance level r between 0.06 and 0.48 (step

of 0.06) using $\mathbf{m}= 1, 2,$ and $3.$

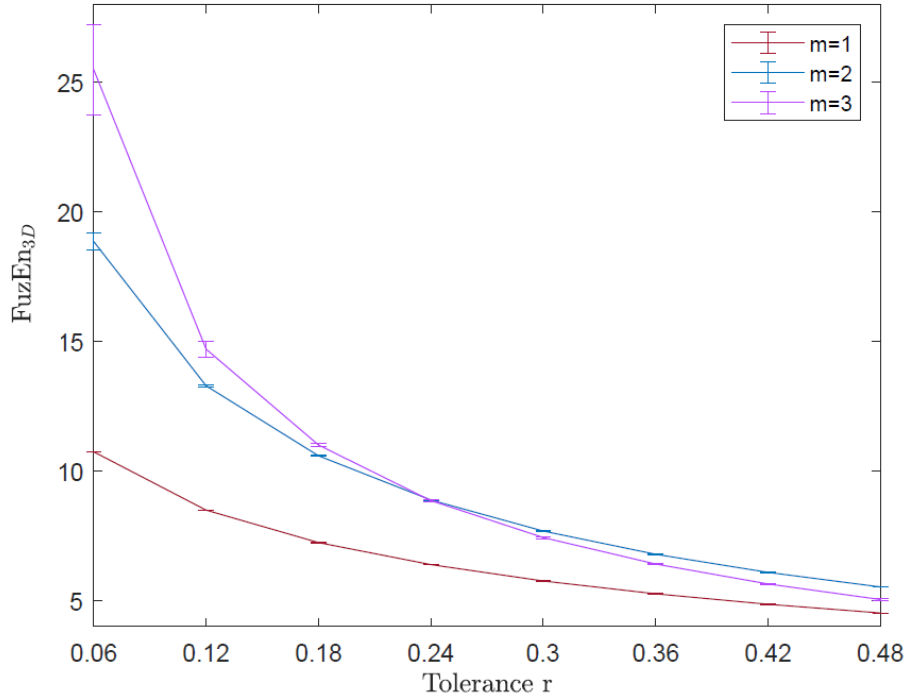


Figure 4.39 – $FuzEn_{3D}$ for white noise cubes with a varying tolerance level r between 0.06 and 0.48 using $\mathbf{m}= 1, 2,$ and $3.$

The results in Figure 4.39 show the consistency of $FuzEn_{3D}$ for varying r and \mathbf{m} values and the low standard deviation of the results upon repetition. These results are similar to those obtained by the uni- and bidimensional fuzzy entropy, providing low limitations for the possible choices in the initial parameters.

4.8.2 $FuzEn_{3D}$ for $MIX_{3D}(p)$ volumes

Ten cubes of $MIX_{3D}(p)$ volumes for each p value were generated and analyzed by $FuzEn_{3D}$. The parameters were set as $r = 0.2$, $n = 2$, p increased from 0 till 1 with a step of 0.1 and \mathbf{m} varied as $= 1, 2,$ and $3.$ The results illustrated in Figure 4.40 show the ability of $FuzEn_{3D}$ to properly quantify increasing irregularity degrees. $FuzEn_{3D}$ values increased gradually with the increase in p value from 0 to 1. The results were consistent for the three \mathbf{m} values which shows the low sensitivity to the choice of \mathbf{m} . We also note the low standard deviation upon repetition. This is an important characteristic

of the developed methods because it shows the ability of repeatability for the obtained results range. This is achieved even when dealing with random textures such as $MIX_{3D}(p)$ processes and illustrates the method's consistency.

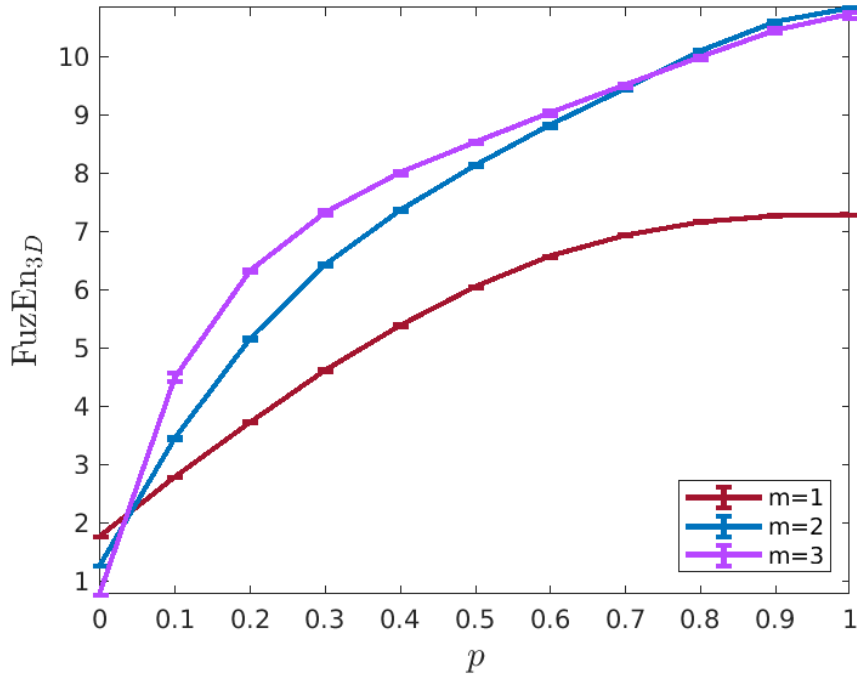


Figure 4.40 – Mean and standard deviation of $FuzEn_{3D}$ for ten repetitions applied to $MIX_{3D}(p)$ using $\mathbf{m}=1, 2,$ and 3 .

For quantifying irregularity of different degrees the uni-, bi-, and tri-dimensional entropy measures illustrate a similar behavior [42, 26, 28, 27]. For the upcoming test the parameters are chosen as $\mathbf{m}=3$ and $r=0.2$ within the range verified in our validation tests and that recommended by some previous publications.

4.8.3 Shuffling

Theoretically, shuffling increases the irregularity of data. Thus entropy values are expected to increase upon shuffling. We tested the change in entropy calculations for ten $MIX_{3D}(p)$ cubes and their ten shuffled versions for each p . The results are plotted as the mean and standard deviation of the results obtained. The parameters were defined as $\mathbf{m}=3, r=0.2, n=2$ and p increased from 0 till 1 with a step of 0.1.

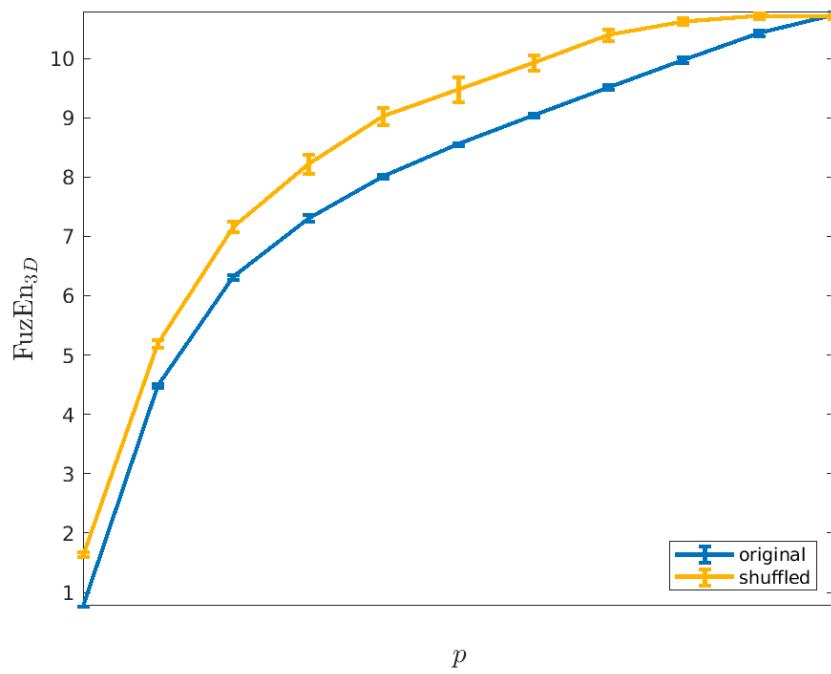


Figure 4.41 – $FuzEn_{3D}$ for $MIX_{3D}(p)$ of ten original and ten shuffled volumes for each p .

The results in Figure 4.41 are in accordance with the theoretical assumption where all the shuffled cubes show higher entropy values than the original $MIX_{3D}(p)$ cubes. The results are also similar to those obtained with $FuzEn_{2D}$ and $DistrEn_{2D}$ [20, 28].

4.8.4 Pattern-based volumes

Similar to the test performed by [157], we generated six pattern-based cubes to test the differentiation ability of $FuzEn_{3D}$ to different textural/pattern behaviors. The cubes were displayed previously in Figure 4.8. The results are presented in Table 4.12.

Table 4.12 – $FuzEn_{3D}$ results for pattern-based volumes.

| Cubes | Cube 1 | Cube 2 | Cube 3 | Cube 4 | Cube 5 | Cube 6 |
|--------------|--------|--------|--------|--------|---------|---------|
| $FuzEn_{3D}$ | 0.0000 | 0.0443 | 0.0000 | 0.1404 | 10.1504 | 26.6905 |

As we can observe, $FuzEn_{3D}$ illustrates a proper evaluation for the cubes' irregularity degree in accordance with our visual interpretation and the theoretical assumption of the irregularity order. As indicated by the cubes' patterns, cube 1 till 4 show very regular patterns and consecutive alteration between white and black pixels for cubes 2, 3, and 4. This justifies the very low entropy values in the first 4 cubes. To be more precise, cube 2 of half black and half white pixels, reflects a higher entropy value than that of the black cube however a lower value than that of the diagonal striped cube. This agrees with the fact that the black stripes cube is more irregular than cube 2. For cubes 1 and 3 the zero values reflect the high predictably and regularity of the aforementioned cube patterns. This could be also justified by the distance function that is always constant no matter which cubes we consider or \mathbf{m} embedding dimension. Now for cubes 5 and 6, $FuzEn_{3D}$ shows a proper assessment for their order of irregularity. As we can observe the cube 5 (Gaussian distribution) shows a much higher entropy value than the totally regular volumetric patterns. However the most irregular among them, cube 6, uniform random distribution, illustrates the highest entropy value.

In other words, periodic repetitive patterns reflect a low entropy value *i.e.* low irregularity (highly expected behavior), whereas more random textural behavior reflects higher entropy values (low predictability). The latter is shown in the $FuzEn_{3D}$ results proving its ability to gradually quantify the volumes' irregularity degrees.

4.8.5 MSF_{3D} for noise volumes

To verify the consistency of MSF_{3D} on the multiscale level, we study the evaluation of $FuzEn_{3D}$ for the color noise cubes over several scale factors; *i.e.* MSF_{3D} for the colored noise cubes. We employ ten noise cubes of $50 \times 50 \times 50$ voxels with different power spectra ($1/f^\beta$): white, pink, brown, and blue noise cubes. The initial parameters are set as $\mathbf{m}=3$, $r=0.2$, $n=2$, and $\tau_{max}=10$.

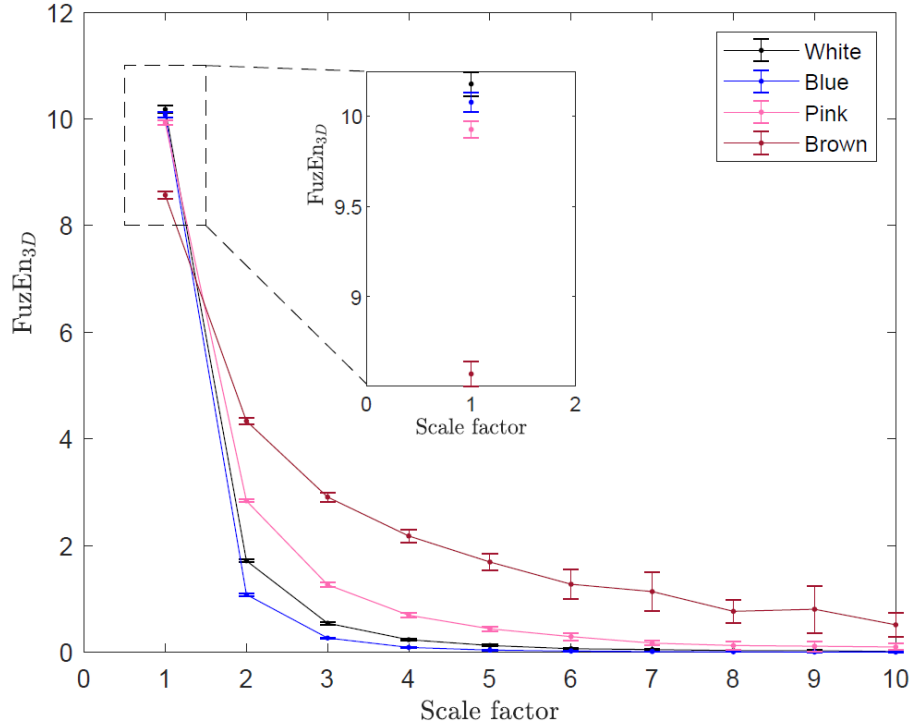


Figure 4.42 – MSF_{3D} for ten noise cubes with different power spectra ($1/f^\beta$): white, pink, brown, and blue noise.

As illustrated previously, white noise is of highly irregular nature. However when studied over several scale factors it has a low complexity. Then comes the blue noise that is less irregular than white noise but it also has low complexity over several scale factors (when down-sampled). On the other hand, pink and brown noise types are of long term correlations, where they show lower irregularity than white and blue noises but they possess a higher complexity. This is illustrated by their relatively higher entropy values over several scale factors.

In agreement with the theoretical explanation and the results of other uni- and bidi-

mensional entropy measures, MSF_{3D} shows an ability to properly evaluate the actual irregularity and complexity of the studied noise volumes. The results are depicted in Figure 4.42. The results of scale factor $\tau=1$ are magnified. They illustrate the proper order in irregularity for the evaluated noise volumes.

The results are in accordance with the uni- and bidimensional entropy measures' behavior with noise data [27, 19, 88, 91, 26].

4.9 Conclusion

In this chapter we presented the validation tests for the developed entropy measures. They illustrate low sensitivity to change in parameters, consistency upon repetition, and promising results with the validation tests that were designed for each specific measure.

As a summary, we compared the unidimensional $FuzEn_{1D}$ measure to the herein proposed bidimensional version $FuzEn_{2D}$. $FuzEn_{2D}$ forms a basic measure for the methods that are proposed afterwards. Consequently, thorough validation exams were performed to validate its behavior at first and compare it with other uni- and bidimensional entropy measures. Moreover, we employed some verification tests for the multiscale approach MSF_{2D} that analyzes texture images over several scale factors. After the successful application of $FuzEn_{2D}$ on gray scale images, we upgraded the fuzzy entropy concept to deal with colored images through three different approaches to handle trichromatic images. The validation tests are also promising and shows good potential for application on colored image textures

Afterwards, we utilized some validation tests for the tridimensional entropy measures in their single and multiple scale approach. $FuzEn_{3D}$ shows low sensitivity to change in parameters, consistency upon repetition, proper quantification for the volumes' irregularity, and promising multiscale behavior in the assessment of noise volumes.

MEDICAL APPLICATIONS AND DISCUSSION

5.1 Introduction

In this chapter we present our findings on medical images and discuss them. The results are obtained for bidimensional medical images (dermoscopic images) and tridimensional scans (HRCT and MRI). First, we start with the PXE dermoscopic images in gray scale and colored space which were evaluated with MSF_{2D} and colored fuzzy entropy measures, respectively. Then, we present our findings on dermoscopic melanoma and melanocytic nevi images also in gray scale and colored spaces. In addition, for the bidimensional applications, we perform a study for microcirculatory assessment using our proposed $FuzEnC_{2D}$. Finally, we integrate the bidimensional concept in the volumetric application to study the scans of HRCT images for COPD patients using $pMFuzEn_{3D}$.

After that, for the 3D applications, we present the results obtained using $MFE_{n_{3D}}$ on HRCT images for IPF patients and on MRI images for uterine fibroma after uterine artery embolization. Finally, we will present our very recent findings on COVID-19 patients CT scans.

5.2 Bidimensional Entropy for PXE Dermoscopic Images

A bidimensional entropy method estimates the irregularity of an image or texture based on repetitions of its patterns. Consequently and based on the fact that the primary PXE manifestation is by the appearance of papules that show some patterns in the texture of dermoscopic images, we propose to analyze those dermoscopic images using the bidimensional entropy measures. Note that in the PXE patients' skin dermoscopic images,

the changed textural behavior cannot be always objectively identified. This fact makes a computer-based image analysis technique of a greater importance.

As mentioned previously, bidimensional entropy measures evaluate irregularity within the studied images and have the ability to recognize textures with different degrees of irregularity. Thus, we analyze PXE dermoscopic images using $FuzEn_{2D}$ and compare our results to those of the well-known $SampEn_{2D}$. The analysis is performed not only at the first scale factor, but also over several scale factors to deal with their high and low frequency components and uncover the in depth information and assess the actual complexity of the aforementioned dermoscopic images using MSF_{2D} and MSE_{2D} presented in section 5.2.1. Then, we analyze those dermoscopic images as colored using $FuzEnC_{2D}$, $FuzEnV_{2D}$, and $FuzEnM_{2D}$ to reveal the possible important information in the color of those PXE images presented in section 5.2.2.

We studied the dermoscopic images for 15 PXE patients from a reference center for PXE in the department of dermatology of Angers Hospital, France. The diagnosis of PXE was based on a combination of established criteria for indisputable PXE (clinically suggestive skin lesions, angioid streaks on funduscopy, histological demonstration of fragmented and calcified elastic fibers on skin biopsy) as well as ABCC6 gene mutations. The images were taken using FotoFinder bodystudio ATBM for total body mapping and dermoscopy, see Figure 5.1. Please note that such a number of subjects is noticeable for this rare disease. Before images acquisition, the patients signed written assents and the study was performed in agreement with the Declaration of Helsinki, (CB 2009-01 and # of ClinicalTrials.gov: NCT01446380).

A dermoscopic image from the neck showing papules and a dermoscopic image from a normal skin zone (ventral zone) were taken from each of the 15 patients. Examples of two patients' dermoscopic images for healthy skin regions and neck regions showing papules are displayed in Figure 5.2.

5.2.1 Gray scale dermoscopic images

After converting the 30 images obtained to gray scale, we normalized them by subtracting their mean and dividing the result by the standard deviation. A random region of 489×490 pixels from the recorded dermoscopic images was studied using both MSF_{2D} and MSE_{2D} .

The results for PXE dermoscopic images are depicted in Figure 5.3. To evaluate the performance of MSF_{2D} vs. MSE_{2D} in discriminating the diseased from healthy groups,



Figure 5.1 – FotoFinder bodystudio ATBM for total body mapping and dermoscopy. Adapted from [163].

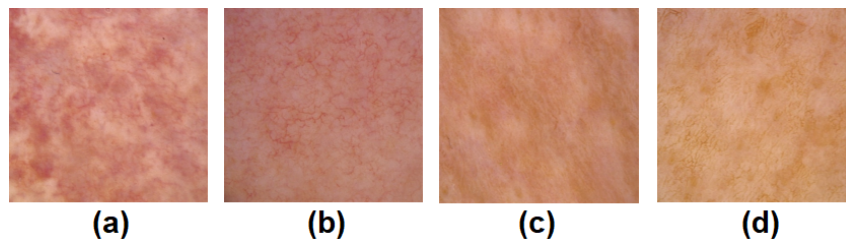


Figure 5.2 – Dermoscopic images for: (a) and (c) zones with papules, (b) and (d) normal zones.

we considered their statistical significance and effect size. To test if a significant statistical difference is found between the entropy values of the two skin regions, we employed the paired t -test at each scale factor. A statistical significance was defined for corrected p -values strictly lower than 0.05. The obtained p -values were corrected for multiple comparisons over scale factors by the Bonferroni correction method. For MSE_{2D} , no statistical significance was found. However, MSF_{2D} is able to significantly discriminate the group of neck images with papules from that of normal skin images at scale factors $\tau = 1$ and $\tau = 2$. The corrected p -values, p_{cor} , were respectively 0.03 and 0.04. Moreover, a higher spread of MSE_{2D} values was observed. For the other scale factors, no significant statistical difference between the two skin regions was observed.

After verifying statistically the presence of a deterministic difference between entropy values of the two kinds of skin regions, we considered the size of this difference and evaluated the strength of our statistical claim by calculating the effect size using Cohen’s d [164, 165, 166]. Cohen’s d evaluates how different two groups are (herein, entropy values for healthy zones compared to those with papules at each τ) [164]. The higher the d value is, the larger the difference or effect size will be. Table 5.1 explains the significance of the d values [164, 167].

Table 5.1 – Interpretation of the Cohen’s d values [164, 167].

| Effect’s size | Very small | Small | Medium | Large | Very large | Huge |
|---------------|------------|-------|--------|-------|------------|------|
| d | 0.01 | 0.20 | 0.50 | 0.80 | 1.20 | 2.0 |

The d values for MSF_{2D} and MSE_{2D} for $\tau = 1, 2, 3,$ and 4 are displayed in Table 5.2. It is found that the d values for MSF_{2D} represent a “Large” size of difference between the compared groups (especially for the above verified $\tau = 1$ and 2). However, the d values for MSE_{2D} represent “Small” or “Medium” effect sizes.

Table 5.2 – Cohen’s d values for MSF_{2D} and MSE_{2D} at $\tau = 1, 2, 3,$ and 4 for the normal skin regions vs. the regions with papules in pseudoxanthoma elasticum images.

| τ | 1 | 2 | 3 | 4 |
|-----------------------|-------|-------|-------|-------|
| d for $FuzEn_{2D}$ | 0.977 | 0.952 | 0.777 | 0.508 |
| d for $SampEn_{2D}$ | 0.226 | 0.669 | 0.773 | 0.531 |

On the whole, the results show that MSF_{2D} has a statistically significant ability to differentiate the two studied groups at the first 2 scale factors with noticeable large effect size values suggesting the advantage of our developed MSF_{2D} over MSE_{2D} . Therefore,

MSF_{2D} could form a useful tool to help clinicians in the early diagnosis of PXE accurately (using the results for $\tau = 1$ and 2). Furthermore, normal skin regions show higher complexity compared to the regions with papules because of the higher over all $FuzEn_{2D}$ values over several scale factors, see Figure 5.3. This is in agreement with the literature in which healthy body systems are expected to have higher complexity than diseased systems [91, 88].

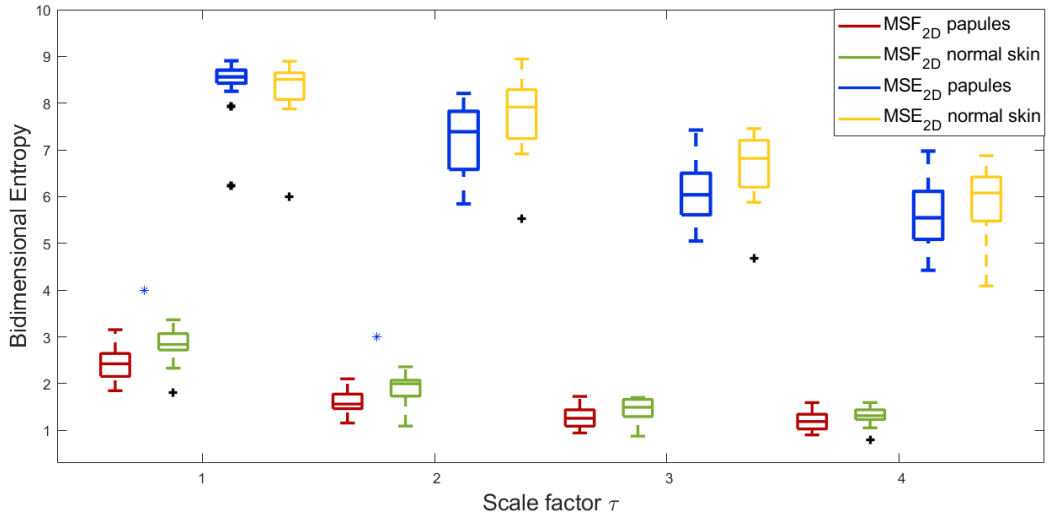


Figure 5.3 – For scale factors $\tau= 1$ till 4: MSF_{2D} for the zones with papules (dark red) and normal skin zones (green), and MSE_{2D} for zones with papules (blue) and normal skin zones (yellow). The * signifies the presence of statistically significant difference between the two groups.

5.2.2 Colored dermoscopic images

After the successful findings on gray scale images using MSF_{2D} we employ the colored entropy algorithms, $FuzEnC_{2D}$, $FuzEnV_{2D}$, and $FuzEnM_{2D}$, to reveal the information hidden within the color components of our studied PXE images.

We employed the same database as the one mentioned in the previous section and the same region of interest, ROI. The images were obtained as colored and processed using the single- and multi-channel bidimensional colored fuzzy entropy measures. The parameters were set as $n=2$, $\mathbf{m}=2$, and $r=0.15$.

To validate the results obtained, we performed the Wilcoxon signed rank test for paired samples (because both dermoscopic images are from the same patients for every

subject) where a p -value < 0.05 shows a statistically validated ability for a method to distinguish the two sample groups. We obtained statistical significance in differentiating the healthy from the papules skin zone for the Blue channel using $FuzEnC_{2D}$ with $p = 0.02$, see Figure 5.4. Furthermore, with $FuzEnV_{2D}$ we obtained $p = 0.005$, see Figure 5.5. $FuzEnM_{2D}$ showed $p=0.05$, which cannot be considered as statistically significant, however, we display the results in Figure 5.6.

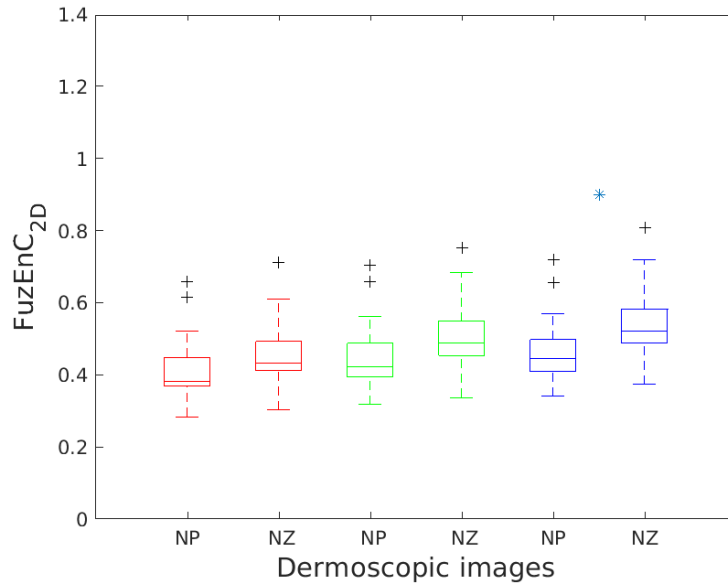


Figure 5.4 – $FuzEnC_{2D}$ for 30 colored dermoscopic images of a region showing PXE papules (NP: neck with papules) and healthy skin region (NZ: normal zone). The colors red, green, and blue represent the R, G, and B channels, respectively. Statistical significance is obtained for the blue channel ($p=0.02$). The * signifies the presence of statistically significant difference between the two groups.

Moreover, we calculate the Cohen's d value for evaluating the actual effect size of the statistically significant difference. We obtain Large effect size values, $d = 0.71$ and $d = 0.81$ for $FuzEnC_{B2D}$ and $FuzEnV_{2D}$, respectively. This also confirms our statistical claim and better validates our results for the Blue channel using $FuzEnC_{2D}$ and for the whole images using $FuzEnV_{2D}$ in identifying healthy from PXE affected skin zones.

5.2.3 Conclusion

PXE is a rare disease that causes several cutaneous, cardiovascular, and ophthalmic complications. Thus, the earlier the diagnosis is, the better the monitoring and preven-

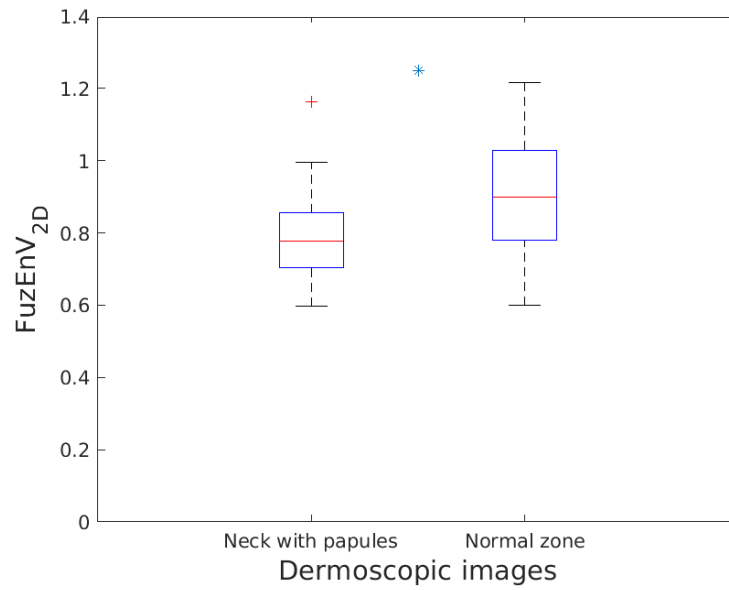


Figure 5.5 – $FuzEnV_{2D}$ for 30 dermoscopic images of a region showing PXE papules (neck with papules) and a healthy skin region (normal zone). Statistical significance is obtained with $p=0.005$. The * signifies the presence of statistically significant difference between the two groups.

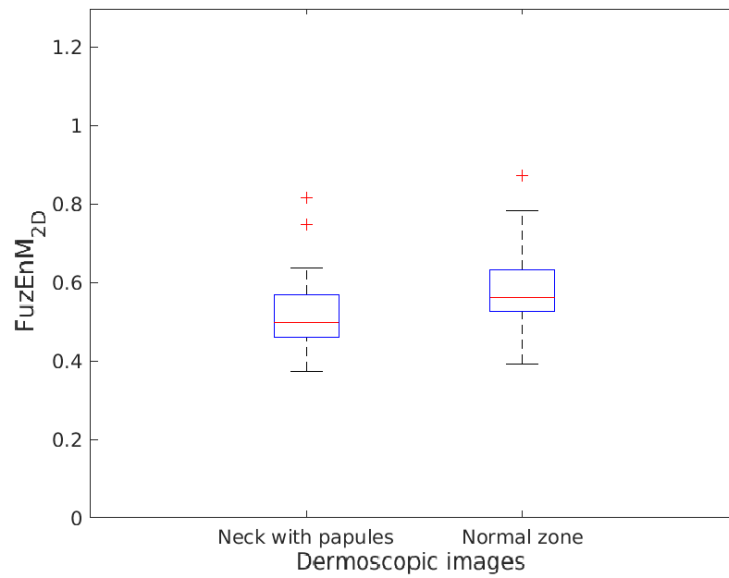


Figure 5.6 – $FuzEnM_{2D}$ for 30 dermoscopic images of a region showing PXE papules (neck with papules) and a healthy skin region (normal zone). $FuzEnM_{2D}$ showed $p=0.05$.

tion will be. PXE establishes a certain textural behavior that cannot be always identified visually even through dermoscopy. This creates an essential need for developing an objective technique that can identify the presence of this disease in its early stages (the initial cutaneous symptoms). The primary fuzzy entropy results seem to be promising in distinguishing a group of healthy skin images from diseased ones. In the future, it would also be interesting to use the proposed measures to track how the skin pathology evolves upon potential treatment follow up, due to the fact that there is no definite treatment for this disorder yet. This contribution would influence the research in this field and could help in its escalation.

Apart from that and before developing $FuzEn_{2D}$, we performed a brief study using $SampEn_{2D}$, but we present it in the Annex as it is less relevant herein, please see section 6.2.

5.3 Melanoma and Melanocytic Nevi

The target of the medical application of our study in this section is to differentiate the deadliest type of skin cancer, melanoma, from the benign melanocytic nevi. These two widely spread types of pigmented skin lesions are often mistaken in diagnosis and detection, especially in their early stages. Moreover, early diagnosis and excision could vastly increase the survival rate [122, 123, 124].

To achieve our goal, we process dermoscopic images of melanoma (see section 1.6.4) and melanocytic nevi. For the application to dermoscopic images (gray scale and colored), we used samples from the “Human Against Machine with 10000 training images”, *HAM10000* [168]. The dataset is composed of dermoscopic images for pigmented lesions. It contains dermoscopic images of: melanocytic nevi, melanoma, dermatofibroma, actinic keratoses, basal cell carcinoma, and benign keratosis [168, 169]. The data collection was approved by the ethics review committee at the Medical University of Vienna and the University of Queensland. For more detailed information about the dermoscopic dataset please refer to [169].

5.3.1 Gray scale dermoscopic images

We employed 30 dermoscopic images randomly chosen from two different diagnostic categories (see examples in Figure 5.7). The studied dermoscopic images are for 15 patients with melanoma (a malignant neoplasm) and 15 patients with melanocytic nevi (a benign neoplasm). MSF_{2D} was applied to the central 430×450 pixels of those dermoscopic images. We used MSF_{2D} with parameters: $n = 2$, $\mathbf{m} = 2$, $r = 0.25$, and scale factor τ from 1 to 20.

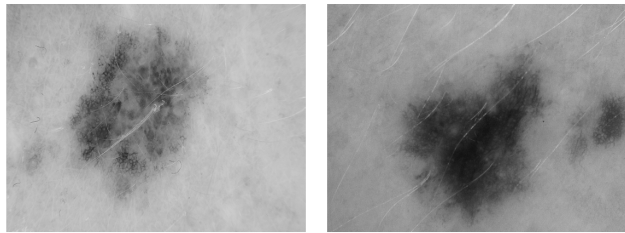


Figure 5.7 – Image of melanoma (right) and melanocytic nevi (left) in gray scale.

To study the significance of results obtained with the two groups of dermoscopic images, we performed Friedman test with Bonferroni correction and obtained statistically significant values with $p_{cor} = 0.0022, 0.0158, 0.0158, 0.0158, 0.0022, 0.0022$, for scale factors $\tau = 1, 16, 17, 18, 19, 20$, respectively. In addition, we calculated the Cohen’s d values for the for scale factors $\tau = 1, 16, 17, 18, 19, 20$, and obtained 1.21, 1.41, 1.47, 1.55, 1.63, and 1.67, respectively. The Cohen’s d values reflect “Very Large” effect size values, which validate even more our statistical results. For the reference on the Cohen’s d interpretation please see Table 5.1. Box plots for the significantly different scale factors are presented in Figure 5.8. The scale factor $\tau = 1$ shows an outlier for melanocytic nevi but still accounts for a significant statistical difference. The results illustrate the ability of MSF_{2D} to distinguish melanoma from melanocytic nevi on the specified scale factors. Thus, MSF_{2D} forms a potential diagnostic tool for helping clinicians categorizing skin dermoscopic images as benign or malignant lesions and assisting in early diagnosis.

Our findings proved $FuzEn_{2D}$ being a suitable measure for medical use on dermoscopic images through its extension, MSF_{2D} . This opens up the opportunity to employ $FuzEn_{2D}$ and MSF_{2D} on other medical images and extend this study for a larger number of subjects. Those results were presented in our publication [28].

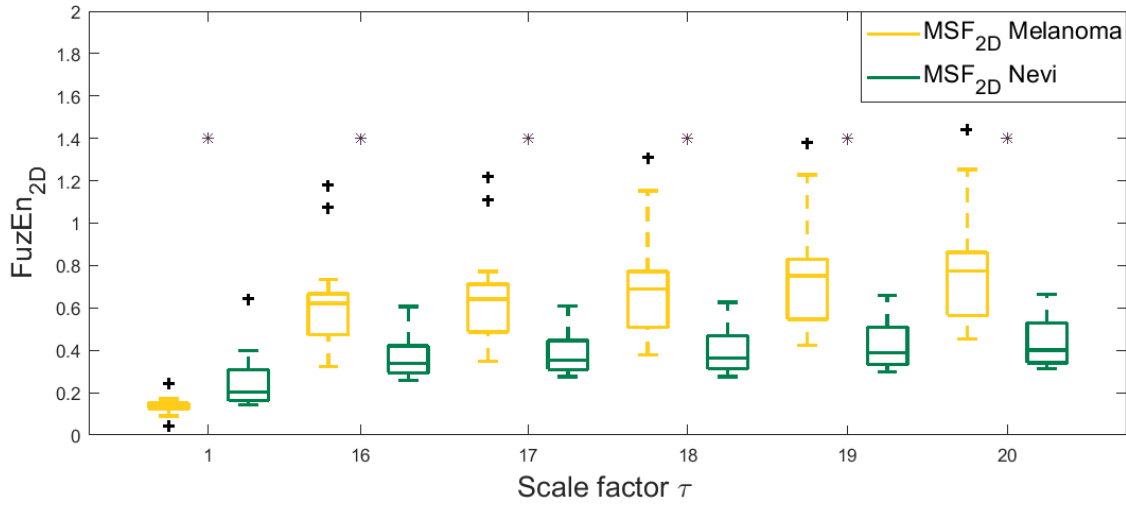


Figure 5.8 – MSF_{2D} for 15 melanoma (yellow) and 15 melanocytic nevi (green) dermoscopic images. The * signifies the presence of statistically significant differences between the two groups.

5.3.2 Colored dermoscopic images

For this application on medical images, we study the effect of different color spaces and compare our results to those obtained with gray level co-occurrence matrices [48], the probably most used texture analysis technique. We employed the co-occurrence matrices of each channel (integrative way) for comparing the results to our single-channel approach, and its extended 3D co-occurrence matrices [49] for comparing the results to our multi-channel approaches. We thus adopted the following procedure:

- 2D co-occurrence matrices were created considering 4 orientations (0° , 45° , 90° , and 135°), 4 interpixel distances (1, 2, 4, and 8), and 8 gray levels ($N_g=8$) to be compared with $FuzEnC_{2D}$.
- 3D co-occurrence matrices were created considering 13 orientations [49], 4 interpixel distances (1, 2, 4, and 8), and 8 gray levels to be compared with $FuzEnV_{2D}$ and $FuzEnM_{2D}$.

Then, we calculated the Haralick features for each co-occurrence matrix (for each orientation and distance). Finally, the average of features for all matrices was calculated to be compared with $FuzEnC_{2D}$, $FuzEnV_{2D}$, and $FuzEnM_{2D}$ values. Among the 14 features originally proposed by Haralick *et al.* [48], only six are commonly employed by researchers due to their correlation with the other eight, see Table 1.1.

We calculated $FuzEnC_{2D}$, $FuzEnV_{2D}$, and $FuzEnM_{2D}$ for 40 melanoma images and 40 melanocytic nevi images from the *HAM10000* dataset [169] in the color spaces RGB, HSV, and YUV. For choosing the region of interest (ROI) of melanoma and melanocytic nevi images, we segmented the lesion as shown in Figure 5.9. Then, the central region of 128×128 pixels was selected, see Figure 5.9 (d). By adopting this procedure, we ensured that the same number of pixels was processed (equally sized images) and that no region outside the lesion was included. The parameters r and \mathbf{m} were set to 0.15 and 2, respectively.

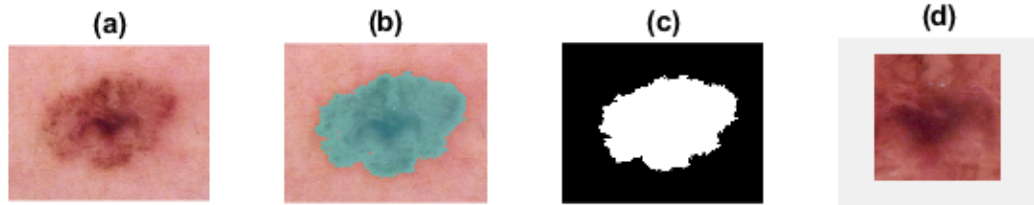


Figure 5.9 – Dermoscopic images segmentation for choosing the ROI.

To validate the statistical significance of $FuzEnC_{2D}$, $FuzEnV_{2D}$, and $FuzEnM_{2D}$ in differentiating melanoma from melanocytic nevi images, we used the Mann-Whitney U test. The resulting p -values are presented in Table 5.4. $FuzEnC_{2D}$ shows statistical significance (for $p_{cor} < 0.05$) in differentiating melanoma and melanocytic nevi for the R, G, B, H, Y, and V channels. The p values were corrected using the Bonferroni method for the 40 subjects, p_{cor} . In addition, using $FuzEnV_{2D}$ and $FuzEnM_{2D}$, melanoma and melanocytic nevi images are identified as statistically different for the 3 color spaces. In addition, we calculate the Cohen’s d to further validate our obtained statistical results, see Table 5.3. Most d values reflect “Large”, “very Large”, and “Huge” effect size (refer to Table 5.1), which validates the differentiation ability of our proposed measures.

Furthermore, we compared $FuzEnC_{2D}$ results with Haralick features from 2D co-occurrence matrices. The results show that $FuzEnC_{2D}$ obtains lower p -values than Haralick features for the G, H, Y, and U channels and none of the methods result in statistical significance for the S channel. Additionally, we compared $FuzEnV_{2D}$ and $FuzEnM_{2D}$ results with Haralick features from 3D co-occurrence matrices, see Figures 5.10 and 5.11.

Table 5.3 – Cohen’s d -values for $FuzEnC_{2D}$, $FuzEnV_{2D}$, and $FuzEnM_{2D}$ of 40 melanoma and 40 melanocytic nevi dermoscopic images in the 3 color spaces: RGB, HSV, and YUV.

| | $FuzEnC_{K1}$ | $FuzEnC_{K2}$ | $FuzEnC_{K3}$ | $FuzEnV_{2D}$ | $FuzEnM_{2D}$ |
|-----|---------------|---------------|---------------|---------------|---------------|
| RGB | 1.50 | 1.89 | 1.97 | 2.71 | 2.19 |
| HSV | 1.14 | 0.23 | 0.27 | 1.14 | 1.14 |
| YUV | 1.10 | 0.58 | 0.70 | 1.00 | 1.09 |

$FuzEnV_{2D}$ and $FuzEnM_{2D}$ clearly surpassed Haralick features as p -values obtained for the results of both entropy measure are mostly lower than those of Haralick features. Moreover, using Haralick features some results do not show statistical significance ($p < 0.05$), whereas all the three colored entropy measures show evident statistical significance in differentiating melanoma from melanocytic nevi, except in $FuzEnC_{2D}$ results in S and V channels.

Table 5.4 – Mann-Whitney u test p -values for $FuzEnC_{2D}$, $FuzEnV_{2D}$, and $FuzEnM_{2D}$ of 40 melanoma and 40 melanocytic nevi dermoscopic images in the 3 color spaces: RGB, HSV, and YUV.

| | $FuzEnC_{K1}$ | $FuzEnC_{K2}$ | $FuzEnC_{K3}$ | $FuzEnV_{2D}$ | $FuzEnM_{2D}$ |
|-----|-----------------------|------------------------|------------------------|------------------------|------------------------|
| RGB | 3.35×10^{-9} | 7.07×10^{-12} | 3.47×10^{-11} | 9.01×10^{-13} | 4.11×10^{-12} |
| HSV | 2.90×10^{-5} | 5.74×10^{-2} | 1.53×10^{-1} | 2.90×10^{-5} | 2.90×10^{-5} |
| YUV | 9.80×10^{-6} | 1.79×10^{-3} | 5.81×10^{-4} | 4.59×10^{-5} | 1.11×10^{-5} |

In addition to the p -values test, the receiver operating characteristic (ROC) and area under the ROC curve (AUROC) of the results can be used as a criterion to measure the discriminative ability of our proposed measures. Since the best results (lowest p -values) were obtained for the RGB color space, we further plot the ROC curves (using [170]) for its $FuzEnC_{2D}$, $FuzEnV_{2D}$, and $FuzEnM_{2D}$ results, see Figures 5.12, 5.13, and 5.14, respectively.

Moreover, the AUC, sensitivity, specificity, accuracy, and precision are determined for the RGB, HSV, and YUV color spaces in Tables 5.5, 5.6, and 5.7, respectively. The results show that $FuzEnC_{2D}$ has high accuracy and AUC values for R, G, B, H, Y, U, and V channels and the multichannel approaches ($FuzEnV_{2D}$ and $FuzEnM_{2D}$) for all the color spaces. For all entropy measures, the best accuracy and AUC were obtained for the RGB color space.

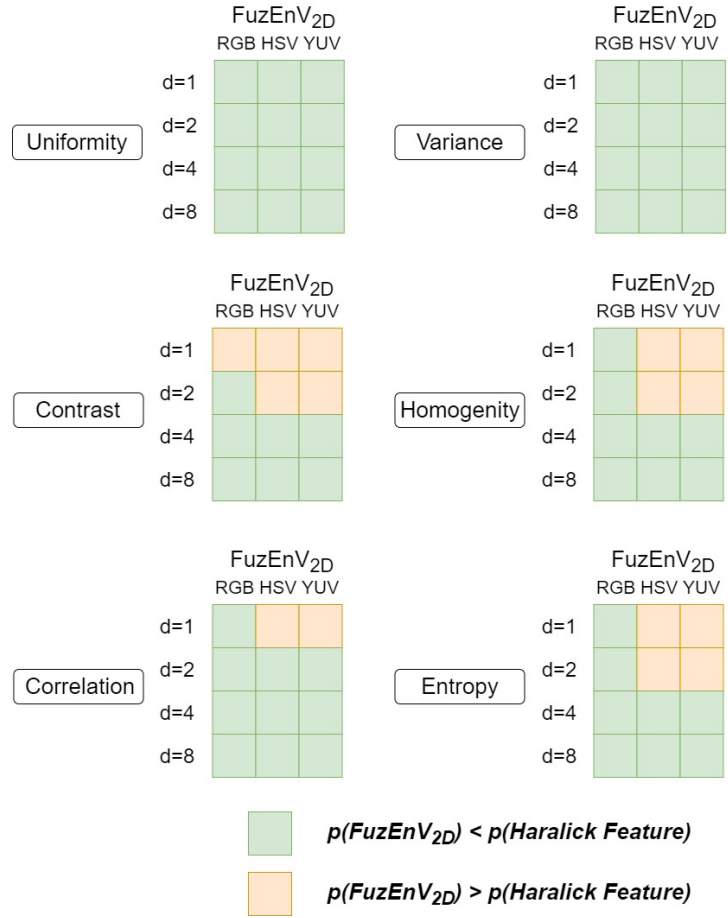


Figure 5.10 – $FuzEnV_{2D}$ and Haralick features p -values of 40 melanoma and 40 melanocytic nevi dermoscopic images in the 3 color spaces: RGB, HSV, and YUV. d represents the interpixel distances for the co-occurrence matrices.

Table 5.5 – ROC analysis for $FuzEnC_{2D}$, $FuzEnV_{2D}$, and $FuzEnM_{2D}$ results of 40 melanoma and 40 melanocytic nevi images in RGB.

| | $FuzEnC_{2D}$ | | | $FuzEnV_{2D}$ | $FuzEnM_{2D}$ |
|-------------|---------------|-------|-------|---------------|---------------|
| | U_R | U_G | U_B | U | U |
| AUC | 0.884 | 0.945 | 0.930 | 0.964 | 0.950 |
| Sensitivity | 0.825 | 0.925 | 0.900 | 0.925 | 0.925 |
| Specificity | 0.850 | 0.850 | 0.825 | 0.950 | 0.900 |
| Accuracy | 0.837 | 0.887 | 0.862 | 0.937 | 0.912 |
| Precision | 0.846 | 0.860 | 0.837 | 0.948 | 0.902 |

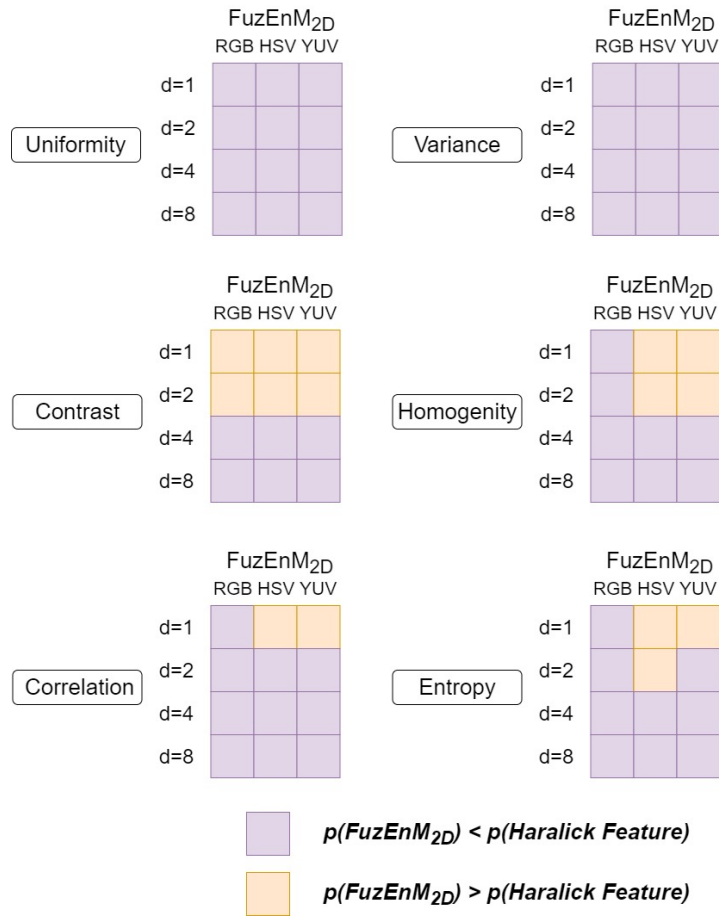


Figure 5.11 – $FuzEnM_{2D}$ and Haralick features p -values of 40 melanoma and 40 melanocytic nevi dermoscopic images in the 3 color spaces: RGB, HSV, and YUV. d represents the interpixel distances for the co-occurrence matrices.

Table 5.6 – ROC analysis for $FuzEnC_{2D}$, $FuzEnV_{2D}$, and $FuzEnM_{2D}$ results of 40 melanoma and 40 melanocytic nevi images in HSV.

| | $FuzEnC_{2D}$ | | | $FuzEnV_{2D}$ | $FuzEnM_{2D}$ |
|-------------|---------------|-------|--------|---------------|---------------|
| | U_H | U_S | U_V | U | U |
| AUC | 0.771 | 0.376 | 0.406 | 0.771 | 0.771 |
| Sensitivity | 0.650 | 0.325 | 0.225 | 0.650 | 0.650 |
| Specificity | 0.850 | 0.600 | 0.850 | 0.850 | 0.850 |
| Accuracy | 0.750 | 0.462 | 0.5375 | 0.750 | 0.750 |
| Precision | 0.812 | 0.448 | 0.600 | 0.812 | 0.812 |

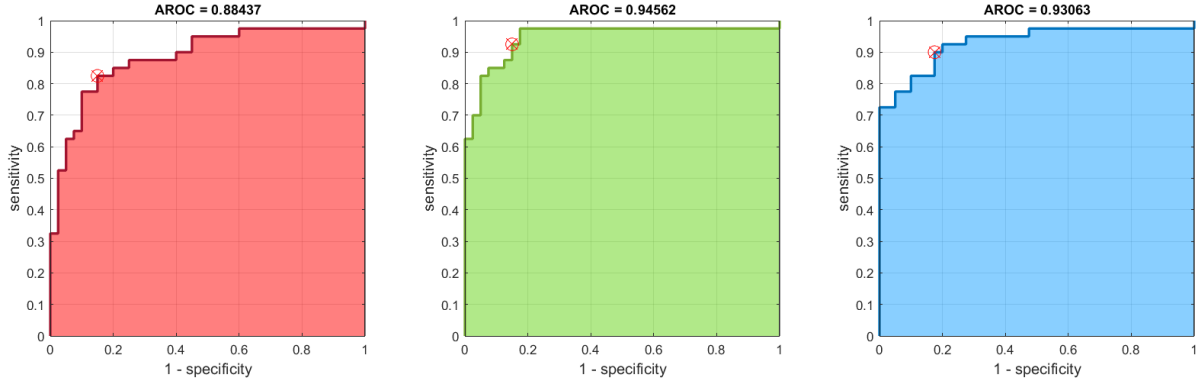


Figure 5.12 – ROC curves for $FuzEnC_{2D}$ results of the 40 melanoma and 40 melanocytic nevi images in the RGB color space. The curves are for $FuzEnC_{R2D}$, $FuzEnC_{G2D}$, and $FuzEnC_{B2D}$ from left to right.

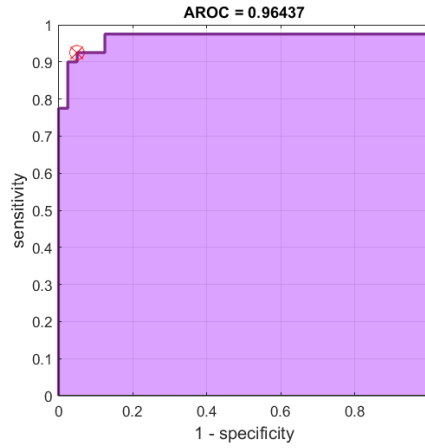


Figure 5.13 – ROC curve for $FuzEnV_{2D}$ results of the 40 melanoma and 40 melanocytic nevi images in the RGB color space.

Table 5.7 – ROC analysis for $FuzEnC_{2D}$, $FuzEnV_{2D}$, and $FuzEnM_{2D}$ results of 40 melanoma and 40 melanocytic nevi images in YUV.

| | $FuzEnC_{2D}$ | | | $FuzEnV_{2D}$ | $FuzEnM_{2D}$ |
|-------------|---------------|-------|-------|---------------|---------------|
| | U_Y | U_U | U_V | U | U |
| AUC | 0.787 | 0.703 | 0.723 | 0.765 | 0.785 |
| Sensitivity | 0.725 | 0.750 | 0.700 | 0.750 | 0.725 |
| Specificity | 0.750 | 0.650 | 0.700 | 0.725 | 0.750 |
| Accuracy | 0.737 | 0.700 | 0.700 | 0.737 | 0.737 |
| Precision | 0.743 | 0.681 | 0.700 | 0.731 | 0.743 |

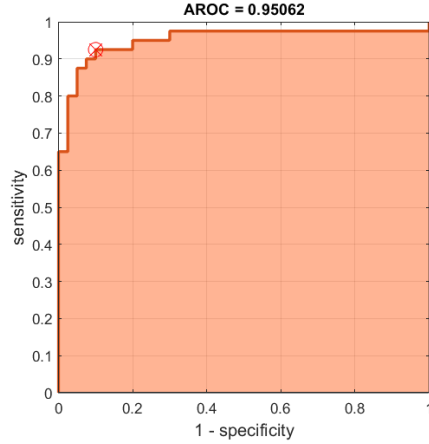


Figure 5.14 – ROC curve for $FuzEnM_{2D}$ results of the 40 melanoma and 40 melanocytic nevi images in the RGB color space.

Finally, we can say that the three entropy measures were able to differentiate both pigmented skin lesions. This was validated statistically by p -values, especially in the RGB color space. In the latter, $FuzEnC_{2D}$, achieved accuracies of 83.7%, 88.7%, 86.2% and AUC of 88.4%, 94.5%, 93%. On the other hand, $FuzEnV_{2D}$, reached an accuracy of 93.7% and AUC of 96.4%. In addition, $FuzEnM_{2D}$ showed an accuracy of 91.2% and AUC of 95.0%.

Moreover, $FuzEnV_{2D}$ and $FuzEnM_{2D}$ outperform both $FuzEnC_{2D}$ and the classical descriptors, Haralick features, in differentiating the two similar malignant melanoma and benign melanocytic nevi dermoscopic images. These preliminary results could be the groundwork for developing an objective computer-based tool for helping medical doctors in melanoma that is often mistaken with the benign melanocytic nevi or is properly diagnosed in its late stages. We limited our investigation to three-channel color images. Consequently, future work could be directed towards multi-spectral color images. Moreover, we intend to compare our results with other texture analysis algorithms.

5.4 Cutaneous Microcirculation Assessment

In this section, we evaluate dermoscopic images showing skin regions at rest and during heating using $FuzEnC_{2D}$ [29]. The goal is to test if our method is able to distinguish two kinds of microcirculation states, *i.e.* resting state and vasodilated microcirculation. For more details about the cutaneous microcirculation please refer to Chapter 1,

section 1.6.2. This is of special importance as several studies stated that microvascular dysfunction might be a direct indicator for cardiovascular diseases. Moreover, monitoring hemodynamic coherence between the micro- and macro-circulations using a fast and easily-accessible manner is particularly important for bedridden patients surveillance [108, 106, 107].

The dermoscopic images of nine healthy volunteers (8 women and 1 man, age: 36.5 ± 11 years) were studied. The nine volunteers provided written consents for participating and the study was performed in accordance with the Declaration of Helsinki. We employed 18 skin dermoscopy images (256×256 pixels) for 2 different cutaneous microcirculatory states: at rest (normal) and during heating (vasodilation). The images were taken at the department of dermatology of Angers Hospital, France using a *Medicam800HD* system with a resolution of 1920×1080 full HD and 2 megapixels. Vasodilation is the state of blood vessel dilatation which is accomplished by warming up the inspected skin region in our study. Applying heat locally dilates the microcirculatory vessels and eventually increases local skin blood flow. Heat (> 40 °C) was applied for a duration of 2 minutes to a region at 3 cm from the antecubital fossa on the left arm of every volunteer.

Results

For our application on dermoscopic medical images, the results are shown in Figure 5.15. To validate the significance of our results we used the Wilcoxon signed rank test where a statistically proven significance is defined for $p < 0.05$. We obtained statistical significance for the red and green channels (\mathbf{U}_R and \mathbf{U}_G) with p -values 0.01 and 0.03 respectively.

We used Haralick texture descriptors – the probably most commonly used image texture descriptors – for comparing the results with those of our proposed *FuzEnC_{2D}* (for more details please refer to section 1.1.1). The results are presented in Table 5.8. The “–” sign replaces the undefined values. Using Wilcoxon signed rank test, no statistically proven significance was found between the two microcirculation states using the Haralick features. This proves an advantage for *FuzEnC_{2D}* by its ability to statistically differentiate the vasodilated and normal microvascular states whereas Haralick texture descriptors cannot.

The results show statistically proven differentiation for the red and green channels

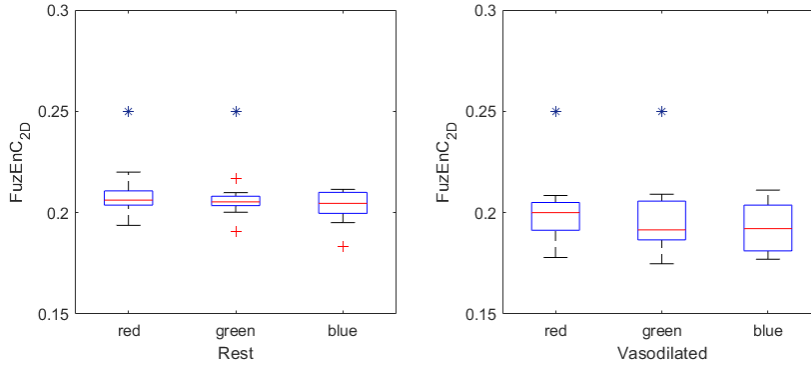


Figure 5.15 – $FuzEnC_{2D}$ for the dermoscopic images at rest and with vasodilation. The * signifies the presence of statistically significant differences between the two groups.

Table 5.8 – Mean and standard deviation of Haralick features for \mathbf{U}_R , \mathbf{U}_G , and \mathbf{U}_B for dermoscopic images of 9 individuals.

| Normal | \mathbf{U}_R | \mathbf{U}_G | \mathbf{U}_B |
|------------------|--------------------|-------------------|-------------------|
| Variance | 0.184 ± 0.142 | 0.144 ± 0.098 | 0.261 ± 0.105 |
| Uniformity | 0.666 ± 0.239 | 0.728 ± 0.169 | 0.467 ± 0.201 |
| Distortion | 0.000 ± 0.001 | 0.000 ± 0.001 | 0.000 ± 0.004 |
| Entropy | – | – | – |
| Homogeneity | 0.907 ± 0.070 | 0.928 ± 0.049 | 0.870 ± 0.054 |
| Inverse variance | – | – | – |
| Vasodilated | | | |
| Variance | 0.159 ± 0.128 | 0.194 ± 0.111 | 0.231 ± 0.105 |
| Uniformity | 0.708 ± 0.223 | 0.598 ± 0.225 | 0.521 ± 0.206 |
| Distortion | 0.0003 ± 0.000 | 0.001 ± 0.002 | 0.000 ± 0.002 |
| Entropy | – | – | – |
| Homogeneity | 0.920 ± 0.064 | 0.903 ± 0.055 | 0.884 ± 0.052 |
| Inverse variance | – | – | – |

whereas no statistical significance was found using Haralick features. Only $FuzEnC_{2D}$ was used for analyzing the dermoscopic microcirculation images in this study, because it was our first experiment in applying colored entropy measures to dermoscopic images. Based on these promising results, we started developing the other colored entropy approaches. For the other studies presented in this manuscript on colored images, we use the three developed colored entropy measures.

In the future we will be continuing this study for a larger number of individuals and once validated, it would serve as an interesting technique helping medical doctors in the assessment of cutaneous microcirculation states. This is of particular importance for bedridden patients. It would provide a feasible, non-invasive, and fast microcirculation assessment technique. Furthermore, having the ability to study irregularity of colored images and textures enables us to extend the application to various fields and different medical images. This study was published as a conference paper [29].

5.5 Chronic Obstructive Pulmonary Diseases (COPD)

We proposed a pseudo-three dimensional multiscale fuzzy entropy measure ($pMFuzEn_{3D}$) to analyze CT scan volumes based on our developed MSF_{2D} . We process high resolution CT scans (HRCT) of patients with chronic obstructive pulmonary diseases (COPD). $pMFuzEn_{3D}$ consists in computing $FuzEn_{2D}$ for each scan at different scales and gathering all the entropy results on the same plot. In our study, we used $pMFuzEn_{3D}$ to process HRCT scans from 22 subjects divided into 3 groups: 10 scans of subjects with emphysema, 8 scans for normal lung subjects, and 4 scans of subjects with airways disease. The scans were taken at the respiratory outpatient clinic at Aalborg University Hospital and the associated Rehabilitation Center, Denmark. The people involved wrote written consents in according to the declaration of Helsinki and agreed on the participation in the studies on COPD [131]. The scans were acquired using Discovery CT750HD CT machine (General Electric Company, Fairfield, CT, USA). They were handled and inspected by a team of three physicians, pulmonologist, and two radiologists.

We calculated $pMFuzEn_{3D}$ for the mentioned HRCT scans. For this purpose, the parameter \mathbf{m} , threshold r , and fuzzy membership function were 2, 0.25, and Gaussian distribution, respectively. The scale factor τ varied from 1 to 20. The results for one of the

patients with emphysema is presented in Figure 5.16. The latter shows that $pMFuzEn_{3D}$ is able to reveal entropy differences with scales and between slices. Continuing this work for a larger number of HRCT scans could lead us to some useful medical findings in the field of COPD. Further studies will also be developed for groups with different degrees of emphysema.

These results came from our first application for adapting bidimensional entropy measures to volumetric data, using $pMFuzEn_{3D}$. The results were promising and encouraged us to develop the 3D based entropy measures. For the other applications on 3D medical data, we will be employing the volumetric entropy measures directly.

With all what is going on in the world right now and the spread of the new SARS-CoV-2 virus which is a type of pulmonary diseases, this study gains more attention. Provided the sufficient resources we should continue in analyzing those images to probably provide a digital tool to aid medical doctors in identifying and staging the encountered lung diseases using a computer-based objective method. This study was submitted as a one page paper and presented in an invited session for “Identification of Cardiopulmonary Function” at the EMBC 2019.

5.6 Idiopathic Pulmonary Fibrosis (IPF)

After performing validation tests for our tridimensional entropy measure and its multiscale approach, we applied it to lung HRCT scans of healthy and Idiopathic Pulmonary Fibrosis (IPF) patients. MFE_{3D} algorithm was applied to a dataset of 52 volumetric HRCT scans for 26 healthy subjects and 26 IPF patients. The study included 43 male and 9 female subjects. The average age of the subjects was 76.8 ± 8.5 years which is in agreement with the typical age of IPF incidence. This work was performed in collaboration with university of Coimbra, Portugal.

The patients with IPF were recruited at the competence center for rare pulmonary diseases in the department of Respiratory Medicine at Rennes University Hospital, Rennes-France. These patients were diagnosed with stable IPF, as defined in multidisciplinary discussions, having no infection or exacerbation in the 8 weeks preceding their first appointment. The study was performed in accordance with the Declaration of Helsinki under the IRB approval number 19.82.

The healthy individuals for this study are subjects who underwent HRCT scans to rule out various pathologies. Their HRCT scans were verified by an expert chest radiologist

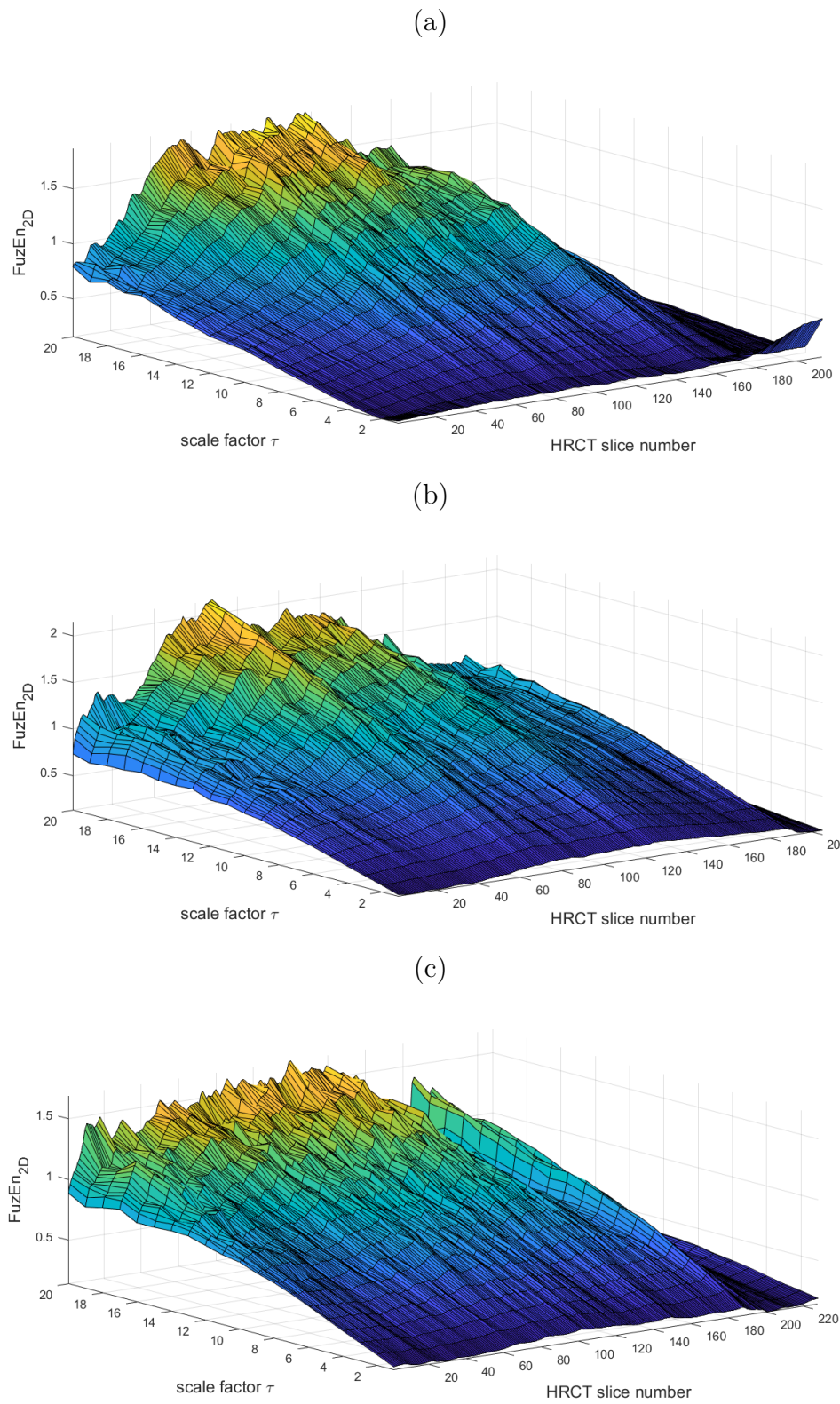


Figure 5.16 – $pMFuzEn_{3D}$ for HRCT scans of: (a) normal (b) a patient with emphysema and (c) airways diseases.

to confirm the absence of abnormal structures within the lung parenchyma and thus be considered as healthy.

All the HRCT scans were obtained with a dose of 100 kVp and 120 kVp for 32 and 20 subjects, respectively, and the reconstruction matrices were of 512×512 pixels per scan, with a pixel spacing mean value of 0.731 ± 0.046 mm. Most of the scans were performed without IV contrast. The slice thickness was either 1.25 mm (34 subjects), 1.00 mm (14 subjects), or 0.625 mm (4 subjects). For each individual, a volume of $50 \times 50 \times 50$ voxels, from the basal and sub-pleural pulmonary region, has been segmented, resulting in volume heights up to 62.5 mm when considering 50 slices along the z-axis.

The segmentation procedure was performed by scanning the HRCT scans bottom-up, searching for a volume with less of 5% zero-values pixels (totally dark region) to avoid external regions of the lung. The bottom-up procedure was adopted due to the typical basal and peripheral predominance of IPF, because IPF patients are mostly affected in the basal and peripheral regions of the lungs [171, 172]. The first volume fitting the description was the one being selected. The volume selection is clearly illustrated by [27] knowing that the HRCT scans are composed of $512 \times 512 \times Nz$ voxels, see Figure 5.17. These volumes were segmented from the right lung (as a random selection). Based on that, the segmentation procedure was generalized and automatically performed for all the subjects. Within these volumes, typical UIP (usual interstitial pneumonitis) patterns were evaluated using our proposed entropy measure MFE_{3D} .

The average of $FuzEn_{3D}$ values at each scale factor τ for the HRCT scans of healthy individuals and IPF patients are presented in Figure 5.18. The parameters were set as $\mathbf{m} = 3$, $r = 0.2$, $n = 2$, and $\tau_{max} = 10$. It is observed that for most scale factors the average $FuzEn_{3D}$ for healthy subjects are lower than those of IPF patients.

To validate the statistical significance of the results obtained a Wilcoxon rank sum test (for independent groups) was performed. Statistically significant differences were considered for p -values strictly less than 0.05. This was observed for five scale factors: $\tau = 3, 4, 6, 7$, and 8 with p -values 2.9×10^{-5} , 7.0×10^{-6} , 1.9×10^{-5} , 3.9×10^{-5} , and 2.5×10^{-5} , respectively. An “*” sign is indicated in Figure 5.18 for the scale factors on which $FuzEn_{3D}$ is statistically significantly different for healthy and IPF lung scans.

The results showed MSF_{3D} 's ability to distinguish healthy from IPF HRCT scans on five scale factors. This is illustrated especially for scale factors: $\tau = 3, 4, 6, 7$, and 8 . Moreover, the effect size (Cohen's d) was calculated for the statistically significant scale factors results and “Large” to “very Large” effect size values were obtained. The latter

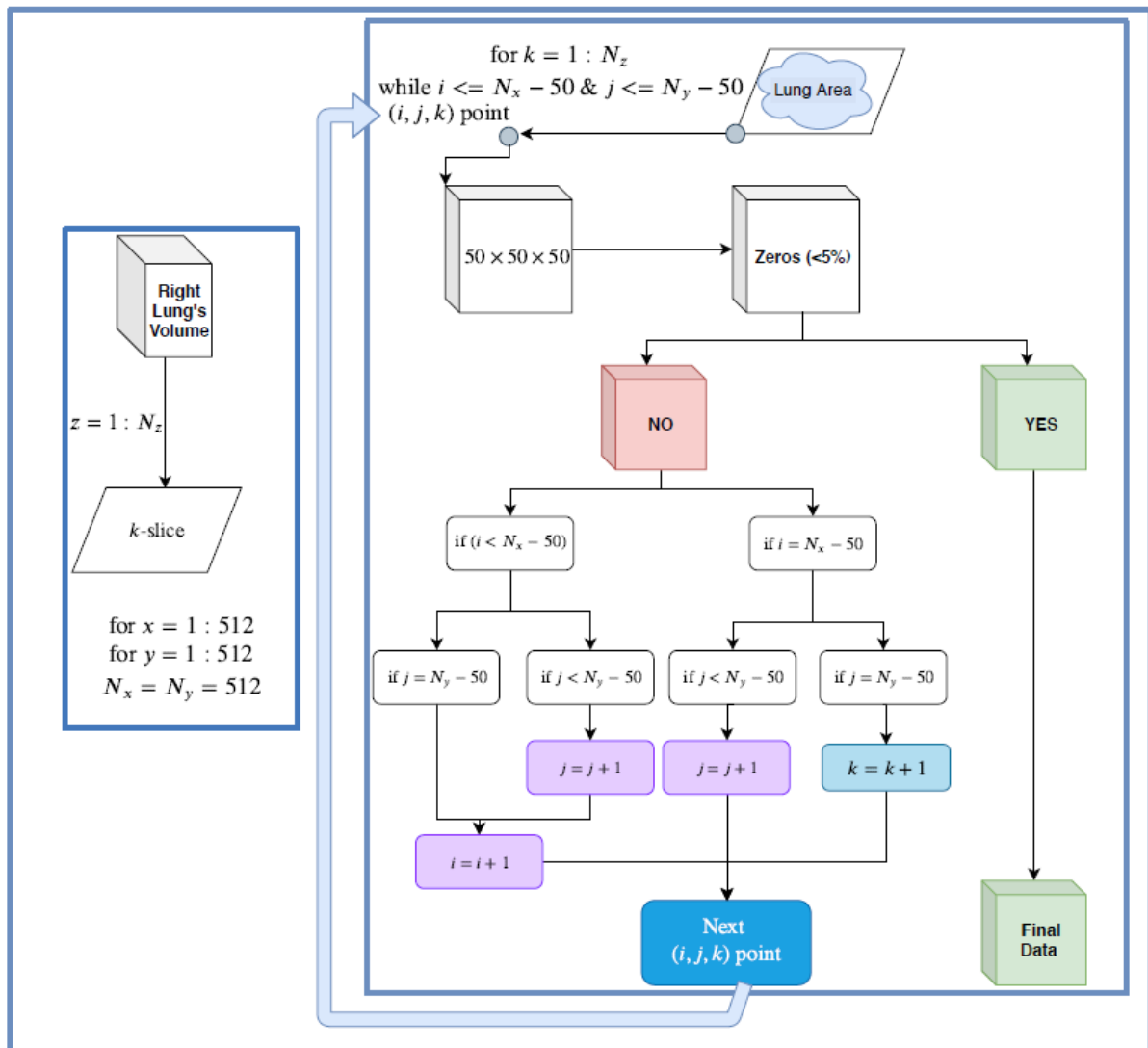


Figure 5.17 – Illustration for the selection process of the volume to be evaluated by MSF_{3D} from the HRCT scans. Adapted from [27].

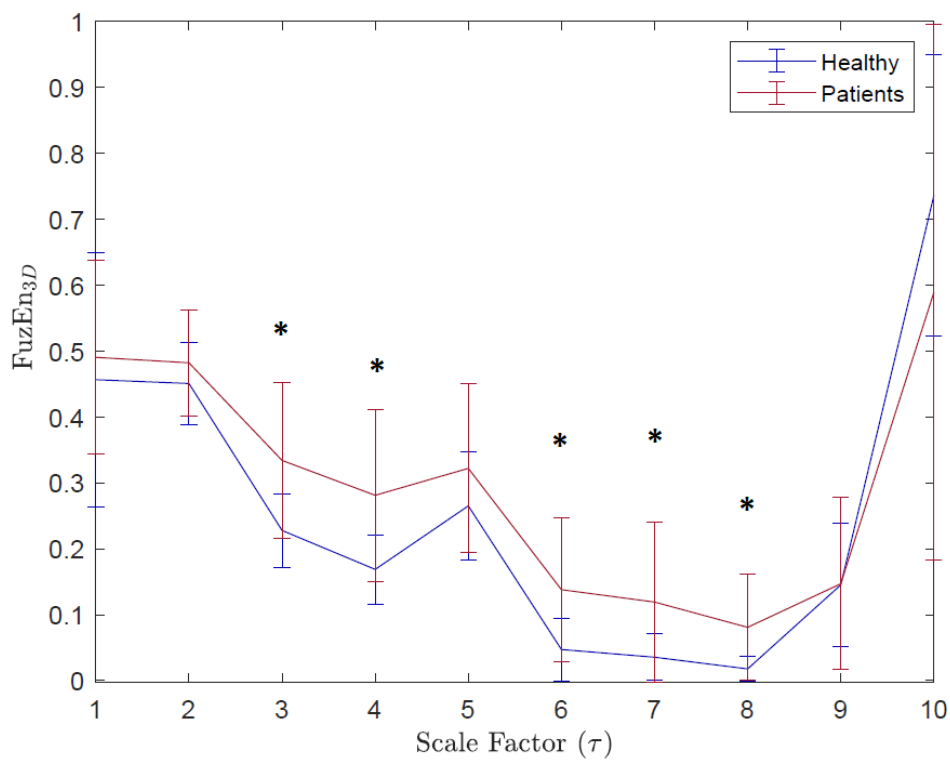


Figure 5.18 – Mean MSF_{3D} results for the CT scans of healthy individuals and IPF patients, for parameters $\mathbf{m} = 3$, $r = 0.2$, and $n = 2$. The * signifies the presence of statistically significant differences between the two groups.

validated even more the ability of MSF_{3D} to distinguish the two compared groups, healthy and IPF suffering subjects. Based on those promising results, MSF_{3D} could be seen as a potential screening tool aimed to do a preliminary identification of UIP patterns in the future.

The development of a multiscale tridimensional fuzzy entropy algorithm could be a useful tool in the evaluation of HRCT of patients with IPF for early detection and quantification of the UIP patterns, through a irregularity and complexity assessment. The study on IPF patients was published as a journal paper in the *IEEE journal of biomedical health and informatics, JBHI* [27].

5.7 COVID-19

The outbreak of this novel version of coronavirus (SARS-CoV-2) causing COVID-19, encouraged intensive research race to provide answers for all the questions raised concerning:

- its background or origin
- its diagnosis
- the evolution of the disease with time
- the long term effects on patients
- and of course the possible cure.

Starting from our responsibility and the ability of the image processing tools that we have developed, we performed a study on COVID-19 patients scans (for medically confirmed cases) and compared them to the results obtained for IPF in the previous section. This work was also performed in collaboration with the University of Coimbra, Portugal.

The acquisition of the studied COVID-19 patients' CT scans was performed at the University Hospital of Rennes, France between March 26 and April 17 of 2020, under the IRB approval number 19.6 in accordance with the Declaration of Helsinki. The COVID-19 patients underwent a reverse transcription polymerase chain reaction (RT-PCR) test for SARS-CoV-2 and then a non-contrast chest CT scan for the positive SARS-CoV-2 patients was acquired.

The IPF patients were diagnosed with stable IPF and were followed up with, at the competence center for rare pulmonary diseases, Department of Respiratory Medicine,

University Hospital of Rennes, France. The healthy subjects were those who had chest CT scans that were verified by expert radiologists to show no abnormal lung structures. For more information about this dataset please refer to the previous section 5.6.

The whole dataset is composed of a total of 103 CT scans: 51 of patients diagnosed by COVID-19, 26 patients diagnosed by IPF, and 26 healthy subjects, see Table 5.9 for more details. The selected volumes to be evaluated followed the bottom to top scanning and a $50 \times 50 \times 50$ voxels region of interest (ROI) is chosen from the right lung for all subjects. The segmentation procedure and volumes selection is detailed in the previous section 5.6, see Figure 5.17.

Table 5.9 – Characteristics of the studied population.

| | Mean age | Number of CT scans |
|-------------------|-------------------|--------------------|
| Healthy subjects | 48.19 ± 14.84 | 26 |
| IPF patients | 74.96 ± 9.38 | 26 |
| COVID-19 patients | 58.84 ± 14.87 | 51 |

MSF_{3D} is calculated for the 103 scans and the parameters are defined as: $\mathbf{m}= 3$, $r = 0.2$, $n = 2$, and $\tau_{max}=10$. The results are depicted in Figure 5.19 as the mean and standard deviation for the entropy values.

We can observe a unique curve for the results of each group of subjects, however in order to prove their statistical significance, we used the Mann–Whitney U test in a pair-wise comparison. In addition, the Cohen’s d for effect size is calculated for each statistical result. The statistical results are displayed in Table 5.10. Refer to Table 5.1 for the interpretation of Cohen’s d .

The results indicate that MSF_{3D} was able to differentiate IPF from healthy scans for 5 scale factors $\tau= 3, 4, 6, 7$, and 8. Moreover, for COVID-19 compared to healthy scans, a statistically proven differentiation ability is revealed for all scale factors τ , except $\tau = 2$ with “Large” to “very Large” effect size values. The latter validates even more our statistically significant results. In addition, for distinguishing IPF scans from COVID-19 scans, the statistical results showed that MSF_{3D} was capable of doing so for all calculated τ , except $\tau=5$ and 10.

The results came to be very encouraging, especially that they illustrate a promising outcome for COVID-19 patients. This study is submitted and under revision.

We also suggested calculating the complexity index CI for unique for from $\tau_1 = 1$ to $\tau_2 = 8$, see Figure 5.20. CI is unique for each ROI and is defined as the sum of the entropy

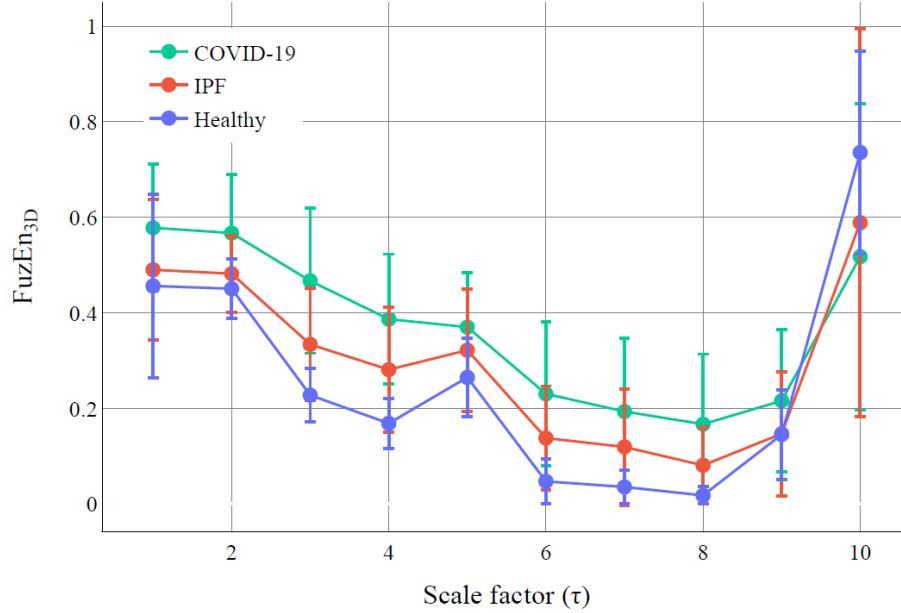


Figure 5.19 – Mean and standard deviation for the MSF_{3D} values for healthy subjects, idiopathic pulmonary fibrosis (IPF), and COVID-19 patients for scale factors $\tau = 1$ to 10.

Table 5.10 – Mann–Whitney U test p -values and Cohen’s d values for MSF_{3D} results of healthy, IPF, and COVID-19 confirmed subjects. The * sign indicates the presence of a statistically significant difference between the compared groups at a given scale factor.

| Scale factor τ | Healthy – IPF | | Healthy – COVID-19 | | COVID-19 – IPF | |
|---------------------|-------------------------|------|-------------------------|------|-------------------------|------|
| | p | d | p | d | p | d |
| 1 | 2.09×10^{-1} | 0.19 | 3.44×10^{-5} * | 0.78 | 1.97×10^{-2} * | 0.63 |
| 2 | 8.37×10^{-2} | 0.43 | 6.22×10^{-6} * | 1.09 | 2.60×10^{-3} * | 0.77 |
| 3 | 2.88×10^{-5} * | 1.15 | 0.00×10^{-9} * | 1.86 | 7.88×10^{-5} * | 0.94 |
| 4 | 7.00×10^{-6} * | 1.13 | 0.00×10^{-9} * | 1.89 | 6.01×10^{-4} * | 0.78 |
| 5 | 1.26×10^{-1} | 0.52 | 8.01×10^{-6} * | 1.00 | 1.30×10^{-1} | 0.40 |
| 6 | 1.92×10^{-5} * | 1.08 | 0.00×10^{-9} * | 1.45 | 2.34×10^{-3} * | 0.66 |
| 7 | 3.38×10^{-5} * | 0.93 | 0.00×10^{-9} * | 1.25 | 1.56×10^{-3} * | 0.51 |
| 8 | 2.45×10^{-5} * | 1.08 | 1.11×10^{-9} * | 1.23 | 3.00×10^{-3} * | 0.66 |
| 9 | 5.27×10^{-1} | 0.01 | 2.61×10^{-2} | 0.53 | 2.54×10^{-2} * | 0.48 |
| 10 | 7.43×10^{-2} | 0.45 | 1.07×10^{-3} * | 0.75 | 5.86×10^{-1} | 0.20 |

values for some consecutive scale factors from τ_1 to τ_2 as:

$$CI = \sum_{\tau_1}^{\tau_2} FuzEn_{3D}. \quad (5.1)$$

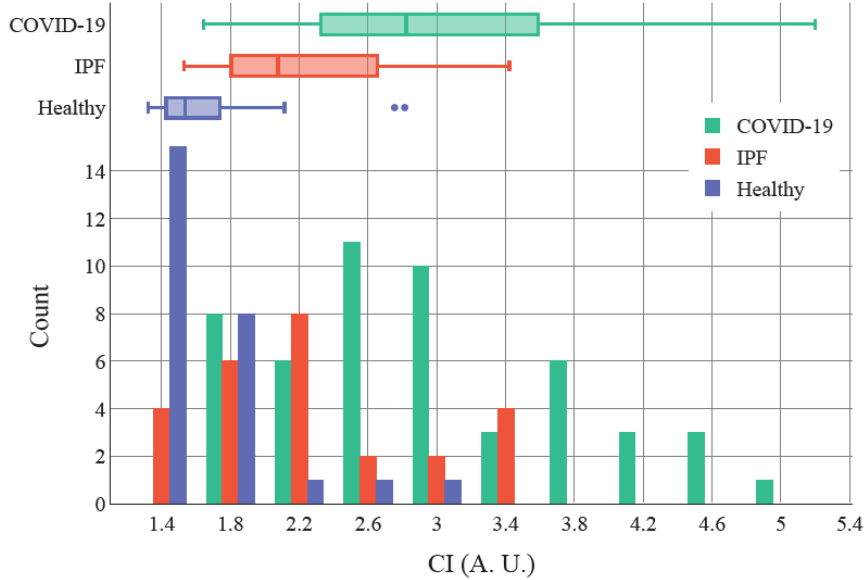


Figure 5.20 – Complexity index for COVID-19, IPF, and healthy subjects' results.

5.8 Uterine Artery Embolization (UAE)

The clinical dataset processed in this work is composed of 60 volumetric magnetic resonance images (MRI) collected from twenty women diagnosed with uterine fibroids and qualified for uterine artery embolization (UAE). These images were recorded in the Centre Hospitalier Régional Universitaire (CHRU) – Brest, France.

The purpose of this study is to evaluate the efficacy of (UAE) by applying our developed measure to MRI data recorded at three different time intervals, just before, ten days after, and six months after UAE (D0, D10, and M6).

The average age of the patients was 43 ± 4 years which is in line with the standard incidence age of uterine fibroids. Five (25%) of participants were symptomatic (bleeding, pelvic pain, urinary signs, etc.). T2 sagittal without gadolinium MRI images taken before UAE were compared to those taken 10 days and 6 months after the procedure. For all

patients, a significant reduction in mean uterine volume and in dominant fibroid volume was noted after the embolization. All patients had an excellent recuperation and were able to return to their normal activity. After the procedure, few patients experienced minimal bleeding. Three (15%) of participants had persisting urinary signs after procedure. None reported any new clinical issue during the follow-up period.

The first step in the data processing was to extract the fibroid region for each patient. The smallest volume selected was $96 \times 96 \times 28$ voxels and the largest sized $210 \times 210 \times 28$ voxels. The fibroids selection was customized for each patient due to the fact that for each case the fibroids existed at a different location and were of various sizes. For patients with several fibroids, the largest was considered. After that, the selected fibroids volumes were processed using MSF_{3D} . The parameters were set as $\mathbf{m}=2$, $r=0.24$, $n=2$, and $\tau_{max}=10$.

Then a complexity index, CI, based on [173] is calculated. This values is unique for each ROI and is defined as the sum of the entropy values for some consecutive scale factors from τ_1 to τ_2 as:

$$CI = \sum_{\tau_1}^{\tau_2} FuzEn_{3D}. \quad (5.2)$$

For our findings, we choose $\tau_1=8$ and $\tau_2=10$ based on the curves' behavior. Between the aforementioned scale factors the curves behave in a similar way, that is why we chose those exact two values for the complexity index. The results are depicted in Figure 5.21. Then for validating the statistical significance for differentiating the three acquisitions (D0, D10, and M6) we calculated the p -values between each 2 groups using the Wilcoxon rank sum test. The p -values are displayed in Table 5.11.

Table 5.11 – The p -values for the complexity index for $\tau_1=8$ and $\tau_2=10$ between pairs of D0, D10, and M6.

| | D0-D10 | D10-M6 | D0-M6 |
|------------|----------------------|----------------------|----------------------|
| p -value | 4.2×10^{-4} | 3.2×10^{-4} | 1.9×10^{-4} |

The three p -values are less than 0.05. This indicates that MSF_{3D} was able to distinguish the three MRI set of images of the three states D0, D10, and M6 for a complexity index composed between the scale factors $\tau=8$ and $\tau=10$.

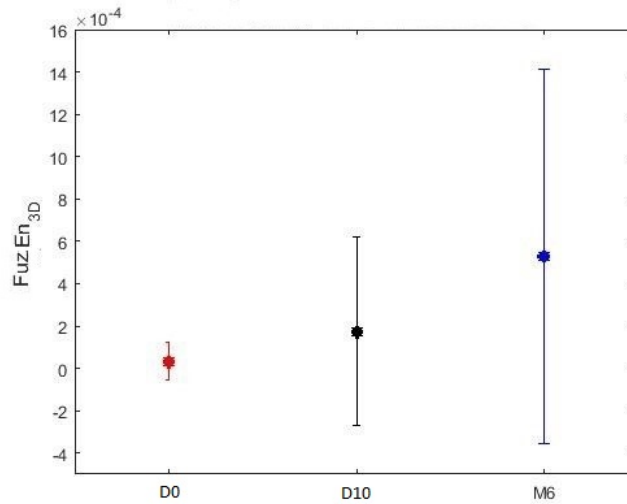


Figure 5.21 – Mean and standard deviation for the complexity index for MSF_{3D} from $\tau=8$ till $\tau=10$ for UAE patients at the three time intervals D0, D10, and M6. The parameters for MSF_{3D} were set as $\mathbf{m}=2$, $r=0.24$, $n=2$, and $\tau_{max}=10$.

5.9 Conclusion

In this chapter we presented our results on medical data. We employed our developed measures to study bidimensional gray scale and colored dermoscopic images of PXE, melanoma, and melanocytic nevi. We also performed a study on the colored dermoscopic images for cutaneous microcirculation assessment. These studies illustrated promising results so we continued with applying our developed tridimensional measures on volumetric medical data. We presented herein analysis for CT, HRCT, and MRI data for different medical cases such as COPD, IPF, UAE, and COVID-19. Some of the results are preliminary but they illustrated to be very promising. Several continuation paths could be taken based on those results.

CONCLUSION AND PERSPECTIVES

Developing computer-based measures for applications in the medical field helps improve prognostic, diagnostic, follow up, and predictive ability. It provides objective assessment for the data and aids medical doctors in making decisions, identifying abnormalities, and eventually saving lives.

As presented in this manuscript, we have developed entropy measures based on the information theory concept [26, 27, 28, 29, 30, 31]. These methods were illustrated to possess an ability to analyze gray scale images, colored images, and finally volumes. Several validation tests were performed for each measure separately. In addition to the specially designed tests for each measure, they are were validated upon:

- changes in the initial parameters: tolerance level, moving template size, and similarity degree function
- ability to quantify the increasing irregularity degrees in the bidimensional and tridimensional levels
- complexity evaluation for the analyzed gray scale images and volumes through the multiscale approach

Our proposed texture analysis tools found successful applications on different kinds of medical images.

Since the 2010's, entropy measures have been extended from the 1D to the 2D case to deal with images and are forming potent bidimensional irregularity measures. In our work, we studied a new 2D entropy measure – the so-called bidimensional fuzzy entropy ($FuzEn_{2D}$) – that outperforms existing bidimensional entropy measures. We first assessed its sensitivity to parameters, then analyzed its behavior upon rotation and translation, and finally showed its multiscale application in the biomedical field (dermoscopic images). To validate the output of the newly introduced $FuzEn_{2D}$ and its multiscale extension, a set of synthetic images based on several concepts in image processing (including power of noise and degree of randomness) and texture datasets were used. The results for synthetic images illustrate that $FuzEn_{2D}$ has low sensitivity to the chosen parameters

and it is rotation and translation invariant. Moreover, it outperforms the already existing bidimensional entropy measures. We then employed our developed measure, and its multiscale version MSF_{2D} , to PXE dermoscopic images.

PXE is a rare disease that causes several cutaneous, cardiovascular, and ophthalmic complications. Thus, the earlier the diagnosis is, the better the monitoring and prevention will be. PXE establishes a certain textural behavior on the skin that cannot be always identified visually even through dermoscopy. This creates an essential need for developing an objective technique that can identify the presence of this disease in its early stages (the initial cutaneous symptoms).

We proposed an image processing framework to help in the detection of papules from dermoscopic images. We employed our newly developed MSF_{2D} on a PXE dermoscopic images dataset. The primary MSF_{2D} results seem to be promising in distinguishing a group of healthy skin images from diseased ones with statistically significant values for the first two scale factors with noticeable large effect sizes.

In the future, it would also be interesting to use MSF_{2D} to track how the skin pathology evolves upon potential treatment follow up, due to the fact that there is no definite treatment for this disorder yet. This contribution would influence the research in this field and could help in its escalation. The results of $FuzEn_{2D}$ and MSF_{2D} for the synthetic and real images illustrate the potential of the proposed method in analyzing various images in different possible applications.

Moreover, using MSF_{2D} we evaluated dermoscopic melanoma (malignant lesion) and melanocytic nevi (benign lesion) images and the results are found to be interesting for a potential diagnostic application.

Furthermore, after the successful finding on gray scale images using MSF_{2D} we employed the colored approach to reveal the information hidden within the color components of our studied PXE images and other dermoscopic images.

Texture analysis is a subject of intensive focus in research due to its significant role in the field of image analysis. It is a fast-evolving research topic. However, few are the studies focusing on colored texture analysis. Therefore, based on the importance of the information that could be revealed by colors in images, we introduced the new colored bidimensional fuzzy entropy measure in its single-channel approach, $FuzEnC_{2D}$, and multi-channel approaches, $FuzEnV_{2D}$ and $FuzEnM_{2D}$. We investigated their sensitivity

to parameters and ability to identify images with different irregularity degrees. Moreover, we studied their behavior with colored Brodatz images in different color spaces. After verifying the results with test images, we employed those methods for analyzing dermoscopic images of the deadliest type of skin cancer, melanoma, and the benign melanocytic nevi. Furthermore, we investigated the PXE colored images for potential important findings besides the gray scale analysis using MSF_{2D} . In addition, a preliminary study on the cutaneous microcirculation assessment for dermoscopy images was performed.

The bidimensional proposed algorithms showed very promising results for 2D medical images. To expand our medical application we developed a tridimensional entropy measure and its multiscale approach as well to study volumetric scans. $FuzEn_{3D}$ and MSF_{2D} were applied to CT scans, HRCT scans, and MRI scans belonging to patients of COVID-19, IPF, and uterine fibroma, respectively. This application was unique and allowed us to investigate volumetric data differently. The results are very encouraging and urged us to continue in this scope for the coming research work as well.

Perspectives and future steps

Several interesting research work pathways could be taken based on the work performed in this manuscript. The research world is leaning towards computer aided diagnosis tools in which our developed algorithms could play an important role. First we could start by comparing all the results obtained by our developed entropy measures with those given by other texture feature extraction algorithms (different from the ones found in the manuscript). This would provide validation on a larger scale. Then, based on those results, we could increase the number of processed images or volumetric scans and use also other datasets for the discussed medical cases in order to guarantee reproducible results with different datasets.

Nevertheless, remote diagnosis is also being considered as one of the important topics nowadays. The COVID-19 outbreak highlighted again the need for remote diagnosis using the available platforms especially for such highly infectious diseases. Enhancement of computer based diagnosis methods, including our developed algorithms, could highly serve this domain with ensuring the least possible contact between the medical doctors and patients. In addition, long term monitoring for some diseases could be made much easier with computer based methods over distance. Diagnosis could become more accessible and feasible globally.

As the discipline of non-linear statistics continues to prove its encouraging results,

we would suggest introducing our methods into the machine learning applications as a future step. Our developed measures have proven their consistency each applied separately. However, in machine learning we could combine their outputs and investigate their classification efficiency when employed all together. This path could be employed for bidimensional gray scale and colored images measures, as well as, the volumetric measures.

Upgrading to end-to-end analysis might lead to even better results. As the obtained medical images, especially for 3D scans, pass through some major pre-processing steps adapted to the human visual perception, we would propose starting trial with end-to-end analysis. In other words, introducing images directly from the machine to the algorithm without passing by the image enhancement and pre-processing techniques might have even better results.

Expanding the colored entropy measures study and investigating adapted application and analysis for each of the different color space families. As the colored texture image domain is very wide with utilization in various fields.

Although the used fuzzy function ($\exp(-(d^m)^2/r)$) led to interesting results, other fuzzy functions could be also investigated.

Last but not least, several multiscale approaches could emerge based on our work. For the bidimensional entropy measures, a multiscale approach could be also introduced for the colored textures. This should reveal some extra in depth information contained in the coarse-grained versions of the colored texture images. Moreover, different coarse-graining methods could be employed for the bidimensional and tridimensional entropy measures. We only utilized two coarse-graining methods in this manuscript. Thus, it would be interesting to investigate all the others for the gray scale, colored, and volumetric data.

EXTRA ACTIVITIES AND PUBLICATIONS

Communications

Throughout my Ph.D. studies I have been always encouraged by my supervisor, Pr Anne Humeau-Heurtier, to expand my knowledge, communicate to other scientific groups our findings, and have fruitful discussions. This was made possible especially by:

- Oral presentation in an invited session entitled: “Identification of Cardiopulmonary Function” at the IEEE 41st International Engineering in Medicine and Biology Conference, (IEEE EMBC) 2019 conference, Berlin - Germany.
- Poster presentation at IEEE EMBC 2019, Berlin-Germany.
- Oral and poster presentations at the 5th International Conference on Advances in Biomedical Engineering, ICABME 2019, Tripoli - Liban.
- Oral presentation at the 12th International Biomechanics Medical Diagnostics Locomotion and Rehabilitation Conference BIOMDLORE 2018, Białystok - Poland.
- Virtually attending the IEEE 42st International Engineering in Medicine and Biology Conference, (IEEE EMBC) 2020 conference, Montreal - Canada.
- Virtually attending the “Journée Scientifique du CRMR PXE Angers Centre de Simulation”, CHU d’Angers-France 2020.
- and finally by our collaborations with national and international universities and hospitals: Harvard University (Boston, US), University of Coimbra (Portugal), Aalborg University (Denmark), Lebanese University (Lebanon), University Hospital of Angers – Department of Dermatology (Angers, France), University Hospital of Rennes (Rennes, France), University Hospital of Brest (Brest, France), University Hospital of Aalborg – Department of Respiratory Diseases (Aalborg, Denmark).

List of publications

During the past three years we have accomplished several publications either as journal papers or conference papers. Please find them listed below:

- Hilal, M., Berthin, C., Martin, L., Azami, H., Humeau-Heurtier, A., Bidimensional Multiscale Fuzzy Entropy and its Application to Pseudoxanthoma Elasticum. IEEE Transactions on Biomedical Engineering, Volume: 67, Issue: 7, p.2015 - 2022, 2019.
- Gaudêncio, A. S. F., Vaz, P. G., Hilal, M., Cardoso, J. M., Mahé, G., Lederlin, M., Humeau-Heurtier, A., Tri-dimensional Multiscale Fuzzy Entropy Applied To CT Scans Of Idiopathic Pulmonary Fibrosis Patients. IEEE Journal of Biomedical and Health Informatics, in press.
- Gaudêncio, A. S. F., Vaz, P. G., Hilal, M., Mahé, G., Lederlin, M., Humeau-Heurtier, A., Cardoso, J. M., Evaluation of Covid-19 chest computed tomography: a texture analysis based on three-dimensional entropy. (*submitted*).
- Hilal, M., Humeau-Heurtier, A., Bidimensional Fuzzy Entropy: Principle Analysis and Biomedical Applications. 41st Annual International Conference of the IEEE Engineering in Medicine and Biology Society (EMBC), July 2019, Berlin, Allemagne, Proceedings p. 4811-4814.
- Hilal, M., Gaudencio, A. S. F., Berthin, C., Vaz, P. G., Cardoso, J., Martin, L., Humeau-Heurtier, A., Bidimensional Colored Fuzzy Entropy Measure: a Cutaneous Microcirculation Study. 5th International Conference on Advances in Biomedical Engineering (ICABME), Liban, October 2019, IEEE, Proceedings p. 1-4.
- Hilal, M., Berthin, C., Martin, L., Humeau-Heurtier, A., Skin Alterations in Pseudoxanthoma Elasticum Patients Highlighted by the Bi-Dimensional Sample Entropy Algorithm. 12th International Biomechanics Medical Diagnostics Locomotion and Rehabilitation Conference (BIOMDLORE), Białystok – Pologne, June 2018, Proceedings p. 1-6.
- Gaudencio, A. S. F., Hilal, M., Vaz, P. G., Cardoso, J., Humeau-Heurtier, A., Bi-dimensional colored fuzzy entropy applied to melanoma dermoscopic images. Accepted in Entropy 2020–The Scientific tool of the 21st century that was postponed to Entropy 2021 and will take place May 2021 in Porto, Portugal.

Teaching

I have been teaching at the IUT d'Angers and Polytech Angers as a Doctorante Contractuelle à Activité Complémentaire d'Enseignement (DCACE) since 2018. The modules that I taught are detailed in the table below according to the year, discipline, establishment and the number of hours. My total teaching volume is 132 hours.

| Module | Niveau | Année universitaire | Etablissement | Volume |
|--------------------------------|---|---------------------|-----------------|--------|
| TP Traitement d'Images | DUT 1 | 2017/2018 | IUT d'Angers | 8 h |
| TP Capteurs | 2 ^{ème} année cycle préparatoire intégré | 2018/2019 | Polytech Angers | 16 h |
| TP Automatique | 2 ^{ème} année cycle préparatoire intégré | 2018/2019 | Polytech Angers | 16 h |
| TP Outils Logiciels sur Scilab | DUT 1 Génie électrique et informatique industrielle | 2018/2019 | IUT d'Angers | 15 h |
| Statistiques et Probabilités | DUT 2 Génie électrique et informatique industrielle | 2018/2019 | IUT d'Angers | 15 h |
| TP Capteurs | 2 ^{ème} année cycle préparatoire intégré | 2019/2020 | Polytech Angers | 32 h |
| TP Outils Logiciels sur Scilab | DUT 1 Génie électrique et informatique industrielle | 2019/2020 | IUT d'Angers | 15 h |
| Module Maths1 | DUT 1 Génie électrique et informatique industrielle | 2019/2020 | IUT d'Angers | 15 h |

Workshops and other responsibilities

I had the chance to co-supervise an engineering student and a research masters student during their internships at LARIS. It was such an important experience in my professional career and taught me a lot.

I attended a total of 150 hours of classes and workshops among which there was some pedagogic trainings, machine learning workshops, scientific communications classes, and team management skills.

I also participated at the IUT international week in its 2018 and 2019 editions. It was an enriching experience. I had the chance to be involved and meet teachers and researchers from different countries.

I participated in the Nuit des Chercheurs that took place for 2 consecutive years

at Le Quai - Angers and attended the scientific communication workshop. These two experiences allowed me to improve my communication skills and my ability to explain a complex scientific idea to people of different backgrounds, ages, and education levels.

I attended with GdR ISIS (Information, Signal, Image and ViSion) the following workshops: 2nd meeting on medical image analysis and IA for COVID-19 (May 2020), Evaluation de la qualité subjective et objective de données 3D (June 2020), Journée “Carrières en Signal, Image & Vision” à destination des doctorants (March 2019).

6.1 Annex Chapter 1

Extra illustrations for the skin structure 6.1.

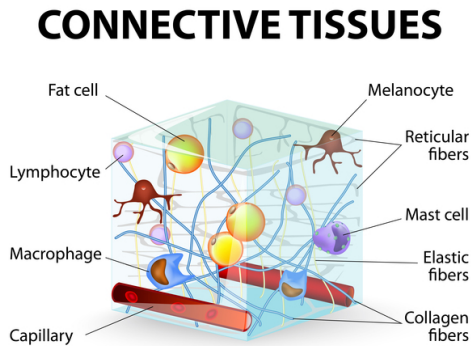


Figure 6.1 – PXE manifestation in the skin targets the elastic fibers in the mid and deep dermis. Adapted from [113].

6.2 Annex Chapter 5

Gray scale dermoscopic images using $SampEn_{2D}$

Before developing $FuzEn_{2D}$ we performed a brief study using $SampEn_{2D}$ (section 1.4.2) on dermoscopic images of 7 patients (6 women and 1 man; 53.1 ± 14.6 years old) [30]. We considered 7 dermoscopic images from a healthy region and 7 dermoscopic images from a region showing papules (neck region). The images are from the same database as the one described in section 5.2.

Our objective was also suggesting an image processing framework to help the clinician in distinguishing healthy skin from skin with papules, in dermoscopic data. Our frame-

work was based on the recently-introduced bidimensional version of the sample entropy measure, $SampEn_{2D}$. This study was published as a conference paper [30].

In our work, the parameters chosen for the computation of the bidimensional sample entropy were $\mathbf{m}= 2$ and $r = 0.15$. The results obtained from $SampEn_{2D}$ are shown in Figure 6.2. From the latter, we observe that the mean bidimensional entropy value of the

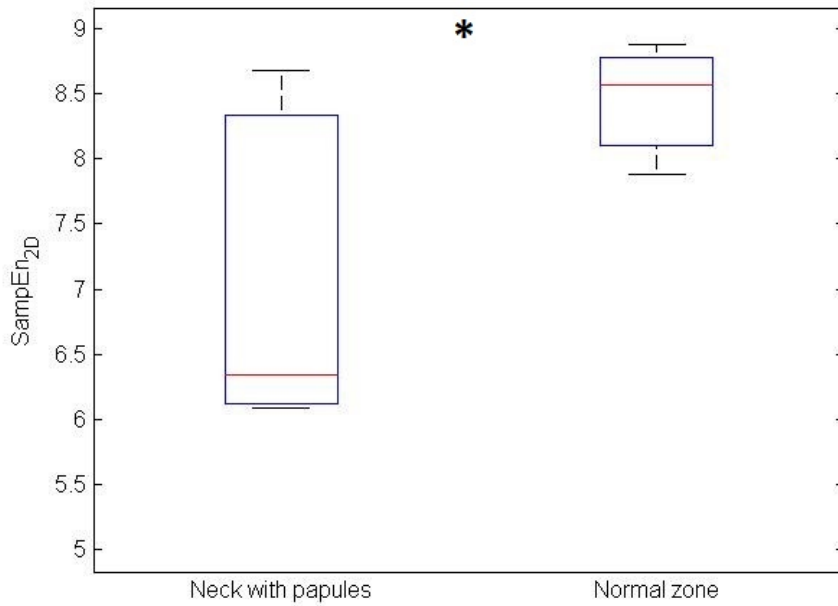


Figure 6.2 – Boxplots of the bidimensional sample entropy ($SampEn_{2D}$) values obtained from dermoscopy images recorded in PXE patients on the neck (zone with papules) and on a normal zone. The * signifies the presence of statistically significant differences between the two groups

neck images is lower than the one of the normal zone. A statistical analysis is performed to analyze if these differences could be considered as significant. For this purpose, the Wilcoxon signed rank test was used. A p -value strictly less than 0.05 was considered to define statistical significance. The results show that $p = 0.03125$. The bidimensional sample entropy values are therefore statistically significantly lower for dermoscopic images recorded in the neck than for dermoscopic images recorded in a normal zone.

Afterwards we developed this study using our newly developed $FuzEn_{2D}$ and extended it to the multiscale approach for a larger population gray scale dermoscopic images, see Section 5.2.1. Later on, we studied the dermoscopic images using the colored entropy

measures, see Section 5.2.2.

BIBLIOGRAPHY

- [1] Anne Humeau-Heurtier, « Texture feature extraction methods: A survey », *in: IEEE Access* 7 (2019), pp. 8975–9000.
- [2] Tiecheng Song et al., « Spatially weighted order binary pattern for color texture classification », *in: Expert Systems with Applications* (2020), p. 113167.
- [3] Li Liu et al., « From BoW to CNN: Two decades of texture representation for texture classification », *in: International Journal of Computer Vision* 127.1 (2019), pp. 74–109.
- [4] Li Liu et al., « Local binary features for texture classification: Taxonomy and experimental study », *in: Pattern Recognit.* 62 (2017), pp. 135–160.
- [5] Thanh Phuong Nguyen, Ngoc-Son Vu, and Antoine Manzanera, « Statistical binary patterns for rotational invariant texture classification », *in: Neurocomputing* 173 (2016), pp. 1565–1577.
- [6] Xianbiao Qi et al., « LOAD: Local orientation adaptive descriptor for texture and material classification », *in: Neurocomputing* 184 (2016), pp. 28–35.
- [7] Sheng Wang et al., « Local N -Ary pattern and its extension for texture Classification », *in: IEEE Trans. Circuits Syst. Video Technol.* 25.9 (2015), pp. 1495–1506.
- [8] Jun Zhang et al., « Scale invariant texture representation based on frequency decomposition and gradient orientation », *in: Pattern Recognit. Lett.* 51 (2015), pp. 57–62.
- [9] André R Backes, Alexandre S Martinez, and Odemir M Bruno, « Texture analysis using graphs generated by deterministic partially self-avoiding walks », *in: Pattern Recognit.* 44.8 (2011), pp. 1684–1689.
- [10] Elisa Scalco and Giovanna Rizzo, « Texture analysis of medical images for radiotherapy applications », *in: The British journal of radiology* 90.1070 (2017), p. 20160642.

-
- [11] G Castellano et al., « Texture analysis of medical images », *in: Clinical radiology* 59.12 (2004), pp. 1061–1069.
- [12] Manohar Latha and Ganesan Kavitha, « Segmentation and texture analysis of structural biomarkers using neighborhood-clustering-based level set in MRI of the schizophrenic brain », *in: Magnetic Resonance Materials in Physics, Biology and Medicine* 31.4 (2018), pp. 483–499.
- [13] Ajay Kumar and Grantham KH Pang, « Defect detection in textured materials using Gabor filters », *in: IEEE Transactions on industry applications* 38.2 (2002), pp. 425–440.
- [14] Laura Pérez-Barnuevo, Sylvie Lévesque, and Claude Bazin, « Automated recognition of drill core textures: A geometallurgical tool for mineral processing prediction », *in: Minerals Engineering* 118 (2018), pp. 87–96.
- [15] M Chica-Olmo and F Abarca-Hernandez, « Computing geostatistical image texture for remotely sensed data classification », *in: Computers & Geosciences* 26.4 (2000), pp. 373–383.
- [16] Minh-Tan Pham, Sébastien Lefèvre, and François Merciol, « Attribute profiles on derived textural features for highly textured optical image classification », *in: IEEE Geoscience and Remote Sensing Letters* 15.7 (2018), pp. 1125–1129.
- [17] Xiaoyang Tan and Bill Triggs, « Enhanced local texture feature sets for face recognition under difficult lighting conditions », *in: IEEE transactions on image processing* 19.6 (2010), pp. 1635–1650.
- [18] Young Deok Chun, Nam Chul Kim, and Ick Hoon Jang, « Content-based image retrieval using multiresolution color and texture features », *in: IEEE Transactions on Multimedia* 10.6 (2008), pp. 1073–1084.
- [19] Luiz Eduardo Virgili Silva et al., « Two-dimensional sample entropy: assessing image texture through irregularity », *in: Biomed. Phys. Eng. Express* 2.4 (2016), p. 045002.
- [20] Hamed Azami, Javier Escudero, and Anne Humeau-Heurtier, « Bidimensional distribution entropy to analyze the irregularity of small-sized textures », *in: IEEE Signal Process. Lett.* 24.9 (2017), pp. 1338–1342.

-
- [21] Christopher John Moore, « A threshold structure metric for medical image interrogation: The 2D extension of approximate entropy », *in: IV 2016, 20th Int. Conf. IEEE*, pp. 336–341.
- [22] Hamed Azami et al., « Two-dimensional dispersion entropy: An information-theoretic method for irregularity analysis of images », *in: Signal Processing: Image Communication* 75 (2019), pp. 178–187.
- [23] Jia-Rong Yeh, Chung-Wu Lin, and Jiann-Shing Shieh, « An approach of multiscale complexity in texture Analysis of lymphomas », *in: IEEE Signal Process. Lett.* 18.4 (2011), pp. 239–242.
- [24] Luciano Zunino et al., « Permutation entropy based time series analysis: Equalities in the input signal can lead to false conclusions », *in: Physics Lett. A* 381.22 (2017), pp. 1883–1892.
- [25] Luiz Fernando Segato dos Santos et al., « Multidimensional and fuzzy sample entropy (SampEnMF) for quantifying H&E histological images of colorectal cancer », *in: Comput. Biol. Med.* 103 (2018), pp. 148–160.
- [26] Mirvana Hilal et al., « Bidimensional Multiscale Fuzzy Entropy and its application to pseudoxanthoma elasticum », *in: IEEE Trans. Biomed. Eng.* 67.7 (2019), pp. 2015–2022.
- [27] Andreia Sofia F. Gaudêncio et al., « Three-dimensional Multiscale Fuzzy Entropy Applied To CT Scans Of Idiopathic Pulmonary Fibrosis Patients », *in: IEEE journal of Biomedical and Health Informatics* (), in press.
- [28] Mirvana Hilal and Anne Humeau-Heurtier, « Bidimensional fuzzy entropy: Principle analysis and biomedical applications », *in: Conf Proc IEEE Eng Med Biol Soc. (EMBC)*, IEEE, 2019, pp. 4811–4814.
- [29] Mirvana Hilal et al., « Bidimensional colored fuzzy entropy measure: a cutaneous microcirculation study », *in: 5th International Conf. on Advances in Biomed. Eng. (ICABME)*, IEEE, 2019, pp. 1–4.
- [30] Mirvana Hilal et al., « Skin alterations in pseudoxanthoma elasticum patients highlighted by the bi-dimensional sample entropy algorithm », *in: 2018 International Conference BIOMDLORE*, IEEE, 2018, pp. 1–6.

-
- [31] Andreia Sofia F. Gaudêncio et al., « Bi-dimensional colored fuzzy entropy applied to melanoma dermoscopic images », *in: Entropy 2020 – The Scientific tool of the 21st century*, 2020.
- [32] Phil Brodatz, *Textures: a photographic album for artists and designers*, Dover Pubns, 1966.
- [33] Safia Abdelmounaime and He Dong-Chen, « New Brodatz-based image databases for grayscale color and multiband texture analysis », *in: ISRN Machine Vision 2013* (2013).
- [34] *Brodatz texture dataset*, <http://www.uu.uio.no/~tranden/brodatz.html>, Accessed: 2018-04-20.
- [35] *Artificial periodic and their synthesized textures*, https://graphics.stanford.edu/projects/texture/demo/synthesis_eero.html, Accessed: 2018-04-20.
- [36] Francesco Bianconi et al., « Automatic classification of granite tiles through colour and texture features », *in: Expert Syst. with Appl.* 39.12 (2012), pp. 11212–11218.
- [37] Antonio Fernández et al., « Evaluation of robustness against rotation of LBP, CCR and ILBP features in granite texture classification », *in: Machine Vision and Appl.* 22.6 (2011), pp. 913–926.
- [38] Gustaf Kylberg, *The Kylberg Texture Dataset v. 1.0*, External report (Blue series) 35, Centre for Image Analysis, Swedish University of Agricultural Sciences and Uppsala University, Uppsala, Sweden, Sept. 2011.
- [39] Yanxi Liu, Wen-Chieh Lin, and James Hays, « Near-regular texture analysis and manipulation », *in: ACM Transactions on Graphics (TOG)* 23.3 (2004), pp. 368–376.
- [40] A. Ravishankar Rao and Gerald L. Lohse, « Identifying high level features of texture perception », *in: CVGIP: Graphical Models and Image Processing* 55.3 (1993), pp. 218–233.
- [41] Hideyuki Tamura, Shunji Mori, and Takashi Yamawaki, « Textural features corresponding to visual perception », *in: IEEE Transactions on Systems, man, and cybernetics* 8.6 (1978), pp. 460–473.
- [42] Luiz Eduardo Virgilio Silva et al., « Two-dimensional multiscale entropy analysis: applications to image texture evaluation », *in: Signal Process.* 147 (2018), pp. 224–232.

-
- [43] Anne Humeau-Heurtier, Ana Carolina Mieko Omoto, and Luiz Eduardo Virgilio Silva, « Bi-dimensional multiscale entropy: relation with discrete Fourier transform and biomedical application », *in: Comput. Med. Biol.* (2018).
- [44] Shahera Hossain and Seiichi Serikawa, « Texture databases—a comprehensive survey », *in: Pattern Recognition Letters* 34.15 (2013), pp. 2007–2022.
- [45] Francesco Bianconi and Antonio Fernández, « An appendix to “Texture databases—A comprehensive survey” », *in: Pattern recognition letters* 45 (2014), pp. 33–38.
- [46] P Mohanaiah, P Sathyanarayana, and L GuruKumar, « Image texture feature extraction using GLCM approach », *in: International journal of scientific and research publications* 3.5 (2013), pp. 1–5.
- [47] Andrés Larroza, Vicente Bodi, David Moratal, et al., « Texture analysis in magnetic resonance imaging: review and considerations for future applications », *in: Assessment of cellular and organ function and dysfunction using direct and derived MRI methodologies* (2016), pp. 75–106.
- [48] Robert M Haralick, Karthikeyan Shanmugam, and Its’ Hak Dinstein, « Textural features for image classification », *in: IEEE Trans. Syst. Man Cybern. Syst.* 6 (1973), pp. 610–621.
- [49] Carl Philips et al., « Directional invariance of co-occurrence matrices within the liver », *in: 2008 International Conference on Biocomputation, Bioinformatics, and Biomedical Technologies*, IEEE, 2008, pp. 29–34.
- [50] Jianguo Zhang and Tieniu Tan, « Brief review of invariant texture analysis methods », *in: Pattern recognition* 35.3 (2002), pp. 735–747.
- [51] Andrzej Materka, Michal Strzelecki, et al., « Texture analysis methods—a review », *in: Technical university of lodz, institute of electronics, COST B11 report, Brussels* 10.1.97 (1998), p. 4968.
- [52] Christoph Palm, « Color texture classification by integrative co-occurrence matrices », *in: Pattern recognition* 37.5 (2004), pp. 965–976.
- [53] André Ricardo Backes, Dalcimar Casanova, and Odemir Martinez Bruno, « Color texture analysis based on fractal descriptors », *in: Pattern Recognition* 45.5 (2012), pp. 1984–1992.
- [54] Alexandru Drimborean and Paul F Whelan, « Experiments in colour texture analysis », *in: Pattern recognition letters* 22.10 (2001), pp. 1161–1167.

-
- [55] Qing Xu, Jie Yang, and Siyi Ding, « Color texture analysis using the wavelet-based hidden Markov model », *in: Pattern Recognition Letters* 26.11 (2005), pp. 1710–1719.
- [56] Vincent Arvis et al., « Generalization of the cooccurrence matrix for colour images: application to colour texture classification », *in: Image Analysis & Stereology* 23.1 (2004), pp. 63–72.
- [57] Olivier Alata et al., « Choice of a pertinent color space for color texture characterization using parametric spectral analysis », *in: Pattern Recognition* 44.1 (2011), pp. 16–31.
- [58] Francesco Bianconi et al., « Theoretical and experimental comparison of different approaches for color texture classification », *in: Journal of Electronic Imaging* 20.4 (2011), p. 043006.
- [59] Ludwig Boltzmann, « The second law of thermodynamics », *in: Theoretical physics and philosophical problems*, Springer, 1974, pp. 13–32.
- [60] Claude Elwood Shannon, « A mathematical theory of communication », *in: Bell Syst. Technical J.* 27.3 (1948), pp. 379–423.
- [61] Sanjoy Basu, *Illustration example*, Available from: <https://medium.com/@sanjoybasu/entropy-from-thermodynamics-to-machine-learning-d82239256462>, accessed: April, 2020.
- [62] Marta Borowska, « Entropy-based algorithms in the analysis of biomedical signals », *in: Studies in Logic, Grammar and Rhetoric* 43.1 (2015), pp. 21–32.
- [63] Geoff Dougherty, *Digital image processing for medical applications*, Cambridge University Press, 2009.
- [64] Annick Lesne, « Shannon entropy: a rigorous notion at the crossroads between probability, information theory, dynamical systems and statistical physics », *in: Mathematical Structures in Computer Science* 24.3 (2014).
- [65] Steven M Pincus, « Approximate entropy as a measure of system complexity. », *in: Proc. Natl. Acad. Sci.* 88.6 (1991), pp. 2297–2301.
- [66] Steve Pincus, « Approximate entropy (ApEn) as a complexity measure », *in: Chaos: An Interdisciplinary Journal of Nonlinear Science* 5 (1995), pp. 110–117.

-
- [67] Joshua S Richman and J Randall Moorman, « Physiological time-series Analysis using approximate entropy and sample entropy », *in: Am. J. Physiol.* 278.6 (2000), H2039–H2049.
- [68] Weiting Chen et al., « Characterization of surface EMG signal based on fuzzy entropy », *in: IEEE Trans. Neural. Syst. Rehabil. Eng.* 15.2 (2007), pp. 266–272.
- [69] Peng Li et al., « Assessing the complexity of short-term heartbeat interval series by distribution entropy », *in: Medical & Biological Eng. & Computing* 53.1 (2015), pp. 77–87.
- [70] Christoph Bandt and Bernd Pompe, « Permutation entropy: a natural complexity measure for time series », *in: Physical review letters* 88.17 (2002), p. 174102.
- [71] Mostafa Rostaghi and Hamed Azami, « Dispersion entropy: A measure for time-series analysis », *in: IEEE Signal Processing Letters* 23.5 (2016), pp. 610–614.
- [72] Hamed Azami, Alberto Fernández, and Javier Escudero, « Refined multiscale fuzzy entropy based on standard deviation for biomedical signal analysis », *in: Medical & biological engineering & computing* 55.11 (2017), pp. 2037–2052.
- [73] Eva Cirugeda-Roldan et al., « Comparative study of entropy sensitivity to missing biosignal data », *in: Entropy* 16.11 (2014), pp. 5901–5918.
- [74] Yuzhen Cao et al., « Characterization of complexity in the electroencephalograph activity of Alzheimer’s Disease based on fuzzy entropy », *in: Chaos* 25.8 (2015), p. 083116.
- [75] Xavier Bornas et al., « Sample entropy of ECG time series of fearful flyers: preliminary results. », *in: Nonlinear dynamics, psychology, and life sciences* 10.3 (2006), pp. 301–318.
- [76] Hong-Bo Xie et al., « Complexity analysis of the biomedical signal using fuzzy entropy measurement », *in: Appl. Soft Comput.* 11.2 (2011), pp. 2871–2879.
- [77] Mosabber U Ahmed et al., « A multivariate multiscale fuzzy entropy algorithm with application to uterine EMG complexity analysis », *in: Entropy* 19.1 (2017), p. 2.
- [78] Dariusz S Radomski, « A multivariate sample entropy of differentiated electrohysterographical signals for an identification of an uterine labor activities », *in: Inform. Technologies in Biomedicine, Volume 4*, Springer, 2014, pp. 303–310.

-
- [79] Steven M Pincus and Richard R Viscarello, « Approximate entropy: a regularity measure for fetal heart rate analysis », *in: Obstet Gynecol* 79.2 (1992), pp. 249–255.
- [80] Malihe Sabeti, Serajeddin Katebi, and Reza Boostani, « Entropy and complexity measures for EEG signal classification of schizophrenic and control participants », *in: Artificial intelligence in medicine* 47.3 (2009), pp. 263–274.
- [81] U Rajendra Acharya et al., « Automated diagnosis of epileptic EEG using entropies », *in: Biomedical Signal Processing and Control* 7.4 (2012), pp. 401–408.
- [82] Joshua S Richman, Douglas E Lake, and J Randall Moorman, « Sample entropy », *in: Methods in Enzymology*, vol. 384, Elsevier, 2004, pp. 172–184.
- [83] Raul Alcaraz and Jose Joaquin Rieta, « A review on sample entropy applications for the non-invasive analysis of atrial fibrillation electrocardiograms », *in: Biomedical Signal Processing and Control* 5.1 (2010), pp. 1–14.
- [84] Xu Zhang and Ping Zhou, « Sample entropy analysis of surface EMG for improved muscle activity onset detection against spurious background spikes », *in: Journal of Electromyography and Kinesiology* 22.6 (2012), pp. 901–907.
- [85] Weiting Chen et al., « Measuring complexity using fuzzyen, apen, and sampen », *in: Med. Eng. Phys.* 31.1 (2009), pp. 61–68.
- [86] Chengyu Liu et al., « Analysis of heart rate variability using fuzzy measure entropy », *in: Comput. Biol. Med.* 43.2 (2013), pp. 100–108.
- [87] Guo-liang Xiong et al., « A comparative study on ApEn, SampEn and their fuzzy counterparts in a multiscale framework for feature extraction », *in: Journal of Zhejiang University SCIENCE A* 11.4 (2010), pp. 270–279.
- [88] Costa, Madalena and Goldberger, Ary L. and Peng, C.K, « Multiscale entropy analysis of complex physiologic time series », *in: Phys. Rev. Lett.* 89.6 (2002), p. 068102.
- [89] Hamed Azami and Javier Escudero, « Coarse-graining approaches in univariate multiscale sample and dispersion entropy », *in: Entropy* 20.2 (2018), p. 138.
- [90] Anne Humeau-Heurtier, « The multiscale entropy algorithm and its variants: a review », *in: Entropy* 17.5 (2015), pp. 3110–3123.

-
- [91] Madalena Costa, Ary L Goldberger, and C-K Peng, « Multiscale entropy analysis of biological signals », *in: Phys. Rev. E* 71.2 (2005), p. 021906.
- [92] Shuen-De Wu et al., « Modified multiscale entropy for short-term time series analysis », *in: Physica A: Statistical Mechanics and its Applications* 392.23 (2013), pp. 5865–5873.
- [93] Hamed Azami and Javier Escudero, « Amplitude-and fluctuation-based dispersion entropy », *in: Entropy* 20.3 (2018), p. 210.
- [94] Haroldo V Ribeiro et al., « Complexity-entropy causality plane as a complexity measure for two-dimensional patterns », *in: PloS one* 7.8 (2012), e40689.
- [95] Caron M Grin, Kent P Friedman, and Jane M Grant-Kels, « Dermoscopy: a review. », *in: Dermatologic clinics* 20.4 (2002), pp. 641–6.
- [96] Matthew G Fleming et al., « Techniques for a structural analysis of dermatoscopic imagery », *in: Comput. Med. Imaging Graph.* 22.5 (1998), pp. 375–389.
- [97] « Chapter 3 - Dermoscopy », *in: Imaging in Dermatology*, ed. by Michael R. Hamblin, Pinar Avci, and Gaurav K. Gupta, Boston: Academic Press, 2016, pp. 13–28.
- [98] Harold Kittler et al., « Diagnostic accuracy of dermoscopy », *in: The lancet oncology* 3.3 (2002), pp. 159–165.
- [99] Aimilios Lallas et al., « Management rules to detect melanoma », *in: Dermatology* 226.1 (2013), pp. 52–60.
- [100] Hiroshi Sakai et al., « Assessment of the colors of melanin pigment in acral compound nevus by using a novel dermoscopy technique with surgical light illumination and saturation analysis », *in: Dermatology practical & conceptual* 4.4 (2014), p. 51.
- [101] Michael Binder et al., « Epiluminescence microscopy: a useful tool for the diagnosis of pigmented skin lesions for formally trained dermatologists », *in: Archives of dermatology* 131.3 (1995), pp. 286–291.
- [102] Z. Paštar D. Ćurković and K. Kostović, « Dermoscopy and early melanoma », *in: Collegium Antropologicum* 39.3 (2015), pp. 791–795.
- [103] Irwin M Braverman, « The cutaneous microcirculation », *in: Journal of Investigative Dermatology Symposium Proceedings*, vol. 5, 1, Elsevier, 2000, pp. 3–9.

-
- [104] Cristina Pires Camargo and Rolf Gemperli, « Endothelial Function in Skin Microcirculation », *in: Endothelium and Cardiovascular Diseases*, Elsevier, 2018, pp. 673–679.
- [105] Matthieu Roustit and Jean-Luc Cracowski, « Assessment of endothelial and neurovascular function in human skin microcirculation », *in: Trends in pharmacological sciences* 34.7 (2013), pp. 373–384.
- [106] Philippe Franco do Amaral Tafner et al., « Recent advances in bedside microcirculation assessment in critically ill patients », *in: Revista Brasileira de terapia intensiva* 29.2 (2017), p. 238.
- [107] Can Ince, « Hemodynamic coherence and the rationale for monitoring the microcirculation », *in: Crit Care* 19.3 (2015), S8.
- [108] Geoffroy Hariri et al., « Narrative review: clinical assessment of peripheral tissue perfusion in septic shock », *in: Ann Intensive Care* 9.1 (2019), p. 37.
- [109] Sam Eriksson, Jan Nilsson, and Christian Stureson, « Non-invasive imaging of microcirculation: a technology review », *in: Med Devices (Auckl)* 7 (2014), p. 445.
- [110] Anne Humeau-Heurtier et al., « Relevance of laser Doppler and laser speckle techniques for assessing vascular function: state of the art and future trends », *in: IEEE Trans Biomed Eng* 60.3 (2013), pp. 659–666.
- [111] Carl J Pepine, « Clinical implications of endothelial dysfunction », *in: Clin Cardiol* 21.11 (1998), pp. 795–799.
- [112] M Naouri et al., « Manifestations of Pseudoxanthoma Elasticum in childhood », *in: Br. J. Dermatol.* 161.3 (2009), pp. 635–639.
- [113] Genetics Home Reference. Bethesda (MD): The Library, *National Library of Medicine (US)*, Available from: <https://ghr.nlm.nih.gov/condition/pseudoxanthoma-elasticum>, reviewed: January 2015, published: March 31, 2020, accessed: April, 2020.
- [114] Nicolas Chassaing et al., « Pseudoxanthoma Elasticum: a clinical, pathophysiological and genetic update including 11 novel ABCC6 Mutations », *in: J. Med. Genet.* 42.12 (2005), pp. 881–892.
- [115] S Kawashima et al., « Dermoscopic features of Pseudoxanthoma Elasticum », *in: Clin Exp Dermatol.* 43.2 (2018), pp. 175–179.

-
- [116] Barbara Marconi et al., « Pseudoxanthoma Elasticum and skin: Clinical manifestations, histopathology, pathomechanism, perspectives of treatment », *in: Intractable & Rare Diseases Research* 4.3 (2015), pp. 113–122.
- [117] John F Klement et al., « Targeted ablation of the ABCC6 gene results in ectopic mineralization of connective tissues », *in: Mol Cell Biol.* 25.18 (2005), pp. 8299–8310.
- [118] Daniela Quaglino et al., « The multifaceted complexity of genetic diseases: a lesson from pseudoxanthoma elasticum », *in: Advances in the study of genetic disorders* (2011), pp. 289–318.
- [119] Kenneth H Neldner and Berthold Struk, « Pseudoxanthoma elasticum », *in: Connective tissue and its heritable disorders. 2nd ed. New York: Wiley-Liss* (2002), pp. 561–83.
- [120] Leon J Schurgers, Jouni Uitto, and Chris P Reutelingsperger, « Vitamin K-dependent carboxylation of matrix Gla-protein: a crucial switch to control ectopic mineralization », *in: Trends in molecular medicine* 19.4 (2013), pp. 217–226.
- [121] Kenneth H Neldner, « Pseudoxanthoma Elasticum », *in: Int. J. of Dermatology* 27.2 (1988), pp. 98–100.
- [122] M Emre Celebi, Noel Codella, and Allan Halpern, « Dermoscopy image analysis: overview and future directions », *in: IEEE J. Biomed. Health Inform.* 23.2 (2019), pp. 474–478.
- [123] Lidia Talavera-Martinez, Pedro Bibiloni, and Manuel González-Hidalgo, « Computational Texture Features of Dermoscopic Images and Their Link to the Descriptive Terminology - A Survey », *in: Comput. Methods Programs Biomed.* (2019), p. 105049.
- [124] Catarina Barata, M Emre Celebi, and Jorge S Marques, « A survey of feature extraction in dermoscopy image analysis of skin cancer », *in: IEEE J. Biomed. Health Inform.* 23.3 (2018), pp. 1096–1109.
- [125] Marlene Machado, Jorge Pereira, and Rui Fonseca-Pinto, « Classification of reticular pattern and streaks in dermoscopic images based on texture analysis », *in: J. Med. Imaging* 2.4 (2015), p. 044503.

-
- [126] Rahil Garnavi, Mohammad Aldeen, and James Bailey, « Computer-aided diagnosis of melanoma using border-and wavelet-based texture analysis », *in: IEEE Trans. Inf. Technol. Biomed.* 16.6 (2012), pp. 1239–1252.
- [127] Aurora Sáez et al., « Statistical detection of colors in dermoscopic images with a texton-based estimation of probabilities », *in: IEEE J. Biomed. Health Inform.* 23.2 (2018), pp. 560–569.
- [128] A Gola Isasi, B Garcia Zapirain, and A Méndez Zorrilla, « Melanomas non-invasive diagnosis application based on the ABCD rule and pattern recognition image processing algorithms », *in: Comput. Biol. Med.* 41.9 (2011), pp. 742–755.
- [129] M Emre Celebi and Azaria Zornberg, « Automated quantification of clinically significant colors in dermoscopy images and its application to skin lesion classification », *in: IEEE systems journal* 8.3 (2014), pp. 980–984.
- [130] M Emre Celebi et al., « A methodological approach to the classification of dermoscopy images », *in: Comput. Med. Imaging Graph.* 31.6 (2007), pp. 362–373.
- [131] Ulla Møller Weinreich et al., « The effect of comorbidities on COPD assessment: a pilot study », *in: International journal of chronic obstructive pulmonary disease* 10 (2015), p. 429.
- [132] Norbert F Voelkel, Shiro Mizuno, and Carlyne D Cool, « The Spectrum of Pulmonary Disease in COPD », *in: COPD*, Springer, 2017, pp. 195–207.
- [133] FL 32207 2019 Emed Multispecialty Group Jacksonville, *COPD*, Available from: <https://emedmultispecialtygroup.com/2018/02/26/copd-can-treated-risks/>, accessed: April, 2020.
- [134] Theo Vos et al., « Global, regional, and national incidence, prevalence, and years lived with disability for 310 diseases and injuries, 1990–2015: a systematic analysis for the Global Burden of Disease Study 2015 », *in: The Lancet* 388.10053 (2016), pp. 1545–1602.
- [135] Yu Shi et al., « Prediction of progression in idiopathic pulmonary fibrosis using CT scans at baseline: A quantum particle swarm optimization-Random forest approach », *in: Artificial intelligence in medicine* 100 (2019), p. 101709.
- [136] Lung National Heart and Blood Institute, *IPF*, Available from: <https://www.nhlbi.nih.gov/health-topics/idiopathic-pulmonary-fibrosis>, accessed: April, 2020.

-
- [137] Thomas J Gross and Gary W Hunninghake, « Idiopathic pulmonary fibrosis », *in: New England Journal of Medicine* 345.7 (2001), pp. 517–525.
- [138] Talmadge E King Jr, Annie Pardo, and Moisés Selman, « Idiopathic pulmonary fibrosis », *in: The Lancet* 378.9807 (2011), pp. 1949–1961.
- [139] Joseph P Lynch III and John A Belperio, « Idiopathic pulmonary fibrosis », *in: Diffuse Lung Disease* (2020), p. 171.
- [140] Mayo Foundation for Medical Education and Research (MFMER), *Uterine embolization*, Available from: <https://www.mayoclinic.org/diseases-conditions/uterine-fibroids/diagnosis-treatment/drc-20354294>, accessed: April, 2020.
- [141] Yoshiko Ueno et al., « Endometrial carcinoma: MR imaging–based texture model for preoperative risk stratification—a preliminary analysis », *in: Radiology* 284.3 (2017), pp. 748–757.
- [142] Natally Horvat et al., « MR imaging of rectal cancer: radiomics analysis to assess treatment response after neoadjuvant therapy », *in: Radiology* 287.3 (2018), pp. 833–843.
- [143] Andreas Wibmer et al., « Haralick texture analysis of prostate MRI: utility for differentiating non-cancerous prostate from prostate cancer and differentiating prostate cancers with different Gleason scores », *in: European radiology* 25.10 (2015), pp. 2840–2850.
- [144] Huihui Xie et al., « Preliminary utilization of radiomics in differentiating uterine sarcoma from atypical leiomyoma: Comparison on diagnostic efficacy of MRI features and radiomic features », *in: European journal of radiology* 115 (2019), pp. 39–45.
- [145] Yulia Lakhman et al., « Differentiation of uterine leiomyosarcoma from atypical leiomyoma: diagnostic accuracy of qualitative MR imaging features and feasibility of texture analysis », *in: European radiology* 27.7 (2017), pp. 2903–2915.
- [146] Jasper Fuk-Woo Chan et al., « A familial cluster of pneumonia associated with the 2019 novel coronavirus indicating person-to-person transmission: a study of a family cluster », *in: The Lancet* 395.10223 (2020), pp. 514–523.
- [147] Zheng Ye et al., « Chest CT manifestations of new coronavirus disease 2019 (COVID-19): a pictorial review », *in: European radiology* (2020), pp. 1–9.

-
- [148] Adam Bernheim et al., « Chest CT findings in coronavirus disease-19 (COVID-19): relationship to duration of infection », *in: Radiology* (2020), p. 200463.
- [149] Carole Jalaber et al., « Chest CT in COVID-19 pneumonia: a review of current knowledge », *in: Diagnostic and Interventional Imaging* (2020).
- [150] Yicheng Fang et al., « Sensitivity of chest CT for COVID-19: comparison to RT-PCR », *in: Radiology* (2020), p. 200432.
- [151] Vincent CC Cheng et al., « Escalating infection control response to the rapidly evolving epidemiology of the Coronavirus disease 2019 (COVID-19) due to SARS-CoV-2 in Hong Kong », *in: Infection Control & Hospital Epidemiology* 41.5 (2020), pp. 493–498.
- [152] Nanshan Chen et al., « Epidemiological and clinical characteristics of 99 cases of 2019 novel coronavirus pneumonia in Wuhan, China: a descriptive study », *in: The Lancet* 395.10223 (2020), pp. 507–513.
- [153] Hong-Bo Xie et al., « Fuzzy entropy and its application for enhanced subspace filtering », *in: IEEE Trans. Fuzzy Syst.* 26.4 (2018), pp. 1970–1982.
- [154] Jie Xiang et al., « The detection of epileptic seizure signals based on fuzzy entropy », *in: J. Neurosci. Methods* 243 (2015), pp. 18–25.
- [155] Hamed Azami et al., « Fuzzy entropy metrics for the analysis of biomedical signals: assessment and comparison », *in: IEEE Access* 7 (2019), pp. 104833–104847.
- [156] Hong-Bo Xie et al., « Cross-fuzzy entropy: a new method to test pattern synchrony of bivariate time series », *in: Inform. Sciences* 180.9 (2010), pp. 1715–1724.
- [157] Christopher Moore and Thomas Marchant, « The approximate entropy concept extended to three dimensions for calibrated, single parameter structural complexity interrogation of volumetric images », *in: Physics in Medicine & Biology* 62.15 (2017), p. 6092.
- [158] TE Marchant and CJ Moore, « Novel 3D Approximate Entropy parameter for Quality Assessment of CT/CBCT Images », *in: Radiotherapy and Oncology*, vol. 99, 2011, S457–S458.
- [159] Tom Marchant et al., « Quantifying structure regularity in fluorescence microscopy cell images using a novel multi-dimensional approximate entropy metric », *in: 2011 18th IEEE International Conference on Image Processing*, IEEE, 2011, pp. 3085–3088.

-
- [160] Jean-Marc Girault and Anne Humeau-Heurtier, « Centered and averaged fuzzy entropy to improve fuzzy entropy precision », *in: Entropy* 20.4 (2018), p. 287.
- [161] Pascal Getreuer, *Colorspace Transformations*, <https://www.mathworks.com/matlabcentral/fileexchange/28790-colorspace-transformations>, MATLAB Central File Exchange, Accessed: 25/09/2019.
- [162] *Colored Brodatz Texture*, <http://multibandtexture.recherche.usherbrooke.ca/>, Accessed: 25/11/2019.
- [163] FotoFinder Systems, *FotoFinder bodystudio ATBM for total body mapping and dermoscopy*. Available from: <https://www.fotofinder.de/fr/technologie/diagnostic-du-cancer-de-la-peau/bodystudio-atbm/>, accessed: April, 2020.
- [164] Jacob Cohen, *Statistical power analysis for the behavioral sciences*, Routledge, 2013.
- [165] Harald Hentschke and Maik C Stüttgen, « Computation of measures of effect size for neuroscience data sets », *in: Eur. J. Neurosci.* 34.12 (2011), pp. 1887–1894.
- [166] Lee A Becker, « Effect size (ES) », *in: Retrieved September 9* (2000), p. 2007.
- [167] Shlomo S Sawilowsky, « New effect size rules of thumb », *in: Journal of Modern Applied Statistical Methods* 8.2 (2009), p. 26.
- [168] Philipp Tschandl, *The HAM10000 dataset, a large collection of multi-source dermatoscopic images of common pigmented skin lesions*, version V1, 2018.
- [169] Philipp Tschandl, Cliff Rosendahl, and Harald Kittler, « The HAM10000 dataset: A large collection of multi-source dermatoscopic images of common pigmented skin lesions », *in: arXiv preprint arXiv:1803.10417* (2018).
- [170] Víctor Martínez-Cagigal, *ROC curve*, <https://www.mathworks.com/matlabcentral/fileexchange/52442-roc-curve>, MATLAB Central File Exchange, Accessed: 05/12/2019.
- [171] David A Lynch et al., « Diagnostic criteria for idiopathic pulmonary fibrosis: a Fleischner Society White Paper », *in: The Lancet Respiratory Medicine* 6.2 (2018), pp. 138–153.
- [172] Ganesh Raghu et al., « Diagnosis of idiopathic pulmonary fibrosis. An official ATS/ERS/JRS/ALAT clinical practice guideline », *in: American journal of respiratory and critical care medicine* 198.5 (2018), e44–e68.

-
- [173] Madalena D Costa and Ary L Goldberger, « Generalized multiscale entropy analysis: Application to quantifying the complex volatility of human heartbeat time series », *in: Entropy* 17.3 (2015), pp. 1197–1203.

Titre : Mesures bas es sur la th orie de l'information pour l'analyse d'images : D veloppement de mesures d'entropie bidimensionnelles et tridimensionnelles pour l' valuation de la texture des images et applications au domaine biom dical.

Mot cl s : Entropie, th orie de l'information, textures, irr gularit , complexit .

R sum  : Le d veloppement de mesures informatis es pour le domaine m dical contribue   am liorer la capacit  de diagnostic, de pronostic et de suivi. Cela fournit une  valuation objective des donn es et aide les m decins   identifier des anomalies et   prendre des d cisions. Dans ce manuscrit de th se, nous avons d velopp  des mesures d'entropie bas es sur la th orie de l'information. Nous montrons que ces m thodes ont la capacit  de quantifier l'irr gularit  des images en niveaux de gris, des images couleurs, et enfin des volumes. Nos algorithmes ont trouv  des applications prometteuses dans l'analyse de texture pour diff rents cas cliniques : traite-

ment d'images de dermoscopie de m lanome, de pseudoxanthome  lastique et l'analyse de la microcirculation cutan e. En outre, apr s des r sultats concluants sur des images en niveaux de gris, nous avons utilis  l'approche couleurs sur l'images de dermoscopie. Enfin, pour  tendre nos applications m dicales, nous avons utilis  nos mesures d'entropie tridimensionnelles pour analyser des acquisitions volum triques. Ces m thodes ont permis d' tudier des tomographies, des tomographies haute r solution et des volumes IRM dans des cas cliniques de COVID-19, de fibrose pulmonaire idiopathique et de fibrome ut rin, respectivement.

Title: Information-theory based measures for image analysis: Development of two- and three-dimensional entropy measures for image texture evaluation and their application to the biomedical field.

Keywords: Entropy, information theory, textures, irregularity, complexity, medical images.

Abstract: Developing computer-based measures for applications in medical field helps to improve prognostic, diagnostic, follow up, and predictive abilities. It provides objective assessment for the data and aids medical doctors in making decisions, identifying abnormalities, and eventually saving lives. In this thesis manuscript, we developed entropy measures based on the information theory concept. These methods were illustrated to possess an ability to analyze irregularity of gray scale images, colored images, and finally volumes. Our proposed algorithms found promis-

ing applications in texture analysis for different medical cases such as melanoma, pseudoxanthoma elasticum, and cutaneous microcirculation analysis. Furthermore, after the successful findings on gray scale images, we employed the colored approach for dermoscopic images. Finally, to expand the medical applications, we used our tridimensional entropy measure to study volumetric scans. These methods were employed to study CT scans, HRCT scans, and MRI scans for COVID-19, idiopathic pulmonary fibrosis, and uterine fibroma cases, respectively.